

2011

# Rationalizing the structures of Zintl and polar intermetallic phases

Fei Wang  
Iowa State University

Follow this and additional works at: <https://lib.dr.iastate.edu/etd>

 Part of the [Chemistry Commons](#)

## Recommended Citation

Wang, Fei, "Rationalizing the structures of Zintl and polar intermetallic phases" (2011). *Graduate Theses and Dissertations*. 11943.  
<https://lib.dr.iastate.edu/etd/11943>

This Dissertation is brought to you for free and open access by the Iowa State University Capstones, Theses and Dissertations at Iowa State University Digital Repository. It has been accepted for inclusion in Graduate Theses and Dissertations by an authorized administrator of Iowa State University Digital Repository. For more information, please contact [digirep@iastate.edu](mailto:digirep@iastate.edu).

**Rationalizing the structures of Zintl and polar intermetallic phases**

by

**Fei Wang**

A dissertation submitted to the graduate faculty  
in partial fulfillment of the requirements for the degree of

**DOCTOR OF PHILOSOPHY**

Major: Inorganic Chemistry

Program of Study Committee:

Gordon J. Miller, Major Professor

John D. Corbett

Mark S. Gordon

Vitalij K. Pecharsky

Patricia A. Thiel

Iowa State University

Ames, Iowa

2011

Copyright © Fei Wang, 2011. All rights reserved.

***Dedicated to Mom and Dad.***

## TABLE OF CONTENTS

Acknowledgement .....	v
Chapter 1. Introduction .....	1
1.1 The Specialties of Zintl and Polar Intermetallic Phases .....	1
1.2 Zintl-Klemm Formalism – Success and Limitations .....	2
1.3 Rationalizing Structures with Quantum Mechanical Calculations .....	4
1.4 Handling the Coloring Problem .....	6
1.5 Layout of the Dissertation .....	7
1.6 References .....	8
Chapter 2. Experimental and Computational Techniques, in General .....	11
2.1 Syntheses .....	11
2.2 Characterization .....	11
2.3 Computations .....	12
2.4 References .....	13
Chapter 3. Revisiting the Zintl-Klemm Concept I: Alkali Metal Trielides .....	15
3.1 Abstract .....	15
3.2 Introduction .....	15
3.3 Computational Details .....	20
3.4 Results and Discussions .....	25
3.5 Conclusions .....	40
3.6 Acknowledgements .....	41
3.7 References .....	41
3.8 Supporting Information .....	46
Chapter 4. Revisiting the Zintl-Klemm Concept II: $A_2AuBi$ ( $A =$ Alkali Metals) .....	56
4.1 Abstract .....	56
4.2 Introduction .....	56
4.3 Computational Details .....	58
4.4 Results and Discussions .....	60
4.5 Conclusions .....	73
4.6 Acknowledgements .....	73
4.7 References .....	73
4.8 Supporting Information .....	76



Chapter 5. $\text{EuAg}_x\text{Al}_{11-x}$ with the $\text{BaCd}_{11}$ -Type Structure: Phase Width, Coloring, and Electronic Structure .....	78
5.1 Abstract .....	78
5.2 Introduction .....	78
5.3 Experiments .....	80
5.4 Results and Discussions .....	82
5.5 Conclusions .....	91
5.6 Acknowledgements .....	91
5.7 References .....	91
5.8 Supporting Information .....	94
Chapter 6. $\text{EuAg}_x\text{Al}_{11-x}$ with the $\text{BaHg}_{11}$ -Type Structure: Composition, Coloring, and Competition with the $\text{BaCd}_{11}$ -Type Structure .....	103
6.1 Abstract .....	103
6.2 Introduction .....	103
6.3 Experiments .....	105
6.4 Results and Discussions .....	107
6.5 Conclusions .....	118
6.6 Acknowledgements .....	118
6.7 References .....	119
6.8 Supporting Information .....	122
Chapter 7. Stacking Polymorphs in $\text{Gd}_5\text{Si}_4$ , $\text{Gd}_5\text{Ge}_4$ , and $\text{Gd}_5\text{Si}_2\text{Bi}_2$ : A Computational Investigation .....	132
7.1 Introduction .....	132
7.2 Computational Details .....	133
7.3 Results and Discussions .....	135
7.4 Conclusions .....	139
7.5 References .....	140
Chapter 8. Conclusions and Future Work .....	142

## Acknowledgement

Upon the completion of my graduate study, I would really like to show my gratitude to my teachers, colleagues, and friends who made my time in Iowa State University a lifelong memory. First of all, I shall thank my major professor, Dr. Gordon J. Miller. His expertise in solid state chemistry and patience in helping students make him an exemplary mentor. I have learned from him not just chemistry but also how to be a good researcher. I would then like to express my gratitude to Dr. John D. Corbett, Dr. Mark S. Gordon, Dr. Vitalij K. Pecharsky, and Dr. Patricia A. Thiel for serving in my Program of Study Committee. I have learned so much from them through discussions and their classes.

I also wish to thank Dr. Warren Straszheim, who devoted great efforts in Scanning Electron Microscopy characterization for my samples, and Dr. Mike Schmidt, who offered enormous help in installing and maintaining VASP on CRUNCH. I should also thank Dr. German Samolyuk and Dr. Dajiang Liu for they taught me a lot in computations. I owe tremendous gratitude to all my colleagues in Miller's and Corbett's groups. Dr. Tae-Soo You, Dr. Sumohan Misra, Dr. Hyunjin Ko, and Dr. Mi-Kyung Han trained me in experimental and computational techniques. Dr. Srinivasa Thimmaiah, Dr. Qisheng Lin, Dr. Shalabh Gupta, Dr. Hui Wang, and Jakoah Brgoch offered me great helps all the time. My research could not have been done without the support from NSF 02-441092 and 06-05949. Our computations were all done on the CRUNCH system, supported by Computation Advisory Committee project 202-17-10-08-0005 of Iowa State University.

I would also like to express my appreciation to all my friends in Ames, including my host family Ed and Margreet van Ouwerkerk, the families of Foote's, Reese's, Hansen's, Hinson's, Dubrovskiy's and Luiken's, the "Wednesday men's lunch club", and all of my Chinese buddies, for making my life out of lab colorful, enjoyable, and full of fun.

This dissertation is dedicated to my parents. Their unvarying love, support, and encouragement have enabled me to reach the completion of my graduate education. I owe everything I have today to them!

## Chapter 1

### Introduction

#### 1.1 The Specialties of Zintl and Polar Intermetallic Phases

Zintl phases<sup>1-8</sup> are those compounds composed of electropositive metals (e.g. alkali metals, alkaline earth metals, and rare earth metals) and electronegative metals around the “Zintl line”, which divides columns 13 and 14 in the periodic table. Polar intermetallic phases<sup>9-11</sup> have the definition similar to Zintl phases but, in general, the electronegativity difference ( $\Delta\chi$ ) between the constituting electropositive and electronegative metals is smaller than in Zintl phases. However, there is no specific critical  $\Delta\chi$  that separates Zintl phases and polar intermetallics.

These phases keep intriguing solid-state chemists. The reasons lie in both their virtues for applications and their theoretical challenges. Many Zintl and polar intermetallic phases exhibit novel properties, so they are promising for many applications, for example, superconductors,<sup>12</sup> thermoelectric materials,<sup>13-18</sup> hydrogen storage materials,<sup>19-20</sup> and enhanced magnetocaloric materials.<sup>21</sup> So it is valuable to investigate further their properties and potential applications. Since properties are the expression of structures in both real space (crystal structure) and reciprocal space (electronic structure), a good understanding of the structures of Zintl and polar intermetallic phases is required.

On the other hand, rationalizing their structures imposes theoretical challenges because they do not fall into any of the three classical categories of crystalline solids – metallic, ionic, and covalent. This can be conveniently visualized with the van Arkel-Ketelaar triangle<sup>22-23</sup> (Figure 1.1). In this triangle, the horizontal axis is the average electronegativity and the vertical axis is the electronegativity difference between the constituting elements. Here the electronegativity values are the so-called “absolute electronegativity”:<sup>24</sup>

$$\chi = \frac{1}{2}(I + A) ;$$

$I$  and  $A$  are the ionization energy and electron affinity, respectively. The left base vertex of the triangle represents the classical “metals”, where the constituting elements are all electropositive, featuring highly delocalized valence electrons. Starting from the metal vertex, going along the base line, the electronegativity of the constituting elements increases. As a result, valence electrons tend to localize into spaces between atoms and there is the transition from “metallic phases” to “covalent

phases”. Going from the metal vertex toward the top vertex, the electronegativity difference gets larger and larger. Valence electrons tend to localize around the atoms of the constituting elements with higher electronegativity and there is the transition from “metallic phases” to “ionic phases”.

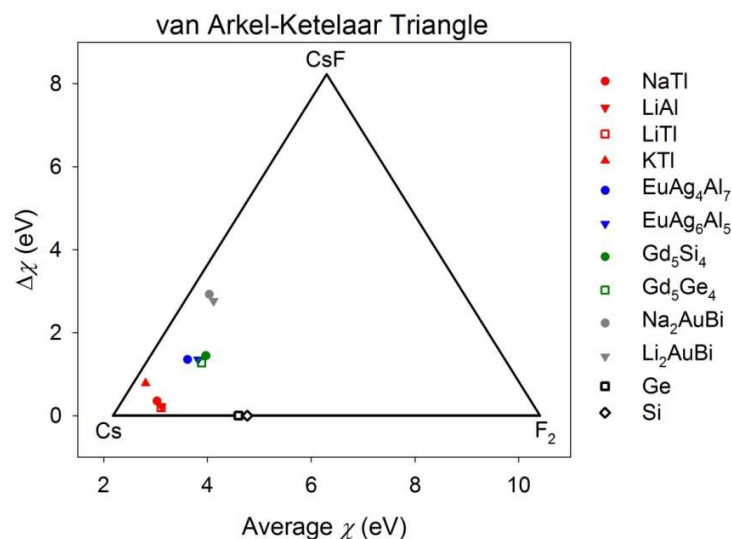


**Figure 1.1.** The van Arkel-Ketelaar triangle and the locations of the phases investigated.

We marked the phases studied in this dissertation in the van Arkel-Ketelaar triangle. Overall, all of them are closer to the metallic vertex than to the other two. However, they surely deviate from the metallic vertex, especially  $\text{Na}_2\text{AuBi}$  and  $\text{Li}_2\text{AuBi}$ . They all have  $\Delta\chi$  larger than classical metals, so charge transfer and, thus, ionicity is expected. Their average  $\chi$  values are also all larger than classical metals, with some of them having average  $\chi$  close to Ge and Si, the classical covalent crystals. So covalency should also be expected in these phases.

Therefore, Zintl and polar intermetallic phases represent classes of compounds which are intermediate among metallic, ionic, and covalent solids. The method to rationalize the structures of these three classical phases (see Chapter 3) cannot be effectively applied to Zintl and polar intermetallics. To effectively rationalize their structures, we have to comprehensively consider metallicity, ionicity, and covalency.

## 1.2 Zintl-Klemm Formalism – Success and Limitations

A simple but decent rule to rationalize the structures of Zintl and polar intermetallic phases is the Zintl-Klemm formalism.<sup>8</sup> The essences of this formalism are valence electron transfer from

electropositive to electronegative atoms and covalent interactions between the latter. For instance, in one of the most frequently quoted Zintl phases, NaTl,<sup>25</sup> Na donates its one 3s valence electron to Tl and the formal Tl behaves like a pseudo-tetrel atom, each forming four “covalent bonds” with four other Tl and constructing a diamond-type network. This means that we can treat Zintl and polar intermetallic phases as two-component systems. The electropositive atoms are “cationic” electron donors, charge balancers, and spacers. The electronegative atoms form “anionic” frameworks held together by “covalent” interactions and so their structures can be rationalized with the well-known electron counting rules such as the octet rule and Wade’s rules.<sup>26-27</sup>

In spite of its simplicity, the Zintl-Klemm formalism is successful in structural rationalization for many Zintl and polar intermetallic phases. Its success should be attributed to its consideration of electron transfer and covalency in compounds consisting of metallic or semimetallic elements. However, due to its oversimplification, it also has limitations. Firstly, although it takes electron transfer and covalency into account, it has not yet thoroughly considered ionicity and metallicity. The metallic interactions, which are between positively charged cores (nuclei plus core electrons) and highly delocalized valence electrons, are not included in the Zintl-Klemm formalism at all. For ionicity, although there is electron transfer, the structural effects of the electrostatic interactions between “cations” and “anionic” frameworks, i.e. ionic interactions, are not considered, either. Secondly, the same electronegative atoms can construct into different frameworks which all fit the Zintl-Klemm formalism. For instance, in LiSi,<sup>28</sup> Si forms a three-dimensional extended network, each Si atom “connected” to three other Si atoms. In NaSi,<sup>29</sup> Si atoms form isolated tetrahedra. They both agree with the octet rule and thus the Zintl-Klemm formalism: the formal Si has 5 valence electrons so needs 3 bonds to achieve an octet. But the Zintl-Klemm formalism does not explain the causes of different Si frameworks. Thirdly, the “anionic” frameworks often consist of late transition metals. Thus *d* electrons may play important roles in constructing the “anionic” frameworks. Consequently, those well-known electron counting rules, which are established for *s-p* systems, may not work effectively in *s-p-d* systems. Lastly, crystallographic studies of Zintl and polar intermetallics with more than one electronegative elements reveal that the sites in the “anionic” frameworks are often statistically shared by two or more electronegative elements. It is also frequently observed that some sites prefer one element over the other. This raises the “coloring problem”<sup>30</sup> – how to distribute atoms and why?

Therefore, to better understand the structures of Zintl and polar intermetallic phases, we need to explore these questions that are not covered by the Zintl-Klemm concept. And this requires synergic

efforts in both experimental and theoretical investigations. The purpose of experiments, including syntheses and characterizations, is to observe the crystal structures of Zintl and polar intermetallics and how they respond to the changes in the controllable experimental variables, *e.g.* composition, temperature, and pressure. The details of experiments can be found in Chapter 2 and the experimental section in each following chapter. The experimental results can then be theoretically rationalized. Since there are not yet any established empirical rules for these questions uncovered by the Zintl-Klemm formalism, we have to resort to quantum mechanics, which is the source and justification of all established empirical rules. The methods and the theoretical machinery employed in calculations and rationalizations are discussed in the following section. Conclusions drawn from theoretical rationalizations, if necessary, can be tested with further experiments.

### 1.3 Rationalizing Structures with Quantum Mechanical Calculations

The questions to answer when we rationalize the structures of Zintl and polar intermetallics are, given a chemical composition, at certain external conditions, among several possible structures, which one will it adopt and why. To answer them, we can build iso-compositional computational models according to these possible structures, execute quantum mechanical calculations upon them, and analyze the results. The process of analysis is principally the same with the process of analyzing a simple molecule, for instance, NO<sub>2</sub>, as briefly discussed below.

NO<sub>2</sub> is a bent-shaped molecule with the bond angle 134.1°. <sup>31</sup> Here we studied why it is not linear as in CO<sub>2</sub> and why it does not bend to a smaller bond angle, *e.g.* 125°. Calculations using the General Atomic and Molecular Electronic Structure System (*GAMESS*)<sup>32-33</sup> upon the three model molecules firstly provide us with the total energy,  $E_{TOT}$ , listed in Table 1.1. It shows that the experimental structure (bond angle 134.1°) has the lowest  $E_{TOT}$  among these 3 models. Straightening up and bending further both lead to higher  $E_{TOT}$ .  $E_{TOT}$  is the preliminary answer to the question – NO<sub>2</sub> adopt its experimental structure because it affords the lowest total energy. It is also an overall indicator of the validity of calculations – computational results match experimental observations. However,  $E_{TOT}$  is not so informative. To find out why the observed structure offers the lowest energy, we need further analysis.

People put primary emphasis onto the electronic structure in analyzing computational results. This is effective but sometimes insufficient. The molecular orbital (MO, Fock orbitals actually) diagrams of the three model NO<sub>2</sub> molecules are shown in Figure 1.2. Comparing the first two model molecules we can see that, while the other orbitals are comparable in energy, the energy of HOMO,  $E_{HOMO}$ , is

significantly lower in the bent molecule than in the linear one by 2.472 eV (Table 1.1). Figure 1.3 shows that this is because bending the molecule causes constructive interference between the upper lobes of O  $2p_z$  and lower lobes of N  $2p_z$  and, thus, eliminate a node in the HOMO. This well-known frontier orbital argument can partially explain why bent is preferred to linear. However, it is an incomplete rationalization yet.

$E_{\text{HOMO}}$  is only a part of  $E_{\text{TOT}}$ . Firstly, we need to consider not just the HOMO, but also the other MO's. So, the sum of the energies of all MO's (or all eigenvalues),  $E_{\text{eigen}}$ , needs to be considered. In the Hartree-Fock method we employed for calculation,  $E_{\text{eigen}}$  double counts the electron-electron interaction,  $E_{\text{e-e}}$ . Rectifying it, we get the electronic energy,  $E_{\text{eigen}} - E_{\text{e-e}} = E_{\text{electronic}}$ . Then, we also need to consider the electrostatic repulsions between the nuclei,  $E_{\text{N-N}}$ .  $E_{\text{TOT}}$  is the combination of  $E_{\text{electronic}}$  and  $E_{\text{N-N}}$ . The analysis of electronic structure is only dealing with  $E_{\text{electronic}}$ , not  $E_{\text{TOT}}$ . Although it explains why  $\text{NO}_2$  is bent rather than linear, it still cannot tell us why  $\text{NO}_2$  does not bend further.

Figure 1.2 and Table 1.1 reveal that on bending from  $180^\circ$  to  $134.1^\circ$  then to  $125^\circ$ , the energy of HOMO monotonously decreases and so are  $E_{\text{eigen}}$  and  $E_{\text{electronic}}$ . So, bending will not stop at  $134.1^\circ$  according to electronic structure analysis. However, countering  $E_{\text{electronic}}$ ,  $E_{\text{N-N}}$  monotonously increases with bending. From  $180^\circ$  to  $134.1^\circ$ , a decrease in  $E_{\text{electronic}}$  overcomes an increase in  $E_{\text{N-N}}$ , so  $E_{\text{TOT}}$  decreases. But from  $134.1^\circ$  to  $125^\circ$ , increase in  $E_{\text{N-N}}$  overcomes decrease in  $E_{\text{electronic}}$  so  $E_{\text{TOT}}$  increases – further bending is not favored. Therefore, we have to consider both electronic structure and nucleus-nucleus interactions, the latter of which could be easily overlooked.

**Table 1.1.** The energy terms of  $\text{NO}_2$  calculated with *GAMESS*.

Bond Angle	$180^\circ$	$134.1^\circ$	$125^\circ$
$E_{\text{HOMO}}$ (eV)	2.472	0	-0.607
$E_{\text{eigen}}$ (eV)	4.775	0	-0.125
$E_{\text{e-e}}$ (eV)	-28.944	0	16.341
$E_{\text{electronic}}$ (eV)	33.719	0	-16.466
$E_{\text{N-N}}$ (eV)	-32.566	0	16.618
$E_{\text{TOT}}$ (eV)	1.154	0	0.152

The structural rationalization of Zintl and polar intermetallic phases will follow a procedure analogous to what is shown above. We can calculate  $E_{\text{TOT}}$  and analyze the electronic structure, which, instead of an MO diagram for molecules, is usually expressed for extended structures as density of states (DOS), crystal orbital Hamiltonian population (COHP),<sup>34</sup> and band structure. It can also be visualized through crystal orbital sketches and valence electron density maps. We also need to consider  $E_{\text{N-N}}$ , which is included in the electrostatic or Madelung term,  $E_{\text{ES}}$ , in the Kohn-Sham

method.<sup>35</sup> Besides, we also need to evaluate the effect of metallicity and ionicity, which are not present in molecular species. Metallicity can be evaluated with  $E_{ES}$  and ionicity with the Madelung energy  $E_{Madelung}$ . The details of these energy terms and the rationalization procedure can be found in Chapter 3.

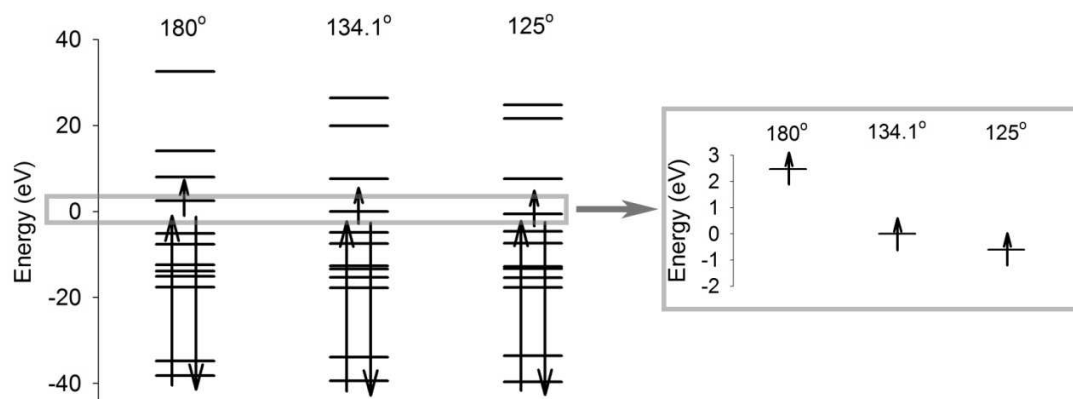


**Figure 1.2.** The MO diagrams of  $\text{NO}_2$  calculated with *GAMESS*.

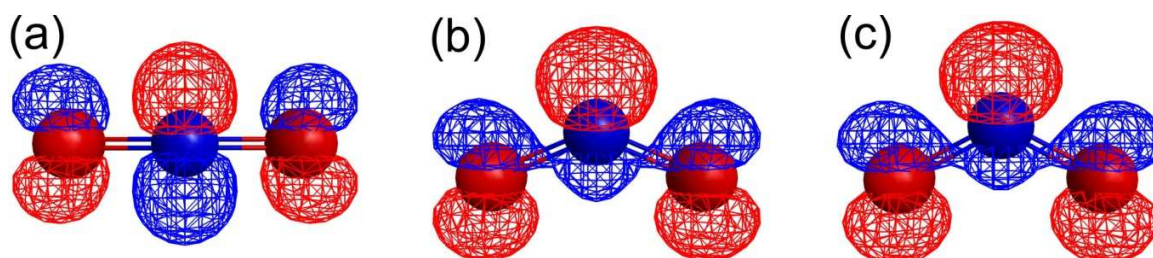


**Figure 1.3.** The HOMO ( $6a_1$ ) in (a) linear  $\text{NO}_2$  (bond angle  $180^\circ$ ), (b) bent  $\text{NO}_2$  (bond angle  $134.1^\circ$ ), (c) bent  $\text{NO}_2$  (bond angle  $125^\circ$ ).

#### 1.4 Handling the Coloring Problem

As mentioned in Section 1.2, the coloring problem occurs when there are more than one element constructing the “anionic” frameworks of Zintl and polar intermetallic phases. Finding out how to distribute different atoms on the sites of an “anionic” framework is essential in rationalizing its structure. The criterion of a preferred distribution of different atoms (or “coloring scheme”) is that it provides lower  $E_{\text{TOT}}$ .



One efficient way to determine which coloring scheme is favorable over the others is done with a population analysis upon a “uniform reference frame”.<sup>30,36</sup> To study a certain framework, we can hypothetically construct it with only one element, execute quantum mechanical calculations upon such a uniform reference frame, and analyze the valence electron population on each site. When constructing the same framework with more than one element, the site with higher population favors the more electronegative atom. This is because the more electronegative atom has valence orbitals with the lower energy. Positioning such atoms onto the site(s) with higher electron population(s) means more electrons are filling the lower-energy orbitals and this will lower the electronic energy.

Another aspect to consider about the coloring problem is to compare the numbers of heteroatomic and homoatomic contacts in competing coloring schemes. We can calculate several tentative coloring schemes with different numbers of heteroatomic and homoatomic contacts and see which one gives the lowest  $E_{TOT}$ . For example, if more heteroatomic than homoatomic contacts leads to lower  $E_{TOT}$ , then, with the help of computer, we can then generate all possible coloring schemes and find the one(s) with the most heteroatomic contacts.

## 1.5 Layout of the Dissertation

Chapter 2 lists the experimental and computational methods we employed in all work included in this dissertation. With these techniques, we addressed the questions raised in Section 1.2, questions which are not covered with the Zintl-Klemm formalism, by investigating the projects described in the following chapters.

In Chapter 3 we theoretically studied some well-known Zintl phases, alkali metal trielides. We showed that it is insufficient to consider just charge transfer and covalency and that the structures of Zintl phases should really be understood as results of the balance among the effects of metallicity, ionicity, and covalency. Factors such as atomic size, relativistic effects, and electronegativity can tip the balance and cause structural variation. This work has been submitted to *Journal of the American Chemical Society*.

In Chapter 4, we studied  $\text{Na}_2\text{AuBi}$ , synthesized in our group earlier.<sup>37</sup> It is isoelectronic with  $\text{Li}_2\text{AuBi}$  and  $\text{NaTl}$  but it adopts a structure totally different from the double diamond structure adopted by the other two. Calculations revealed that its structure is also stabilized by covalency (thus fitting the Zintl-Klemm concept) and its difference from the double diamond structure (which also fits Zintl-Klemm concept) stems from the larger size of Na over Li and the involvement of Au  $5d$  states in

covalent interactions. This work has also been submitted to *Journal of the American Chemical Society*. Also preliminary aspects of the work presented in Chapter 3 and 4 have been published in *Structure and Bonding*.

Chapter 5 and 6 report our work in the  $\text{EuAg}_x\text{Al}_{11-x}$  ternary system. Experimentally we observed how the structures of the systems switch between two competing structure types,  $\text{BaCd}_{11}$ - and  $\text{BaHg}_{11}$ -type, in response to a change in composition and temperature. We then theoretically explained our experimental observations. Site preferences and site sharing between Ag and Al atoms and the coloring problem are investigated in detail. This work has been published in *Chemistry of Materials*.

Chapter 7 includes some theoretical work upon  $\text{Gd}_5\text{Tt}_4$  systems, where Tt includes Si, Ge, Bi, and mixtures of them. These are materials with significant magnetocaloric effects. They feature similar structural motifs, i.e.,  $\text{Gd}_5\text{Tt}_4$  “slabs”, but have different stacking sequences of these slabs. We carried out calculations attempting to figure out the causes for these differences.

## 1.6 Reference:

- (1) Zintl, E.; Dullenkopf, W. *Z. Phys. Chem.* **1932**, *B16*, 183.
- (2) Zintl, E.; Brauer, G. *Z. Phys. Chem.* **1933**, *B20*, 245.
- (3) Zintl, E. *Angew. Chem.* **1939**, *52*, 1.
- (4) Schäfer, H.; Eisenmann, B.; Müller, W. *Angew. Chem. Intl. Ed. Engl.* **1973**, *12*, 694.
- (5) Schäfer, H.; Eisenmann, B. *Rev. Inorg. Chem.* **1981**, *3*, 29.
- (6) Schäfer, H. *Ann. Rev. Mater. Sci.* **1985**, *15*, 1.
- (7) Nesper, R. *Prog. Solid State Chem.* **1990**, *20*, 1.
- (8) *Chemistry, Structure, and Bonding of Zintl Phases and Ions*; Kauzlarich, S. M., Ed.; VCH: Weinheim, Germany, 1996.
- (9) (a) Belin, C.; Tillard-Charbonnel, M. *Prog. Solid State Chem.* **1993**, *22*, 59. (b) Belin, C.; Tillard-Charbonnel, M. *Coord. Chem. Rev.* **1998**, *180*, 529.
- (10) Corbett, J. D. *Angew. Chem., Intl. Ed.* **2000**, *39*, 670.

- (11) Häussermann, U.; Amerioun, S.; Eriksson, L.; Lee, C.-S.; Miller, G. J. *J. Am. Chem. Soc.* **2002**, *124*, 4371.
- (12) Curro, N. J., Caldwell, T., Bauer, E. D., Morales, L. A., Graf, M. J., Bang, Y., Balatsky, A. V., Thompson, J. D., Sarrao, J. L. *Nature* **2005**, *434*, 622.
- (13) Kanatzidis, M. G. *Recent Trends in Thermoelectric Materials Research I*; Series: Semiconductors and Semimetals; Academic: San Diego, 2001; Vol. 69, 51.
- (14) Gascoin, F.; Ottensmann, S.; Stark, D.; Haïle, S. M.; Snyder, G. J. *Adv. Funct. Mater.* **2005**, *15*, 1860.
- (15) Shawna R. B.; Kauzlarich, S. M.; Gascoin, F.; Snyder, G. J. *Chem. Mater.* **2006**, *18*, 1873.
- (16) Condron, C. L.; Kauzlarich, S. M. *Inorg. Chem.* **2007**, *46*, 2556.
- (17) Kauzlarich, S. M.; Brown, S. R.; Snyder, G. J. *Dalton Trans.* **2007**, 2099.
- (18) Snyder, G. J.; Toberer, E. S. *Nature Mater.* **2008**, *7*, 105.
- (19) Kadir, K.; Sakai, T.; Uehara, I. *J. Alloy. Compd.* **2000**, *302*, 112.
- (20) Liu, Y. F.; Cao, Y. H.; Huang, L. Gao, M. X.; Pan, H. G. *J. Alloy. Compd.* **2011**, *509*, 675.
- (21) Gschneidner Jr, K. A., Pecharsky, V. K., Tsokol, A. O. *Rep. Prog. Phys.* 2005, *68*, 1479.
- (22) van Arkel, A. E. *Molecules and Crystals in Inorganic Chemistry*. Interscience: New York, 1956.
- (23) Ketelaar, J. A. A. *Chemical Constitution; An Introduction to the Theory of the Chemical Bond*, 2nd edn. Elsevier: Amsterdam, 1958.
- (24) Pearson, R. G. *Inorg. Chem.* **1988**, *27*, 734.
- (25) Zintl, E.; Woltersdorf, G. *Z. Elektrochem.* **1935**, *41*, 876.
- (26) Wade, K. *Adv. Inorg. Chem. Radiochem.* **1977**, *18*, 1.
- (27) Mingos, D. M. P. *Adv. Organomet Chem.* **1977**, *15*, 1.
- (28) Evers, J.; Oehlinger, G.; SEXTL, G. *Angew. Chem.* **1993**, *105*, 1532.
- (29) Witte, J.; von Schnering, H. G. *Z. Anorg. Allg. Chem.* **1964**, *327*, 260.

- (30) Miller, G. J. *Eur. J. Inorg. Chem.* **1998**, 523.
- (31) Herzberg, G. *Electronic Spectra and Electronic Structure of Polyatomic Molecules*. Van Nostrand: New York, 1966.
- (32) Schmidt, M.W.; Baldrige, K. K.; Boatz, J. A.; Elbert, S. T.; Gordon, M. S.; Jensen, J. H.; Koseki, S.; Matsunaga, N.; Nguyen, K. A.; Su, S.; Windus, T. L.; Dupuis, M.; Montgomery, J. A. *J. Comput. Chem.* **1993**, *14*, 1347.
- (33) Gordon, M. S.; Schmidt, M. W. Advances in electronic structure theory: GAMESS a decade later; in *Theory and Applications of Computational Chemistry: the first forty years*. Dykstra, C. E.; Frenking, G.; Kim, K. S.; Scuseria, G. E., Ed.; Elsevier: Amsterdam, 2005, pp.1167.
- (34) Dronskowski, R.; Blöchl, P. *J. Phys. Chem.* **1993**, *97*, 8617.
- (35) Kohn, W.; Sham, L. J. *Phys. Rev.* **1965**, *140*, A1133.
- (36) Gimarc, B. M. *J. Am. Chem. Soc.* 1983, *105*, 1979.
- (37) Kim, S.-J.; Miller, G. J.; Corbett, J. D. *Z. Anorg. Allg. Chem.* **2010**, *636*, 67.

## Chapter 2

### Experimental and Computational Techniques, in General

In this chapter, we describe the experimental and computational techniques in general. This includes what techniques were employed, what purposes they were serving, and what their advantages and disadvantages are. The specific details for each problem can be found in each of the following chapters.

#### 2.1 Syntheses

##### 2.1.1 Arc Melting

For syntheses, we melted mixtures of metals using an electric arc furnace housed in an inert atmosphere glove box. The electric arc generates temperatures higher than 2000 °C and melts samples in just a few seconds. However, we cannot precisely control its temperature and the rate of heating and cooling. The high temperature of arc melting can also vaporize metals with low boiling points, *e.g.* Eu, causing material loss.

##### 2.1.2 Tube Furnace Heating

The arc-melted samples were sealed in tantalum tubes then in evacuated silica jackets and annealed using tube furnaces. With tube furnaces, we could program the temperature profiles and thus control the annealing temperature and the rate of heating and cooling. The tube furnaces have a high temperature limit, 1200 °C.

#### 2.2 Characterization

##### 2.2.1 X-Ray Crystallography

Both single crystal and powder techniques were employed for X-ray diffraction (XRD). Single crystal XRD provides three-dimensional diffraction patterns, so it offers higher efficiency than powder XRD in solving and refining crystal structures. However, its results largely depend on the availability and quality of the single crystals. Moreover, the mass of the single crystal is on the scale of a microgram, so it does not give the average structure of the whole sample, which is around 0.5 g.

For powder XRD, we ground about 0.1 g sample and took several milligrams for diffraction. So the refinement results, especially the lattice parameters, are a course-grained average over the whole

sample. The powder technique does not require high quality single crystals, either. Moreover, the one-dimensional powder patterns, although less informative than the single crystal diffraction patterns, can be used for “finger print” identification of the phases present in samples. But, it is not efficient to determine the occupancies of different atoms on their shared crystallographic sites because occupancies often correlate with other parameters during powder refinement.

### 2.2.2 Magnetometry and Microscopy

We measured the temperature dependent magnetic susceptibilities of our  $\text{EuAg}_x\text{Al}_{11-x}$  systems. The reciprocal susceptibility vs temperature data were fit according to the Curie-Weiss law to calculate the effective moment, from which we could determine whether Eu is divalent or trivalent.

Scanning electron microscopy and energy-dispersive spectroscopy were utilized to check the homogeneity and measure the compositions of the samples.

## 2.3 Computations

### 2.3.1 EHT Calculation

Extended Hückel Theory (EHT)<sup>1</sup> is semi-empirical rather than first-principles. The construction of the Hamiltonian matrix and the solution of the eigenfunctions are completed only once, without self-consistent iterations. So, it takes much shorter time than first-principles calculations. Also, it employs Slater-type atomic orbitals as the basis set and provides convenient electron population analysis, so the computational results can be easily understood with classical chemical concepts such as “bonding orbitals”, “antibonding orbitals”, “bond order”, and “charge transfer”.

The disadvantage of EHT calculations is that it involves significant approximations. For instance, it has  $E_{\text{eigen}} = E_{\text{TOT}}$ , and there are no explicit repulsion terms, either between nuclei or between electrons, in EHT, either. So, its accuracy is lower than first-principles calculations and its results are usually considered as semi-quantitative or even qualitative.

### 2.3.2 TB-LMTO-ASA Calculation

We employed two techniques for first-principles calculations. The first one is Tight Binding Linear Muffin Tin Orbital with Atomic Spheres Approximation (TB-LMTO-ASA).<sup>2</sup> It is a self-consistent calculation, so it takes more time than EHT, which also means that it has higher accuracy. It models the potential energy with a spherical muffin-tin potential and also uses atomic orbitals as a basis set. It

offers a population analysis analogous to that in EHT, so the calculation results also provide “chemical” interpretations.

However, the Atomic Spheres Approximation really imposes limitations upon this LMTO calculation. It makes an atomic sphere around each atom in the unit cell and ensures that the total volume of the atomic spheres is equal to the volume of the unit cell. To fill the unit cell, very often, we need to generate unphysical “empty spheres”. And the calculated  $E_{\text{TOT}}$  is largely affected by the size of atomic spheres and empty spheres and the overlap between them. This means that we cannot easily compare different structures with the same composition because the overlaps between atomic spheres and, sometimes, the number of empty spheres will be different.

### 2.3.3 VASP Calculation

We also did first-principles calculations using the Vienna ab initio simulation package (VASP).<sup>3-5</sup> VASP employs pseudopotentials<sup>6</sup> and its basis functions are plane waves. Among EHT, TB-LMTO-ASA, and VASP, VASP is the most time-consuming but also provides the highest accuracy. There is no atomic sphere involved so it can compare two different structures with the same composition. It is also capable of optimizing crystal structures. This is very valuable especially when we compare two model structures one of which is experimentally observed and the other is hypothetical. We have no experimental reference for the hypothetical structure but it is often a local minimum on the potential energy surface. Thus, structural optimization can help us to determine it.

The plane wave basis set of VASP is not as straightforward from a chemist’s viewpoint as the atomic orbital basis set. Luckily, VASP allows us to project the calculated wave functions onto the atomic orbitals so we can still interpret the results in chemical terms. Overall, VASP provides satisfying results which match experiments and offer sensible structural rationalizations. The only flaw of VASP found in our work is that it overestimates lattice parameters, especially when heavy elements, such as Tl, are involved.

### 2.4 Reference:

- (1) Hoffmann, R. *J. Chem. Phys.* **1963**, *39*, 1397.
- (2) Jepsen, O.; Andersen O. K. *TB-LMTO*, version 47; Max-Planck-Institut für Festkörperforschung, Stuttgart, Germany, 2000.

(3) (a) Kresse, G.; Hafner, J. *Phys. Rev. B* **1993**, *47*, 558. (b) Kresse, G.; Hafner, J. *Phys. Rev. B* **1994**, *49*, 14251.

(4) Kresse, G.; Furthmüller, J. *Comput. Mat. Sci.* **1996**, *6*, 15.

(5) Kresse, G.; Furthmüller, J. *Phys. Rev. B* **1996**, *54*, 11169.

(6) Kresse, G.; Joubert, D. *Phys. Rev.* **1999**, *59*, 1758.



## Chapter 3

### Revisiting the Zintl-Klemm Concept I: Alkali Metal Trielides

Modified from a paper submitted to *Inorganic Chemistry*

Fei Wang and Gordon J. Miller

#### 3.1 Abstract

To enhance understanding of the Zintl-Klemm concept, which is useful for characterizing semimetallic and semiconducting “valence” compounds, and to more effectively rationalize the structures of Zintl phases, we studied numerous possible structures of LiAl, LiTl, NaTl, and KTl using first-principles quantum mechanical calculations. An approach to consider the relative effects of covalent, ionic, and metallic interactions by partitioning the total energy is presented. An assessment of all of these effects is important for understanding the total structural behavior of Zintl phases. In particular, valence electron transfer and anisotropic covalent interactions, explicitly employed by the Zintl-Klemm concept, are often in competition with isotropic, volume-dependent metallic and ionic interaction terms. Furthermore, factors like relativistic effects, electronegativity differences, and atomic size ratios between the alkali metal and triel atoms can affect the competition by enhancing or weakening one of the three contenders and thus cause structural variations. This partitioning of the total energy, coupled with analysis of the electronic density of states curves, correctly predicts and rationalizes the structures of LiAl, LiTl, NaTl, and KTl, as well as identifies a pressure-induced phase transition in KTl from its structure based on  $[Tl_6]$  distorted octahedra to the double diamond NaTl-type.

#### 3.2 Introduction

One ultimate goal of solid-state science is to design and prepare materials with desired properties. Properties are the expression of structures – both crystal and electronic structures, with the latter deducible from the former through quantum mechanics. So, it is essential to possess a sound understanding of the structures of solids, including comprehension of the principles that govern the congregation of atoms into structures, which can change in response to variations in chemical composition and external conditions.

In particular, to rationalize their structures, crystalline solids have been classically categorized into three model classes – ionic, metallic, and covalent. This can be shown with a van Arkel-Ketelaar

triangle<sup>1,2</sup> (Figure 1), where the horizontal axis is the average electronegativity (expressed with the configuration energy,  $CE^{3-5}$ ) of the constituent elements and the vertical axis is the electronegativity difference ( $\Delta CE$ ) between them. The difference among metallic, ionic, and covalent substances is the behavior of valence electrons in both real and reciprocal spaces. The classical metals are found around the lower left vertex of the triangle. Here, both the average  $CE$  and  $\Delta CE$  are small, and the valence electrons are largely delocalized. In an “ideal metal”, the valence electrons are described as a homogeneous electron gas embedded with positively charged cores, i.e., nuclei plus core electrons. In reciprocal space, valence electrons populate continuous energy bands without band gaps around the Fermi level. As we deviate from the metallic region, valence electrons tend to localize. At the top vertex, around which ionic compounds are found,  $\Delta CE$  is large, and the valence electrons tend to localize around the atoms with higher  $CE$ . Toward the lower right vertex, the average  $CE$  increases while  $\Delta CE$  remains small, and, thus, valence electrons tend to localize between atoms, i.e. engage in covalent bonding. Along the base of the triangle, therefore, metals transform to covalent crystals, such as Si, and eventually to molecular substances. Localization of valence electrons in real space in both ionic and covalent directions can be considered as a charge density wave (CDW)<sup>6</sup> distortion, an effect which is echoed by the opening of band gaps in reciprocal space. Due to the different behaviors of valence electrons in metallic, ionic, and covalent solids, each of them typically employs its own structural rationalization.

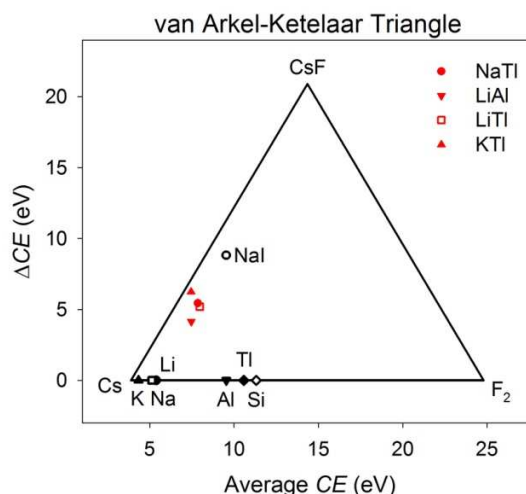


**Figure 1.** The van Arkel-Ketelaar triangle. Electronegativity is quantified by the configuration energy ( $CE$ ).<sup>3-5</sup>

The structures of metals and ionic crystals can be reasoned by examining the electrostatic or Madelung energy – they adopt the structures affording the lowest electrostatic energy. But their

electrostatic energies are evaluated in different ways. An ionic solid is perceived as a collection of spherical ions. Its electrostatic interaction, called Madelung energy, is between all charged ions and can be calculated as:<sup>7</sup>

$$E_{Madelung} = \frac{M}{4\pi\epsilon_0} \frac{Z_1 Z_2 e^2}{r_0} \quad (1)$$

where  $Z_1$  and  $Z_2$  are the charges of the cation and anion;  $\epsilon_0$  is the vacuum permittivity;  $r_0$  is the nearest neighbor distance between neighboring cation and anion; and  $M$  is the Madelung constant, which is only dependent on structure type, can be calculated using an Ewald summation,<sup>8</sup> and has been tabulated for many known structure types.<sup>9</sup>

A metal is usually simplistically described as positively charged ions, or “cores”, submerged in the valence electron gas. Its electrostatic energy is thus defined as the total Coulomb interaction within a system consisting of positively charged ions and a homogeneous, charge-compensating free electron gas.<sup>10</sup> This includes the ion-ion repulsion and the attraction between ions and free electron gas. Its calculation takes a form similar to that for an ionic crystal:

$$E_{ES} = \alpha_M \frac{Z^2}{R_a} \quad (2)$$

Elements:

$$E_{ES} = \frac{1}{R_a} (Z_A^2 \alpha_{AA} + Z_A Z_B \alpha_{AB} + Z_B^2 \alpha_{BB}) \quad (3)$$

Binary Compounds:

Here  $R_a$  is the average atomic radius;  $Z$ ,  $Z_A$  and  $Z_B$  are the charges of the cations, and  $\alpha_M$ ,  $\alpha_{AA}$ ,  $\alpha_{AB}$ , and  $\alpha_{BB}$  are Madelung constants, which can also be calculated with techniques similar to the Ewald summation.<sup>11</sup>

Atoms in a covalent crystal are held together by covalent bonding, so the structure can be rationalized in the same way as for a molecule. The stability of a covalent crystal stems from the lowering in electronic energy with respect to the isolated free atoms - valence orbitals of constituent atoms interact with one another to form bonding and antibonding crystal orbitals; and by populating bonding orbitals, the energy of valence electrons gets lower. Therefore, covalent crystals will adopt the structures that maximize bonding interactions and provide the lowest electronic energy.

It is important to point out that, although crystalline solids are categorized into these three model classes, it is difficult to draw clear dividing lines between them because the variations between the three classes are gradual rather than abrupt. They can even be described using the same theoretical model. Burdett<sup>12</sup> has argued that, just like covalent species, metals can be described with a tight-binding scheme, *viz.* their energy bands are also formed through orbital overlap. So there is no essential difference between “covalent bonds” and “metallic bonds”. It is only that in metals the electronic driving force for the CDW distortion is too small to cause electron localization and opening of band gaps. Such continuity between metallic, ionic, and covalent solids means that there are solids that may exhibit metallicity, ionicity, and covalency simultaneously and cannot be approximated into any one of these three model classes. And indeed, there are such solids, for instance, Zintl phases. For such intermediate solids, the structural rationalization becomes challenging.

Zintl phases are those intermetallic compounds composed of electropositive metals (e.g. alkali metals, alkaline metals, or rare earth metals) and electronegative metals or semimetals around the “Zintl Line”, the line dividing groups 13 and 14. They have been long studied<sup>13-20</sup> and keep intriguing solid-state chemists for many reasons, one of which is that they are promising in many applications especially as thermoelectric materials.<sup>21-26</sup> The structures of Zintl phases can be understood with the Zintl-Klemm concept. For example, the most frequently quoted Zintl phase, NaTl,<sup>27</sup> adopts a double diamond structure – Na and Tl both form diamond substructures which interpenetrate one another. The rationalization is that Na donates its 3s electron to Tl. The resulting formal Tl<sup>-</sup> anion, with 4 valence electrons, behaves as a pseudo tetrel atom, each of which forms 4 covalent bonds and adopts the diamond structure. Each Na<sup>+</sup> cation acts as a charge balancer and space filler.

Although it is simplistic, the Zintl-Klemm concept works decently in rationalizing the structures of Zintl phases. Its success stems from its consideration of charge transfer and covalent interactions in intermetallic compounds, implying that Zintl phases, although composed of metallic or semimetallic elements, involve ionic and covalent interactions as well. This is also what we can expect from the van Arkel-Ketelaar triangle (Figure 1). The phases we studied in this work are also marked in the triangle. We can see that they all deviate from the metal vertex significantly. In term of  $\Delta CE$ , they are all around 5 eV, over a half of 8.81 eV, the  $\Delta CE$  of NaI which is an ionic crystal. In term of average  $CE$ , they are all between 7.5 and 8 eV, over a half of 11.33 eV, the average  $CE$  of Si. These indicate that Zintl phases are a class of compounds bridging metallic, ionic, and atomic (covalent) crystals. And indeed, Zintl phases exhibit features resembling nonmetallic solids, *e.g.* narrow homogeneity

ranges or “precise” compositions, as in valence compounds, and poor conductivity or semiconductivity.<sup>24</sup>

Meanwhile, the Zintl-Klemm concept also has limitations. For instance, LiTl,<sup>28</sup> which is isoelectronic with NaTl, adopts a CsCl-type structure, which defies the Zintl-Klemm concept. Such limitations stem from the oversimplification of the concept. It considers charge transfer but does not consider the consequent electrostatic interaction between “cations” and “anions” as in ionic crystals. Moreover, Zintl phases are made with metals or semimetals, so they are expected to retain metallic character. For instance, NaTl has an electrical conductivity of  $1.23 \times 10^{-4} \Omega^{-1}\cdot\text{cm}^{-1}$  at 20 °C and it decreases with increasing temperature.<sup>29</sup> It is impossible to build up highly charged cations and anions in such compounds. Therefore, to rationalize the structures of Zintl phases, we need to comprehensively evaluate ionicity, metallicity, and covalency.

Thanks to the tremendous development in computing techniques, quantum mechanical calculations have been greatly advanced since the establishment of the Zintl-Klemm concept. This endows us with the possibility to examine Zintl phases in more sophisticated ways than just counting valence electrons and bonds. For instance, we can quantitatively evaluate metallicity and covalency simultaneously by partitioning the calculated total energy into an electrostatic term and an electronic term. In our work, we have employed first principles density functional theory calculations to revisit some well known Zintl phases. The results are presented in two reports. This first one is on alkali metal trielides – LiAl, LiTl, NaTl, and KTI.

Firstly, since metallic and ionic interactions are also expected in Zintl phases, why do most alkali metal trielides not adopt those structures commonly observed in ionic crystals and metals? To answer this, we compared a spectrum of structures for LiAl, LiTl, NaTl, and KTI. Besides the observed NaTl-type, CsCl-type, and KTI-type structures, we also considered some 1:1 structures ubiquitous among ionic crystals and alloys. These include the CuAu-type (*fcc*), AuCd-type (*hcp*), NaCl-type, and BaCu-type, which contains planar  $6^3$  nets of Cu (Figure 2). Secondly, as mentioned above, LiTl does adopt the CsCl-type structure,<sup>28</sup> which frequently occurs for ionic salts and binary alloys and cannot be rationalized through the Zintl-Klemm formalism. This is intriguing considering that LiAl,<sup>30</sup> LiGa,<sup>31</sup> and LiIn<sup>32</sup> all obey the Zintl-Klemm rule and adopt the NaTl-type structure at ambient conditions, and, of course, so does NaTl itself.<sup>20</sup> To understand this, quantum mechanical calculations were carried out to compare LiAl, LiTl and NaTl. Moreover, at ambient conditions, KTI takes a thoroughly different structure containing  $\text{Tl}_6$  distorted octahedra (Figure 2)<sup>33</sup> with local point symmetry  $C_{2h}$ . Every Tl can

still be perceived as four-bonded and, indeed, Si atoms form similar octahedral clusters in the gas phase.<sup>34</sup> So, the Zintl-Klemm rule is formally obeyed, but it cannot explain the cause of the difference between KTI and NaTI. Also, under pressures higher than 2 kbar, KTI becomes isosteric with NaTI.<sup>35</sup> Such structural effects of external pressure on Zintl phases have not yet been discussed, which is also addressed here. With these efforts in this report and the following one, we intend to provide a better understanding of the structures of Zintl phases by analyzing the full Zintl-Klemm concept using quantum mechanical calculations.

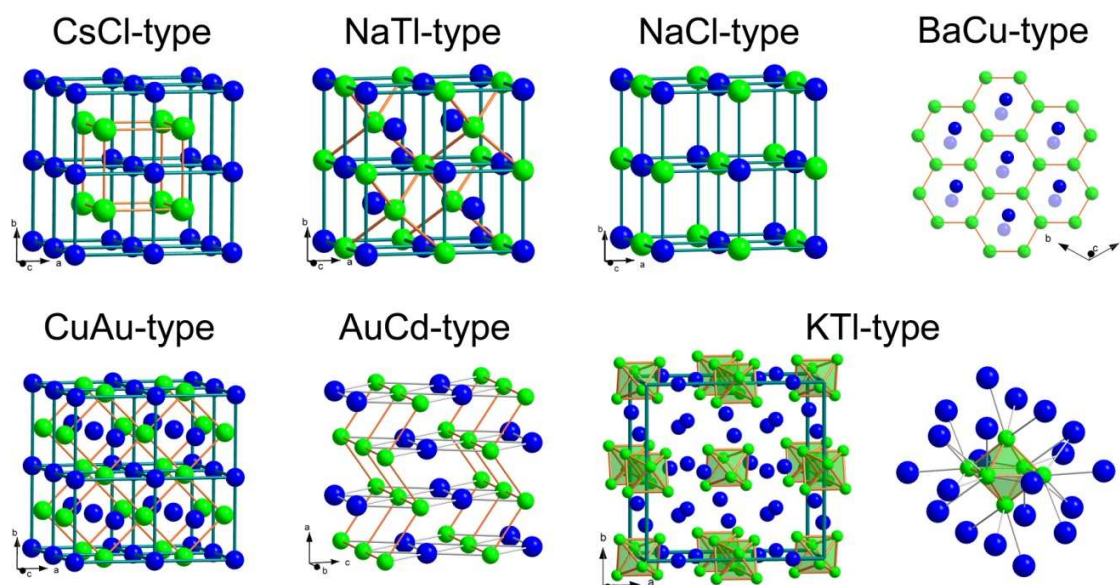


**Figure 2.** The seven structure types investigated. Blue: Li/Na/K; green: Al/Tl.

### 3.3 Computational Details

#### 3.3.1 Model Structures

Seven model structures, NaTI-, KTI-, BaCu-, CsCl-, NaCl-, CuAu- (*fcc*), and AuCd-type (*hcp*), were studied for each of the four compositions, LiAl, LiTI, NaTI, and KTI. For each composition, the seven model structures were built with equal volumes per formula unit ( $V_{f.u.}$ ), which were taken from the experimental values.<sup>27,28,30,33</sup> The structural details of these models are listed in Table 1. Among the seven structure types, the NaTI-, the CsCl-, the NaCl-, and the CuAu-type (*fcc*) structures are cubic and all atoms are located at symmetrically special sites, so the only variable for these structures is  $V_{f.u.}$ . For the AuCd-type (*hcp*) structure, besides  $V_{f.u.}$ , the aspect ratio ( $c/a$ ) is also a free variable. We set  $c/a = (8/3)^{1/2}$  so that it has an ideal *hcp* geometry. There are more degrees of freedom in the KTI- and

the BaCu-type structures. After setting  $V_{f.u.}$ , the aspect ratios ( $c/a$  and  $b/a$ ) and atomic coordinates ( $x$ ,  $y$ , and  $z$ ) remain variable. To determine these structural parameters, we executed structural optimization with VASP (details are included in “VASP Calculations”). The details of optimized KTI- and BaCu-type structures can be found in the section, “Results and Discussion”, and in Supporting Information.

### 3.3.2 VASP Calculations

**Table 1.** Details of model structures.

Structure	Atom	Wyck.	x	y	z	Structure	Atom	Wyck.	x	y	z
NaTl-type $Fd\bar{3}m$	Li/Na/K	$8a$	0	0	0	CsCl-type $Pm\bar{3}m$	Li/Na/K	$1a$	0	0	0
$a = (8V_{f.u.})^{\frac{1}{3}}$	Al/Tl	$8b$	1/2	1/2	1/2	$a = (V_{f.u.})^{\frac{1}{3}}$	Al/Tl	$1b$	1/2	1/2	1/2
KTI-type $Cmce$	Li/Na/K1	$8e$	1/4	y	1/4	NaCl-type $Fm\bar{3}m$	Li/Na/K	$4a$	0	0	0
$a = \left(24V_{f.u.} \frac{a}{b} \frac{a}{c}\right)^{\frac{1}{3}}$	Li/Na/K2	$8d$	x	0	0	$a = (4V_{f.u.})^{\frac{1}{3}}$	Al/Tl	$4b$	1/2	1/2	1/2
$b = \frac{b}{a}a$ , $c = \frac{c}{a}a$	Li/Na/K3	$8f$	0	y	z	AuCd-type $Pnma$	Li/Na/K	$2f$	1/4	1/2	5/6
	Al/Tl1	$16g$	x	y	z	$b = (2V_{f.u.}/\sqrt{8})^{\frac{1}{3}}$	Al/Tl	$2e$	1/4	0	1/3
	Al/Tl2	$8f$	0	y	z	$a = \sqrt{8/3}b$ , $c = \sqrt{3}b$					
BaCu-type $P6_3/mmc$	Li/Na/K	$4f$	1/3	2/3	z	CuAu-type $P4/mmm$	Li/Na/K1	$1a$	0	0	0
$a = \left(\frac{8V_{f.u.}}{\sqrt{3}} \frac{a}{c}\right)^{\frac{1}{3}}$ , $c = \frac{c}{a}a$	Al/Tl1	$2b$	0	0	1/4	$a = c = (2V_{f.u.})^{\frac{1}{3}}$	Li/Na/K2	$1c$	1/2	1/2	0
	Al/Tl2	$2d$	1/3	2/3	3/4		Al/Tl	$2e$	0	1/2	1/2

The Vienna *ab initio* simulation package (VASP)<sup>36-38</sup> was employed to calculate the energies, band structures, and valence electron density maps of all model structures. In all calculations, we used the projector augmented-wave (PAW) pseudopotentials<sup>39</sup> and the Perdew-Burke-Ernzerhof generalized gradient approximation (PBE-GGA).<sup>40</sup> Energy and total charge density were integrated in reciprocal space with a  $7 \times 7 \times 7$  Monkhorst-Pack  $k$ -points mesh.<sup>41</sup> The energy cutoffs for calculating energies and optimizing structures are 240.3 eV for LiAl, 140.0 eV for LiTl, 102.0 eV for NaTl, and 116.7 eV for KTI. This affords a convergence in total energy to less than 1 meV per atom. Band structures and valence electron maps were calculated for LiAl, LiTl, and NaTl in the NaTl-type structure. In these calculations the energy cutoffs are set to higher values: 300.4 eV for LiAl, 175.0 eV for LiTl, and



127.5 eV for NaI. The calculated band structures and valence electron density maps were plotted with *wxDragon*.<sup>42</sup> Structural optimizations were exerted upon the BaCu- and the KTI-type structures to determine their aspect ratios and atomic positions for each of the four compositions. During these optimizations, the volumes of the unit cells were fixed and the conjugate gradient algorithm<sup>43</sup> was applied.

Besides the calculations upon all model structures at equal (experimental) volume per f.u. for each composition, we also isotropically varied the volumes to investigate the effect of size. Energy vs. volume ( $E(V)$ ) curves were plotted and fitted to the Murnaghan equation of state,<sup>44</sup> from which we could determine the equilibrium volumes  $V_{eq}$ , *i.e.*, the volume at the minimum of an  $E(V)$  curve. Calculations were then completed upon model structures at  $V_{eq}$  values.

### 3.3.3 Partitioning the Total Energy in VASP

VASP conveniently calculates the metallic electrostatic energy ( $E_{ES}$ ) according to equations (2) and (3). It includes the repulsion between cores and the attraction between the cores and the homogeneous electron gas (HEG):

$$E_{ES} = V_{core-core} + V_{core-HEG} \quad (4)$$

This term reflects the effect of the “metallic interaction”. According to equation (3), when we compare the  $E_{ES}$  terms of different alkali metal trielides,  $Z_1$  and  $Z_2$  are the same - +1 for alkali metals and +3 for triels. The difference only comes from  $R_a$  (size) and the Madelung constant (structure type). If we make the comparison at equal volumes per f.u.,  $R_a$  is equalized and the difference in  $E_{ES}$  only quantifies the difference between the Madelung constants of the structures. The identity of alkali metals or triels does not matter.

By subtracting  $E_{ES}$  from the total energy ( $E_{TOT}$ ), which includes core-core repulsion, core-valence electron (VE) attraction, interactions between valence electrons (Coulomb, exchange, and correlation), and the kinetic energy of valence electrons:

$$E_{TOT} = V_{core-core} + V_{core-VE} + V_{VE-VE} + T_{VE} \quad (5)$$

we obtain the electronic energy term ( $E_{electronic}$ ):

$$E_{electronic} = E_{TOT} - E_{ES} = V_{core-VE} - V_{core-HEG} + V_{VE-VE} + T_{VE} \quad (6)$$



which can be rewritten as:

$$E_{\text{electronic}} = (V_{\text{core-VE}} - V_{\text{core-HEG}}) + (V_{\text{VE-VE}} - V_{\text{HEG-HEG}}) + (T_{\text{VE}} - T_{\text{HEG}}) + V_{\text{HEG-HEG}} + T_{\text{HEG}} \quad (7)$$

The first three terms in parentheses are the contributions to the electronic energy caused by the difference between real valence electrons and the homogeneous electron gas, or, by valence electron inhomogeneity, *i.e.* localization, which includes covalent bonding, charge transfer (ionicity), formation of lone pairs, etc. The last two terms are the energy of homogeneous electron gas alone, terms which are independent from the positions of atoms, and, as such, have no relationship with structure types. The kinetic energy of homogeneous electron gas,  $T_{\text{HEG}}$ , is a functional of valence electron density,  $n$ <sup>45</sup>:

$$T_{\text{HEG}} = 3^{\frac{5}{3}} \pi^{\frac{4}{3}} \frac{\hbar^2}{10m} V n^{\frac{5}{3}} \quad (8)$$

$V_{\text{HEG-HEG}}$  depends on  $n$  and the volume per f.u. and it can be calculated as:<sup>46</sup>

$$V_{\text{HEG-HEG}} = \frac{n^2}{2} \iint \frac{d\vec{r}d\vec{r}'}{|\vec{r}-\vec{r}'|} \quad (9)$$

If we compare  $E_{\text{electronic}}$  of several iso-compositional structures at equal volumes per f.u. (so  $n$  also equal), the last two terms will make no difference because they are independent of structure types but only depend on  $n$  and volume. The difference among  $E_{\text{electronic}}$  values will, thus, mainly come from the first three terms – the differences in valence electron localization among the various structures. This outcome can be confirmed by our results of VASP calculations on Na and Si (Table 2).

For Na, which is close to an ideal metal, its valence electrons closely resemble a homogeneous electron gas ( $\text{VE} \approx \text{HEG}$ ). The energy caused by valence electron localization is, therefore, close to zero, and the electronic energy term is:

$$E_{\text{electronic}} \approx V_{\text{HEG-HEG}} + T_{\text{HEG}} \quad (10)$$

We compared the real Na (*hcp*) and a hypothetical diamond-type Na at the same volume per f.u. ( $37.80 \text{ \AA}^3/\text{f.u.}$ <sup>47</sup>). As discussed above,  $V_{\text{HEG-HEG}}$  and  $T_{\text{HEG}}$  do not differentiate between structure types. So,  $E_{\text{electronic}}$  of *hcp* and diamond-type Na are expected to be very close to each other. The difference in  $E_{\text{TOT}}$  will be mainly from  $E_{\text{ES}}$ . This is exactly what we see in Table 2, which shows that the two

structures have almost equal  $E_{\text{electronic}}$  but that  $E_{\text{ES}}$  is lower in *hcp*, so that *hcp* has the lower  $E_{\text{TOT}}$  and is the preferred structure.

By contrast, for two iso-compositional phases which afford strong covalent interactions, valence electron densities deviate significantly from the homogeneous electron gas, so the first three terms in equation (7) are not zero and  $E_{\text{electronic}}$  depends on the positions of atom cores, *i.e.*, structure types. The comparison between real Si (diamond-type) and a hypothetical *hcp* Si (Table 2) at equal volumes per atom ( $20.03 \text{ \AA}^3/\text{atom}^{48}$ ) shows that although  $E_{\text{ES}}$  is still lower for *hcp*,  $E_{\text{electronic}}$  values are significantly different and counteract  $E_{\text{ES}}$ , even overruling it, and rendering a lower  $E_{\text{TOT}}$  for the diamond structure.

Therefore, by partitioning  $E_{\text{TOT}}$  into  $E_{\text{ES}}$  and  $E_{\text{electronic}}$ , and comparing these values at equal volumes per f.u., we can segregate the effects of metallic interactions out by examining  $E_{\text{ES}}$  to see which structure is favored if valence electrons are highly delocalized. We can also evaluate the effects of valence electron localization by examining  $E_{\text{electronic}}$ . This includes both covalency and ionicity, which cannot be further separated into energy terms with only VASP. But we can analyze the ionicity effects by calculating the ionic Madelung energy with the Ewald technique<sup>8</sup> assuming a +1 charge on each alkali metal atom and a -1 charge on each triel atom and evaluate the covalency effects using LMTO calculations.

**Table 2.** Comparison of energy terms between *hcp* and diamond structures for Na and Si.

Comp.	V ( $\text{\AA}^3/\text{atom}$ )	Energy Terms	<i>hcp</i>	diamond
Na	37.80	$E_{\text{ES}}$ (eV/f.u.)	-6.6808	-6.2629
		$E_{\text{electronic}}$ (eV/f.u.)	0.2161	0.2193
		$E_{\text{TOT}}$ (eV/f.u.)	-6.4647	-6.0436
Si	20.03	$E_{\text{ES}}$ (eV/f.u.)	-120.8270	-112.5655
		$E_{\text{electronic}}$ (eV/f.u.)	13.1953	4.0853
		$E_{\text{TOT}}$ (eV/f.u.)	-107.6317	-108.4802

### 3.3.4 LMTO Calculations

We used the Stuttgart *Tight-Binding, Linear-Muffin-Tin Orbital* program with *Atomic Sphere Approximation* (TB-LMTO-ASA)<sup>49</sup> to calculate electronic structures, which are shown as density of states (DOS) and crystal orbital Hamiltonian population (COHP)<sup>50</sup> curves. We also evaluated covalency effects by calculating integrated COHP (ICOHP) values, which scale with the energy lowering due to covalent interactions. This lowering is with respect to the energies of electrons in non-interacting valence atomic orbitals, and not to the homogeneous electron gas as in  $E_{\text{electronic}}$

calculated with VASP. So, ICOHP cannot be numerically compared with  $E_{\text{electronic}}$ . Nevertheless, it can be used to evaluate the stabilization caused by covalent interactions.

For all LMTO calculations, the exchange and correlation energy was treated with the von Barth-Hedin local density approximation.<sup>51</sup> The basis sets included the valence  $s$  and  $p$  orbitals of all elements:  $2s$  and  $2p$  of Li,  $3s$  and  $3p$  of Na and Al,  $4s$  and  $4p$  of K, and  $6s$  and  $6p$  of Tl. The Wigner-Seitz radii of atomic spheres were adjusted by an automatic procedure<sup>52</sup> and empty spheres were generated where they were necessary so that the unit cells were filled by Wigner-Seitz spheres with overlaps ranging from 7.55% to 10.22%. The first Brillouin zone was sampled with an  $8 \times 8 \times 8$   $k$ -points mesh.

### 3.4 Results and Discussion

#### 3.4.1 Comparison of Different Structure Types

Table 3 compares the energy terms of the seven structure types calculated with VASP, the triel-triel distances in these structures, the ICOHP values calculated with LMTO, and the ionic Madelung energies calculated with the Ewald technique<sup>8</sup> assuming a +1 charge on each alkali metal atom and a -1 charge on each triel atom. These results are all calculated at equal volumes per f.u. for each composition. Supporting Information also includes the DOS and COHP curves of these structures calculated with LMTO.

In the NaTl-, BaCu-, and KTl-type structures, the Al/Tl substructures are, respectively, diamond, graphite sheets, and distorted  $(\text{Al/Tl})_6$  octahedra. These are all structures adopted by tetrels, either in the solid or gaseous states (gaseous Si forms  $\text{Si}_6$  octahedra).<sup>34</sup> So, if we apply the Zintl-Klemm rule, treating formal  $\text{Al}^-/\text{Tl}^-$  as pseudo-tetrel atoms and considering only the covalent interaction between them, the NaTl-, BaCu-, and KTl-type structures are all plausible options. The CsCl- and the NaCl-type structures cannot be rationalized with the Zintl-Klemm rule and are commonly observed in ionic crystals. Metals are known for adopting *fcc* and *hcp* structures. So the CuAu- (*fcc*) and AuCd-type (*hcp*) structures are expected to be favored by metallic systems. However, they also satisfy the Zintl-Klemm formalism – for CuAu- and AuCd-type alkali metal trielides, every triel atom is also “bonded” to four neighboring triel atoms (Figure 2), just as in the NaTl-type structure, but in a different geometry. In the *fcc*-like, CuAu-type structure, triel atoms form planar sheets of squares and, in the *hcp*-like, AuCd-type structure, they form puckered sheets of squares.

By comparing the triel-triel distances in these equivolume structures (Table 3), we see that for each composition, the NaTl-, KTI-, and BaCu-type structures have the smallest  $r_{\text{triel-triel}}$ . (There is one exception, the KTI-type LiTl, whose  $r_{\text{Tl-Tl}}$  is larger than the CuAu- and AuCd-type LiTl. The reason is discussed in the section “The KTI-type Structure”.) Their DOS and COHP curves (Supporting Information) reveal features resembling covalent crystals – the Fermi levels are located at the crossover in COHP curves between filled bonding and empty antibonding states, *i.e.*, bond optimization, and, in DOS curves, at state-deficient regions, *i.e.*, pseudogap. The smallest  $r_{\text{triel-triel}}$  and “bond optimization” result in the most negative ICOHP values – these three structures have the lowest ICOHP values (again, with the KTI-type LiTl as an exception). Therefore, these three types of structures gain the largest stabilization through triel-triel covalent interactions.

The NaCl-type structures have the largest  $r_{\text{triel-triel}}$  values. Consequently, they have the weakest triel-triel interactions and, thus, the ICOHP values are the highest among all. The CsCl-type structures have smaller  $r_{\text{triel-triel}}$  than the NaCl-type structures, but still larger than the other structures. The COHP curves (Supporting Information) show that the triel-triel interactions are not optimized and triel-triel antibonding states are populated. As a result, the CsCl-type structures have the second highest ICOHP values, only lower than the NaTl-type structures. So these two structure types experience the least stabilization through triel-triel covalent interactions.

The CuAu- and the AuCd-type structures have intermediate  $r_{\text{triel-triel}}$  values and optimized triel-triel COHP curves (Supporting Information), in accordance that they also fit the Zintl-Klemm formalism. Their ICOHP values are also intermediate – higher than the NaTl-, KTI-, and BaCu-type and lower than the NaCl- and CsCl-type structures.

By comparing the energy terms in Table 3, above all, the  $\Delta E_{\text{TOT}}$  (the  $E_{\text{TOT}}$  values of the CsCl-type structures are taken as reference) values predict the correct structures – for all compositions, the lowest  $\Delta E_{\text{TOT}}$  occurs at the experimentally observed structure types.  $\Delta E_{\text{electronic}}$ , when compared at the same volume per f.u., quantifies solely the effects of valence electron localization including covalent bonding. It shows the same pattern with ICOHP – the lowest values for the NaTl-, KTI-, and BaCu-type and the highest values for the NaCl- and CsCl-type.  $\Delta E_{\text{ES}}$ , reflecting metallicity, and  $\Delta E_{\text{Madelung}}$ , reflecting ionicity, both reveal the exact opposite trend - the highest in the NaTl-, KTI-, and BaCu-type and the lowest in the NaCl- and CsCl-type. These comparisons reveal the competition between covalency, metallicity, and ionicity. Covalent interactions stabilize structures that fit the Zintl-Klemm formalism by affording short distances and optimized orbital interactions between electronegative

atoms. These structures have low  $\Delta E_{\text{electronic}}$  and ICOHP values. Metallic and ionic interactions prefer the relatively isotropic structures that give low  $\Delta E_{\text{ES}}$  and  $\Delta E_{\text{Madelung}}$  and do not follow the Zintl-Klemm rule. Therefore, any rationalization of the structures of Zintl and polar intermetallic phases should not be based solely on covalency, but on the competition between covalency, metallicity, and ionicity. As we can see from the discussion below about the NaTl-, the CsCl-, and the KTI-type structures, any factors affecting covalency, metallicity, and ionicity can “tip” the balance between them and lead to structural variation.

**Table 3.** Comparison of electrostatic, electronic, total energy terms calculated with VASP, Al/Tl-Al/Tl distances, ICOHP values calculated with LMTO, and the ionic Madelung energy values of the seven structure types for LiAl, LiTl, NaTl, and KTI. For each composition, all structures have the same volume per f.u. The energy terms of the CsCl-type structures are taken as reference. The bold numbers are the  $E_{\text{TOT}}$  of experimental structure of each composition.

		NaTl-type	KTI-type	BaCu-type	CsCl-type	NaCl-type	CuAu-type (fcc)	AuCd-type (hcp)
LiAl 31.84 Å <sup>3</sup> /f.u.	$\Delta E_{\text{TOT}}$ (eV/f.u.)	-0.1553	0.2651	0.1188	0	1.0487	-0.0235	-0.0734
	$\Delta E_{\text{ES}}$ (eV/f.u.)	1.3064	5.2514	3.5190	0	0.4137	1.1189	1.2783
	$\Delta E_{\text{electronic}}$ (eV/f.u.)	-1.4617	-4.9863	-3.4002	0	0.6350	-1.1424	-1.3517
	$r_{\text{Al-Al}}$ (Å)	2.745	2.652 - 2.790	2.489	3.169	3.557	2.824	2.824
	$\text{ICOHP}_{\text{Al-Al}}$ (eV/f.u.)	-3.35	-3.12	-2.50	-1.56	-0.53	-2.51	-2.60
	$\Delta E_{\text{Madelung}}$ (eV/f.u.)	1.3076	2.1882	1.3555	0	-0.7562	1.1165	1.2723
LiTl 40.64 Å <sup>3</sup> /f.u.	$\Delta E_{\text{TOT}}$ (eV/f.u.)	0.1985	0.1944	0.4475	0	0.4370	0.1285	0.0921
	$\Delta E_{\text{ES}}$ (eV/f.u.)	1.2054	0.5543	2.6584	0	0.3831	1.0329	1.1785
	$\Delta E_{\text{electronic}}$ (eV/f.u.)	-1.0069	-0.3599	-2.2108	0	0.0539	-0.9044	-1.0864
	$r_{\text{Tl-Tl}}$ (Å)	2.977	3.271 - 3.624	2.746	3.438	3.859	3.063	3.063
	$\text{ICOHP}_{\text{Tl-Tl}}$ (eV/f.u.)	-2.03	-1.51	-2.07	-0.88	-0.42	-1.58	-1.66
	$\Delta E_{\text{Madelung}}$ (eV/f.u.)	1.2054	1.2554	1.1663	0	-0.6971	1.0293	1.1728
NaTl 51.61 Å <sup>3</sup> /f.u.	$\Delta E_{\text{TOT}}$ (eV/f.u.)	-0.0446	0.0758	0.1590	0	0.4161	0.0027	-0.0286
	$\Delta E_{\text{ES}}$ (eV/f.u.)	1.1131	2.8263	3.3329	0	0.3534	0.9534	1.0886
	$\Delta E_{\text{electronic}}$ (eV/f.u.)	-1.1577	-2.7505	-3.1739	0	0.0627	-0.9506	-1.1172
	$r_{\text{Tl-Tl}}$ (Å)	3.224	3.150 - 3.732	2.886	3.723	4.179	3.317	3.317
	$\text{ICOHP}_{\text{Tl-Tl}}$ (eV/f.u.)	-1.80	-1.56	-1.63	-0.74	-0.31	-1.31	-1.37
	$\Delta E_{\text{Madelung}}$ (eV/f.u.)	1.1131	1.6122	1.3041	0	-0.6437	0.9504	1.0829
KTI* 78.32 Å <sup>3</sup> /f.u.	$\Delta E_{\text{TOT}}$ (eV/f.u.)	-0.1338	-0.2328	-0.1587	0	0.3637	0.0227	-0.0119
	$\Delta E_{\text{ES}}$ (eV/f.u.)	0.9686	8.0375	5.5078	0	0.3082	0.8307	0.9481
	$\Delta E_{\text{electronic}}$ (eV/f.u.)	-1.1024	-8.2703	-5.6665	0	0.0555	-0.8080	-0.9600
	$r_{\text{Tl-Tl}}$ (Å)	3.705	3.107 - 3.708	3.133	4.278	4.802	3.812	3.812
	$\text{ICOHP}_{\text{Tl-Tl}}$ (eV/f.u.)	-1.43	-1.78	-1.98	-0.69	-0.16	-1.04	-1.06
	$\Delta E_{\text{Madelung}}$ (eV/f.u.)	0.9686	2.5046	1.4665	0	-0.5601	0.8272	0.9425

\* For KTI in its own structure, the data are from the structure optimized with VASP instead of experimental structure from reference 33. The comparison between the optimized and experimental structures can be found in Supporting Information.

### 3.4.2 The CsCl- and the NaTl-Type Structures

Among the seven structure types, the NaTl- and the CsCl-type structures both occur for alkali metal trielides. These two structure types are closely related: atoms occupy the same positions and only differ in the way they are distributed among these positions in the two structures (or, in short, different “coloring schemes”<sup>53</sup>). While the NaTl-type structure follows the Zintl-Klemm rule and affords optimized covalent interactions, the CsCl-type structure defies the Zintl-Klemm rule and is favored by metallicity and ionicity – it always has  $\Delta E_{ES}$  and  $\Delta E_{Madelung}$  than the NaTl-type structure (Table 3).

The competition between the CsCl- and the NaTl-type structures has been studied by many researchers.<sup>54-58</sup> Some of these works based their arguments upon “size effects”.<sup>55-57</sup> The rationalization is that the NaTl-type structure is obtained when the two following conditions are satisfied: (1) the larger atom is compressible, and (2) the radius ratio between the larger atom and the smaller atom is close to 1. These will ensure “contact” between the smaller atoms and stabilize the structure.

Other works, just as we did above, partitioned energy in different ways and rationalized that the competition between the two structures is a result of the competition between different energy terms.<sup>54,58</sup> Inglesfield’s argument<sup>54</sup> is based on the interplay between the two energy terms  $U_{metallic}$  and  $U_{sc}$ .  $U_{metallic}$  is the band energy assuming a spherical Fermi surface, i.e. assuming the compound is a simple metal whose electrons behave like a free electron gas.  $U_{sc}$ , named as “semiconductor term”, is the energy caused by the formation of band gaps.  $U_{metallic}$  prefers the CsCl-type structure and  $U_{sc}$  favors the NaTl-type structure. Inglesfield also pointed out by calculating the bonding charge that electrons are expected to concentrate between triel atoms, so Zintl’s covalent bonding picture is justifiable. However, he did not demonstrate how covalent bonding should affect those energy terms. In fact,  $U_{sc}$  is an evaluation of bonding because, from a chemist’s view, the formation of a band gap in the DOS is often the result of covalent bonding – bonding states are lowered and antibonding states are raised in energy, generating a gap in the DOS.

Using the TB-LMTO-ASA method, Christensen<sup>58</sup> partitioned the total energy into a Madelung term and a band energy term. The Madelung term is the electrostatic energy calculated as in equation (1), where  $Z_1$  and  $Z_2$  are the calculated charges of different atomic spheres; and the band energy is the sum of the energies of the occupied one-electron eigenstates. The Madelung term is lower (more negative) in the CsCl-type structure. This, above all, can be expected from equation (1): the Madelung

constants for these two structures are 1.76267 for the CsCl-type structure and 1.51343 for the NaTl-type structure.<sup>10</sup> So, given the same volume and charges on “cations” and “anions”, the CsCl-type structure provides lower Madelung energy. Moreover, Christensen’s work also showed that charge transfer is more significant in the CsCl-type structure, or, it has larger absolute values for  $Z_1$  and  $Z_2$ , further lowering Madelung energy. Therefore, ionicity favors the CsCl-type structure.

Counteracting the Madelung term, the band energy is always lower in the NaTl-type structure. Christensen claimed that this indicates that covalent bonding prefers the NaTl-type structure because the band energy “contains all the effects of bonding and hybridization”. The effect of any metallic term was not discussed here. Actually, the band energy from TB-LMTO-ASA surely contains the effect of covalent bonding, but it is improper to assign it solely to covalency. The effect of metallic interactions may also be reflected here. For example, for *hcp* Na, the total energy calculated with LMTO is  $-323.81$  Ry per atom, which is entirely from the band energy, because the ionic Madelung energy term is 0. Here, the band energy depicts a metallic picture because we do not expect significant covalent bonding in Na. In Zintl phases, where metallicity and covalency coexist, the band energy quantifies both effects. To complete Christensen’s methodology, metallic electrostatic energy should be evaluated. The electrostatic energy terms in Table 3 clearly show that metallicity favors the CsCl-type structure. This is in accordance with equation (3), if we take +1 and +3 for  $Z_{\text{Li}}$  and  $Z_{\text{Tl}}$ , with the Madelung constants in the literature,<sup>10</sup> the metallic electrostatic energies of these two structures are  $E_{ES}(\text{CsCl-type}) = -8.16959/R_a$  and  $E_{ES}(\text{NaTl-type}) = -8.02789/R_a$ , so at the same volume per f.u.,  $E_{ES}(\text{CsCl-type})$  is more negative than  $E_{ES}(\text{NaTl-type})$ . So the CsCl-type structure is also a better choice for metallic interactions. Therefore, that the band energy is lower in the NaTl-type structure is not because of metallicity. Christensen’s conclusion is right after all: covalency favors the NaTl-type structure. This also agrees with our ICOHP values in Table 3 – the NaTl-type structure always has lower ICOHP (thus, more energy lowering through covalent interactions) than the CsCl-type structure.

While all these works systematically studied the two structure types, it remains unexplained why LiTl is the only one that adopts the CsCl-type structure. Substitution of Li for Na or Tl for other triels both result in the NaTl-type structure. Apparently, covalency is overruled by metallicity and/or ionicity in LiTl but not in the other alkali metal trielides. To investigate this, we compared LiTl with LiAl and NaTl.

### 3.4.3 LiAl, LiTl, and NaTl

The initial comparisons were made between the two structure types at equal volumes per f.u.. The experimental volumes per f.u. of LiAl (31.84 Å<sup>3</sup>/f.u.),<sup>30</sup> LiTl (40.64 Å<sup>3</sup>/f.u.),<sup>28</sup> and NaTl (51.61 Å<sup>3</sup>/f.u.)<sup>27</sup> were taken. At each volume, the NaTl- and the CsCl-type model structures were built, calculated, and compared for each of the three compositions: LiAl, LiTl, and NaTl.

The comparison of energy terms calculated with VASP is tabulated in Table 4. The total energy ( $\Delta E_{\text{TOT}}$ ) values predict the right structures, at all three volumes, the NaTl-type structure has lower energy in LiAl and NaTl ( $\Delta E_{\text{TOT}}$  negative) but higher in LiTl ( $\Delta E_{\text{TOT}}$  positive). Therefore, the competition between the NaTl- and the CsCl-type structures in alkali metal trielides cannot be attributed solely to a size effect as in some of the previous reports<sup>55-57</sup> mentioned above. Even if we equalize the size effect, they still favor different structures.

The metallic electrostatic energy values are always lower for the CsCl-type structure ( $\Delta E_{\text{ES}}$  always positive) for all compositions and volumes, indicating once again that metallic interaction favors the CsCl-type structure. The electronic terms are always lower for the NaTl-type structure ( $\Delta E_{\text{electronic}}$  always negative). Although  $\Delta E_{\text{electronic}}$  contains factors from both ionic and covalent interactions, its favoritism toward the NaTl-type structure must originate from covalency because, as discussed above, ionicity favors the CsCl-type structure. So, covalent bonding stabilizes the NaTl-type structure and it is competing with metallic and ionic interactions. Table 4 also shows that, just as what we can expect from equations (2) and (3), when volumes are equal, all three compositions have equal  $\Delta E_{\text{ES}}$ . (It is not exactly equal at 31.84 Å<sup>3</sup>/f.u. This can be attributed to the fact that the pseudopotentials employed in the calculations deviate from being spherical as in equations (2) and (3) at the vicinities of the atom cores. So when volume is small, *i.e.*, cores are close to each other, the result will deviate from what we would expect from equations (2) and (3).) But LiTl has the least negative  $\Delta E_{\text{electronic}}$ . As a result, covalency wins in LiAl and NaTl ( $\Delta E_{\text{electronic}}$  overcomes  $\Delta E_{\text{ES}}$ ) but loses in LiTl ( $\Delta E_{\text{ES}}$  overcomes  $\Delta E_{\text{electronic}}$ ).

We then examined the covalent interactions between the triel atoms by calculating the ICOHP values with LMTO (Table 5) and also by plotting the valence electron density maps (Figure 3) with VASP, which show close correspondence with each other. From the charge density maps, above all, we can see that Zintl-Klemm's covalent bonding picture is justifiable, especially for LiAl at 31.84 Å<sup>3</sup>/f.u. – valence electrons are concentrated between Al atoms within cylindrical regions along Al-Al axial directions, a picture of chemical bonds. This is in sharp contrast with the CsCl-type structures (Supporting Information), in which valence electrons are enriched within slightly distorted spherical



regions centered on triel atoms. Therefore, the NaTl-type structure has stronger Al/Tl-Al/Tl orbital interactions than the CsCl-type structure. Corresponding to this, the ICOHP values in Table 5 show that the Al/Tl-Al/Tl interaction in the NaTl-type structure lowers energy more significantly (i.e., more negative ICOHP) than in the CsCl-type structure.

**Table 4.** The difference in energy terms,  $\Delta E = E(\text{NaTl-type}) - E(\text{CsCl-type})$ , between the CsCl- and NaTl-type structures in LiAl, LiTl, and NaTl calculated at three fixed volumes, which are the experimental volumes of LiAl, LiTl, and NaTl.

Comp.	Energy Terms	31.84 Å <sup>3</sup> /f.u.	40.64 Å <sup>3</sup> /f.u.	51.61 Å <sup>3</sup> /f.u.
LiAl	$\Delta E_{ES}$ (eV/f.u.)	1.3064	1.2054	1.1131
	$\Delta E_{\text{electronic}}$ (eV/f.u.)	-1.4617	-1.3801	-1.2494
	$\Delta E_{TOT}$ (eV/f.u.)	-0.1553	-0.1747	-0.1363
LiTl	$\Delta E_{ES}$ (eV/f.u.)	1.3075	1.2054	1.1131
	$\Delta E_{\text{electronic}}$ (eV/f.u.)	-0.9123	-1.0069	-1.0415
	$\Delta E_{TOT}$ (eV/f.u.)	0.3952	0.1985	0.0716
NaTl	$\Delta E_{ES}$ (eV/f.u.)	1.3076	1.2054	1.1131
	$\Delta E_{\text{electronic}}$ (eV/f.u.)	-1.3234	-1.2508	-1.1577
	$\Delta E_{TOT}$ (eV/f.u.)	-0.0158	-0.0454	-0.0446

We can also see that size is indeed an important factor. At larger volumes (longer triel-triel distances), valence electrons are distributed more around the triel atoms and less between them, i.e., a weaker covalent interaction. The stabilization through covalent Al/Tl-Al/Tl interactions also gets smaller (less negative ICOHP in Table 5) with increasing volume. The effect of size is discussed in more detail in the next section.

However, size is not the only factor. Tl and Al atoms do not behave the same even at the same volume. At the same triel-triel distance, Tl-Tl interactions are weaker than Al-Al because valence electrons are distributed less between atoms and more around them. Pawlowska reported similar results calculated with the LMTO method.<sup>59</sup> In consistency with this, the ICOHP values of Al-Al contacts are always higher than those of Tl-Tl for the same structure at the same volume.

The  $\Delta\text{ICOHP}$  (=  $\text{ICOHP}(\text{NaTl-type}) - \text{ICOHP}(\text{CsCl-type})$ ) values in Table 5 also show the same pattern as  $\Delta E_{\text{electronic}}$  in Table 4: at each volume, LiTl and NaTl have less negative  $\Delta\text{ICOHP}$  values than LiAl, demonstrating that, relative to the CsCl-type structure, the NaTl-type structure provides less stabilization in thallides than in aluminides through covalent interactions.

The reason why Tl-Tl bonds are weaker than Al-Al can be found by comparing the band structures of NaTl-type LiAl, LiTl, and NaTl (Figure 4). Figure 4 shows that these band structures are similar

except around the special  $k$ -points  $\Gamma$  (0, 0, 0) and  $L$  ( $\pi/a$ ,  $\pi/a$ ,  $\pi/a$ ). The bands at these two  $k$ -points are examined in detail by projecting them onto the spherical harmonics (valence orbitals) of each atom and plotting their electron density maps (Supporting Information). Irreducible representation symbols taken from the Bilbao Crystallographic Server<sup>60</sup> were assigned to these bands according to their eigenvectors.

**Table 5.** The triel-triel ICOHP values calculated for LiAl, LiTl, and NaTl in both the CsCl- and NaTl-type structures with LMTO method.  $\Delta\text{ICOHP} = \text{ICOHP}(\text{NaTl-type}) - \text{ICOHP}(\text{CsCl-type})$ .  $\text{ICOHP}_{s-s}$  is the ICOHP of Al 3s-3s interactions and Tl 6s-6s interactions.

Comp.	ICOHP (eV/f.u.)	31.84 Å <sup>3</sup> /f.u.	40.64 Å <sup>3</sup> /f.u.	51.61 Å <sup>3</sup> /f.u.
LiAl	ICOHP <sub>Al-Al</sub> (CsCl-type)	-1.56	-1.24	-0.96
	ICOHP <sub>Al-Al</sub> (NaTl-type)	-3.35	-2.76	-2.17
	$\Delta\text{ICOHP}_{\text{Al-Al}}$	-1.79	-1.52	-1.21
	ICOHP <sub>s-s</sub> (NaTl-type)	-0.06	0.08	0.13
LiTl	ICOHP <sub>Tl-Tl</sub> (CsCl-type)	-1.10	-0.88	-0.69
	ICOHP <sub>Tl-Tl</sub> (NaTl-type)	-2.36	-2.00	-1.59
	$\Delta\text{ICOHP}_{\text{Tl-Tl}}$	-1.26	-1.11	-0.90
	ICOHP <sub>s-s</sub> (NaTl-type)	0.33	0.32	0.25
NaTl	ICOHP <sub>Tl-Tl</sub> (CsCl-type)	-1.19	-0.95	-0.74
	ICOHP <sub>Tl-Tl</sub> (NaTl-type)	-2.75	-2.25	-1.74
	$\Delta\text{ICOHP}_{\text{Tl-Tl}}$	-1.56	-1.30	-1.00
	ICOHP <sub>s-s</sub> (NaTl-type)	0.31	0.31	0.23

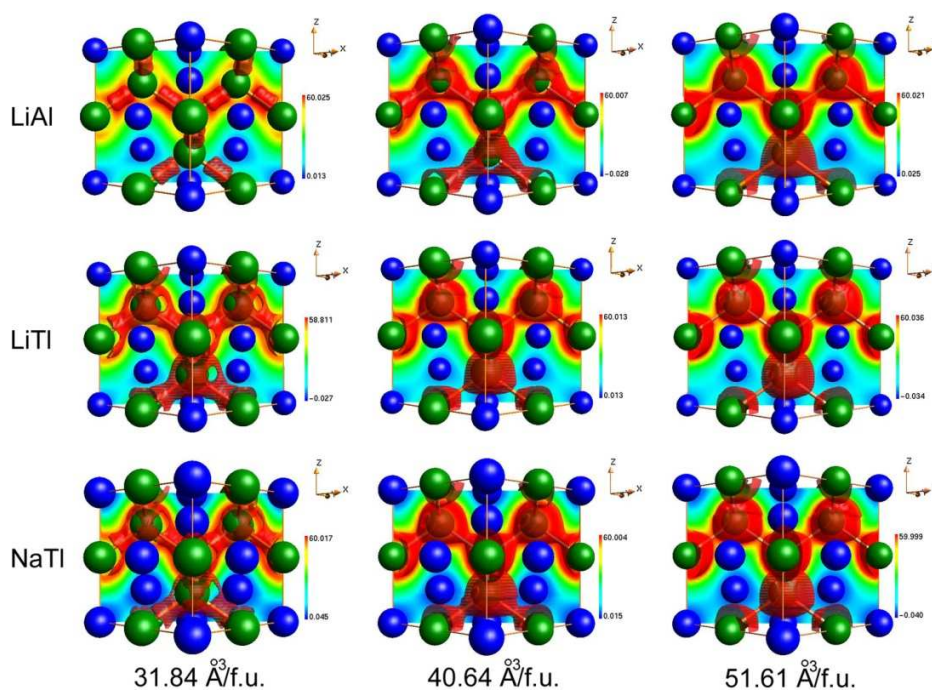


**Figure 3.** Valence electron density maps of NaTl-type LiAl, LiTl, and NaTl calculated with VASP.

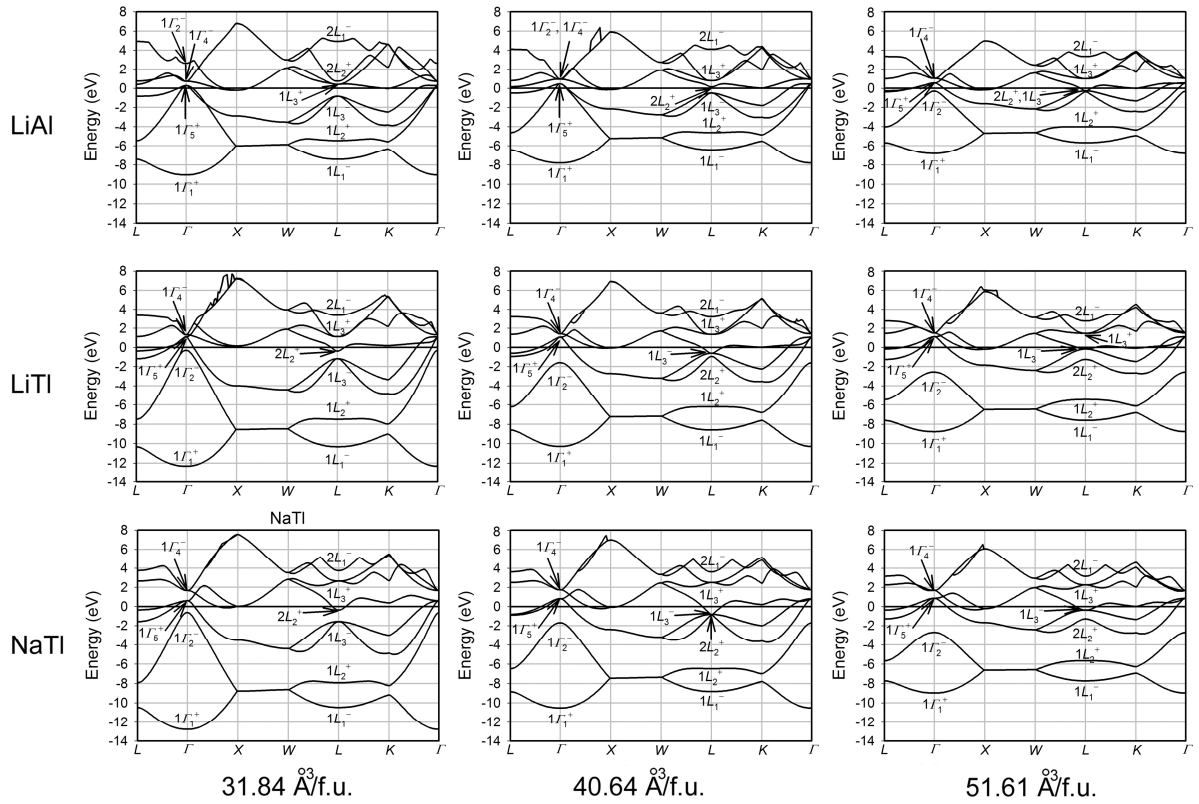


**Figure 4.** Band structures of NaTl-type LiAl, LiTl, and NaTl calculated with VASP.

Special attention was drawn to  $1I_2^-$  and  $2L_2^+$  bands, which are always below the Fermi level ( $E_F$ ) in thallides, but above  $E_F$  in LiAl except at 51.61 Å<sup>3</sup>/f.u.. The eigenvectors of these two bands are tabulated in Supporting Information. Both  $1I_2^-$  and  $2L_2^+$  are mainly composed of the Al/Tl  $s$  orbitals. Crystal orbitals sketches can be drawn for these two bands according to their eigenvectors, with Al/Tl  $s$  orbitals represented as spheres and the phase relationships specified with black and white color (Figure 5).  $1I_2^-$  is clearly antibonding with every  $s$  orbital surrounded by four other  $s$  orbitals with opposite phase.  $2L_2^+$  is partially antibonding – every  $s$  orbital is surrounded by one in-phase and three opposite-phase  $s$  orbitals. The valence electron density maps (also in Figure 5, only LiAl and LiTl are shown, NaTl is similar to LiTl) are consistent with the sketch – electron density depletion can be found between neighboring Al/Tl atoms in both LiAl and NaTl-type LiTl for these two bands. Therefore,  $s$ - $s$  antibonding states are empty in aluminides (except at large volume) but populated in thallides, rendering weaker interactions between Tl atoms and less stabilization through covalency in thallides. This should be attributed to the fact that for Tl, its  $s$  orbital is more contracted with respect to  $p$  orbitals due to its poor shielding effect of  $d$  and  $f$  electrons and its strong relativistic effects.<sup>61</sup>

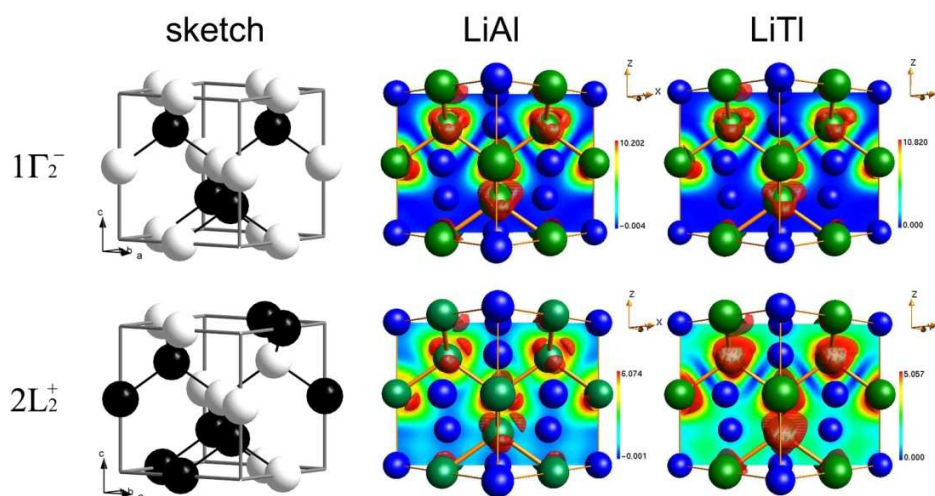


**Figure 5.** The crystal orbital sketches and valence electron density maps of  $1\Gamma_2^-$  and  $2L_2^+$  bands in LiAl (at  $31.84 \text{ \AA}^3/\text{f.u.}$ ) and NaTl-type LiTl (at  $40.64 \text{ \AA}^3/\text{f.u.}$ ). Only Tl/Al  $s$  orbitals are shown because Tl/Al  $p$  orbitals and Li orbitals have much smaller contributions (Supporting Information). Black and white colors specify the phase relationships. Blue – Li; green – Al/Tl.

The ICOHP values (Table 5) agree with this conclusion. The  $\text{ICOHP}_{s-s}$  values of Tl-Tl interactions are positive and decrease when the volume increases. So the Tl  $6s$ - $6s$  interactions are “antibonding” and, by increasing the volume (thus Tl-Tl distances), the antibonding interaction gets relieved. By contrast, the  $\text{ICOHP}_{s-s}$  values of Al-Al interactions are negative at small volumes and increase as the volume gets larger. And, they are always much lower than  $\text{ICOHP}_{s-s}$  values of Tl-Tl pairs. So, the Al  $3s$ - $3s$  interactions are “bonding” at small volume and, by increasing the volume, the bonding interaction is weakened. But they never destabilize structures as much as Tl  $6s$ - $6s$  orbital interactions.

Therefore, all data, including  $\Delta E_{\text{electronic}}$ , ICOHP, valence electron density maps, band structures, and eigenvectors show that thallides are less stabilized by covalent interactions than aluminides in the double-diamond-type structure.

Additionally, the two thallides do not exhibit equal covalent interactions. Both  $\Delta E_{\text{electronic}}$  (Table 4) and  $\Delta \text{ICOHP}$  (Table 5) are less negative in LiTl than in NaTl, showing that LiTl has less stabilization through Tl-Tl covalent interactions than NaTl. This can be rationalized by comparing the charge transfer from the alkali metal atom to Tl. Table 6 lists the  $\text{IDOS}(E_F)$  values of each atom in NaTl-type LiTl and NaTl. These numbers do not mean exactly the number of valence electrons on each atom, because when IDOS is calculated, the “overlap population” is always evenly divided between atoms<sup>7</sup>

and this leads to overestimation for electropositive atoms and underestimation for electronegative atoms. But, they are still informative. By comparing the IDOS values at the same volume, (1) Na has smaller IDOS value than Li and (2) Tl has higher IDOS in NaTl than in LiTl. This means that Na donates more valence electrons to Tl. It is in accordance with the electronegativity values of Li and Na. The absolute electronegativities are 3.01 eV for Li and 2.85 eV for Na.<sup>62</sup>

The optimum number of valence electrons for covalent bonding in a diamond structure is 4 per atom. Fewer valence electrons will weaken the bonds and destabilize the structure. For instance, when doping boron into silicon, according to the phase diagram,<sup>63</sup> the maximum amount of doping is 3.06 %atom of boron at 1385 °C and much lower at room temperature. The same principle applies for the Tl diamond-type sublattice in the NaTl-type structure. To achieve 4 valence electrons per Tl, the alkali metal atoms must donate all valence electrons (1 per atom). In NaTl-type LiTl and NaTl, neither Li nor Na donates all valence electrons, but since Na donates more than Li, it affords stronger Tl-Tl bonding and stabilizes the Tl diamond sublattice better.

**Table 6.** IDOS values of each atom in NaTl-type LiTl and NaTl calculated with LMTO method.

Comp.	IDOS( $E_F$ ) (/f.u.)	31.84 Å <sup>3</sup> /f.u.	40.64 Å <sup>3</sup> /f.u.	51.61 Å <sup>3</sup> /f.u.
LiTl	Li	1.30	1.16	1.06
	Tl	2.70	2.84	2.94
NaTl	Na	1.05	1.00	0.94
	Tl	2.95	3.00	3.06

In conclusion, among LiAl, LiTl, and NaTl, LiTl gains the least stabilization from triel-triel covalent interactions in the NaTl-type structure. This is why covalency is overruled by metallicity and ionicity in LiTl and it defies the Zintl-Klemm rule and adopts the CsCl-type structure, which is favored by metallicity and ionicity.

### 3.4.4 Volume Effect

In all discussions above, we have been comparing the CsCl- and the NaTl-type structures at equal volume per f.u.. This treatment successfully revealed the factors that are independent from volume, including relativistic effects and differences in charge transfer. However, for any given composition, different structures (polymorphs) do not have to have equal volumes per f.u.. For instance, at room temperature, the volume of diamond is 5.6730 Å<sup>3</sup>/atom<sup>64</sup> and graphite 8.8214 Å<sup>3</sup>/atom<sup>65</sup>. Therefore, the CsCl- and the NaTl-type structures may form at different volumes as well and the volume difference will also affect their relative stability.

To study such volume effects, we varied the volume and examined how the total energy responds in the CsCl- and the NaTl-types LiAl, LiTl, and NaTl (Figure 6). The calculated  $E_{\text{TOT}}(V)$  curves were fitted with the Murnaghan equation of state,<sup>44</sup> from which we obtained the bulk moduli of these phases. The calculated bulk moduli of LiAl and NaTl in their observed double diamond structure are, respectively,  $4.71 \times 10^{11}$  and  $1.75 \times 10^{11}$  dyne/m<sup>2</sup>, which are only slightly smaller than the experimental values,  $5.07 \times 10^{11}$  and  $1.86 \times 10^{11}$  dyne/m<sup>2</sup>.<sup>66</sup> Moreover, we also obtained the equilibrium volumes ( $V_{\text{eq}}$ ), the volume at the minima of the curves (Table 7). These are the predicted volumes of the corresponding structures at zero pressure and 0 K. The energy terms and ICOHP were calculated for all structures at their  $V_{\text{eq}}$  and also tabulated in Table 7.

In general, VASP predicts volumes larger than the experimental values, especially for thallides. This can be attributed to the PBE-GGA<sup>40</sup> used in VASP, an approximation which has been found to overestimate lattice parameters.<sup>67,68</sup> Despite this defect, VASP does predict the right structure for each composition – the overall minima occur in the curves of the NaTl-type structure for LiAl and NaTl, and in the curve of the CsCl-type structure for LiTl.

The CsCl- and the NaTl-type structures have different  $V_{\text{eq}}$ . The difference  $\Delta V_{\text{eq}}$  with respect to the CsCl-type is much larger in LiTl ( $+3.30 \text{ \AA}^3/\text{f.u.}$ ) than in LiAl ( $+0.98 \text{ \AA}^3/\text{f.u.}$ ) and NaTl ( $-0.67 \text{ \AA}^3/\text{f.u.}$ ). This can be explained by examining the radius ratios between the alkali metal ( $r_{\text{A}}$ ) and the triel atoms ( $r_{\text{triel}}$ ). The two structures will have the same volume when  $r_{\text{A}}/r_{\text{triel}} = 1$ , while the greater this ratio deviates from 1, the larger the volume difference is. The covalent radii of Li, Na, Al, and Tl are, respectively, 1.28(7) Å, 1.66(9) Å, 1.21(4) Å, and 1.45(7) Å.<sup>69</sup> LiAl has smaller  $\Delta V_{\text{eq}}$  than LiTl because  $r_{\text{Li}}/r_{\text{Al}}$  (1.06) is closer to 1 than  $r_{\text{Li}}/r_{\text{Tl}}$  (0.88).  $r_{\text{Na}}/r_{\text{Tl}}$  (1.14) is slightly farther from 1 than  $r_{\text{Li}}/r_{\text{Tl}}$ . The smaller and negative  $\Delta V_{\text{eq}}$  of NaTl than LiTl can be attributed to the higher compressibility of the larger atoms – Na in NaTl than Tl in LiTl.

The large positive  $\Delta V_{\text{eq}}$  will make the NaTl-type structure even more unfavorable by  $E_{\text{ES}}$ . Besides the difference in Madelung constant,  $E_{\text{ES}}$  is proportional to  $R_{\text{a}}^{-1}$  or  $V^{-1/3}$  (equation (3)). Table 7 shows that  $E_{\text{ES}}$  are higher in the NaTl-type structure for LiAl, LiTl, and NaTl. And, LiTl has the most positive  $\Delta V_{\text{eq}}$  among the three so it also has the most positive  $\Delta E_{\text{ES}}$ . So the previous reports whose arguments are based on “size effects”<sup>55-57</sup> are right in this point: it is beneficial for the NaTl-type structure to have an  $r_{\text{A}}/r_{\text{triel}}$  close to 1, and the larger atom has good compressibility. However, the reason is not that the smaller atoms want to be in close contact, because LiTl adopts the CsCl-type structure where Li-Li distances are even larger ( $r_{\text{eq,Li-Li}} = 3.498 \text{ \AA}$ ) than in the NaTl-type structure ( $r_{\text{eq,Li-Li}} = 3.108 \text{ \AA}$ ).



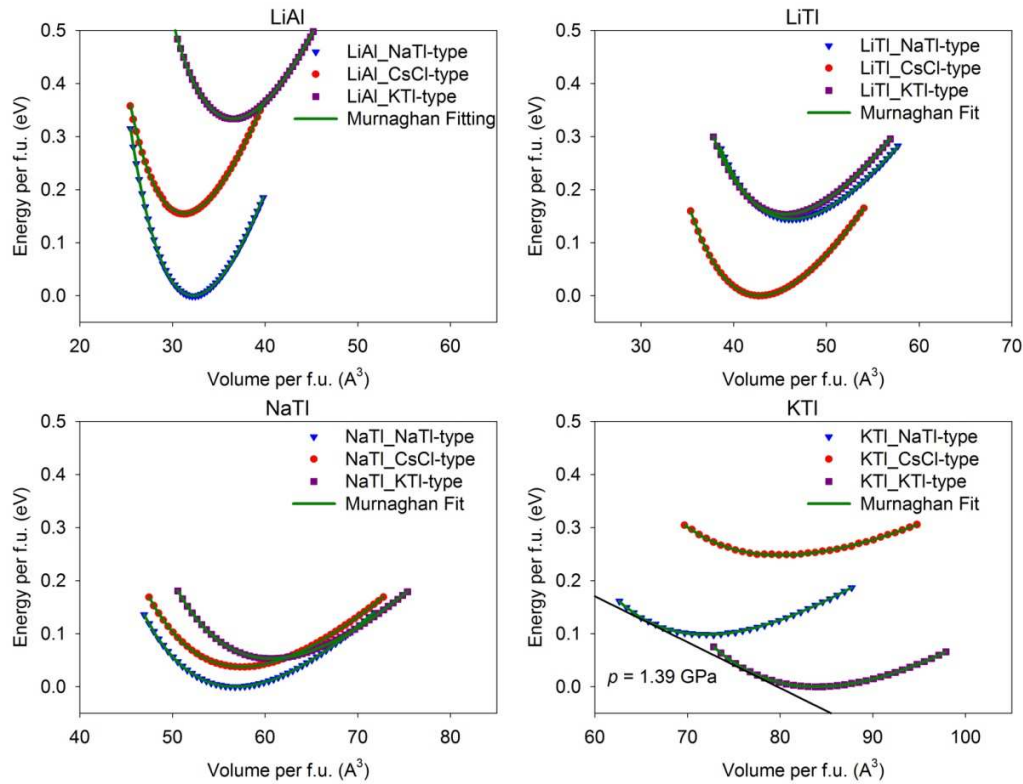


**Figure 6.**  $E_{TOT}(V)$  curves of LiAl, LiTl, NaTl, and KTI in the NaTl-, CsCl-, and KTI-type structures.  $\Delta E = E(\text{NaTl-type}) - E(\text{CsCl-type})$ .

$E_{\text{electronic}}$  are still always lower in the NaTl-type structure, although  $E_{\text{electronic}}$  does not only include the effect of valence electron localization. When two structures are compared at different volumes, their average valence electron densities ( $n$ ) are different. Both  $V_{\text{HEG-HEG}}$  and  $T_{\text{HEG}}$  are functionals of  $n$  so they also contribute to  $\Delta E_{\text{electronic}}$  (equation (7)). According to equation (8),  $T_{\text{TEG}}$  is proportional to  $n^{5/3}$  and  $V$ , so it is proportional to  $V^{-2/3}$ . In equation (9),  $n^2$  is proportional to  $V^{-2}$  and the integral is proportional to  $V^{-1/3}$  so  $V_{\text{HEG-HEG}}$  is proportional to  $V^{-7/3}$ . So, when volume gets larger from the CsCl- to the NaTl-type structure ( $\Delta V_{\text{eq}} > 0$ ), as in LiAl and LiTl, these two terms both decrease, contributing to the negative  $\Delta E_{\text{electronic}}$ . In NaTl,  $\Delta V_{\text{eq}} < 0$ , so  $V_{\text{HEG-HEG}}$  and  $T_{\text{HEG}}$  increase from the CsCl- to the NaTl-type structure. The negative  $\Delta E_{\text{electronic}}$  here must be the effect of valence electron localization or covalent interactions. Currently, we cannot precisely calculate these two terms so we cannot quantitatively evaluate the effect of valence electron localization from  $\Delta E_{\text{electronic}}$  yet. However, ICOHP values reveal that triel-triel covalent interactions still provide more stabilization in the NaTl-type structure – it always has lower ICOHP values. And ionicity still favors the CsCl-type structures –  $\Delta E_{\text{Madelung}}$  is always positive for the NaTl-type structures.

**Table 7.** The equilibrium volumes obtained from fitting  $E(V)$  curves and the energy terms and ICOHP calculated at these equilibrium volumes. The energy terms of the CsCl-type structures are taken as reference.

	LiAl	LiTl	NaTl	KTl
$V_{\text{exp}} (\text{\AA}^3/\text{f.u.})$	31.84	40.64	51.61	78.32
$V_{\text{eq,CsCl-type}} (\text{\AA}^3/\text{f.u.})$	31.28	42.81	57.49	80.07
$V_{\text{eq,NaTl-type}} (\text{\AA}^3/\text{f.u.})$	32.26	46.21	56.82	72.00
$V_{\text{eq,KTl-type}} (\text{\AA}^3/\text{f.u.})$	36.55	45.57	60.62	83.95
$\Delta E_{\text{ES,CsCl-type}} (\text{eV}/\text{f.u.})$	0	0	0	0
$\Delta E_{\text{ES,NaTl-type}} (\text{eV}/\text{f.u.})$	2.0842	2.9681	0.8046	-5.5255
$\Delta E_{\text{ES,KTl-type}} (\text{eV}/\text{f.u.})$	8.8295	2.0216	3.8844	4.8230
$\Delta E_{\text{electronic,CsCl-type}} (\text{eV}/\text{f.u.})$	0	0	0	0
$\Delta E_{\text{electronic,NaTl-type}} (\text{eV}/\text{f.u.})$	-2.2390	-2.9237	-0.8417	5.3759
$\Delta E_{\text{electronic,KTl-type}} (\text{eV}/\text{f.u.})$	-8.6501	-1.8679	-3.8683	-5.0712
$\Delta E_{\text{TOT,eq,CsCl-type}} (\text{eV}/\text{f.u.})$	0	0	0	0
$\Delta E_{\text{TOT,eq,NaTl-type}} (\text{eV}/\text{f.u.})$	-0.1548	0.1444	-0.0371	-0.1496
$\Delta E_{\text{TOT,eq,KTl-type}} (\text{eV}/\text{f.u.})$	0.1794	0.1536	0.0161	-0.2482
$\text{ICOHP}_{\text{triel-triel,CsCl-type}} (\text{eV}/\text{f.u.})$	-1.59	-0.84	-0.66	-0.69
$\text{ICOHP}_{\text{triel-triel,NaTl-type}} (\text{eV}/\text{f.u.})$	-3.36	-1.87	-1.62	-1.65
$\text{ICOHP}_{\text{triel-triel,KTl-type}} (\text{eV}/\text{f.u.})$	-2.86	-0.76	-1.34	-1.66
$\Delta E_{\text{Madelung,CsCl-type}} (\text{eV}/\text{f.u.})$	0	0	0	0
$\Delta E_{\text{Madelung,NaTl-type}} (\text{eV}/\text{f.u.})$	1.3984	1.3658	1.0480	0.7513
$\Delta E_{\text{Madelung,KTl-type}} (\text{eV}/\text{f.u.})$	2.5609	1.3809	1.6607	2.5539

Therefore, comparisons at different  $V_{\text{eq}}$  achieve the same conclusion – covalency favors the NaTl-type structure and competes with metallicity, which favors the CsCl-type structure. And finally,  $\Delta E_{\text{TOT}}$  shows that volume relaxation of the two structures does not change their relative stability –  $E_{\text{TOT}}$  is still lower for the NaTl-type structure in LiAl and NaTl and higher in LiTl.

### 3.4.5 The KTI-Type Structure

The distorted  $\text{Tl}_6$  octahedra in the KTI-type structure, as previously mentioned, resembles gaseous  $\text{Si}_6$ . The structure fits the Zintl-Klemm formalism and features optimized triel-triel interactions (Supporting Information). The mysteries here include (1) KTI adopts this structure instead of the other covalency stabilized structure, the NaTl-type; (2) this structure is only obtained in KTI but not the other alkali metal trielides; and (3) it transforms to the NaTl-type structure under pressure.

One of the major differences between the NaTl- and the KTI-type structures is that the symmetry of the NaTl-type requires equal alkali-alkali ( $r_{\text{A-A}}$ ), alkali-triel ( $r_{\text{A-triel}}$ ), and triel-triel ( $r_{\text{triel-triel}}$ ) distances (if we only consider the nearest neighbors); whereas there is no such restriction in the KTI-type structure. Table 8 lists the interatomic distances in the KTI-type structure and compares them with the interatomic distances in the NaTl-type structure ( $r_{\text{NaTl-type}} = r_{\text{A-A}} = r_{\text{A-triel}} = r_{\text{triel-triel}}$ ) at the same volume per f.u..



For KTI, the KTI-type structure has  $r_{\text{Tl-Tl}} < r_{\text{K-Tl}} < r_{\text{NaTl-type}} < r_{\text{K-K}}$ , in accordance with the fact that the K atom (covalent radius 2.03 Å<sup>69</sup>) is larger than Tl (1.45 Å). LiTl is exactly opposite to KTI –  $r_{\text{Li-Li}} < r_{\text{Li-Tl}} < r_{\text{NaTl-type}} < r_{\text{Tl-Tl}}$ , also in accordance with the size difference between Li (1.28 Å) and Tl (1.45 Å). For the KTI-type LiAl and NaTl,  $r_{\text{A-triel}} < r_{\text{triel-triel}} < r_{\text{NaTl-type}} < r_{\text{A-A}}$ .  $r_{\text{triel-triel}}$  is still smaller than  $r_{\text{NaTl-type}}$  but to a much lesser degree (0.06-0.09 Å in LiAl and ~0.07 Å in NaTl) than in KTI (0.1-0.6 Å).  $r_{\text{triel-triel}}$  affects both metallicity and covalency.

**Table 8.** The interatomic distances of alkali metal trielides in the KTI-type structure optimized with VASP at their experimental volume per f.u.. The bold numbers are those distances shorter than  $r_{\text{NaTl-type}}$ .

LiAl $r_{\text{NaTl-type}} = 2.745 \text{ \AA}$	LiTl $r_{\text{NaTl-type}} = 2.977 \text{ \AA}$	NaTl $r_{\text{NaTl-type}} = 3.224 \text{ \AA}$	KTI $r_{\text{NaTl-type}} = 3.705 \text{ \AA}$
Li1 – Li1 3.008 Å ×2	Li1 – Li2 2.778 Å ×2	Na1 – Na2 3.264 Å ×2	K1 – K1 4.111 Å ×2
Li2 2.912 Å ×2	Li2 – Li3 2.782 Å ×2	Na2 – Na3 3.379 Å ×2	K2 – K2 4.034 Å ×2
Li3 3.127 Å ×2			K2 – K3 4.152 Å ×2
Li3 – Li3 2.996 Å ×2	Li1 – Tl1 2.829 Å ×2	Na1 – Tl1 3.106 Å ×2	K3 – K3 4.265 Å ×2
Li1 – Al1 2.671 Å ×2	2.952 Å ×2	3.233 Å ×2	K1 – Tl1 3.631 Å ×2
2.700 Å ×2	Tl2 2.923 Å ×2	3.455 Å ×2	3.726 Å ×2
Li2 – Al1 2.587 Å ×2	Li2 – Tl1 2.809 Å ×2	Na2 – Tl1 3.102 Å ×2	K2 – Tl1 3.618 Å ×2
2.872 Å ×2	Tl2 2.765 Å ×2	3.223 Å ×2	3.885 Å ×2
Li2 – Al2 2.588 Å ×2	Li3 – Tl1 2.946 Å ×2	Tl2 3.074 Å ×2	Tl2 3.629 Å ×2
2.588 Å ×2	2.997 Å ×2	Na3 – Tl1 3.198 Å ×2	K3 – Tl1 3.612 Å ×2
Al1 2.617 Å ×2	Tl2 2.779 Å	3.232 Å ×2	3.658 Å ×2
Al2 2.578 Å	2.928 Å	Tl2 3.104 Å	Tl2 3.699 Å
2.816 Å	3.121 Å	3.145 Å	4.054 Å
3.112 Å			4.098 Å
Al1 – Al1 2.687 Å	Tl1 – Tl1 3.367 Å	Tl1 – Tl1 3.292 Å	Tl1 – Tl1 3.482 Å
2.790 Å	3.386 Å	3.575 Å	3.610 Å
Al2 2.652 Å	3.406 Å	3.605 Å	Tl2 3.107 Å
2.663 Å	Tl2 3.271 Å	Tl2 3.150 Å	3.130 Å
Al2 – Al2 2.665 Å	3.304 Å	3.152 Å	Tl2 – Tl2 3.708 Å

Since the triel core has the charge +3, larger than +1 of the alkali metal core, shorter/longer  $r_{\text{triel-triel}}$  will cause higher/lower  $V_{\text{core-core}}$  (equation (4)) and thus higher/lower  $E_{\text{ES}}$ .  $r_{\text{triel-triel, KTI-type}}$  is shorter than  $r_{\text{NaTl-type}}$  for all compositions except for LiTl, and accordingly,  $\Delta E_{\text{ES, KTI-type}}$  values are higher than  $\Delta E_{\text{ES, NaTl-type}}$  for all compositions except for LiTl (Table 3). So, metallicity favors the double diamond structure over the triel octahedron structure for all compositions except for LiTl.

For covalency, the ICOHP values in Table 3 reveal that for KTI, the KTI-type structure offers ICOHP values lower than the NaTl-type structure. The case is opposite for the other compositions. This can surely be attributed to the much smaller  $r_{\text{Tl-Tl}}$  than  $r_{\text{NaTl-type}}$  in only KTI, but not the other cases. Therefore, in KTI, to covalency, the triel octahedron is a better structural solution than the double

diamond network. But in LiAl, LiTl, and NaTl, the double diamond network offers more covalent stabilization than the octahedron.

$\Delta E_{\text{Madelung}}$  is always higher in the KTI-type structure than in the NaTI-type structure for all examples, indicating that ionicity prefers the latter. This can also be well understood by comparing the interatomic distances. For LiAl, NaTl, and KTI,  $r_{\text{triel-triel}}$  (“anion-anion”) is shorter than  $r_{\text{NaTI-type}}$ , and for LiTl,  $r_{\text{Li-Li}}$  (“cation-cation”) is shorter than  $r_{\text{NaTI-type}}$ . Shorter “anion-anion” and “cation-cation” both lead to higher ionic Madelung energy.

Therefore, among these alkali metal trielides, the specialty of KTI is that the size of K is much larger than Tl. The double diamond structure, which requires  $r_{\text{K-K}} = r_{\text{K-Tl}} = r_{\text{Tl-Tl}}$ , results in too long Tl-Tl distances to efficiently stabilize the structure through covalent interactions. But the less symmetrical KTI-type structure allows  $r_{\text{Tl-Tl}}$  much smaller than  $r_{\text{K-Tl}}$  and  $r_{\text{K-K}}$  and is thus better stabilized by Tl-Tl covalent interaction. Although metallicity and ionicity counteract covalency and favors the double diamond structure, covalency overcomes these factors and the KTI-type structure offers lower total energy.

The other alkali metal atoms are close to triel atoms in size or even smaller. At the same volume per f.u.,  $r_{\text{Tl-Tl}}$  in the KTI-type structure is only slightly shorter or even longer than those in the NaTI-type structure. So the KTI-type structure is not advantageous over the NaTI-type structure in covalency, and therefore it is not adopted by them.

The  $E_{\text{TOT}}(V)$  curves of the KTI-type structure for LiAl, LiTl, NaTl, and KTI are calculated with VASP and also shown in Figure 6. They are consistent with experiments – the KTI-type structure has the lowest  $E_{\text{TOT,eq}}$  only in KTI; not for the other trielides. More importantly, in KTI, we can draw a common tangential line with negative slope for the  $E_{\text{TOT}}(V)$  curves of the KTI- and the NaTI-type structures. Therefore, just as the experiment revealed,<sup>35</sup> KTI can transform into the NaTI-type structure under pressure. This pressure can be calculated as  $-(\partial E_{\text{TOT}}/\partial V) = 1.39$  GPa, which is over 6 times higher than the experimentally measured 0.2 GPa at room temperature.

As discussed above, the disadvantage of NaTI-type KTI is its long Tl-Tl distances and, thus, inefficient covalent interactions. Compression, which shortens Tl-Tl distances, at first alleviates and then eliminates this disadvantage. This is the reason of the pressure induced phase transformation.

### 3.5 Conclusions

By investigating the alkali metal trielides, LiAl, LiTl, NaTl, and KTl, we can see that to understand the structures of Zintl phases, it is insufficient to just consider the effects of covalent interactions between electronegative atoms as in the Zintl-Klemm formalism. Instead, they should be rationalized by examining the competition among metallic, ionic, and covalent effects. Generally, metallicity and ionicity prefer high-symmetry and more isotropic structures, while covalency favors less isotropic structures that afford shorter and optimized orbital interactions between electronegative atoms. Any factors that can enhance or weaken metallic, ionic, and covalent interactions can affect their competition and cause structural variation. Several influential factors were identified in our investigation: relativistic effects, electronegativity differences, and atomic size ratios between constituent elements. Relativistic effects contract the  $6s$  orbitals of Tl atoms and hinder them from participating in covalent interactions, rendering Tl-Tl covalent interactions weaker than Al-Al ones. Electronegativity differences determine the degree of valence electron transfer from the electropositive atoms to the electronegative atoms. Greater transfer in alkali metal trielides can strengthen the covalent interactions between the electronegative atoms. The atomic size ratio is one of the reasons that LiTl forms the CsCl-type structure and also explains why KTl contains  $Tl_6$  octahedra rather than the double diamond structure at ambient pressure. These findings deepen our understanding about the complete structures of Zintl phases.

### 3.6 Acknowledgements

This work is supported by NSF DMR 06-05949 and 10-05765.

### 3.7 References:

- (1) van Arkel, A. E. *Molecules and Crystals in Inorganic Chemistry*; Interscience: New York, 1956.
- (2) Ketelaar, J. A. A. *Chemical Constitution; An Introduction to the Theory of the Chemical Bond*, 2nd ed.; Elsevier: Amsterdam, 1958.
- (3) Allen, L. C. *J. Am. Chem. Soc.* **1989**, *111*, 9003.
- (4) Mann, J. B.; Meek, T. L.; Allen, L. C. *J. Am. Chem. Soc.* **2000**, *122*, 2780.
- (5) Mann, J. B.; Meek, T. L.; Knight, E. T.; Capitani, J. F.; Allen, L. C. *J. Am. Chem. Soc.* **2000**, *122*, 5132.
- (6) Wilson, J. A.; DiSalvo, F. J.; Mahajan, S. *Adv. Phys.* **1975**, *24*, 117.

- (7) Dronskowski, R. *Computational Chemistry of Solid State Materials*; Wiley-VCH: Weinheim, Germany, 2005.
- (8) Ewald, P. P. *Ann. Phys. Leipzig*. **1921**, *64*, 253.
- (9) Waddington, T. C. *Adv. Inorg. Chem. Radiochem.* **1959**, *1*, 157.
- (10) Hafner, J. *From Hamiltonians to phase diagrams*; Springer-Verlag: New York, 1987.
- (11) Fuchs, K. *J. Phys. Condens. Matter*. **1935**, *6*, 8245.
- (12) Anderson, W. P.; Burdett, J. K.; Czech, P. T. *J. Am. Chem. Soc.* **1994**, *116*, 8808.
- (13) Zintl, E.; Dullenkopf, W. *Z. Phys. Chem.* **1932**, *B16*, 183.
- (14) Zintl, E.; Brauer, G. *Z. Phys. Chem.* **1933**, *B20*, 245.
- (15) Zintl, E. *Angew. Chem.* 1939, *52*, 1.
- (16) Schäfer, H.; Eisenmann, B.; Müller, W. *Angew. Chem. Intl. Ed. Engl.* **1973**, *12*, 694.
- (17) Schäfer, H.; Eisenmann, B. *Rev. Inorg. Chem.* **1981**, *3*, 29.
- (18) Schäfer, H. *Ann. Rev. Mater. Sci.* **1985**, *15*, 1.
- (19) Nesper, R. *Prog. Solid State Chem.* **1990**, *20*, 1.
- (20) *Chemistry, Structure, and Bonding of Zintl Phases and Ions*; Kauzlarich, S. M., Ed.; VCH: Weinheim, Germany, 1996.
- (21) Kanatzidis, M. G. *Recent Trends in Thermoelectric Materials Research I*; Series: Semiconductors and Semimetals; Academic: San Diego, 2001; Vol. 69, 51.
- (22) Gascoin, F.; Ottensmann, S.; Stark, D.; Haïle, S. M.; Snyder, G. J. *Adv. Funct. Mater.* **2005**, *15*, 1860.
- (23) Shawna R. B.; Kauzlarich, S. M.; Gascoin, F.; Snyder, G. J. *Chem. Mater.* **2006**, *18*, 1873.
- (24) Condron, C. L.; Kauzlarich, S. M. *Inorg. Chem.* **2007**, *46*, 2556.
- (25) Kauzlarich, S. M.; Brown, S. R.; Snyder, G. J. *Dalton Trans.* **2007**, 2099.

- (26) Snyder, G. J.; Toberer, E. S. *Nature Mater.* **2008**, *7*, 105.
- (27) Zintl, E.; Woltersdorf, G. *Z. Elektrochem.* **1935**, *41*, 876.
- (28) Baden, W.; Schmidt, P. C.; Weiss, A. *Phys. Status Solidi. A* **1979**, *51*, 183.
- (29) Grube, V. G.; Schmidt, A. *Ztschr. Elektrochem.* **1936**, *42*, 201.
- (30) Ehrenberg, H.; Pauly, H.; Knapp, M.; Gröbner, J.; Mirkovic, D. *J. Solid State Chem.* **2004**, *177*, 227.
- (31) Jang, G. E.; Curelaru, I. M.; Hentschel, M. P. *J. Cryst. Growth* **1994**, *141*, 399.
- (32) Kuriyama, K.; Saito, S.; Iwamura, K. *J. Phys. Chem. Solids* **1979**, *40*, 457.
- (33) Dong, Z.; Corbett, J. D. *J. Am. Chem. Soc.* **1993**, *115*, 11299.
- (34) Honea, E. C.; Ogura, A.; Murray, C. A.; Raghavachari, K.; Sprenger, W. O.; Jarrold, M. F.; Brown, W. L. *Nature*, **1993**, *366*, 42.
- (35) Evers, J.; Oehlinger, G. *Phys. Rev. B* **1999**, *59*, 1758.
- (36) (a) Kresse, G.; Hafner, J. *Phys. Rev. B* **1993**, *47*, 558. (b) Kresse, G.; Hafner, J. *Phys. Rev. B* **1994**, *49*, 14251.
- (37) Kresse, G.; Furthmüller, J. *Comput. Mat. Sci.* **1996**, *6*, 15.
- (38) Kresse, G.; Furthmüller, J. *Phys. Rev. B* **1996**, *54*, 11169.
- (39) Kresse, G.; Joubert, D. *Phys. Rev.* **1999**, *59*, 1758.
- (40) Perdew, J. P.; Burke, K.; Ernzerhof, M. *Phys. Rev. Lett.* **1996**, *77*, 3865.
- (41) Monkhorst, H. J.; Pack, J. D. *Phys. Rev. B* **1976**, *13*, 5188.
- (42) Eck, B. *wxDragon*, version 1.4.2; RWTH Aachen University, Aachen, Germany, 2008.
- (43) Press, W. H.; Flannery, B. P.; Teukolsky, S. A.; Vetterling, W. T. *Numerical Recipes*; Cambridge University Press: New York, 1986.
- (44) Murnaghan, F. D. *PNAS* **1944**, *30*, 244.

- (45) Ashcroft, N. W.; Mermin, N. D. *Solid State Physics*; Brooks/Cole: USA, 1976; pp 38.
- (46) Kohn, W.; Sham, L. J. *Phys. Review* **1965**, *140*, A1133.
- (47) Barrett, C. S. *Acta Cryst.* **1956**, *9*, 671.
- (48) Kuestner, H.; Remy, H. *Phys. Zeit.* **1923**, *24*, 25.
- (49) Jepsen, O.; Andersen O. K. *TB-LMTO*, version 47; Max-Planck-Institut für Festkörperforschung, Stuttgart, Germany, 2000.
- (50) Dronskowski, R.; Blöchl, P. J. *Phys. Chem.* **1993**, *97*, 8617.
- (51) von Barth, U.; Hedin, L. *J. Phys. C: Solid State Phys.* **1972**, *5*, 1629.
- (52) Skriver, H. L. In *The LMTO Method: Muffin-Tin Orbitals and Electronic Structure*; Cardona, M., Fulde, P., Queisser, H.-J., Eds.; Springer Series in Solid-State Sciences 41; Springer-Verlag: New York, 1984; p 82.
- (53) Miller, G. J. *Eur. J. Inorg. Chem.* **1998**, 523.
- (54) Inglesfield, J. E. *J. Phys. C: Solid St. Phys.* **1971**, *4*, 1003-1012.
- (55) Pearson, W. B. *The Crystal Chemistry and Physics of Metals and Alloys*; Wiley-Interscience: New York, 1972; p 576.
- (56) McNeil, M. B.; Pearson, W. B.; Bennett, L. H.; Watson, R. E. *J. Phys. C: Solid St. Phys.* **1973**, *6*, 1.
- (57) Schmidt, P. C. *Phys. Rev. B.* **1985**, *31*(8), 5015.
- (58) Christensen, N. E. *Phys. Rev. B* **1985**, *32*, 207.
- (59) Pawłowska, Z.; Christensen, N. E.; Satpathy, S.; Jepsen, O. *Phys. Rev. B* **1986**, *34*, 7080.
- (60) Bilbao Crystallographic Server. <http://www.cryst.ehu.es/> (accessed June 2010).
- (61) Pitzer, K. S. *Acc. Chem. Res.* **1979**, *12*, 271.
- (62) Pearson, R. G. *Inorg. Chem.* **1988**, *27*, 734.
- (63) ASM International. *ASM Handbook, Alloy Phase Diagrams*; USA, 1992; Vol. 3.

- (64) Hom, T.; Kiszenik, W.; Post, B. *J. Appl. Crystallogr.* **1975**, *8*, 457.
- (65) Trucano, P.; Chen, R. *Nature* **1975**, *258*, 136.
- (66) Kuriyama, K.; Saito, S.; Iwamura, K. *J. Phys. Chem. Solids* **1979**, *40*, 457.
- (67) Haas, P.; Tran, F. Blaha, P.; Schwarz, K.; Laskowski, R. *Phys. Rev. B* **2009**, *80*, 195109.
- (68) Stoffel, R. P.; Wessel, C.; Lumey, M.-W.; Dronskowski, R. *Angew. Chem. Int. Ed.* **2010**, *49*, 2.
- (69) Cordero, B.; Gómez, V.; Platero-Prats, A. E.; Revés, M.; Echeverría, J.; Cremades, E.; Barragán, F.; Alvarez, S. *Dalton Trans.* **2008**, 2832.

**Table S1.** The lattice parameters and atomic positions in the optimized KTI- (*Cmce*) and BaCu-type (*P6<sub>3</sub>/mmc*) structures. The experimental KTI structure<sup>26</sup> is also included.

	Atom	Wyck.	x	y	z		Atom	Wyck.	x	y	z
KTI exp. $a = 15.329(4) \text{ \AA}$ $b = 15.069(4) \text{ \AA}$ $c = 8.137(2) \text{ \AA}$	K1	<i>8e</i>	1/4	0.2205(6)	1/4	KTI opt. $a = 15.4631 \text{ \AA}$ $b = 15.1968 \text{ \AA}$ $c = 7.9986 \text{ \AA}$	K1	<i>8e</i>	1/4	0.21862	1/4
	K2	<i>8d</i>	-0.1774(6)	0	0		K2	<i>8d</i>	-0.17814	0	0
	K3	<i>8f</i>	0	0.2005(6)	-0.0751(9)		K3	<i>8f</i>	0	0.20123	-0.06877
	Tl1	<i>16g</i>	0.11306(8)	0.39558(6)	0.0689(1)		Tl1	<i>16g</i>	0.11673	0.39256	0.07556
	Tl2	<i>8f</i>	0	0.5438(1)	0.2193(1)		Tl2	<i>8f</i>	0	0.54360	0.21645
KTI-type LiAl $a = 11.6509 \text{ \AA}$ $b = 11.3048 \text{ \AA}$ $c = 5.8009 \text{ \AA}$	Li1	<i>8e</i>	1/4	0.21478	1/4	KTI-type LiTl $a = 11.3647 \text{ \AA}$ $b = 10.8664 \text{ \AA}$ $c = 7.8975 \text{ \AA}$	Li1	<i>8e</i>	1/4	0.15017	1/4
	Li2	<i>8d</i>	-0.19046	0	0		Li2	<i>8d</i>	-0.15531	0	0
	Li3	<i>8f</i>	0	0.21684	-0.10627		Li3	<i>8f</i>	0	0.18242	-0.10554
	Al1	<i>16g</i>	0.11975	0.38821	0.07862		Tl1	<i>16g</i>	0.14813	0.35879	0.09360
	Al2	<i>8f</i>	0	0.55378	0.29560		Tl2	<i>8f</i>	0	0.58731	0.25872
KTI-type NaTl $a = 12.5385 \text{ \AA}$ $b = 13.1401 \text{ \AA}$ $c = 7.5183 \text{ \AA}$	Na1	<i>8e</i>	1/4	0.18217	1/4	BaCu-type LiAl $a = 4.3113 \text{ \AA}$ $c = 7.9108 \text{ \AA}$	Li	<i>4f</i>	1/3	2/3	0.08298
	Na2	<i>8d</i>	-0.15605	0	0		Al1	<i>2b</i>	0	0	1/4
	Na3	<i>8f</i>	0	0.20685	-0.05971		Al2	<i>2d</i>	1/3	2/3	3/4
	Tl1	<i>16g</i>	0.14257	0.38264	0.12418	BaCu-type LiTl $a = 4.7557 \text{ \AA}$ $c = 8.2989 \text{ \AA}$	Li	<i>4f</i>	1/3	2/3	0.07865
	Tl2	<i>8f</i>	0	0.57367	0.21220		Tl1	<i>2b</i>	0	0	1/4
BaCu-type NaTl $a = 4.9982 \text{ \AA}$ $c = 9.5420 \text{ \AA}$	Na	<i>4f</i>	1/3	2/3	0.07599	BaCu-type KTI $a = 5.4268 \text{ \AA}$ $c = 12.2825 \text{ \AA}$	K	<i>4f</i>	1/3	2/3	0.08793
	Tl1	<i>2b</i>	0	0	1/4		Tl1	<i>2b</i>	0	0	1/4
	Tl2	<i>2d</i>	1/3	2/3	3/4		Tl2	<i>2d</i>	1/3	2/3	3/4



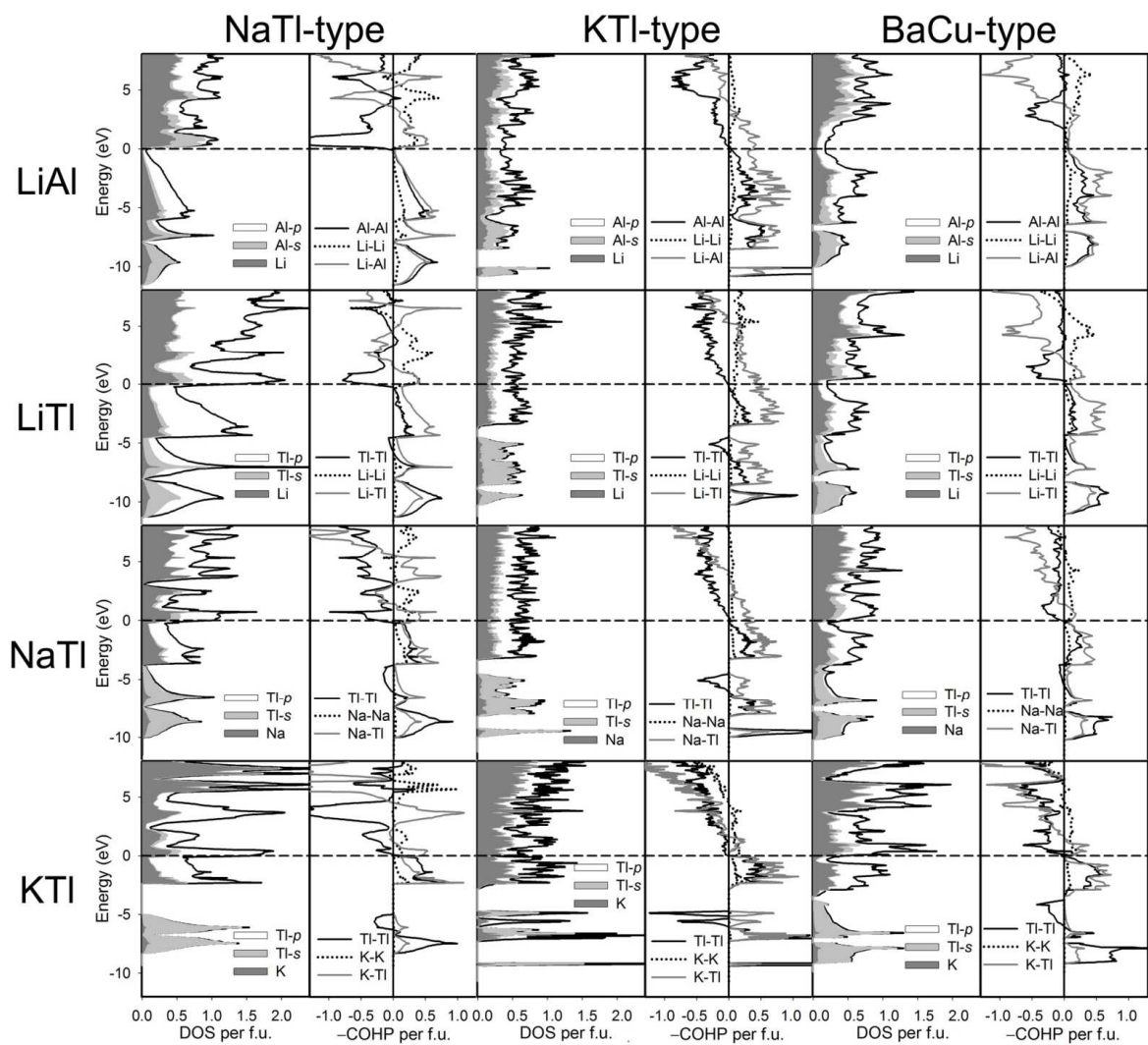


**Figure S1(a).** The DOS and COHP curves of LiAl, LiTi, and KTi in the NaTi-, KTi-, and BaCu-type structures. The dashed lines at 0 eV are the Fermi levels.

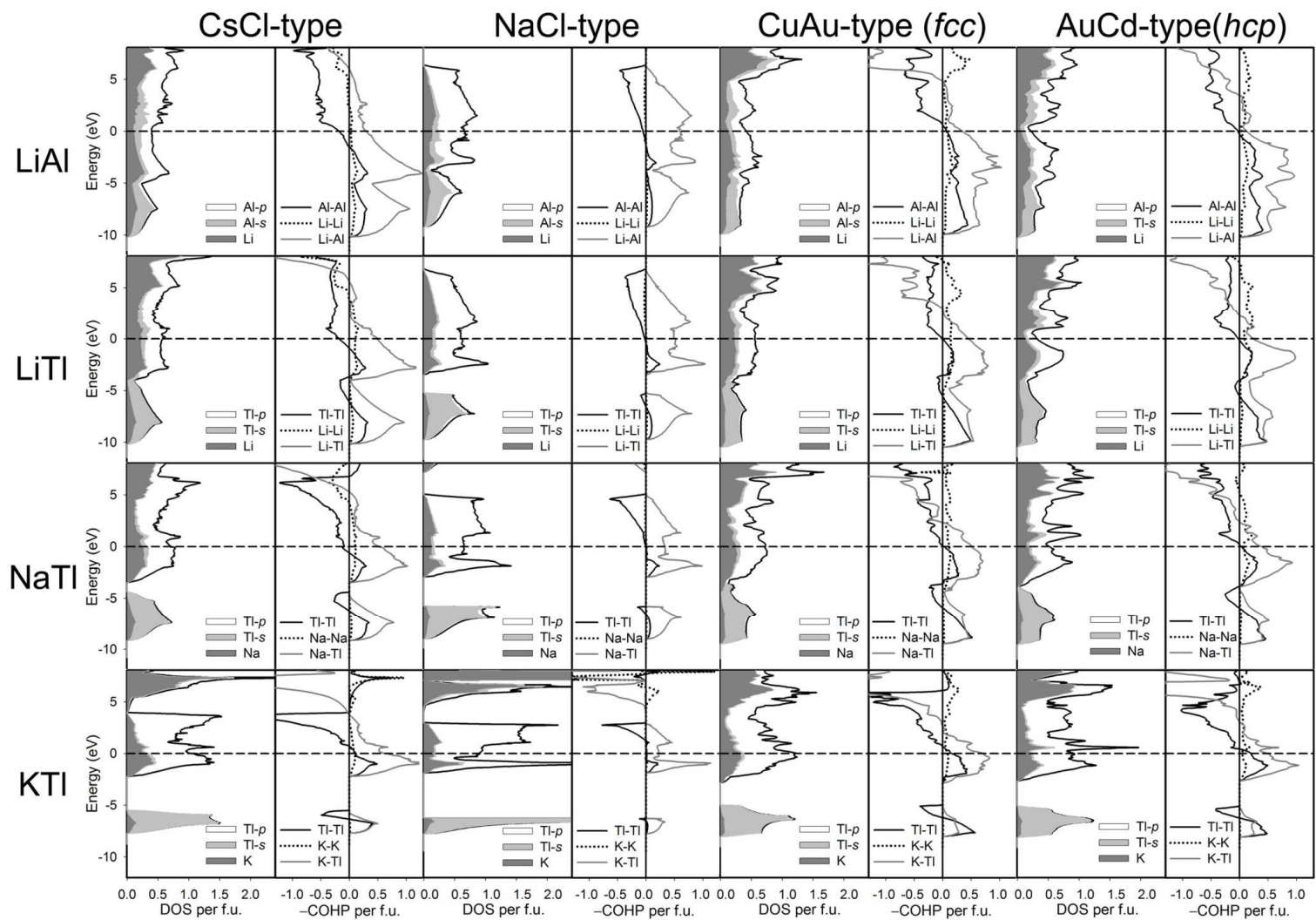


**Figure S1(b).** The DOS and COHP curves of LiAl, LiTi, and KTi in the CsCl-, NaCl-, CuAu-, and AuCd-type structures. The dashed lines at 0 eV are the Fermi levels.

**Table S2(a).** The  $sp$  projections of the wave functions at  $\Gamma$ -point for LiAl.

Irrep.	Energy (eV)	Band No.	Valence Orbitals	Li1 (0, 0, 0)		Li2 (1/4, 1/4, 1/4)		Al1 (3/4, 3/4, 3/4)		Al2 (1/2, 1/2, 1/2)	
				Real	Imag.	Real	Imag.	Real	Imag.	Real	Imag.
$1\Gamma_1^+$	-9.0430	1	$s$	-0.063	-0.013	-0.063	-0.013	-0.246	-0.052	-0.246	-0.052
			$p_y$	0.000	0.000	0.000	0.000	0.000	0.000	0.000	0.000
			$p_z$	0.000	0.000	0.000	0.000	0.000	0.000	0.000	0.000
			$p_x$	0.000	0.000	0.000	0.000	0.000	0.000	0.000	0.000
		2	$s$	0.000	0.000	0.000	0.000	0.000	0.000	0.000	0.000
			$p_y$	-0.003	0.018	0.003	-0.018	-0.020	0.129	0.020	-0.129
			$p_z$	0.003	-0.016	-0.003	0.016	0.019	-0.119	-0.019	0.119
			$p_x$	0.000	0.000	0.000	0.000	0.000	0.000	0.000	0.000
$1\Gamma_5^+$	0.2556	3	$s$	0.000	0.000	0.000	0.000	0.000	0.000	0.000	0.000
			$p_y$	0.000	0.005	0.000	-0.005	0.003	0.037	-0.003	-0.037
			$p_z$	0.000	0.006	0.000	-0.006	0.004	0.047	-0.004	-0.047
			$p_x$	-0.002	-0.023	0.002	0.023	-0.013	-0.167	0.013	0.167
		4	$s$	0.000	0.000	0.000	0.000	0.000	0.000	0.000	0.000
			$p_y$	0.001	0.011	-0.001	-0.011	0.007	0.084	-0.007	-0.084
			$p_z$	0.001	0.011	-0.001	-0.011	0.007	0.084	-0.007	-0.084
			$p_x$	0.001	0.011	-0.001	-0.011	0.007	0.083	-0.007	-0.083
		5	$s$	0.000	0.000	0.000	0.000	0.000	0.000	0.000	0.000
			$p_y$	0.000	0.000	0.000	0.000	0.000	0.000	0.000	0.000
			$p_z$	0.053	0.000	0.053	0.000	-0.073	0.000	-0.073	0.000
			$p_x$	-0.061	0.000	-0.061	0.000	0.084	0.000	0.084	0.000
$1\Gamma_4^-$	0.7262	6	$s$	0.000	0.000	0.000	0.000	0.000	0.000	0.000	0.000
			$p_y$	-0.071	-0.025	-0.071	-0.025	0.099	0.035	0.099	0.035
			$p_z$	0.022	0.008	0.022	0.008	-0.030	-0.011	-0.030	-0.011
			$p_x$	0.014	0.005	0.014	0.005	-0.020	-0.007	-0.020	-0.007
		7	$s$	0.000	0.000	0.000	0.000	0.000	0.000	0.000	0.000
			$p_y$	-0.038	0.000	-0.038	0.000	0.053	0.000	0.053	0.000
			$p_z$	-0.038	0.000	-0.038	0.000	0.053	0.000	0.053	0.000
			$p_x$	-0.038	0.000	-0.038	0.000	0.053	0.000	0.053	0.000
$1\Gamma_2^-$	2.6236	8	$s$	0.026	-0.001	-0.026	0.001	0.422	-0.015	-0.422	0.015
			$p_y$	0.000	0.000	0.000	0.000	0.000	0.000	0.000	0.000
			$p_z$	0.000	0.000	0.000	0.000	0.000	0.000	0.000	0.000
			$p_x$	0.000	0.000	0.000	0.000	0.000	0.000	0.000	0.000

**Table S2(b).** The  $sp$  projections of the wave functions at  $\Gamma$ -point for NaTl-type LiTl.

Irrep.	Energy (eV)	Band No.	Valence Orbitals	Li1 (0, 0, 0)		Li2 (1/4, 1/4, 1/4)		Tl1 (3/4, 3/4, 3/4)		Tl2 (1/2, 1/2, 1/2)	
				Real	Imag.	Real	Imag.	Real	Imag.	Real	Imag.
$1\Gamma_1^+$	-10.2385	1	$s$	0.006	-0.045	0.006	-0.045	0.059	-0.432	0.059	-0.432
			$p_y$	0.000	0.000	0.000	0.000	0.000	0.000	0.000	0.000
			$p_z$	0.000	0.000	0.000	0.000	0.000	0.000	0.000	0.000
			$p_x$	0.000	0.000	0.000	0.000	0.000	0.000	0.000	0.000
$1\Gamma_2^-$	-1.5391	2	$s$	0.016	0.002	-0.016	-0.002	0.654	0.087	-0.654	-0.087
			$p_y$	0.000	0.000	0.000	0.000	0.000	0.000	0.000	0.000
			$p_z$	0.000	0.000	0.000	0.000	0.000	0.000	0.000	0.000
			$p_x$	0.000	0.000	0.000	0.000	0.000	0.000	0.000	0.000
$1\Gamma_5^+$	1.1148	3	$s$	0.000	0.000	0.000	0.000	0.000	0.000	0.000	0.000
			$p_y$	-0.002	0.013	0.002	-0.013	-0.022	0.155	0.022	-0.155
			$p_z$	0.001	-0.011	-0.001	0.011	0.018	-0.128	-0.018	0.128
			$p_x$	0.000	0.000	0.000	0.000	0.000	0.000	0.000	0.000
		4	$s$	0.000	0.000	0.000	0.000	0.000	0.000	0.000	0.000
			$p_y$	0.000	0.002	0.000	-0.002	-0.004	0.027	0.004	-0.027
			$p_z$	0.000	0.003	0.000	-0.003	-0.006	0.042	0.006	-0.042
			$p_x$	0.002	-0.018	-0.002	0.018	0.029	-0.215	-0.029	0.215
		5	$s$	0.000	0.000	0.000	0.000	0.000	0.000	0.000	0.000
			$p_y$	-0.001	0.008	0.001	-0.008	-0.014	0.102	0.014	-0.102
			$p_z$	-0.001	0.009	0.001	-0.009	-0.016	0.113	0.016	-0.113
			$p_x$	-0.001	0.006	0.001	-0.006	-0.009	0.068	0.009	-0.068
6	$s$	0.000	0.000	0.000	0.000	0.000	0.000	0.000	0.000		
	$p_y$	0.020	0.003	0.019	0.003	-0.024	-0.003	-0.024	-0.003		
	$p_z$	0.000	0.000	0.000	0.000	0.000	0.000	0.000	0.000		
	$p_x$	-0.108	-0.015	-0.108	-0.015	0.131	0.018	0.131	0.018		
$1\Gamma_4^-$	1.4772	7	$s$	0.000	0.000	0.000	0.000	0.000	0.000	0.000	0.000
			$p_y$	0.014	0.002	0.014	0.002	-0.017	-0.002	-0.017	-0.002
			$p_z$	0.113	0.016	0.113	0.016	-0.137	-0.019	-0.137	-0.019
			$p_x$	0.001	0.000	0.001	0.000	-0.001	0.000	-0.001	0.000
8	$s$	0.000	0.000	0.000	0.000	0.000	0.000	0.000	0.000		
	$p_y$	-0.095	-0.013	-0.095	-0.013	0.115	0.016	0.115	0.016		
	$p_z$	0.015	0.002	0.015	0.002	-0.018	-0.002	-0.018	-0.002		
	$p_x$	-0.019	-0.003	-0.019	-0.003	0.023	0.003	0.023	0.003		

**Table S2(c).** The *sp* projections of the wave functions at *L*-point for LiAl.

Irrep.	Energy (eV)	Band No.	Valence Orbitals	Li1 (0, 0, 0)		Li2 (1/4, 1/4, 1/4)		Al1 (3/4, 3/4, 3/4)		Al2 (1/2, 1/2, 1/2)	
				Real	Imag.	Real	Imag.	Real	Imag.	Real	Imag.
$1L_1^-$	-7.4304	1	<i>s</i>	0.009	0.001	0.009	0.001	0.253	0.016	-0.253	-0.016
			<i>p<sub>y</sub></i>	0.020	0.001	-0.020	-0.001	0.006	0.000	0.006	0.000
			<i>p<sub>z</sub></i>	0.020	0.001	-0.020	-0.001	0.006	0.000	0.006	0.000
			<i>p<sub>x</sub></i>	0.020	0.001	-0.020	-0.001	0.006	0.000	0.006	0.000
$1L_2^+$	-5.4668	2	<i>s</i>	-0.005	0.078	0.005	-0.078	-0.006	0.096	-0.006	0.096
			<i>p<sub>y</sub></i>	0.000	-0.003	0.000	-0.003	0.003	-0.045	-0.003	0.045
			<i>p<sub>z</sub></i>	0.000	-0.003	0.000	-0.003	0.003	-0.045	-0.003	0.045
			<i>p<sub>x</sub></i>	0.000	-0.003	0.000	-0.003	0.003	-0.045	-0.003	0.045
$1L_3^-$	-0.8427	3	<i>s</i>	0.000	0.000	0.000	0.000	0.000	0.000	0.000	0.000
			<i>p<sub>y</sub></i>	0.008	0.011	-0.008	-0.011	-0.084	-0.114	-0.084	-0.114
			<i>p<sub>z</sub></i>	-0.008	-0.011	0.008	0.011	0.084	0.115	0.084	0.115
		4	<i>p<sub>x</sub></i>	0.000	0.000	0.000	0.000	0.000	0.000	0.000	0.000
			<i>s</i>	0.000	0.000	0.000	0.000	0.000	0.000	0.000	0.000
			<i>p<sub>y</sub></i>	-0.003	-0.003	0.003	0.003	0.032	0.035	0.032	0.035
$1L_3^+$	0.4121	5	<i>p<sub>z</sub></i>	-0.003	-0.003	0.003	0.003	0.031	0.035	0.031	0.035
			<i>p<sub>x</sub></i>	0.012	0.014	-0.012	-0.014	-0.127	-0.140	-0.127	-0.140
			<i>s</i>	0.000	0.000	0.000	0.000	0.000	0.000	0.000	0.000
		6	<i>p<sub>y</sub></i>	0.035	-0.003	0.035	-0.003	-0.011	0.001	0.011	-0.001
			<i>p<sub>z</sub></i>	0.035	-0.003	0.035	-0.003	-0.011	0.001	0.011	-0.001
			<i>p<sub>x</sub></i>	-0.140	0.012	-0.140	0.012	0.043	-0.004	-0.043	0.004
$2L_2^+$	0.7434	7	<i>s</i>	0.000	0.000	0.000	0.000	0.000	0.000	0.000	0.000
			<i>p<sub>y</sub></i>	0.076	0.074	0.076	0.074	-0.023	-0.023	0.023	0.023
			<i>p<sub>z</sub></i>	-0.076	-0.074	-0.076	-0.074	0.023	0.023	-0.023	-0.023
		8	<i>p<sub>x</sub></i>	0.000	0.000	0.000	0.000	0.000	0.000	0.000	0.000
			<i>s</i>	0.003	-0.043	-0.003	0.043	-0.017	0.242	-0.017	0.242
			<i>p<sub>y</sub></i>	-0.001	0.013	-0.001	0.013	0.000	0.004	0.000	-0.004
$2L_1^-$	4.9350	8	<i>p<sub>z</sub></i>	-0.001	0.013	-0.001	0.013	0.000	0.004	0.000	-0.004
			<i>p<sub>x</sub></i>	-0.001	0.013	-0.001	0.013	0.000	0.004	0.000	-0.004
			<i>s</i>	-0.157	-0.010	-0.157	-0.010	0.042	0.003	-0.042	-0.003
		8	<i>p<sub>y</sub></i>	-0.018	-0.001	0.018	0.001	0.010	0.001	0.010	0.001
			<i>p<sub>z</sub></i>	-0.018	-0.001	0.018	0.001	0.010	0.001	0.010	0.001
			<i>p<sub>x</sub></i>	-0.018	-0.001	0.018	0.001	0.010	0.001	0.010	0.001

**Table S2(d).** The  $sp$  projections of the wave functions at  $L$ -point for NaTl-type LiTl.

Irrep.	Energy (eV)	Band No.	Valence Orbitals	Li1 (0, 0, 0)		Li2 (1/4, 1/4, 1/4)		Tl1 (3/4, 3/4, 3/4)		Tl2 (1/2, 1/2, 1/2)	
				Real	Imag.	Real	Imag.	Real	Imag.	Real	Imag.
$1L_1^-$	-8.5455	1	$s$	0.003	0.003	0.003	0.003	0.313	0.278	-0.313	-0.278
			$p_y$	0.010	0.009	-0.010	-0.009	0.004	0.003	0.004	0.003
			$p_z$	0.010	0.009	-0.010	-0.009	0.004	0.003	0.004	0.003
			$p_x$	0.010	0.009	-0.010	-0.009	0.004	0.003	0.004	0.003
$1L_2^+$	-6.1576	2	$s$	-0.038	0.045	0.038	-0.045	-0.186	0.217	-0.186	0.217
			$p_y$	0.001	-0.001	0.001	-0.001	0.021	-0.024	-0.021	0.024
			$p_z$	0.001	-0.001	0.001	-0.001	0.021	-0.024	-0.021	0.024
			$p_x$	0.001	-0.001	0.001	-0.001	0.021	-0.024	-0.021	0.024
$2L_2^+$	-0.8860	3	$s$	0.046	-0.053	-0.046	0.053	-0.203	0.234	-0.203	0.234
			$p_y$	-0.009	0.011	-0.009	0.011	-0.011	0.013	0.011	-0.013
			$p_z$	-0.009	0.011	-0.009	0.011	-0.011	0.013	0.011	-0.013
			$p_x$	-0.009	0.011	-0.009	0.011	-0.011	0.013	0.011	-0.013
$1L_3^-$	-0.5567	4	$s$	0.000	0.000	0.000	0.000	0.000	0.000	0.000	0.000
			$p_y$	-0.014	0.014	0.014	-0.014	0.100	-0.101	0.100	-0.101
			$p_z$	0.014	-0.014	-0.014	0.014	-0.100	0.101	-0.100	0.101
			$p_x$	0.000	0.000	0.000	0.000	0.000	0.000	0.000	0.000
		5	$s$	0.000	0.000	0.000	0.000	0.000	0.000	0.000	0.000
			$p_y$	0.005	0.004	-0.005	-0.004	-0.036	-0.030	-0.036	-0.030
			$p_z$	0.005	0.004	-0.005	-0.004	-0.036	-0.030	-0.036	-0.030
			$p_x$	-0.020	-0.017	0.020	0.017	0.145	0.121	0.145	0.121
		6	$s$	0.000	0.000	0.000	0.000	0.000	0.000	0.000	0.000
			$p_y$	0.026	-0.035	0.026	-0.035	-0.006	0.008	0.006	-0.008
			$p_z$	0.026	-0.035	0.026	-0.035	-0.006	0.008	0.006	-0.008
			$p_x$	-0.103	0.138	-0.103	0.138	0.024	-0.033	-0.024	0.033
7	$s$	0.000	0.000	0.000	0.000	0.000	0.000	0.000	0.000		
	$p_y$	0.109	0.069	0.109	0.069	-0.026	-0.016	0.026	0.016		
	$p_z$	-0.109	-0.069	-0.109	-0.069	0.026	0.016	-0.026	-0.016		
	$p_x$	0.000	0.000	0.000	0.000	0.000	0.000	0.000	0.000		
$2L_1^-$	3.2660	8	$s$	0.114	0.099	0.114	0.099	-0.056	-0.049	0.056	0.049
			$p_y$	0.027	0.024	-0.027	-0.024	-0.001	-0.001	-0.001	-0.001
			$p_z$	0.027	0.024	-0.027	-0.024	-0.001	-0.001	-0.001	-0.001
			$p_x$	0.027	0.024	-0.027	-0.024	-0.001	-0.001	-0.001	-0.001

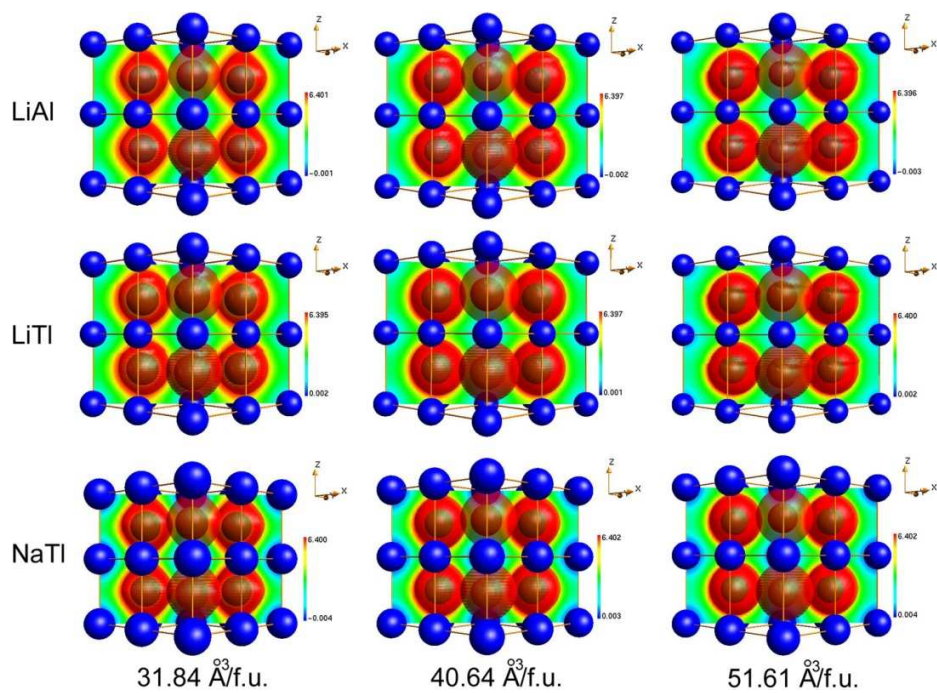


**Figure S2.** Valence electron density maps of CsCl-type LiAl, LiTl, and NaTl.

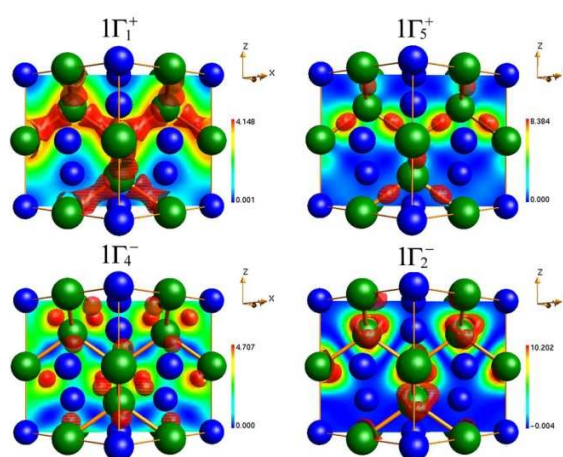


**Figure S3(a).** The electron density maps of the bands at  $\Gamma$ -point for LiAl.



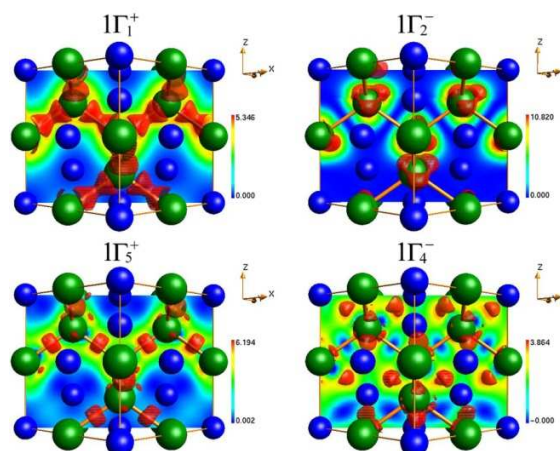


**Figure S3(b).** The electron density maps of the bands at  $\Gamma$ -point for NaTl-type LiTl.  $1\Gamma_4^-$  and  $1\Gamma_5^+$  are both triple degenerate bands; degenerate bands have the same charge map.

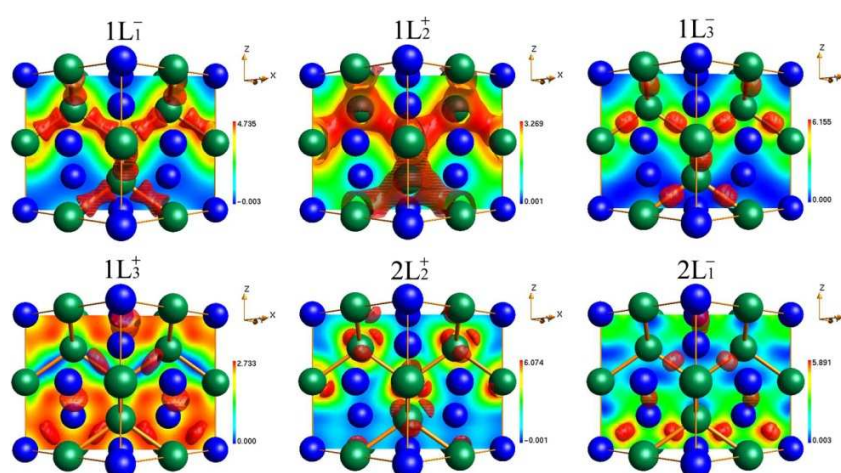


**Figure S3(c).** The electron density maps of the bands at  $L$ -point for LiAl.



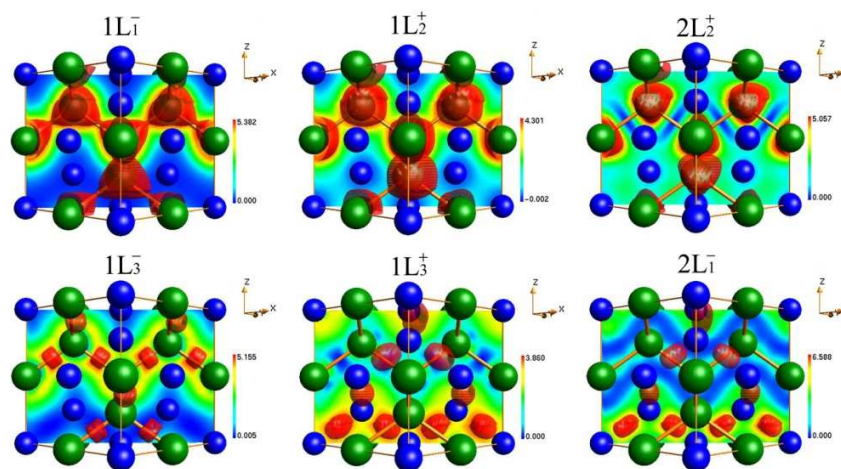


**Figure S3(d).** The electron density maps of the bands at  $L$ -point for NaTl-type LiTl.  $1L_3^-$  and  $1L_3^+$  are both triple degenerate bands; degenerate bands have the same charge map.

## Chapter 4

### Revisiting the Zintl-Klemm Concept II: $A_2AuBi$ ( $A = \text{Alkali Metals}$ )

Modified from a paper submitted to *European Journal of Inorganic Chemistry*

Fei Wang and Gordon J. Miller

#### 4.1 Abstract

Alkali metal gold bismuthides,  $A_2AuBi$ , are isoelectronic with alkali metal thallides,  $ATl = A_2TlTl$ , and yet  $Na_2AuBi$  adopts an orthorhombic structure with a 1-D zigzag “ribbon” structural motif rather than the cubic double diamond structure type of  $NaTl$  as well as  $Li_2AuBi$ . Using first principles quantum mechanical calculations applied to  $A_2AuBi$ , hypothetical “ $A_2HgPb$ ,” and  $A_2TlTl$ , and comprehensively decomposing the total energies into metallicity, ionicity, and covalency components to establish parallels with the qualitative Zintl-Klemm formalism, the factors determining the relative stability between the zigzag “ribbon” and the diamond network are examined. An interplay between volume-dependent energy terms, i.e., metallicity or ionicity, and covalency among the electronegative components determines which structural motif is favored. In  $Na_2AuBi$ , there are two factors stabilizing the zigzag “ribbon.”  $Au 5d$  states significantly interact with  $Bi 6p$  states, especially  $Au 5d_{x^2-y^2}$  with  $Bi 6p_z$  to promote stronger Au-Bi covalent interactions than in the diamond network. This factor does not exist in  $Na_2TlTl$  and “ $A_2HgPb$ ,” where Hg, Tl, and Pb  $5d$  states are well localized. Secondly, the zigzag ribbons provide effective covalent interactions at larger volumes, as in  $Na_2AuBi$ , while effective covalent interactions occur in the diamond network only at smaller volume, as in  $Li_2AuBi$ .

#### 4.2 Introduction

The Zintl-Klemm concept, although simple, can decently rationalize the structures of Zintl phases and polar intermetallic compounds.<sup>1-8</sup> The essence and originality of the Zintl-Klemm concept are that it introduces both charge transfer and covalent interactions into the structural rationalization of compounds composed of metallic elements. For instance, to rationalize the so-called double diamond structure of the well known  $NaTl$ ,<sup>9</sup> the Zintl-Klemm concept claims that, after obtaining one valence electron from each Na atom, each Tl atom has four valence electrons and, although Tl is metal, each formal  $Tl^-$  “anion” will follow the octet rule and form four “covalent” bonds with neighboring  $Tl^-$ . Such success of the Zintl-Klemm concept implies that, pragmatically, it is justifiable and beneficial to consider charge transfer and covalent interactions in intermetallic compounds.

However, the oversimplified modeling of the Zintl-Klemm concept also causes its limitations. In our preceding report, we addressed the structures of alkali metal trielides.<sup>10</sup> Most of them adopt the double diamond structure, but LiTl adopts the CsCl-type structure and cannot be explained using the Zintl-Klemm formalism, whereas KTI features  $Tl_6$  octahedra, i.e., formally  $[Tl_6]^{6-}$ , and the explicit causes of its difference from the double diamond structure also cannot be understood from this simple formalism. Our study showed that to rationalize the structures of Zintl phases, we have to comprehensively consider the interplay among long-range ionic, short-range covalent, and volume-dependent metallic interactions in these intermetallic and metal-metalloid systems. By addressing the cases that defy the Zintl-Klemm rationalization, we are attempting to supplement the Zintl-Klemm concept and deepen our understanding of the structures of Zintl phases.

In this report, we continue this effort by studying an (alkali metal)-gold-bismuth ternary series,  $A_2AuBi$ . The recently synthesized  $Na_2AuBi$ <sup>11</sup> with an orthorhombic structure imposes another challenge to the Zintl-Klemm concept. Its crystal structure is shown in Figure 1. Au and Bi atoms form one-dimensional zigzag “ribbons” aligned along the *c*-axis. Such ribbons consist of linear chains of Au atoms, bridged by Bi atoms on alternating sides. Similar structural motifs are also observed in the isoelectronic gold monohalides.<sup>12-14</sup> The interatomic distances within a  $[AuBi]^{2-}$  ribbon are 2.924(1) Å for Au-Au and 2.752(1) Å for Au-Bi. The ribbons are juxtaposed in the *bc*-planes forming Au/Bi “sheets”. The distance between the Bi atoms from two neighboring ribbons is 4.216(1) Å, much larger than those within a ribbon, so these ribbons are well separated from one another. Na atoms reside between two neighboring Au/Bi sheets. Questions arise when we compare this structure with  $Li_2AuBi$  and NaTl, reformulated as  $Na_2TlTi$ , which both adopt the double diamond structure.

NaTl is isoelectronic with  $Na_2AuBi$  and, considering atomic number, Tl is the “average” of Au and Bi. From this point of view, it is justifiable to expect that Au/Bi and Tl atoms construct the same network, just like boron nitride, BN,<sup>15,16</sup> which is isoelectronic with C and adopts both graphite and diamond structures. However, the Au/Bi zigzag ribbons bear no resemblance with the Tl diamond network.

On the other hand, Au/Bi atoms do construct the diamond network with only heteroatomic (Au-Bi) contacts in  $Li_2AuBi$ , (Figure 1).<sup>17</sup> The Zintl-Klemm formalism works well for this structure. By disregarding the 5*d* electrons of Au, and after gaining the 2*s* electrons from Li, the average valence electron count for each Au and Bi atom is 4 so, on average, each should form 4 “covalent bonds”. If Au is considered as a one-electron donor as well, the valence electron count of Bi is 8, so there should be no Bi-Bi contacts. These are all satisfied in the diamond network with only heteroatomic Au-Bi

contacts, but not in the zigzag ribbons, where each Au atom has contacts with two other Au atoms and two Bi atoms, and each Bi has two contacts with Au atoms. So, on average, each atom has three “bonds” in the ribbons. One possibility is that there is multiple bonding. Just like in graphite, although every C is bonded to only three neighbors, the delocalized  $\pi$  bond makes the fourth “bond” at each atom. Is it also the case in the Au/Bi ribbons? Or do they violate the octet rule so that the Zintl-Klemm concept does not apply to  $\text{Na}_2\text{AuBi}$  at all? Therefore, it is worthy to investigate how these zigzag ribbons are stabilized and why switching from Na to Li and from Au/Bi to Tl both render the structure to transform from orthorhombic with zigzag ribbons to the cubic double diamond structure.

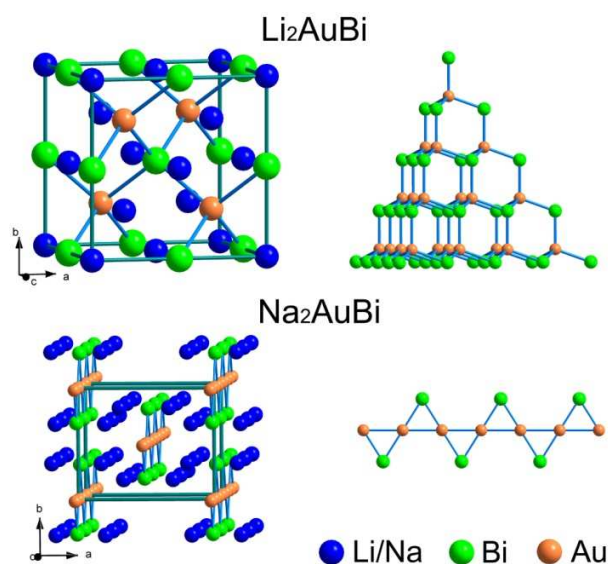


**Figure 1.** Crystal structures of  $\text{Li}_2\text{AuBi}$  and  $\text{Na}_2\text{AuBi}$ .

## 4.3 Computational Details

### 4.3.1 Model Structures

To answer the questions raised above, we built both orthorhombic and cubic model structures for first-principle calculations with the following compositions,  $\text{Li}_2\text{AuBi}$ ,  $\text{Na}_2\text{AuBi}$ , and  $\text{NaTl}$  ( $\text{Na}_2\text{TlTl}$ ). Moreover, we also built model structures for a hypothetical composition, “ $\text{Na}_2\text{HgPb}$ ”, which is considered as intermediate between  $\text{Na}_2\text{AuBi}$  and  $\text{Na}_2\text{TlTl}$ . The details of these model structures are listed in Table 1. The volume per formula unit,  $V_{\text{f.u.}}$ , in our calculations, is equal to either the experimental values or the equilibrium volumes obtained from the energy vs. volume,  $E(V)$ , curves calculated with *VASP* (details can be found in “*VASP* Calculations”). For the cubic model structures,

$V_{f.u.}$  is the only variable. But, for the orthorhombic structures, there are also the atomic fractional coordinates ( $x$  and  $y$ ) and the aspect ratios ( $b/a$  and  $c/a$ ) of the unit cell to be determined. These were done by structural optimization with *VASP*. The obtained lattice parameters and atomic positions are reported in the section “Results and Discussions”.

**Table 1.** Details of Model Structures.

Orthorhombic						Cubic					
<i>Cmcm</i>						<i>F<math>\bar{4}3m</math></i>					
$a = \left(24V_{f.u.} \frac{a}{b} \frac{a}{c}\right)^{\frac{1}{3}}$	Na/Li	8g	$x$	$y$	1/4	$a = \left(4V_{f.u.}\right)^{\frac{1}{3}}$	Na/Li1	4d	3/4	3/4	3/4
	Au/Hg/Tl1	4a	1/2	1/2	0		Na/Li2	4a	0	0	0
	Bi/Pb/Tl2	4c	1/2	$y$	1/4		Au/Hg/Tl1	4c	1/2	1/2	1/2
$b = \frac{b}{a}a, c = \frac{c}{a}a$							Bi/Pb/Tl2	4b	1/4	1/4	1/4

### 4.3.2 VASP Calculations

We used the *Vienna ab initio simulation package (VASP)*<sup>18-20</sup> to optimize the orthorhombic structures and calculate the total energies, band structures, and valence electron density maps of the model structures. The projector augmented-wave (PAW)<sup>21</sup> pseudopotentials were adopted with the Perdew-Burke-Ernzerhof generalized gradient approximation (PBE-GGA).<sup>22</sup> For structural optimization, the conjugate gradient algorithm<sup>23</sup> was applied. The first Brillouin zone was sampled with a  $5 \times 5 \times 5$  Monkhorst-Pack mesh.<sup>24</sup> The energy cutoffs are 242.9 eV for Na<sub>2</sub>AuBi and Li<sub>2</sub>AuBi, 237.8 eV for Na<sub>2</sub>HgPb, and 237.1 eV for Na<sub>2</sub>TlTl. For the calculations of total energies, band structures, and valence electron density maps, a denser  $7 \times 7 \times 7$  Monkhorst-Pack mesh was used and the energy cutoffs were also higher: 303.6 eV for Na<sub>2</sub>AuBi and Li<sub>2</sub>AuBi, 297.3 eV for Na<sub>2</sub>HgPb, and 296.3 eV for Na<sub>2</sub>TlTl. The valence electron density maps were plotted with *wxDragon*.<sup>25</sup>

We scanned total energies of the model structures over certain ranges of volumes to study their energy vs. volume behavior. The cubic model structures were isotropically expanded and compressed while, for the orthorhombic model structures, we optimized the atomic coordinates and the aspect ratios of unit cells at each sampling volume before the total energies are calculated. The obtained  $E(V)$  curves were fitted to the Murnaghan equation of state,<sup>26</sup> from which the equilibrium volumes ( $V_{eq}$ ) were determined. Total energies were then calculated at these  $V_{eq}$ . And again, structural optimization preceded the energy calculation for each orthorhombic model structure at  $V_{eq}$ .

All calculated total energies were partitioned into an electrostatic term ( $E_{ES}$ ) and an electronic term ( $E_{electronic}$ ). By comparing  $E_{ES}$  values of different structures, we can evaluate which structure is favored

if the valence electrons are highly delocalized, as in classical metals. Comparison of  $E_{\text{electronic}}$ , on the other hand, evaluates the effects of valence electron localization, including charge transfer, formation of lone pairs, and covalent bonds. The details of this energy partitioning scheme is included in our preceding reports.<sup>10,27</sup>

### 4.3.3 LMTO Calculations

The Stuttgart *Tight-Binding, Linear-Muffin-Tin Orbital* program with *Atomic Sphere Approximation* (TB-LMTO-ASA)<sup>28</sup> was utilized to calculate the density of states (DOS) and crystal orbital Hamiltonian population (COHP)<sup>29</sup> curves of the model structures. The integrated COHP (ICOHP) values were employed to evaluate the effect of covalent interactions. It quantifies the energy difference between the crystal orbitals and non-interacting atomic orbitals. In all calculations, the exchange and correlation energy was treated with the von Barth-Hedin local density approximation.<sup>30</sup> The basis sets include  $2s$  and  $2p$  for Li,  $3s$  and  $3p$  for Na, and  $5d$ ,  $6s$ , and  $6p$  for Au, Hg, Tl, Pb, and Bi. In some calculations, the  $5d$  of Au, Hg, and Tl were excluded from basis sets. By comparing the results with and without these  $5d$  orbitals, we evaluated their effects in covalent interactions. Reciprocal space integrations were performed with an  $8 \times 8 \times 8$   $k$ -points mesh. The unit cells of the model structures were filled with Wigner-Seitz spheres, the radii of which were adjusted so that the sums of the sphere volumes are equal to the volumes of the unit cells. Empty atomic spheres were generated by the program where they are necessary. The overall overlaps between atomic spheres in all model structures range from 8.07 % to 9.59 %.

## 4.4 Results and Discussions

### 4.4.1 Na<sub>2</sub>AuBi, “Na<sub>2</sub>HgPb”, and Na<sub>2</sub>TlTl

The experimental volumes per f.u. of Na<sub>2</sub>AuBi and NaTl (Na<sub>2</sub>TlTl) are very close, 106.35 and 103.22 Å<sup>3</sup>/f.u., respectively. To find out their differences, we compared the cubic and orthorhombic structures at these two volumes for both Na<sub>2</sub>AuBi and Na<sub>2</sub>TlTl. The hypothetical composition “Na<sub>2</sub>HgPb” was also studied in both structures at these two volumes.

The optimized orthorhombic structures of Na<sub>2</sub>AuBi, “Na<sub>2</sub>HgPb”, and Na<sub>2</sub>TlTl are tabulated in detail in Table 2 and the selected interatomic distances are listed in Table 3. Comparison between the orthorhombic Na<sub>2</sub>AuBi optimized at 106.35 Å<sup>3</sup>/f.u. and its experimental structure<sup>11</sup> shows that the structural optimization shortened  $a$  and  $b$  and elongated  $c$ . The optimized structure also has larger interatomic distances in the zigzag ribbons. But, overall, the differences are small: those between

experimental and optimized lattice parameters are all smaller than 0.05 Å, and all interatomic distances differ by less than 0.07 Å.

**Table 2.** Lattice parameters and atomic positions of the optimized orthorhombic Li<sub>2</sub>AuBi, Na<sub>2</sub>AuBi, “Na<sub>2</sub>HgPb”, and Na<sub>2</sub>TlTl at various volumes. The experimental Na<sub>2</sub>AuBi (exp.) is included for comparison.

		Li <sub>2</sub> AuBi			Na <sub>2</sub> AuBi			Na <sub>2</sub> HgPb			Na <sub>2</sub> TlTl	
V (Å <sup>3</sup> /f.u.)		73.52	106.35	73.52	103.22	106.35	106.35 (exp.)	103.22	106.35	103.22	106.35	
a (Å)		7.7183	9.1362	7.9482	9.2835	9.4253	9.447(2)	9.2649	9.3767	8.6713	8.8213	
b (Å)		6.9904	8.1573	7.0148	7.5963	7.6511	7.700(2)	7.6194	7.6806	7.7969	7.8257	
c (Å)		5.4505	5.7079	5.2744	5.8661	5.8989	5.849(1)	5.8491	5.9066	6.1071	6.1621	
Na/Li	8g	x	0.1810	0.1711	0.1852	0.1815	0.1809	0.182(1)	0.1894	0.1887	0.1885	0.1885
		y	0.3032	0.2363	0.3196	0.3237	0.3235	0.333(1)	0.3207	0.3221	0.3154	0.3160
		z	1/4	1/4	1/4	1/4	1/4	1/4	1/4	1/4	1/4	1/4
Au/Hg/Tl1	4a	x	1/2	1/2	1/2	1/2	1/2	1/2	1/2	1/2	1/2	1/2
		y	1/2	1/2	1/2	1/2	1/2	1/2	1/2	1/2	1/2	1/2
		z	0	0	0	0	0	0	0	0	0	0
Bi/Pb/Tl2	4c	x	1/2	1/2	1/2	1/2	1/2	1/2	1/2	1/2	1/2	1/2
		y	0.1485	0.1956	0.1576	0.1847	0.1875	0.1973(1)	0.1548	0.1578	0.1355	0.1371
		z	1/4	1/4	1/4	1/4	1/4	1/4	1/4	1/4	1/4	1/4

Replacing Au/Bi with Hg/Pb in the orthorhombic structure, at both 106.35 and 103.22 Å<sup>3</sup>/f.u., alters the lattice parameters slightly, but the atomic position of Pb is significantly different from that of Bi. As a result, the Hg-Pb distances in the zigzag ribbons are over 0.2 Å larger than Au-Bi. As for the hypothetical orthorhombic Na<sub>2</sub>TlTl, it has much smaller *a* and much larger *b* and *c* than Na<sub>2</sub>AuBi at the same volume. The interatomic distances in the Tl1/Tl2 zigzag ribbons are much larger than in the Au/Bi ribbons – Tl1-Tl1 is over 0.1 Å larger than Au-Au and Tl1-Tl2 is over 0.4 Å larger than the Au-Bi separation. Moreover, in Na<sub>2</sub>AuBi, the distances between Bi are over 4Å, so the zigzag ribbons are “separated” from one another; but in Na<sub>2</sub>TlTl, the corresponding Tl2···Tl2 distances are just over 3.7 Å, much shorter than Bi···Bi, so the Tl1/Tl2 zigzag ribbons tend to be “cross-linked” to each other.

In the cubic double diamond structure, the symmetry requires uniform nearest neighbor interatomic distances, i.e.,  $d_{\text{Na-Na}} = d_{\text{Na-Au/Hg/Tl1}} = d_{\text{Na-Bi/Pb/Tl2}} = d_{\text{Au/Hg/Tl1-Bi/Pb/Tl2}}$  (we use  $d_{\text{cubic}}$  to represent them all and it is also included in Table 3). In the orthorhombic structure, the distances can be different. Table 3 shows that for Na<sub>2</sub>AuBi, at both 103.22 and 106.35 Å<sup>3</sup>/f.u., the interatomic distances in the zigzag Au/Bi ribbon of the orthorhombic structure are much smaller than  $d_{\text{cubic}}$  ( $d_{\text{cubic}} - d_{\text{Au/Bi-Au/Bi,ortho}} = 0.30-0.45$  Å). This difference is much smaller in “Na<sub>2</sub>HgPb” and Na<sub>2</sub>TlTl, especially the latter, where ( $d_{\text{cubic}} - d_{\text{Tl-Tl,ortho}} < 0.18$  Å, much smaller than ( $d_{\text{cubic}} - d_{\text{Au/Bi-Au/Bi,ortho}}$ ).



**Table 3.** Selected interatomic distances of the optimized orthorhombic structures.  $d_{\text{cubic}}$  is the nearest neighbor distance in the cubic structure. All distances smaller than  $2/3^{1/2}d_{\text{cubic}}$  (second nearest neighbor distance in the cubic structure) are listed.

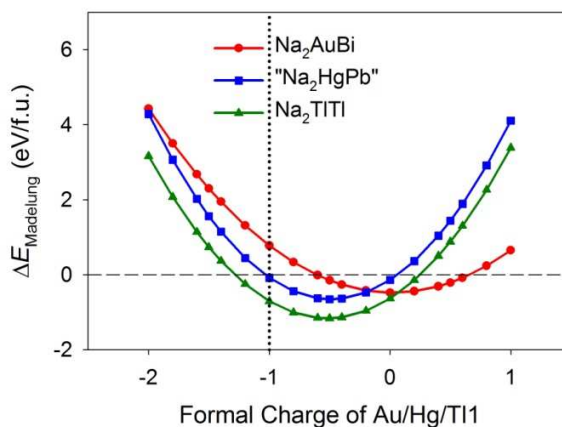
			73.52 Å <sup>3</sup> /f.u. $d_{\text{cubic}} = 2.880 \text{ \AA}$		103.22 Å <sup>3</sup> /f.u. $d_{\text{cubic}} = 3.224 \text{ \AA}$			106.35 Å <sup>3</sup> /f.u. $d_{\text{cubic}} = 3.257 \text{ \AA}$				
			Li <sub>2</sub> AuBi	Na <sub>2</sub> AuBi	Na <sub>2</sub> AuBi	Na <sub>2</sub> HgPb	Na <sub>2</sub> TlTl	Li <sub>2</sub> AuBi	Na <sub>2</sub> AuBi	Na <sub>2</sub> AuBi (exp.)	Na <sub>2</sub> HgPb	Na <sub>2</sub> TlTl
Li/Na-	Li/Na	× 1	<b>2.793</b> Å	2.943 Å	3.370 Å	3.509 Å	3.269 Å	<b>3.126</b> Å	3.409 Å	3.44(1) Å	3.539 Å	3.325 Å
		× 2	3.019 Å	2.995 Å	3.382 Å	3.313 Å	3.391 Å	<b>3.206</b> Å	3.415 Å	3.438(7) Å	3.357 Å	3.426 Å
Au/Hg/Tl1	Au/Hg/Tl1	× 4	2.881 Å	2.989 Å	3.321 Å	3.345 Å	3.324 Å	<b>2.862</b> Å	3.347 Å	3.412(9) Å	3.381 Å	3.355 Å
		× 4	3.133 Å	3.099 Å	3.561 Å	3.505 Å	3.420 Å	–	3.612 Å	3.582(9) Å	3.545 Å	3.464 Å
Bi/Pb/Tl2	Bi/Pb/Tl2	× 2	<b>2.689</b> Å	<b>2.748</b> Å	<b>3.139</b> Å	<b>3.092</b> Å	<b>2.983</b> Å	<b>3.024</b> Å	<b>3.182</b> Å	<b>3.18(1)</b> Å	<b>3.127</b> Å	<b>3.013</b> Å
		× 2	<b>2.789</b> Å	<b>2.790</b> Å	<b>3.219</b> Å	<b>3.143</b> Å	<b>3.044</b> Å	–	3.266 Å	3.29(1) Å	<b>3.180</b> Å	<b>3.084</b> Å
Au/Hg/Tl1-	Au/Hg/Tl1	× 4	3.081 Å	3.024 Å	3.378 Å	3.416 Å	3.485 Å	3.301 Å	3.408 Å	3.400(5) Å	3.446 Å	3.520 Å
		× 1	<b>2.725</b> Å	<b>2.637</b> Å	<b>2.928</b> Å	<b>2.925</b> Å	<b>3.054</b> Å	<b>2.854</b> Å	<b>2.949</b> Å	<b>2.924(1)</b> Å	<b>2.953</b> Å	<b>3.081</b> Å
Bi/Pb/Tl2-	Bi/Pb/Tl2	× 2	<b>2.809</b> Å	<b>2.740</b> Å	<b>2.807</b> Å	<b>3.009</b> Å	3.226 Å	<b>2.864</b> Å	<b>2.809</b> Å	<b>2.752(1)</b> Å	<b>3.015</b> Å	<b>3.231</b> Å
		× 1	–	–	–	–	3.713 Å	–	–	–	–	3.755 Å

The energy differences between the orthorhombic and the cubic structures ( $\Delta E = E_{\text{ortho}} - E_{\text{cubic}}$ ) calculated with *VASP* are listed in Table 4; all agree with experiment. Orthorhombic Na<sub>2</sub>AuBi affords the lower total energy (negative  $\Delta E_{\text{TOT}}$ ) and cubic Na<sub>2</sub>TlTl has the lower total energy (positive  $\Delta E_{\text{TOT}}$ ). “Na<sub>2</sub>HgPb” also has positive  $\Delta E_{\text{TOT}}$  but the difference is much smaller than in Na<sub>2</sub>TlTl. We can also see from Table 4 that the volume difference between 103.22 and 106.35 Å<sup>3</sup>/f.u. does affect the magnitude but does not change the sign of  $\Delta E_{\text{TOT}}$ . So, the structural difference between Na<sub>2</sub>AuBi and Na<sub>2</sub>TlTl is not caused by a volume effect. The electrostatic energy is always lower in the cubic structure, i.e.,  $\Delta E_{\text{ES}}$  always positive, for Na<sub>2</sub>AuBi, “Na<sub>2</sub>HgPb”, and Na<sub>2</sub>TlTl. This indicates that the cubic structure is favored over the orthorhombic structure by highly delocalized valence electrons or metallic interactions. On the other hand, the difference in electronic energy,  $\Delta E_{\text{electronic}}$ , is always negative. Therefore, valence electron localization stabilizes the orthorhombic structure more than the cubic structure.  $\Delta E_{\text{electronic}}$  includes all effects from charge transfer, formation of lone pairs and covalent bonds, viz. the effects of ionicity and covalency are both involved. To evaluate the effects of ionic interactions, we have calculated the Madelung energy,  $E_{\text{Madelung}}$ , using the Ewald technique.<sup>31</sup> We then investigated the covalent interactions between the electronegative atoms (Au/Bi, Hg/Pb, and Tl1/Tl2) by calculating their ICOHP values with the *LMTO* method.



**Table 4.** Energy differences between the orthorhombic and cubic structures,  $\Delta E = E_{\text{ortho}} - E_{\text{cubic}}$ .

Comp.	Energy Terms	73.52 Å <sup>3</sup> /f.u.	103.22 Å <sup>3</sup> /f.u.	106.35 Å <sup>3</sup> /f.u.
Li <sub>2</sub> AuBi	$\Delta E_{\text{ES}}$ (eV/f.u.)	-4.0443		102.1175
	$\Delta E_{\text{electronic}}$ (eV/f.u.)	4.2658	-	-102.6120
	$\Delta E_{\text{TOT}}$ (eV/f.u.)	0.2215		-0.4945
Na <sub>2</sub> AuBi	$\Delta E_{\text{ES}}$ (eV/f.u.)	22.6768	90.8474	98.1157
	$\Delta E_{\text{electronic}}$ (eV/f.u.)	-21.9483	-91.1371	-98.4843
	$\Delta E_{\text{TOT}}$ (eV/f.u.)	0.7285	-0.2897	-0.3686
Na <sub>2</sub> HgPb	$\Delta E_{\text{ES}}$ (eV/f.u.)		53.0567	58.0577
	$\Delta E_{\text{electronic}}$ (eV/f.u.)	-	-52.9061	-57.9580
	$\Delta E_{\text{TOT}}$ (eV/f.u.)		0.1506	0.0997
Na <sub>2</sub> TlTl	$\Delta E_{\text{ES}}$ (eV/f.u.)		2.4928	7.5600
	$\Delta E_{\text{electronic}}$ (eV/f.u.)	-	-2.2125	-7.3193
	$\Delta E_{\text{TOT}}$ (eV/f.u.)		0.2803	0.2407

**Figure 2.** The difference in  $E_{\text{Madelung}}$  between the two structure types calculated at 106.35 Å<sup>3</sup>/f.u.,  $\Delta E_{\text{Madelung}} = E_{\text{Madelung,ortho}} - E_{\text{Madelung,cubic}}$ , calculated at different formal charges on Au/Bi, Hg/Pb, Tl1/Tl2.

To calculate  $E_{\text{Madelung}}$ , Na is simplistically treated as  $\text{Na}^+$ , so that the (AuBi) substructure becomes  $(\text{AuBi})^{2-}$ . Since one cannot precisely divide the two negative formal charges between Au and Bi, we calculated a range of formal charges from “ $(\text{Au}^{2-}\text{Bi}^0)$  through  $(\text{Au}^{-}\text{Bi}^{-})$  and  $(\text{Au}^0\text{Bi}^{2-})$  to  $(\text{Au}^+\text{Bi}^{3-})$ . The difference in Madelung energies,  $\Delta E_{\text{Madelung}} = E_{\text{Madelung,ortho}} - E_{\text{Madelung,cubic}}$ , calculated all at 106.35 Å<sup>3</sup>/f.u. is plotted against the formal charge on Au in Figure 2. The differences calculated at 103.22 Å<sup>3</sup>/f.u. are close and included in Supporting Information. Apparently, the favoritism of ionicity toward the two structure types depends on how the two negative formal charges are assigned to Au and Bi. Between  $\text{Au}^{-0.6}\text{Bi}^{-1.4}$  and  $\text{Au}^{0.6}\text{Bi}^{-2.6}$ ,  $\Delta E_{\text{Madelung}}$  is negative and, beyond this range, positive. Considering their absolute electronegativities,<sup>32</sup> Au at 5.77 eV and Bi at 4.69 eV, we can estimate that Au should have more negative formal charges than Bi, or the formal charge of Au should be more

negative than  $-1$  (to the left of the  $(\text{Au}^-\text{Bi}^-)$  dotted line in Figure 2), which leads to positive  $\Delta E_{\text{Madelung}}$  values according to Figure 2. So, ionicity favors the cubic structure for  $\text{Na}_2\text{AuBi}$ .

The same  $\Delta E_{\text{Madelung}}$  curves were also plotted for “ $\text{Na}_2\text{HgPb}$ ” and  $\text{Na}_2\text{TlTl}$  (Figure 2). The absolute electronegativities of Hg and Pb, respectively, are 4.91 eV and 3.9 eV.<sup>32</sup> So, the formal charge on Hg is expected to be more negative than on Pb (so, also left of the dotted line in Figure 2). Thus  $\Delta E_{\text{Madelung}}$  is expected to be positive in “ $\text{Na}_2\text{HgPb}$ ” as well; however, it is smaller (less positive) than in  $\text{Na}_2\text{AuBi}$ . Thus, for the hypothetical composition “ $\text{Na}_2\text{HgPb}$ ”, ionicity also favors the cubic structure. As for  $\text{Na}_2\text{TlTl}$ , it is Tl vs Tl so it is reasonable to assign  $\text{Tl}^-\text{Tl}^-$ .  $\Delta E_{\text{Madelung}}$  is negative according to Figure 2, so the orthorhombic structure is favored by ionicity.

The discussions above show that, by evaluating only metallicity and ionicity, we cannot yet successfully rationalize the relative stability between the zigzag ribbons and the diamond network in  $\text{Na}_2\text{AuBi}$ , “ $\text{Na}_2\text{HgPb}$ ”, and  $\text{Na}_2\text{TlTl}$ . At the same volume per f.u., metallicity always prefers the diamond network. Ionicity even contradicts with the observed structures - it prefers the cubic structure in  $\text{Na}_2\text{AuBi}$  which adopts the orthorhombic structure, and prefers the orthorhombic structure in  $\text{Na}_2\text{TlTl}$ , which adopts the cubic structure.

To compare covalency between the two structure types, the differences in ICOHP ( $\Delta\text{ICOHP} = \text{ICOHP}_{\text{ortho}} - \text{ICOHP}_{\text{cubic}}$ ) are also calculated at both 103.22 and 106.35  $\text{\AA}^3/\text{f.u.}$  for  $\text{Na}_2\text{AuBi}$ , “ $\text{Na}_2\text{HgPb}$ ”, and  $\text{Na}_2\text{TlTl}$ , and are listed in Table 5. It is evident that  $\Delta\text{ICOHP}$  shows exactly the same pattern with  $\Delta E_{\text{TOT}}$  in Table 4.  $\text{Na}_2\text{AuBi}$  has negative  $\Delta\text{ICOHP}$  at both volumes; “ $\text{Na}_2\text{HgPb}$ ” and  $\text{Na}_2\text{TlTl}$  both have positive  $\Delta\text{ICOHP}$ , which is smaller for “ $\text{Na}_2\text{HgPb}$ ” than for  $\text{Na}_2\text{TlTl}$ . Therefore, although the zigzag ribbons do not follow the octet rule, its stability relative to the diamond network can still be rationalized with the Zintl-Klemm concept – it is the covalent interactions between the electronegative atoms that determine the structure. For  $\text{Na}_2\text{AuBi}$ , the covalent interactions between Au/Bi atoms provide more stabilization by constructing the zigzag ribbon than the diamond network, so it prefers the former. The cases are exactly opposite in “ $\text{Na}_2\text{HgPb}$ ” and  $\text{Na}_2\text{TlTl}$  – the covalent interactions between Hg/Pb atoms and between Tl1/Tl2 atoms stabilize the cubic structure more than the orthorhombic structure, rendering the diamond network more favorable.

To figure out why the Au/Bi combination favors the zigzag ribbon but the isoelectronic Hg/Pb and Tl1/Tl2 combinations favor the diamond network, we studied the DOS and  $-\text{COHP}$  curves of  $\text{Na}_2\text{AuBi}$ , “ $\text{Na}_2\text{HgPb}$ ”, and  $\text{Na}_2\text{TlTl}$ . The curves calculated at 106.35  $\text{\AA}^3/\text{f.u.}$  are shown in Figure 3 and those calculated at 103.22  $\text{\AA}^3/\text{f.u.}$  are quite similar and included in Supporting Information.

For all three compositions in both structures, the majority of states below the Fermi levels are from Au/Bi, Hg/Pb, and Tl valence orbitals. Na also has significant contributions, which implies that Na atoms do not donate all their 3s electrons to the electronegative counterparts. However, there is also an overestimation. For instance, in orthorhombic Na<sub>2</sub>AuBi, the integrated DOS of Na at the Fermi level is 1.065 e<sup>-</sup> per atom, making a formal Na<sup>-0.065</sup> anion. This is because LMTO evenly divides the “overlap population” when it calculates partial DOS and this results in overestimation for electropositive atoms and underestimation of electronegative atoms.<sup>33</sup>

**Table 5.** Difference in ICOHP values between the orthorhombic and the cubic structures ( $\Delta\text{ICOHP} = \text{ICOHP}_{\text{ortho}} - \text{ICOHP}_{\text{cubic}}$ ) calculated with LMTO. The  $\Delta\text{ICOHP}$  values with subscript *sp* are calculated with the 5*d* orbitals of Au, Hg, and Tl1 excluded from basis set.

Comp.	$\Delta\text{ICOHP}$ (eV/f.u.)	73.52 Å <sup>3</sup> /f.u.	103.22 Å <sup>3</sup> /f.u.	106.35 Å <sup>3</sup> /f.u.
Li <sub>2</sub> AuBi	$\Delta\text{ICOHP}_{\text{Au/Bi}}$	1.1132	–	–0.9022
	$\Delta\text{ICOHP}_{\text{Au/Bi,sp}}$	2.9131	–	0.2403
Na <sub>2</sub> AuBi	$\Delta\text{ICOHP}_{\text{Au/Bi}}$	0.4466	–0.1469	–0.3324
	$\Delta\text{ICOHP}_{\text{Au/Bi,sp}}$	1.8806	0.9720	0.7972
Na <sub>2</sub> HgPb	$\Delta\text{ICOHP}_{\text{Hg/Pb}}$	–	1.2052	1.0431
	$\Delta\text{ICOHP}_{\text{Hg/Pb,sp}}$	–	1.4939	1.3511
Na <sub>2</sub> TlTl	$\Delta\text{ICOHP}_{\text{Tl}}$	–	1.8112	1.5779
	$\Delta\text{ICOHP}_{\text{Tl,sp}}$	–	1.8775	1.6398

The Fermi levels coincide with local minima or pseudogaps in all DOS curves and also the bonding-antibonding crossovers in the –COHP curves of Au-Bi, Hg-Pb, and Tl1-Tl2. Thus, although the zigzag ribbon does not satisfy the octet rule, it does provide optimized covalent interactions just like the diamond network. It is also evident that the Hg-Pb and Tl1-Tl2 interactions are weaker in the orthorhombic than in the cubic structure, but the Au-Bi interactions are comparable in both structures.

From the DOS curves, the most significant difference between Na<sub>2</sub>AuBi, “Na<sub>2</sub>HgPb”, and Na<sub>2</sub>TlTl is the relative positions of the 5*d*, 6*s*, and 6*p* states of Au/Bi, Hg/Pb, and Tl1/Tl2. To accentuate this feature, the population weighted band centers are shown in Figure 4. In the Tl1/Tl2 combination, the 5*d* states of Tl1 and Tl2 coincide and are localized around 12 eV below the Fermi level in the DOS curves. The –COHP curves demonstrate that these localized 5*d* states make no significant contributions to Tl-Tl covalent interactions. The band center of the Hg 5*d* states is just above that of Pb 6*s* states. The DOS curves reveal that Hg 5*d* states are also localized around –7.4 eV in the cubic structure and –7.2 eV in the orthorhombic structure, without perceivable contributions to those states right below the Fermi level (–6 to 0 eV). The –COHP curves also show that Hg 5*d* states have no significant contributions in Hg-Pb covalent interactions. In Au/Bi, the band center of Au 5*d* states is

very close to the Bi  $6p$  states, and only 3.5 eV below the Fermi level. The DOS curves tell that, in both structures, Au  $5d$  states are among the states right below the Fermi level. And, the Au-Bi – COHP curves show these states to be bonding, although, in the cubic structure, there is an antibonding “spike” at –3 eV. Therefore, the difference between the isoelectronic Au/Bi, Hg/Pb, and Tl1/Tl2 combinations is that in Hg/Pb and Tl1/Tl2,  $5d$  states are localized and do not significantly contribute to Hg-Pb and Tl-Tl covalent interactions but, in Au/Bi, Au  $5d$  states are actively involved in Au-Bi covalent interactions.

To evaluate the effect of the  $5d$  states of Au, Hg, and Tl1, we excluded them from the basis sets and re-calculated ICOHP values. These results are listed in Table 5 as  $\Delta\text{ICOHP}_{sp}$ . By excluding these  $5d$  states, all  $\Delta\text{ICOHP}$  values increase, i.e., the orthorhombic structure becomes less favored. The largest increase occurs in  $\text{Na}_2\text{AuBi}$  and it is decisive – the sign of  $\Delta\text{ICOHP}$  changes from negative (favoring the orthorhombic structure) to positive (favoring the cubic structure). Therefore, the reason why the zigzag ribbon is only favored by Au/Bi is that Au  $5d$  states stabilize it. Without the effective involvement of  $5d$  states in covalent interactions, as in Hg/Pb and Tl1/Tl2, the diamond network is preferred. This also explains why the zigzag ribbon defies the octet rule but still provides optimized covalent interactions – the octet rule applies when valence states consist of only  $s$  and  $p$  states.

To study how Au  $5d$  states contribute to Au-Bi covalent interactions, we calculated the band structure of orthorhombic  $\text{Na}_2\text{AuBi}$  at  $106.35 \text{ \AA}^3/\text{f.u.}$  and examined the eigenvectors of the bands at certain high symmetry  $k$ -points (Figure 5). The most significant interaction between Au  $5d$  states and Bi orbitals is that between Au  $5d_{x^2-y^2}$  and Bi  $6p_z$ . We located three bands at the  $X (2\pi/a, 0, 0)$ ,  $\Gamma (0, 0, 0)$ , and  $S (\pi/a, -\pi/b, 0)$  points, where  $a$  and  $b$  are lattice parameters. They are indicated with arrows and sketched, along valence electron density maps calculated with *VASP*, in Figure 5 and their eigenvectors are included in Supporting Information. The dominant contributors of these bands exhibit bonding overlap between Au  $5d_{x^2-y^2}$  and Bi  $6p_z$  orbitals, such that the corresponding Au-Au interaction has  $\delta^*$  character along the ribbon.

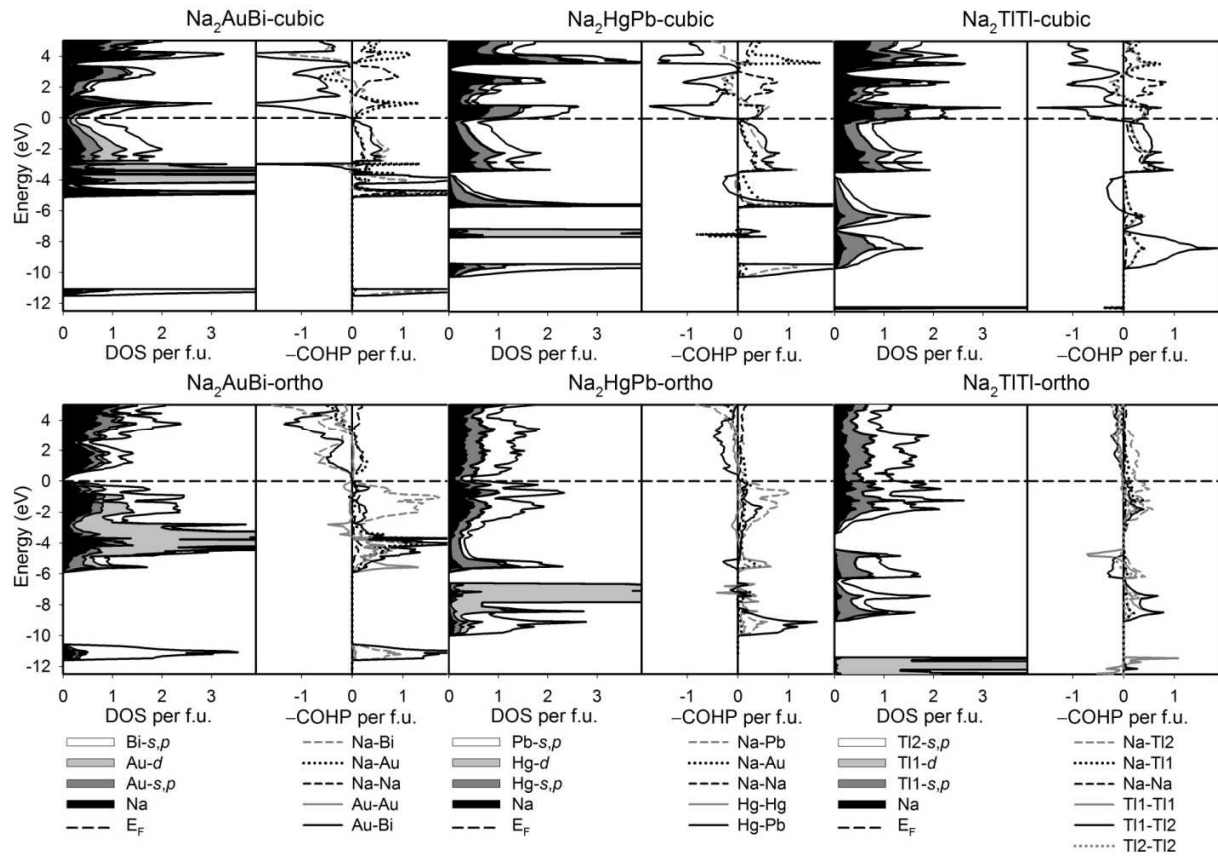


**Figure 3.** DOS and -COHP curves of  $\text{Na}_2\text{AuBi}$ ,  $\text{Na}_2\text{HgPb}$ , and  $\text{Na}_2\text{TlTl}$  in both cubic and orthorhombic structures calculated with LMTO at  $106.35 \text{ \AA}^3/\text{f.u.}$ .

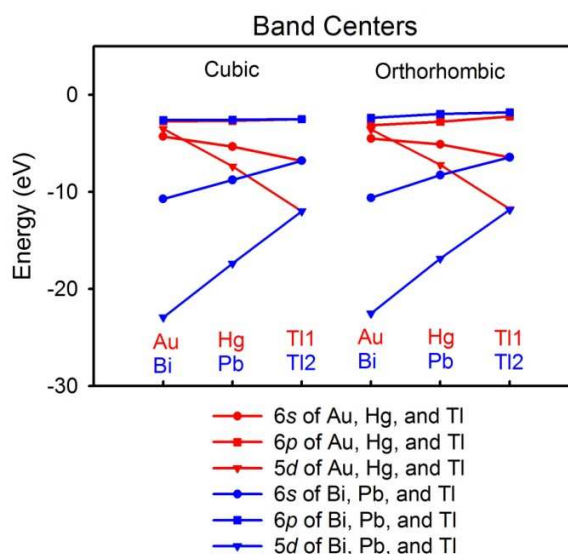


**Figure 4.** Population weighted band centers of the  $5d$ ,  $6s$ , and  $6p$  states of Au/Bi, Hg/Pb, and Tl1/Tl2.

In conclusion, at the two volumes we studied,  $103.22$  and  $106.35 \text{ \AA}^3/\text{f.u.}$ , metallicity stabilizes the cubic structure more than the orthorhombic structure. Ionicity also favors the cubic structure in  $\text{Na}_2\text{AuBi}$ . Covalent interactions between electronegative atoms provide more stabilization in the zigzag ribbon for Au/Bi but, for Hg/Pb and Tl1/Tl2, it is the diamond network that provides more stabilization through covalency. The reason is that unlike Hg and Tl, Au  $5d$  states are actively involved in covalent interactions. So Au/Bi is a  $5d$ - $6s$ - $6p$  system and Hg/Pb and Tl1/Tl2 are essentially  $6s$ - $6p$  systems. While the diamond network satisfies the octet rule and is, thus, a good solution for an  $s$ - $p$  system, the zigzag ribbon is a better solution for a  $d$ - $s$ - $p$  system because it provides effective bonding interactions between  $d$  and  $sp$  states, especially between Au  $5d_{x^2-y^2}$  and Bi  $6p_z$ . And eventually, covalency prevails over metallicity and ionicity in  $\text{Na}_2\text{AuBi}$ , rendering it to adopt the orthorhombic structure.

#### 4.4.2 $\text{Li}_2\text{AuBi}$ and $\text{Na}_2\text{AuBi}$

The experimental volume of  $\text{Li}_2\text{AuBi}$ ,  $73.52 \text{ \AA}^3/\text{f.u.}$ , is much smaller than that of  $\text{Na}_2\text{AuBi}$ ,  $106.35 \text{ \AA}^3/\text{f.u.}$ . Therefore, we studied  $\text{Li}_2\text{AuBi}$  and  $\text{Na}_2\text{AuBi}$  in cubic and orthorhombic structures at both volumes. The optimized orthorhombic structures and selected interatomic distances are also listed in Tables 2 and 3. Compared to orthorhombic  $\text{Na}_2\text{AuBi}$ , orthorhombic  $\text{Li}_2\text{AuBi}$  has smaller  $a$  values at both volumes. Since the  $a$  parameter determines the space between two neighboring “sheets” containing the Au/Bi zigzag ribbons, where the alkali metal atoms reside, it is closely related to the

size of the alkali metal atoms. That Li is smaller than Na effects a smaller  $a$  parameter for  $\text{Li}_2\text{AuBi}$  than for  $\text{Na}_2\text{AuBi}$ . The dimension of the zigzag ribbons, however, is very close between orthorhombic  $\text{Li}_2\text{AuBi}$  and  $\text{Na}_2\text{AuBi}$  at both volumes – the differences in  $d_{\text{Au-Au}}$  and  $d_{\text{Au-Bi}}$  are all smaller than 0.1 Å. Moreover, the volume difference does not significantly affect the dimension of the zigzag ribbons, either. Through compression from 106.35 to 73.52 Å<sup>3</sup>/f.u.,  $d_{\text{Au-Bi}}$  shrinks by only 0.055 and 0.069 Å in orthorhombic  $\text{Li}_2\text{AuBi}$  and  $\text{Na}_2\text{AuBi}$ . The shortening in  $d_{\text{Au-Au}}$  has larger magnitude, 0.129 and 0.312 Å, respectively. By contrast, the same volume difference results in a sharp decrease in the dimension of the diamond network –  $d_{\text{cubic}}$  drops by 1.377 Å from 106.35 to 73.52 Å<sup>3</sup>/f.u..

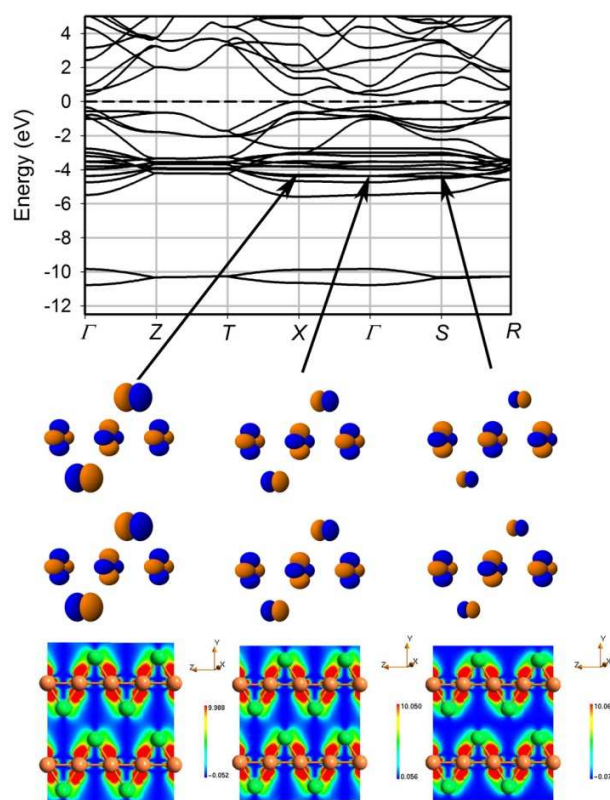


**Figure 5.** Band structure of orthorhombic  $\text{Na}_2\text{AuBi}$  at 106.35 Å<sup>3</sup>/f.u. calculated with VASP and the sketches and valence electron density maps of the three bands demonstrating the interactions between Au  $5d_{x^2-y^2}$  and Bi  $6p_z$ .

The  $\Delta E$  terms calculated with VASP are included in Table 4. Again,  $\Delta E_{\text{TOT}}$  matches experimental observations – it is negative for  $\text{Na}_2\text{AuBi}$  (orthorhombic is favored) and positive for  $\text{Li}_2\text{AuBi}$  (cubic is



avored) at their experimental volumes.  $\Delta E_{\text{TOT}}$  also reveals that the structural difference between  $\text{Li}_2\text{AuBi}$  and  $\text{Na}_2\text{AuBi}$  is caused by a volume effect. At  $73.52 \text{ \AA}^3/\text{f.u.}$ , both  $\text{Li}_2\text{AuBi}$  and  $\text{Na}_2\text{AuBi}$  favor the cubic structure; at  $106.35 \text{ \AA}^3/\text{f.u.}$ , they both prefer the orthorhombic structure.

The  $\Delta\text{ICOHP}$  values (Table 5) once again have the same signs with  $\Delta E_{\text{TOT}}$ , indicating that the structural preference can be rationalized through the covalent interactions between Au/Bi atoms. At  $106.35 \text{ \AA}^3/\text{f.u.}$ ,  $\Delta\text{ICOHP}$  values are negative for both  $\text{Li}_2\text{AuBi}$  and  $\text{Na}_2\text{AuBi}$ , so the zigzag ribbons provide more stabilization through covalency. The situation is reversed at  $73.52 \text{ \AA}^3/\text{f.u.}$  – the diamond network offers more effective covalent interactions between Au/Bi atoms. This is in accordance with the interatomic distances. As mentioned above, from  $106.35$  to  $73.52 \text{ \AA}^3/\text{f.u.}$ , the distances between Au/Bi atoms do not change significantly in the zigzag ribbons, but shrink drastically in the diamond network. So, the latter is expected to experience larger enhancement in covalent interactions upon compression from  $106.35$  to  $73.52 \text{ \AA}^3/\text{f.u.}$ . This is, indeed, the case. For instance, in orthorhombic  $\text{Na}_2\text{AuBi}$ , the compression leads to an ICOHP change from  $-4.52$  to  $-5.62 \text{ eV/f.u.}$  – the difference is  $-1.11 \text{ eV/f.u.}$ . This is less than in cubic  $\text{Na}_2\text{AuBi}$ , whose ICOHP changes from  $-4.19$  to  $-6.08 \text{ eV/f.u.}$ , i.e., by  $-1.89 \text{ eV/f.u.}$ . So, as the volume gets smaller, the diamond network becomes increasingly advantageous in covalency.

Although the 3-D diamond network and the 1-D zigzag ribbon are both options for optimized covalent interactions, they offer advantages and disadvantages over each other at different volumes. For the diamond network, symmetry strictly requires that  $d_{\text{Au-Bi}}$  equals to  $(3^{1/2}/4)a$ , where  $a$  is the lattice parameter of its cubic unit cell, so it is proportional to  $V^{1/3}$ .  $d_{\text{Au-Bi}}$  and  $d_{\text{Au-Au}}$  in the zigzag ribbon do not heavily rely on volume. A change in volume can be absorbed mainly by the separation between the “sheets” containing the zigzag ribbons (lattice parameter  $a$ ) and/or the separation between zigzag ribbons within one “sheet” (lattice parameter  $b$ ), while the interatomic distances within the zigzag ribbons do not vary significantly. As a result, at large volume, the zigzag ribbons provide more effective covalent interactions. On the other hand, to assure effective covalent interactions in the diamond network, the volume cannot become too large.

It is not unique to the  $\text{A}_2\text{AuBi}$  systems that a volume increase causes a 3-D network to break down into a lower dimensional structural motif to retain effective covalent interactions. Rather, this effect is frequently observed in many Zintl phases. For instance,  $\text{NaTl}$  has the diamond Tl network<sup>9</sup> but  $\text{KTl}$ , with a larger volume,<sup>34</sup> breaks down to separated  $\text{Tl}_6$  octahedral clusters. Furthermore,  $\text{LiSi}$ <sup>35</sup> and



LiGe<sup>36</sup> both feature a 3-D network with every Si/Ge atom connected to three other Si/Ge atoms; but in NaSi and NaGe,<sup>37</sup> Si/Ge atoms form isolated Si<sub>4</sub>/Ge<sub>4</sub> tetrahedral clusters.

#### 4.4.3 $E(V)$ Curves

In all discussions above, the cubic and the orthorhombic structures were always compared at equal volumes per f.u.. By doing this, we have successfully identified two factors that affect the relative stability of the zigzag ribbons against the diamond network: (i) the participation of Au  $5d$  states in covalent interactions and (ii) the retention of effective covalent interactions by the zigzag ribbons at higher volume. However, in reality, iso-compositional structures do not form at the same volume. For instance, KTI adopts the structure with the  $Tl_6$  octahedron motif<sup>34</sup> at ambient conditions but changes to the double diamond structure at smaller volume achieved by high pressure.<sup>38</sup> Therefore, for each composition discussed above, it is necessary to scan the total energy over a volume range for both the cubic and the orthorhombic structures and compare them at their equilibrium volumes.

The  $E(V)$  curves calculated with *VASP* are shown in Figure 6 and the  $V_{eq}$  values obtained from a Murnaghan fitting are listed in Table 6, together the differences in energies and ICOHP values between the orthorhombic and the cubic structures at their  $V_{eq}$ . The global minimum, which is the lower minimum of the two  $E(V)$  curves of each composition and, thus, predicts the structure this composition eventually adopts, occurs for the orthorhombic structure in Na<sub>2</sub>AuBi and for the cubic structure in all others, which is in accordance with experiments. But the  $V_{eq}$  values of these global minima, which predict the volumes of these compounds, are all higher than the experimental volumes, especially Na<sub>2</sub>TlTI, whose predicted 112.63 Å<sup>3</sup>/f.u. is more than 9% larger than its experimental 103.22 Å<sup>3</sup>/f.u.. This overestimation of volume is caused by the PBE pseudopotentials<sup>22</sup> we adopted for *VASP* calculations and has been observed in other reports.<sup>39,40</sup>

For each composition,  $V_{eq}(\text{ortho}) > V_{eq}(\text{cubic})$ . Also, the cubic structure always offers lower total energy at smaller volume and the orthorhombic always affords lower total energy at larger volume, revealing, once again, that a volume increase shifts favoritism from the diamond network to the zigzag ribbon structural motif. The energy terms exhibit patterns similar to those in Tables 4 and 5.  $\Delta E_{ES}$  is always positive, so metallicity favors the cubic structure.  $\Delta E_{\text{electronic}}$  is always negative, so the localization of valence electrons stabilizes the orthorhombic structure.  $\Delta \text{ICOHP}$  always bears the same sign with  $\Delta E_{\text{TOT}}$ , so the covalent interactions between the electronegative atoms determine the relative stability between these two structures - the Zintl-Klemm rationalization is valid here. Therefore, these comparisons made at  $V_{eq}$  agree with those made at equal volumes in previous

discussions. The  $E(V)$  curves also reveal that a pressure induced phase transition can be expected in  $\text{Na}_2\text{AuBi}$ : at pressures exceeding ca. 3.285 GPa,  $\text{Na}_2\text{AuBi}$  is predicted to transform from the orthorhombic into the cubic structure. High pressure synthesis and X-ray crystallography are necessary to test this prediction.

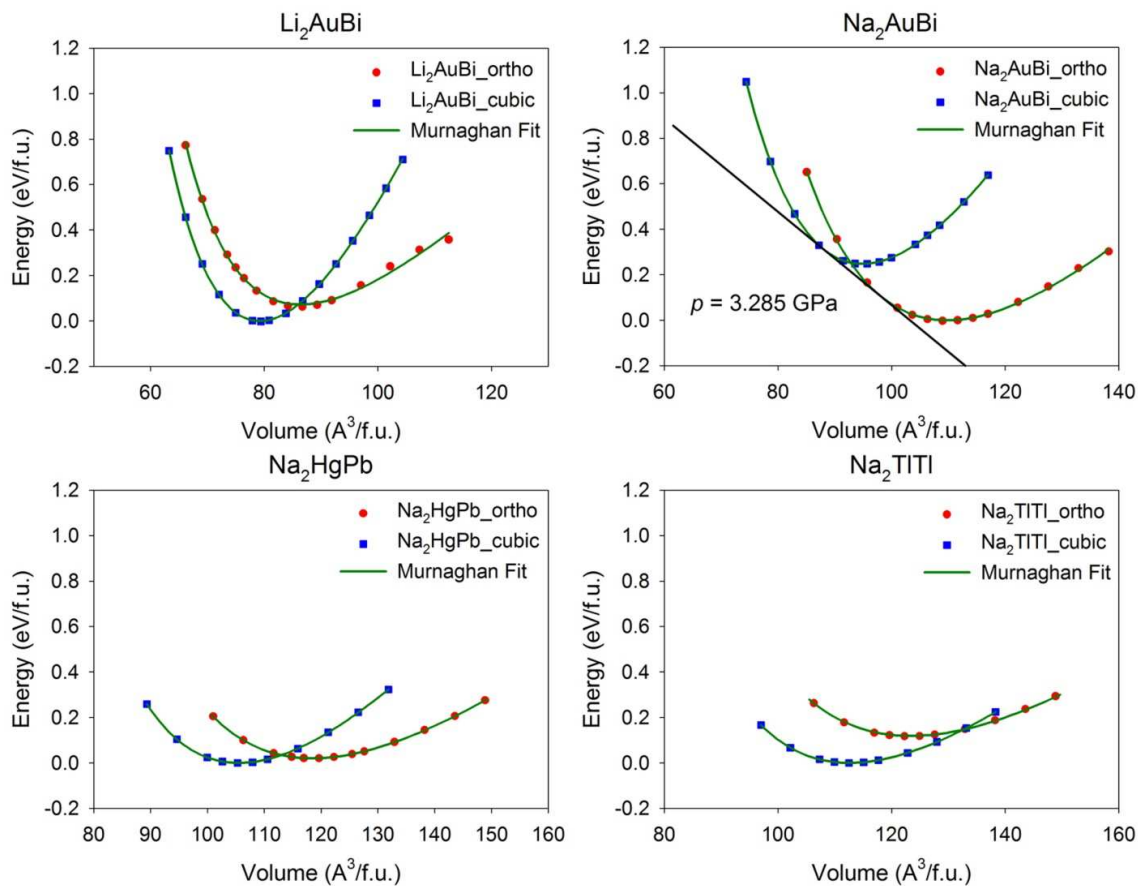


**Figure 6.**  $E(V)$  curves of  $\text{Li}_2\text{AuBi}$ ,  $\text{Na}_2\text{AuBi}$ ,  $\text{Na}_2\text{HgPb}$ , and  $\text{Na}_2\text{TlTl}$  in both the cubic and the orthorhombic structures calculated with *VASP*.

**Table 6.** Equilibrium volumes, differences in energy terms and ICOHP between the orthorhombic and the cubic structures at their equilibrium volumes.

	$V_{\text{eq}}(\text{ortho})$ ( $\text{\AA}^3/\text{f.u.}$ )	$V_{\text{eq}}(\text{cubic})$ ( $\text{\AA}^3/\text{f.u.}$ )	$\Delta E_{\text{ES}}$ (eV/f.u.)	$\Delta E_{\text{electronic}}$ (eV/f.u.)	$\Delta E_{\text{TOT}}$ (eV/f.u.)	$\Delta \text{ICOHP}_{\text{Au/Bi}}$ (eV/f.u.)
$\text{Li}_2\text{AuBi}$	86.41	79.22	80.0454	-79.98152	0.0639	2.0079
$\text{Na}_2\text{AuBi}$	109.82	94.92	187.8556	-188.1054	-0.2498	-0.4306
$\text{Na}_2\text{HgPb}$	118.50	105.53	140.8459	-140.8256	0.0203	0.3857
$\text{Na}_2\text{TlTl}$	123.39	112.63	82.2605	-82.1438	0.1167	0.8109

## 4.5 Conclusions

The zigzag ribbon motif in the orthorhombic structure adopted by  $\text{Na}_2\text{AuBi}$  and the diamond network in the cubic structure adopted by  $\text{Li}_2\text{AuBi}$  and  $\text{Na}_2\text{TlTl}$  are both options for optimized covalent interactions between Au/Bi atoms or Tl atoms. The relative stability between these two structures is determined by which structural motif provides more effective covalent interactions. We identified two important factors that can tune the relative stability. The first one is the involvement of  $5d$  states in covalent interactions, which stabilizes the zigzag ribbon. The second factor is volume. Due to the symmetry restriction, the diamond network cannot afford effective covalent interactions at high volume and yields to the 1-D zigzag ribbon.

By studying  $\text{A}_2\text{AuBi}$  and comparing the two competing structural motifs, we gained some supplemental conclusions about the Zintl-Klemm concept. Firstly, Zintl phases may consist of elements from not only the  $s$  and  $p$  blocks, but also the  $d$  block in the periodic table, so the structures can be much more complex than what we could expect from those well established electron counting rules, e.g., octet and Wade's rules.<sup>41,42</sup> Secondly, the volume effect is important. Larger "cations," which lead to larger volumes, tend to break down a three-dimensional "anionic" network into a lower-dimensional structural motif, which also provides optimized covalent interactions.

## 4.6 Acknowledgements

This work is supported by NSF DMR 06-05949 and 10-05765.

## 4.7 References

- (1) Zintl, E.; Dullenkopf, W. *Z. Phys. Chem.* **1932**, *B16*, 183.
- (2) Zintl, E.; Brauer, G. *Z. Phys. Chem.* **1933**, *B20*, 245.
- (3) Zintl, E. *Angew. Chem.* **1939**, *52*, 1.
- (4) Schäfer, H.; Eisenmann, B.; Müller, W. *Angew. Chem. Intl. Ed. Engl.* **1973**, *12*, 694.
- (5) Schäfer, H.; Eisenmann, B. *Rev. Inorg. Chem.* **1981**, *3*, 29.
- (6) Schäfer, H. *Ann. Rev. Mater. Sci.* **1985**, *15*, 1.
- (7) Nesper, R. *Prog. Solid State Chem.* **1990**, *20*, 1.

- (8) *Chemistry, Structure, and Bonding of Zintl Phases and Ions*; Kauzlarich, S. M., Ed.; VCH: Weinheim, Germany, 1996.
- (9) Zintl, E.; Woltersdorf, G. *Z. Elektrochem.* **1935**, *41*, 876.
- (10) Wang, F.; Miller, G. J. in preparation.
- (11) Kim, S.-J.; Miller, G. J.; Corbett, J. D. *Z. Anorg. Allg. Chem.* **2010**, *636*, 67.
- (12) Janssen, E.M.W.; Folmer, J. C. W.; Wiegers, G. A. *J. Less-Common Met.* **1974**, *38*, 71.
- (13) Janssen, E. M.W.; Wiegers, G. A. *J. Less-Common Met.* **1978**, *57*, 58.
- (14) Jagodzinski, H. *Z. Kristallogr.* **1959**, *112*, 80.
- (15) Pease, R. S. *Acta Cryst.* **1952**, *5*, 356.
- (16) Wentorf, R. H. *J. Chem. Phys.* **1957**, *26*, 956.
- (17) Pauly, H.; Weiss, A.; Witte, H. *Z. Metallkde.* **1968**, *59*, 47.
- (18) (a) Kresse, G.; Hafner, J. *Phys. Rev. B* **1993**, *47*, 558. (b) Kresse, G.; Hafner, J. *Phys. Rev. B* **1994**, *49*, 14251.
- (19) Kresse, G.; Furthmüller, J. *Comput. Mat. Sci.* **1996**, *6*, 15.
- (20) Kresse, G.; Furthmüller, J. *Phys. Rev. B* **1996**, *54*, 11169.
- (21) Kresse, G.; Joubert, D. *Phys. Rev.* **1999**, *59*, 1758.
- (22) Perdew, J. P.; Burke, K.; Ernzerhof, M. *Phys. Rev. Lett.* **1996**, *77*, 3865.
- (23) Press, W. H.; Flannery, B. P.; Teukolsky, S. A.; Vetterling, W. T. *Numerical Recipes*; Cambridge University Press: New York, 1986.
- (24) Monkhorst, H. J.; Pack, J. D. *Phys. Rev. B* **1976**, *13*, 5188.
- (25) Eck, B. *wxDragon*, version 1.4.2; RWTH Aachen University, Aachen, Germany, 2008.
- (26) Murnaghan, F. D. *PNAS* **1944**, *30*, 244.

- (27) Miller, G. J.; Schmidt, M. W.; Wang, F.; You, T.-S. Quantitative Advances in the Zintl-Klemm Formalism. *Structure and Bonding*, Springer: published online, 2010.
- (28) Jepsen, O.; Andersen O. K. *TB-LMTO*, version 47; Max-Planck-Institut für Festkörperforschung, Stuttgart, Germany, 2000.
- (29) Dronskowski, R.; Blöchl, P. *J. Phys. Chem.* **1993**, *97*, 8617.
- (30) von Barth, U.; Hedin, L. *J. Phys. C: Solid State Phys.* **1972**, *5*, 1629.
- (31) Ewald, P. P. *Ann. Phys. Leipzig.* **1921**, *64*, 253-287.
- (32) Pearson, R. G. *Inorg. Chem.* **1988**, *27*, 734.
- (33) Dronskowski, R. *Computational Chemistry of Solid State Materials*; Wiley-VCH: Weinheim, Germany, 2005.
- (34) Dong, Z.; Corbett, J. D. *J. Am. Chem. Soc.* **1993**, *115*, 11299-11303.
- (35) Evers, J.; Oehlinger, G.; Sextl, G. *Angew. Chem.* **1993**, *105*, 1532.
- (36) Menges, E.; Hopf, V.; Schaefer, H.; Weiss, A. *Z. Naturforsch. B* **1969**, *24*, 1351.
- (37) Witte, J.; von Schnering, H. G. *Z. Anorg. Allg. Chem.* **1964**, *327*, 260.
- (38) Evers, J.; Oehlinger, G. *Phys. Rev. B* **1999**, *59*, 1758-1775.
- (39) Haas, P.; Tran, F. Blaha, P.; Schwarz, K.; Laskowski, R. *Phys. Rev. B* **2009**, *80*, 195109.
- (40) Stoffel, R. P.; Wessel, C.; Lumey, M.-W.; Dronskowski, R. *Angew. Chem. Int. Ed.* **2010**, *49*, 2.
- (41) Wade, K. *Adv. Inorg. Chem. Radiochem.* **1977**, *18*, 1.
- (42) Mingos, D. M. P. *Adv. Organomet Chem.* **1977**, *15*, 1.

## 4.8 Supporting Information

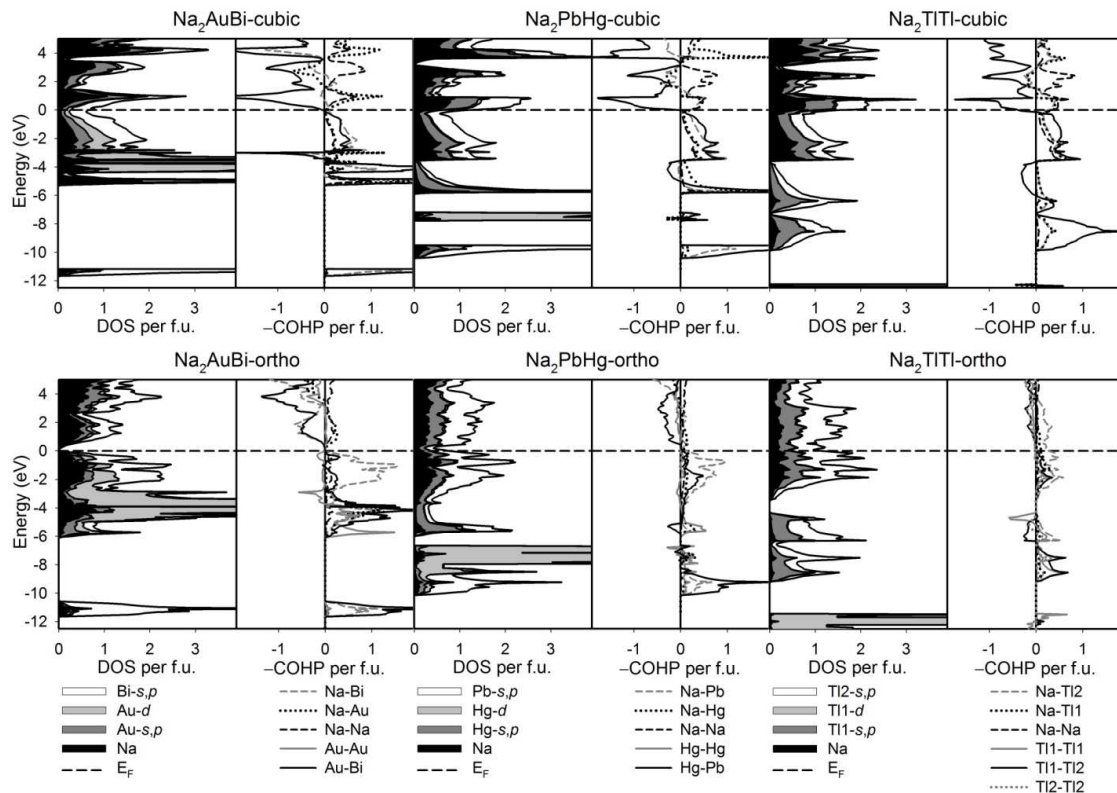


**Figure 1.** DOS and -COHP curves of  $\text{Na}_2\text{AuBi}$ ,  $\text{Na}_2\text{HgPb}$ , and  $\text{Na}_2\text{TlTl}$  in both cubic and orthorhombic structures calculated with LMTO at  $103.22 \text{ \AA}^3/\text{f.u.}$ .

**Table S1(a).** The eigenvectors of the  $d_{x^2-y^2} - p_z$  band at  $X (2\pi/a, 0, 0)$  point.

Atom	x	y	z	s	$p_y$	$p_z$	$p_x$	$d_{xy}$	$d_{yz}$	$d_{z^2}$	$d_{xz}$	$d_{x^2-y^2}$
Na1	0.3191	0.1765	3/4	Real	0	0	0.001	0	0	0	0.003	0
				Imag	0	0	0.002	0	0	0	0	0.003
Na2	0.3191	-0.1765	1/4	Real	0	0	-0.001	0	0	0	-0.003	0
				Imag	0	0	-0.002	0	0	0	0	-0.003
Na3	0.6809	0.1765	3/4	Real	0	0	0.001	0	0	0	-0.003	0
				Imag	0	0	0.002	0	0	0	0	-0.003
Na4	0.6809	-0.1765	1/4	Real	0	0	-0.001	0	0	0	0.003	0
				Imag	0	0	-0.002	0	0	0	0.003	0
Au1	0	0	0	Real	-0.033	0	0	0	0.012	0.025	0	0.081
				Imag	-0.043	0	0	0	0.016	0.032	0	0.103
Au2	0	0	1/2	Real	0.033	0	0	0	0.012	-0.025	0	-0.081
				Imag	0.043	0	0	0	0.016	-0.032	0	-0.103
Bi1	1/2	-0.1875	3/4	Real	0	0	0.064	0	-0.004	0	0	0
				Imag	0	0	0.082	0	-0.005	0	0	0
Bi2	1/2	0.1875	1/4	Real	0	0	-0.064	0	-0.004	0	0	0
				Imag	0	0	-0.082	0	-0.005	0	0	0

**Table S1(b).** The eigenvectors of the  $d_{x^2-y^2} - p_z$  band at  $\Gamma(0, 0, 0)$  point.

Atom	x	y	z		s	$p_y$	$p_z$	$p_x$	$d_{xy}$	$d_{yz}$	$d_{z^2}$	$d_{xz}$	$d_{x^2-y^2}$
Na1	0.3191	0.1765	3/4	Real	0	0	-0.003	0	0	0	0	0	0
				Imag	0	0	-0.006	0	0	0	0	0	-0.001
Na2	0.3191	-0.1765	1/4	Real	0	0	0.003	0	0	0	0	0	0
				Imag	0	0	0.006	0	0	0	0	0	0.001
Na3	0.6809	0.1765	3/4	Real	0	0	-0.003	0	0	0	0	0	0
				Imag	0	0	-0.006	0	0	0	0	0	0.001
Na4	0.6809	-0.1765	1/4	Real	0	0	0.003	0	0	0	0	0	0
				Imag	0	0	0.006	0	0	0	0	0	-0.001
Au1	0	0	0	Real	-0.032	0	0	0	0	0.008	0.024	0	0.049
				Imag	-0.060	0	0	0	0	0.016	0.045	0	0
Au2	0	0	1/2	Real	0.032	0	0	0	0	0.008	-0.024	0	-0.049
				Imag	0.060	0	0	0	0	0.016	-0.045	0	0
Bi1	1/2	-0.1875	3/4	Real	0	0	-0.053	0	0	0.003	0	0	0
				Imag	0	0	-0.099	0	0	0.005	0	0	0
Bi2	1/2	0.1875	1/4	Real	0	0	0.053	0	0	0.003	0	0	0
				Imag	0	0	0.099	0	0	0.005	0	0	0

**Table S1(c).** The eigenvectors of the  $d_{x^2-y^2} - p_z$  band at  $S(\pi/a, -\pi/b, 0)$  point.

Atom	x	y	z		s	$p_y$	$p_z$	$p_x$	$d_{xy}$	$d_{yz}$	$d_{z^2}$	$d_{xz}$	$d_{x^2-y^2}$
Na1	0.3191	0.1765	3/4	Real	0	0	-0.004	0	0	-0.001	0	0	0
				Imag	0	0	0.001	0	0	0	0	0	0
Na2	0.3191	-0.1765	1/4	Real	0	0	-0.001	0	0	0	0	-0.003	0
				Imag	0	0	0	0	0	0	0	0.001	0
Na3	0.6809	0.1765	3/4	Real	0	0	-0.001	0	0	0	0	0.003	0
				Imag	0	0	0	0	0	0	0	-0.001	0
Na4	0.6809	-0.1765	1/4	Real	0	0	-0.004	0	0	0.001	0	0	0
				Imag	0	0	0.001	0	0	0	0	0	0
Au1	0	0	0	Real	-0.057	0	0	0	0	0.020	0.046	0	0.131
				Imag	0.013	0	0	0	0	-0.005	-0.01	0	0
Au2	0	0	1/2	Real	0.057	0	0	0	0	0.020	-0.046	0	-0.131
				Imag	-0.013	0	0	0	0	-0.005	0.01	0	0
Bi1	1/2	-0.1875	3/4	Real	0	0	0.081	0	0	-0.009	0	0	0
				Imag	0	0	-0.018	0	0	0.002	0	0	0
Bi2	1/2	0.1875	1/4	Real	0	0	0.081	0	0	0.009	0	0	0
				Imag	0	0	-0.018	0	0	-0.002	0	0	0

## Chapter 5

### **EuAg<sub>x</sub>Al<sub>11-x</sub> with the BaCd<sub>11</sub>-Type Structure: Phase Width, Coloring, and Electronic Structure**

Modified from a paper published in *Chemistry of Materials*

Fei Wang, Karen Nordell Pearson, and Gordon J. Miller

#### **5.1 Abstract**

The EuAg<sub>x</sub>Al<sub>11-x</sub> (loading composition,  $x = ca. 3-8$ ) ternary system was experimentally and theoretically investigated. According to powder X-ray diffraction, phases adopting the BaCd<sub>11</sub>-type structure (space group  $I4_1/amd$ ,  $Z = 4$ ) were obtained for a narrow composition range, *i.e.*,  $x = ca. 5-6$ . Single crystal X-ray crystallography showed that Ag and Al atoms share  $4b$ ,  $8d$ , and  $32i$  sites and that  $4b$  site distinctly prefers Ag to Al. Eu is divalent in these phases, which was supported by both magnetometry and unit cell dimensional analysis. Comparison with other isostructural *RE*(rare earth)-Ag-Al compounds showed that the BaCd<sub>11</sub>-type structure is stable specifically at the valence electron concentrations (*vec*) of *ca.* 2.1-2.3  $e^-$  per atom. A Mulliken population analysis was performed with Extended Hückel calculations, the result of which explained the observed site preferences of the Ag and Al atoms. TB-LMTO-ASA calculations were used to study the relative energies of various models established according to crystallography and the coloring problem was included by maximizing the number of Ag-Al contacts. The calculated density of states (DOS) and crystal orbital Hamiltonian population (COHP) curves explain the stability of the BaCd<sub>11</sub>-type structure at specifically  $vec = ca. 2.1-2.3 e^-$  per atom in *RE*-Ag-Al ternary compounds.

#### **5.2 Introduction**

Polar intermetallic compounds are an emerging group of inorganic solids attracting attention for their chemical and physical characteristics. They are composed of electropositive metals (*e.g.* alkali metals, alkaline earth metals, and rare earth metals) and electronegative metals (*i.e.* metals around the Zintl border),<sup>1-3</sup> representing an intermediate compound class between classical intermetallic phases, such as Hume-Rothery and Laves phases on the one hand,<sup>4</sup> and valence compounds, *e.g.* Zintl phases,<sup>5</sup> on the other. Polar intermetallics often form complex structures, such as NaZn<sub>13</sub>-, BaCd<sub>11</sub>-, or BaHg<sub>11</sub>-types, which can be significantly different from those of the component metals. Their chemical bonding characteristics also represent a complex interplay among metallic, covalent, and ionic



bonding. Such features of polar intermetallics lead to many extraordinary properties, such as enhanced magnetocaloric effects<sup>6</sup> and superconductivity.<sup>7</sup> From the chemical perspective, polar intermetallics provide a structural and electronic framework for two electronegative elements, which, by themselves, show no binary phases in their equilibrium phase diagrams, to combine, as *e.g.*, Sn and Ge or In and Ge.<sup>8,9</sup> To exploit these properties and design new polar intermetallic materials, it is essential to understand the composition-structure-property relationship in these compounds. The valence electron counting rules, such as those adopted for Hume-Rothery phases<sup>4</sup> and the octet rule for Zintl phases,<sup>5</sup> are insufficiently effective for these intermediate cases. Therefore, new rules need to be established through further systematic investigations into polar intermetallics.

The *RE*(rare earth)-Ag-Al systems have been extensively investigated due, in part, to their structural richness.<sup>10</sup> Among these kaleidoscopic complex structures obtained at various compositions, site sharing between Ag and Al atoms and specific site preferences are commonly observed. Therefore, a thorough investigation into *RE*-Ag-Al ternary systems will largely enrich our understanding of the composition-structure-property relationship in polar intermetallics. However, although synthetic and crystallographic studies have been the major focus thus far for these systems, theoretical investigations have rarely been done. Many questions remain, for example, on the factors influencing the arrangements and distributions of Ag and Al atoms in these intermetallics. Furthermore, we believe that a synergistic effort between experiment and theory will be critical to elucidate the broader relationships needed to successfully target and obtain desired intermetallic systems.

This work involves a part of our efforts devoted to the  $\text{EuAg}_x\text{Al}_{11-x}$  ternary system. Specifically, we will focus on phases adopting the  $\text{BaCd}_{11}$ -type structure. This structure has been reported for many binary phases, such as  $\text{SrCd}_{11}$ ,  $\text{CeZn}_{11}$ ,<sup>11</sup> and  $\text{SrZn}_{11}$ ,<sup>12</sup> showing valence electron concentration (*vec*) slightly greater than  $2.00 e^-$  per atom. The stability of this structure for specific pairs of elements relies significantly on atomic size. Iandelli and Palenzona showed that, for *RE*-Zn binary systems, the  $\text{BaCd}_{11}$ -type structure occurs when *RE* = La, Ce, Pr, Nd, Eu, and Yb, but cannot be obtained with smaller (late) *RE* atoms.<sup>13</sup> Eu and Yb are exceptions because they are divalent and their sizes are comparable with the early trivalent *RE* atoms. Meanwhile, the number of valence electrons also plays an important role. Hückel-type calculations revealed that the  $\text{BaCd}_{11}$ -type structure is the most stabilized at the *vec* value of  $2.1 e^-$  per atom.<sup>14</sup> In  $\text{EuAg}_x\text{Al}_{11-x}$ , by varying the composition, we can tune the number of valence electrons. So the theoretical conclusion can be experimentally tested here.

In this work, both experimental and theoretical investigations were carried out for the  $\text{BaCd}_{11}$ -type  $\text{EuAg}_x\text{Al}_{11-x}$  ternary phases to answer the following questions: (i) at what compositions (and valence electron concentrations) can this phase be obtained; (ii) how are Ag and Al atoms distributed among the various sites in the crystal structure; and (iii) what are the electronic structures and bonding characteristics in these phases and what can be rationalized from them.

### 5.3 Experimental

**Syntheses.**  $\text{EuAg}_x\text{Al}_{11-x}$  specimens were synthesized from the pure metals: Eu (rods, Ames Laboratory, 99.99%), Ag (slugs, Alfa Aesar, 99.99%), and Al (foil, Tenneco). Both our previous study<sup>15</sup> and Denysyuk's report<sup>10a</sup> showed that a single phase with the  $\text{BaCd}_{11}$ -type structure can be obtained at the composition around  $\text{EuAg}_5\text{Al}_6$ . To investigate the homogeneity width for these  $\text{BaCd}_{11}$ -type phases, the metals were mixed with a series of Eu:Ag:Al molar ratios varying from 1:3:8 to 1:8:3. This composition range, shown later by crystallographic results, is sufficiently large to cover the homogeneity width. *Ca.* 0.5 g of each mixture was arc-melted under a high purity argon atmosphere. To ensure thorough reaction, every sample was turned over and re-melted 5 times. The weight loss during melting is between *ca.* 0.3 and 1.0 wt%. The products are all stable towards rapid decomposition in air and water, but react with 40 wt% nitric acid. After reaction, every product was broken into halves: one-half was submitted directly to characterization; the other half was sealed under argon in a tantalum tube, which was then sealed in a silica jacket under vacuum and annealed at 500°C for 40 days in a tube furnace before subsequent characterization.

**X-Ray Crystallography.** Powder X-ray diffraction (XRD) was used to identify the phases in each sample. It was carried out on a Huber Imaging Plate Guinier Camera G670 using monochromatized  $\text{Cu } K\alpha_1$  radiation ( $\lambda = 1.54059 \text{ \AA}$ ). The exposure time was 1 hour and the step size was  $0.005^\circ$ . Full pattern decomposition was performed with the Le Bail technique<sup>16</sup> using the software *LHPM-Rietica*.<sup>17</sup>

For single crystal XRD, small crystals were selected from crushed samples and glued on the tips of capillaries with epoxy. Diffraction was carried out at room temperature on a Bruker *SMART* Apex CCD diffractometer equipped with  $\text{Mo } K\alpha$  radiation ( $\lambda = 0.71073 \text{ \AA}$ ). The data collection was controlled with the *SMART* program.<sup>18</sup> Three sets of frames were collected at  $\varphi = 0^\circ, 120^\circ, \text{ and } 240^\circ$ . For every set,  $\omega$  was scanned from  $332.0^\circ$  to  $150.5^\circ$  with the step size of  $0.3^\circ$ . The exposure time for every frame was 10 s. Data integrations, cell refinements, and absorption corrections were done with the *SAINTE*+<sup>19</sup> and *SADABS* programs.<sup>20</sup> Using the *SHELXTL* package,<sup>21</sup> the crystal structures were

then solved using direct methods and refined by full-matrix least-squares on  $F^2$ . More details about the refinement are listed in Table 2.

**Magnetometry.** A small piece (5.1 mg) was taken from the product with the loading composition  $\text{EuAg}_5\text{Al}_6$ , which is characterized as a  $\text{BaCd}_{11}$ -type “single phase” according to powder XRD. The temperature dependency of its magnetic susceptibility was measured on a Quantum Design MPMS XL Superconducting Quantum Interference Device (SQUID) magnetometer. The magnetic field was fixed at 1 kOe and the temperature was scanned from 5 K to 300 K.

**Electronic Structure Calculations.** To rationalize site preferences for Ag and Al atoms, a Mulliken population analysis was carried out using Extended Hückel calculations.<sup>22</sup> The basis set consisted of single- $\zeta$  Slater orbitals for Al  $3s$  ( $H_{3s-3s} = -11.84$  eV,  $\zeta_{3s} = 1.51$ ) and  $3p$  ( $H_{3p-3p} = -5.99$  eV,  $\zeta_{3p} = 1.17$ ), Ag  $5s$  ( $H_{5s-5s} = -7.58$  eV,  $\zeta_{5s} = 1.82$ ) and  $5p$  ( $H_{5p-5p} = -3.97$  eV,  $\zeta_{5p} = 1.27$ ), and Eu  $6s$  ( $H_{6s-6s} = -5.67$  eV,  $\zeta_{6s} = 1.58$ ).<sup>23</sup> Integrated populations were obtained by using a special points set of 64  $k$ -points in the irreducible wedge of the tetragonal Brillouin zone. Ag  $4d$  and Eu  $4f$  orbitals were treated as core orbitals and not included in the basis sets. These treatments were justified later by further experimental and theoretical investigations: (i) subsequent first principles, electronic structure calculations show that the Ag  $4d$  bands are filled and located *ca.* 5 eV below the Fermi level; and (ii) both unit cell dimensional analysis and magnetometry indicates that Eu behaves divalent with a half-filled, localized set of  $4f$  orbitals. More details are given in the section on Mulliken Populations and Site Preferences.

First principles electronic structure calculations were performed with the Stuttgart Tight-Binding, Linear-Muffin-Tin Orbital program using the Atomic Sphere Approximation (TB-LMTO-ASA).<sup>24</sup> The calculation models were established according to the single crystal XRD results listed in Tables 2 and 3. Further details of the models are given in the section of Calculation Models and Coloring Problem. The von Barth-Hedin local density approximation<sup>25</sup> was employed for the treatment of exchange and correlation energy. The basis set included the  $6s$ ,  $6p$  (downfolded<sup>26</sup>), and  $5d$  states of Eu; the  $5s$ ,  $5p$ , and  $4d$  states of Ag; and the  $3s$ ,  $3p$ , and  $3d$  (downfolded) states of Al. Again, the half-filled  $4f$  states of Eu were treated as core states. The Wigner-Seitz radii of the atomic spheres were 2.32 Å for Eu and 1.53 Å for both Ag and Al, which filled the unit cell with a 7.76 % overlap without introducing any empty spheres. 360 ( $6 \times 6 \times 10$ )  $k$ -points in the irreducible wedge of the tetragonal Brillouin zone were used for integration. The density of states (DOS) and various crystal orbital Hamiltonian populations (COHP)<sup>27</sup> were calculated and plotted.

## 5.4 Results and Discussions

**X-ray Crystallography.** By scanning the loaded composition in  $\text{EuAg}_x\text{Al}_{11-x}$  from “ $\text{EuAg}_3\text{Al}_8$ ” to “ $\text{EuAg}_8\text{Al}_3$ ,” we obtained seven phases, which are listed in Table 1. The powder XRD patterns of the as-cast and annealed samples for “ $\text{EuAg}_5\text{Al}_6$ ” and “ $\text{EuAg}_6\text{Al}_5$ ” are shown in Figure 1 (XRD patterns for samples having  $x = 3, 4, 7,$  and  $8$  are presented in the Supporting Information). This range in composition for  $\text{EuAg}_x\text{Al}_{11-x}$  indicated competition between two different, iso-compositional structures, *i.e.*, the  $\text{BaHg}_{11}$ - vs.  $\text{BaCd}_{11}$ -types, and the  $\text{Th}_2\text{Ni}_{17}$ - vs.  $\text{Th}_2\text{Zn}_{17}$ -types. These structure types occur frequently among the polar intermetallic compounds involving rare earth, late transition metals, and elements from group 13 or 14. Further investigations into these competitive structures will deepen our understanding into the composition-structure relationship of polar intermetallic compounds, which will be the topic of a subsequent paper.

**Table 1.** The phases formed in the arc melted samples.

Loading Composition	$\text{Eu}(\text{Ag},\text{Al})_{11}$ ( $\text{BaCd}_{11}$ )	$\text{Eu}(\text{Ag},\text{Al})_{11}$ ( $\text{BaHg}_{11}$ )	$\text{Eu}_2(\text{Ag},\text{Al})_{17}$ ( $\text{Th}_2\text{Ni}_{17}$ )	$\text{Eu}_2(\text{Ag},\text{Al})_{17}$ ( $\text{Th}_2\text{Zn}_{17}$ )	$\text{Eu}(\text{Ag},\text{Al})_4$ ( $\text{BaAl}_4$ )	$(\text{Ag},\text{Al})_1$ ( <i>fcc</i> )
$\text{EuAg}_3\text{Al}_8$	+	+	+		+	+
$\text{EuAg}_4\text{Al}_7$	+	+			+	+
$\text{EuAg}_5\text{Al}_6$	+					
$\text{EuAg}_6\text{Al}_5$	+					
$\text{EuAg}_7\text{Al}_4$	+			+		+
$\text{EuAg}_8\text{Al}_3$	+			+		+

The  $\text{BaCd}_{11}$ -type phases occurred over the entire range of  $x = 3-8$  in  $\text{EuAg}_x\text{Al}_{11-x}$ , but the “single phase” was only obtained with the arc-melted  $\text{EuAg}_5\text{Al}_6$  and  $\text{EuAg}_6\text{Al}_5$  specimens, in which no other phases were detected by powder XRD (Figure 1). These “single phases” remained stable during annealing: for  $\text{EuAg}_5\text{Al}_6$ , only one small additional peak (at  $2\theta = 34.3^\circ$ , from a  $\text{BaHg}_{11}$ -type structure) appears after annealing (shown with the black arrow in Figure 1); and for  $\text{EuAg}_6\text{Al}_5$ , there is no perceptible change in the powder XRD pattern. This reveals that the phase width of the  $\text{BaCd}_{11}$ -type structure in  $\text{EuAg}_x\text{Al}_{11-x}$  is very narrow, approximately  $\text{EuAg}_5\text{Al}_6$ - $\text{EuAg}_6\text{Al}_5$ .

Crystals were selected from both as-cast and annealed portions of these two “single phase” samples for single crystal XRD. The results of refinement are included in both Table 2 (the  $\text{EuAg}_5\text{Al}_6$  sample) and Table S1 (the  $\text{EuAg}_6\text{Al}_5$  sample, Supporting Information), from which we can see that the refined

compositions are all close to the loading compositions. The atomic coordinates and isotropic thermal parameters of  $\text{EuAg}_{5.07(4)}\text{Al}_{5.93(4)}$  are listed in Table 3. Selected interatomic distances are tabulated in Table 4. Just like in the Ag-Al binary phases and other *RE*(rare earth)-Ag-Al ternaries,<sup>10</sup> site sharing occurs between Ag and Al atoms, which may be attributed to the fact that Ag and Al have similar atomic sizes and electronegativities. Among the three shared sites in the asymmetric unit of  $\text{EuAg}_{5.07(4)}\text{Al}_{5.93(4)}$ , the occupancies of Ag and Al are close to each other on the *8d* and *32i* sites, but differ significantly on the *4b* site, which evidently prefers Ag to Al. These various sites for Ag and Al atoms also show significant differences with respect to interatomic distances: Ag/Al-Ag/Al contacts involving the *4b* sites are longer (*ca.* 2.90-3.00 Å), whereas those involving the *8d* or *32i* sites are significantly shorter (ranging from *ca.* 2.65-2.82 Å). These observed distances compare well with the shortest interatomic distances characterized in the binary Ag-Al close-packed alloys by X-ray powder diffraction, distances which range from *ca.* 2.80-3.03 Å.<sup>28</sup>

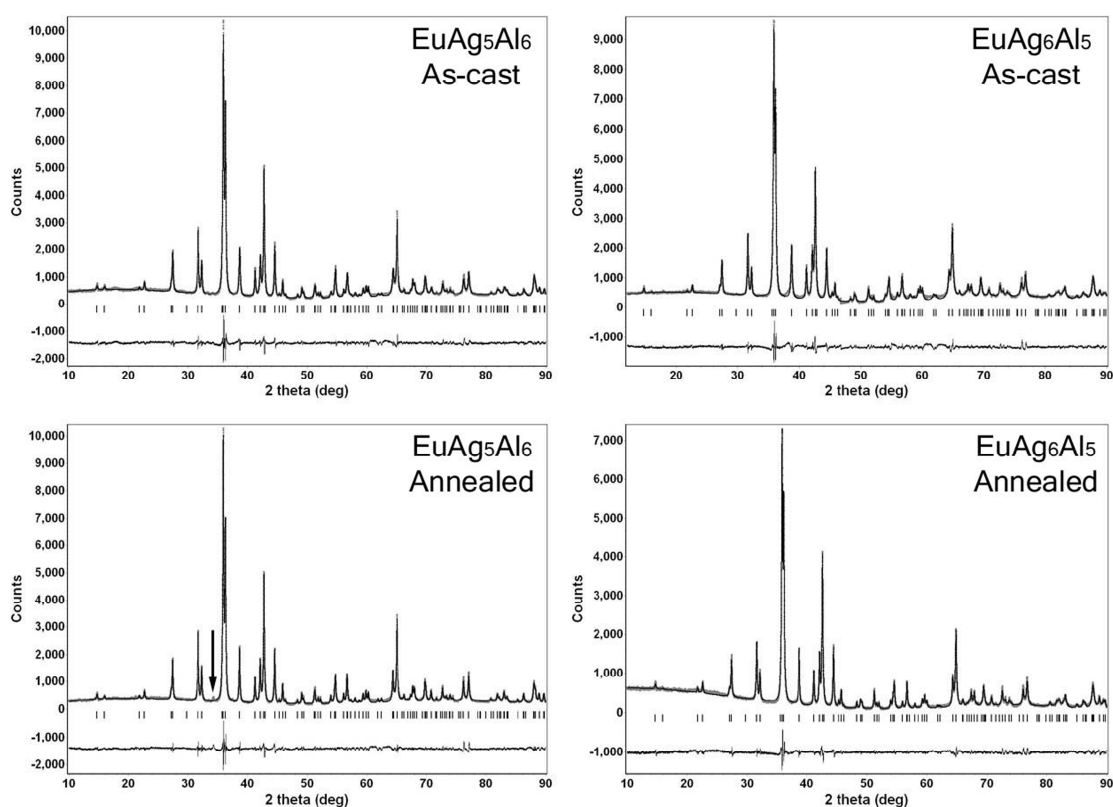


**Figure 1.** The powder patterns of the “single-phase”  $\text{BaCd}_{11}$ -type samples:  $\text{EuAg}_5\text{Al}_6$  and  $\text{EuAg}_6\text{Al}_5$ . The small peak indicated with a black arrow in  $\text{EuAg}_5\text{Al}_6$  (Annealed) is from the  $\text{BaHg}_{11}$ -type structure.

**Table 2.** The crystallographic data and selected refinement parameters of the crystals selected from  $\text{EuAg}_5\text{Al}_6$  samples (both as-cast and annealed).

	As-cast	Annealed
Empirical formula	$\text{EuAg}_{5.07(4)}\text{Al}_{5.93(4)}$	$\text{EuAg}_{4.96(4)}\text{Al}_{6.04(4)}$
Space group	$I4_1/amd$ (No. 141)	$I4_1/amd$ (No. 141)
Lattice parameters	$a = 11.0613(10) \text{ \AA}$ $c = 7.1302(9) \text{ \AA}$	$a = 11.0549(17) \text{ \AA}$ $c = 7.1301(15) \text{ \AA}$
Volume	$872.40(16) \text{ \AA}^3$	$871.4(3) \text{ \AA}^3$
Z	4	4
$\theta$ range	$3.40^\circ$ - $28.22^\circ$	$3.40^\circ$ - $28.23^\circ$
Index ranges	$-14 \leq h \leq 14$ $-14 \leq k \leq 14$ $-9 \leq l \leq 9$	$-14 \leq h \leq 14$ $-11 \leq k \leq 14$ $-6 \leq l \leq 9$
Reflections collected	3504	2352
Independent reflections	297 ( $R_{\text{int}} = 0.0406$ )	298 ( $R_{\text{int}} = 0.0720$ )
Goodness-of-fit on $F^2$	1.140	1.020
Final R indices ( $I > 2\sigma(I)$ )	$R1 = 0.0173$ ; $wR2 = 0.0350$	$R1 = 0.0265$ ; $wR2 = 0.0427$
R indices (all data)	$R1 = 0.0206$ ; $wR2 = 0.0356$	$R1 = 0.0396$ ; $wR2 = 0.0468$
Largest diff. peak/hole	$0.745/-0.918 \text{ e}^-/\text{\AA}^3$	$1.052/-1.099 \text{ e}^-/\text{\AA}^3$

**Table 3.** The atomic coordinates and isotropic displacement parameters of  $\text{EuAg}_{5.07(4)}\text{Al}_{5.93(4)}$ .

Atom	Wyck.	x	y	z	SOF	$U_{\text{iso}}/\text{\AA}^2$
Eu	$4a$	1/2	1/4	5/8	1	0.010(1)
Ag/Al1	$4b$	1/2	1/4	1/8	0.873/0.127(6)	0.015(1)
Ag/Al2	$8d$	1/2	1/2	0	0.458/0.542(4)	0.015(1)
Ag/Al3	$32i$	0.3802(1)	0.4558(1)	0.3260(1)	0.410/0.590(3)	0.014(1)

The  $\text{BaCd}_{11}$ -type structure, which has been described by Häussermann *et al*<sup>14</sup> and Pearson<sup>29</sup>, is shown in Figure 2. The Ag/Al2 ( $8d$ ) and Ag/Al3 ( $32i$ ) sites form strands of edge-sharing tetrahedron stars (Figure 2a), which are aligned along the crystallographic  $c$ -axis and interconnected with each other via the  $8d$  sites. The channels confined by these strands are filled by Eu ( $4a$ ) and Ag/Al1 ( $4b$ ) sites (Figure 2b). The coordination environment of the Eu site, as shown in Figure 2c, consists of 22 Ag/Al atoms. Two Ag/Al1 atoms are located just above and below Eu along the  $c$ -axis. The remaining 20 atoms form three rings: one in the middle is an 8-membered ring composed of Ag/Al3 atoms, which

is “sandwiched” by two 6-membered rings, each composed of two Ag/Al2 atoms and four Ag/Al3 atoms. The coordination environment of the Ag/Al1 (*4b*) site is also shown in Figure 2d. Ag/Al1 lies between the two 6-membered rings mentioned above, which are capped by Eu atoms along the *c*-axis.

**Table 4.** The selected interatomic distances of  $\text{EuAg}_{5.07(4)}\text{Al}_{5.93(4)}$ .

Atom Pair		Distances /Å
Eu —	Ag/Al1 (×2)	3.5651(5)
	Ag/Al2 (×4)	3.8466(3)
	Ag/Al3 (×8)	3.3886(6)
	(×8)	3.5305(6)
Ag/Al1 —	Ag/Al2 (×4)	2.9054(2)
	Ag/Al3 (×8)	2.9990(6)
Ag/Al2 —	Ag/Al3 (×4)	2.7199(6)
	(×4)	2.7483(6)
Ag/Al3 —	Ag/Al3 (×1)	2.6495(11)
	(×1)	2.6661(11)
	(×2)	2.7938(6)
	(×1)	2.8161(11)

**Magnetometry.** The temperature dependencies of the magnetic susceptibility ( $\chi$ ) and the reciprocal susceptibility ( $1/\chi$ ) of the  $\text{EuAg}_5\text{Al}_6$  sample are plotted in Figure 3. It shows that this phase is paramagnetic from 5-300 K and follows a Curie-Weiss behavior. Fitting the  $1/\chi$  vs.  $T$  curve according to the Van Vleck equation gave the effective moment  $\mu_{\text{eff}} = 8.01 \mu_{\text{B}}$ . This value is comparable with the effective moments reported for  $\text{EuPtIn}$  ( $8.0 \mu_{\text{B}}$ )<sup>30</sup> and  $\text{EuAgSn}$  ( $7.97 \mu_{\text{B}}$ )<sup>31</sup>. It is close to the theoretical value of free  $\text{Eu}^{2+}$  ( $7.94 \mu_{\text{B}}$ ). So it can be concluded that Eu is divalent in these phases.

**Comparison with other  $\text{REAg}_x\text{Al}_{11-x}$ .** Besides Eu, the  $\text{BaCd}_{11}$ -type structure was also reported for La, Ce, and Pr systems.<sup>10</sup> The compositions, lattice parameters, and unit cell volumes of these isostructural phases are compared in Table 5. The unit cell volume decreases as the *RE* atom varies from La to Ce to Pr, in accordance with the decreasing sizes of the *RE* atoms, but abruptly increases at Eu. This confirms that Eu is divalent in the  $\text{BaCd}_{11}$ -type phases and the other *RE* atoms are trivalent.

A comparison of their compositions shows that the Eu phases have higher Al contents than the trivalent La, Ce, and Pr counterparts. This compositional discrepancy, however, leads to a consistency in the valence electron concentration (*vec*), which is calculated with the total valence electron count

divided by the number of electronegative metal atoms, e.g. for  $\text{EuAg}_6\text{Al}_5$ ,  $vec = 23/11 \approx 2.09 e^-$  per atom (Ag  $4d$  electrons are considered as core electrons, and ignored for electron counting purposes).

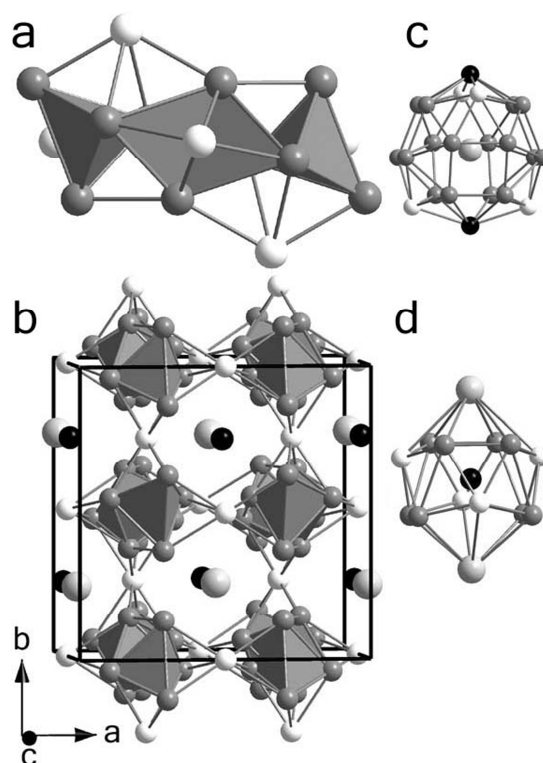


**Figure 2.** The crystal structure of  $\text{BaCd}_{11}$ -type  $\text{EuAg}_x\text{Al}_{11-x}$ . (a) Tetrahedron star strand; (b) Unit cell projected along the  $c$ -axis; (c) The coordination environment of Eu; (d) The coordination environment of the Ag/Al1 site. Eu(4a): large gray; Ag/Al1(4b): small black; Ag/Al2(8d): small white; Ag/Al3(32i): small gray.

The calculated  $vec$  values for the observed phases are also listed in Table 5, all of which fall between 2.1 and 2.3  $e^-$  per atom, which is in agreement with the previously reported 2.1 electrons per atom from Hückel calculation,<sup>14</sup> and yet confirms that this narrow  $vec$  range specifically stabilizes the  $\text{BaCd}_{11}$ -type structure for the  $RE\text{-Ag-Al}$  system. Similar to  $RE\text{-Zn}$  systems,<sup>13</sup> for  $RE\text{-Ag-Al}$ , the atomic sizes of the  $RE$  atoms significantly affect the stability of the  $\text{BaCd}_{11}$ -structure, as it cannot be obtained with smaller and later  $RE$  atoms except for Yb (again, due to its divalency).<sup>10</sup>



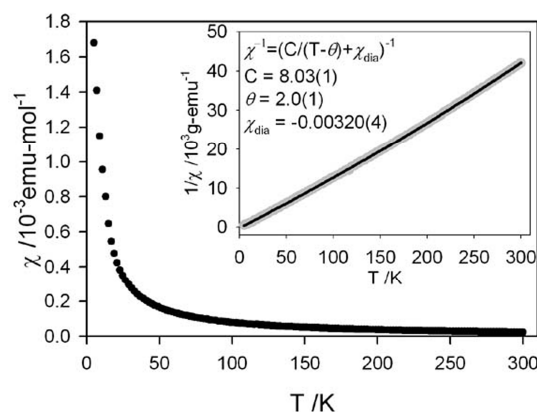


**Figure 3.** The temperature dependencies of the magnetic susceptibility and the reciprocal susceptibility of BaCd<sub>11</sub>-type EuAg<sub>x</sub>Al<sub>11-x</sub>.

**Table 5.** The comparison in unit cell size and *vec* between BaCd<sub>11</sub>-type RE-Ag-Al ternaries.

Composition	Lattice Parameter		V <sub>Unit Cell</sub> / Å <sup>3</sup>	<i>vec</i>	Ref.
	<i>a</i> / Å	<i>c</i> / Å			
LaAg <sub>6.05</sub> Al <sub>4.95</sub> <sup>a</sup>	11.065(2)	7.123(2)	872.1(2)	2.17	10d
CeAg <sub>5.72-6.38</sub> Al <sub>5.28-4.62</sub> <sup>b</sup>	11.0466(3)	7.1101(5)	867.63(6)	2.11-2.24	10a,c
PrAg <sub>5.9(1)</sub> Al <sub>5.1(1)</sub>	11.0262(2)	7.0979(2)	862.94(2)	2.20	10g
EuAg <sub>4.96(4)</sub> Al <sub>6.04(4)</sub>	11.0549(17)	7.1301(15)	871.4(3)	2.28	-
EuAg <sub>5.07(4)</sub> Al <sub>5.93(4)</sub>	11.0613(10)	7.1302(9)	872.4(2)	2.27	-
EuAg <sub>5.80(7)</sub> Al <sub>5.20(7)</sub>	11.0907(11)	7.1174(10)	875.5(2)	2.13	-
EuAg <sub>6.02(5)</sub> Al <sub>4.98(5)</sub>	11.102(3)	7.125(2)	878.3(4)	2.09	-

<sup>a</sup> The uncertainties of composition were not reported.

<sup>b</sup> The lattice parameters correspond to the composition of CeAg<sub>5.4(3)</sub>Al<sub>4.6(3)</sub>.

**Mulliken Population and Site Preferences.** Site preferences for different elements in a chemical structure can be rationalized through a Mulliken population analysis upon *uniform reference frames*.<sup>32,33</sup> Two *uniform reference frames*, i.e., EuAg<sub>11</sub> and EuAl<sub>11</sub>, were established according to the crystallographic results. All Ag/Al mixed sites were assigned to Ag atoms in EuAg<sub>11</sub> and to Al in EuAl<sub>11</sub>. Mulliken populations were calculated at 24 valence electrons per formula unit (*vec* = 24/11 ≈ 2.2 e<sup>-</sup> per atom) and tabulated in Table 6. These results show that among the *4b*, *8d*, and *32i* sites in the BaCd<sub>11</sub>-type structure, the *4b* site has the lowest Mulliken population in both *uniform reference frames*. Therefore, it is energetically favorable to put the atom with higher-energy valence orbitals on this *4b* site, which can explain why the *4b* site prefers Ag atoms to Al atoms.

**Computational Models and The Coloring Problem.** To build the computational models with compositions close to  $\text{EuAg}_5\text{Al}_6$  and  $\text{EuAg}_6\text{Al}_5$  and to include the site sharing by Ag and Al atoms among the crystallographic sites as obtained from the refinements of single crystal XRD experiments, symmetry reduction is required. For example, to build a model with the composition  $\text{EuAg}_6\text{Al}_5$ , we can reduce the tetragonal symmetry to triclinic (space group  $PI$ ) so that the  $4b$ ,  $8d$ , and  $32i$  sites can be broken into 44 independent  $1a$  sites, 24 of which can be assigned to Ag and the other 20 to Al. The remaining challenge here is the “coloring problem,”<sup>33</sup>, *i.e.*, there are multiple ways to assign the mixed sites to Ag and Al atoms. Four randomly chosen coloring schemes, numbered as Models **1-4** and differentiated by their coordination environments at Eu, are illustrated in Figures 4a-4d, all of which give the same composition,  $\text{EuAg}_6\text{Al}_5$ . To build computational models for chemical bonding analysis via DOS and COHP curves, the appropriate coloring schemes must first be determined.

**Table 6.** The Mulliken populations calculated with *uniform reference frames* at 24 valence electrons per f.u.

	EuAg <sub>11</sub>		EuAl <sub>11</sub>	
<i>4a</i>	Eu	0.573	Eu	0.073
<i>4b</i>	Ag1	2.104	Al1	2.083
<i>8d</i>	Ag2	2.112	Al2	2.252
<i>32i</i>	Ag3	2.138	Al3	2.168

The coloring schemes which give the lowest theoretically determined total energies are the most desirable models to compare against experimental results. To locate such coloring schemes, first principles calculations were performed at first upon Models **1-4** using TB-LMTO-ASA. These results are sorted in the first part of Table 7 according to their total energies. Tabulated together are the numbers of heteroatomic (Ag-Al) contacts located in the first coordination environments among these models. It is evident that the more Ag-Al connections, especially shorter Ag-Al contacts, the lower the total energy is. This finding is noteworthy because, by contrast, when the molar ratio is around 1:1, Ag and Al atoms tend to segregate in the binary system into an *hcp*-type  $\delta$ -phase (22.85-41.93 atomic percent Al) and an *fcc*-phase (*ca.* 75.0-100 atomic percent Al).<sup>34</sup>

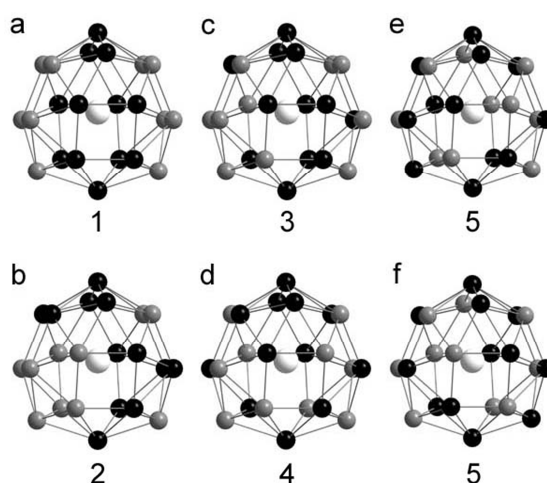


**Figure 4.** The coordination environments of the Eu atoms in the 5 calculation models. All models have the same composition,  $\text{EuAg}_6\text{Al}_5$ . Models **1-4** were randomly established. Model **5** was established by maximizing the number of Ag-Al contacts.

**Table 7.** The total energies and the number of Ag-Al contacts of calculation models.

Model	$E_{\text{total}}/\text{eV}$	Ag-Al Contacts per Unit Cell		
		$< 2.70 \text{ \AA}$	$< 2.80 \text{ \AA}$	$< 3.00 \text{ \AA}$
<b>1</b>	6.923	0	64	104
<b>2</b>	5.899	16	64	88
<b>3</b>	4.879	16	72	104
<b>4</b>	2.909	32	64	104
<b>5</b>	0	32	96	128

According to the results of the randomly structured Models **1-4**, the coloring schemes with the lowest total energy should be the ones with the maximal number of Ag-Al contacts. A straightforward way to find them is to generate all coloring schemes and count their Ag-Al contacts. This was realized with the help of a short program, the details of which are provided in the Supporting Information. By fixing the composition at  $\text{EuAg}_6\text{Al}_5$ , the maximal number of Ag-Al contacts was found within one specific coloring scheme, numbered as Model **5**, in which one-half of the Eu atoms are coordinated as shown in Figure 4e and the other half as Figure 4f. The number of Ag-Al connections in Model **5** is listed in the last row of Table 7, together with the calculated total energy, which is, as expected, lower than the total energies of the randomly chosen Models **1-4**. Therefore, Model **5**, which has the maximal number of Ag-Al contacts, is indeed energetically favorable. Moreover, by comparing

Figure 4 and Figure 2c, it can be seen that the original  $4b$  site in Model 5 is assigned completely to Ag (the site occupancy Ag:Al = 1:0), and the original  $8d$  and  $32i$  sites are both half-filled by Ag atoms and Al atoms (Ag:Al = 0.5:0.5). This is very close to the experimentally observed site occupancies listed in Table 3. All of these results reveal that Model 5 is a good simulation of the experimental structure and, thus, an appropriate computational model for further chemical bonding analysis.

**Density of States and Bonding Characteristics.** DOS and COHP curves were calculated for Model 5 and plotted in Figure 5. The overall shape of the DOS curve follows a parabola, which is the feature of the free-electron DOS, superimposed with the large peak of Ag  $4d$  bands at *ca.*  $-8$  to  $-3$  eV as well as a state-deficient region, *i.e.*, a pseudogap, at *ca.*  $-1$  to  $+2$  eV. The Fermi levels corresponding to *vec* values 2.1-2.3  $e^-$  per atom fall into this pseudogap.

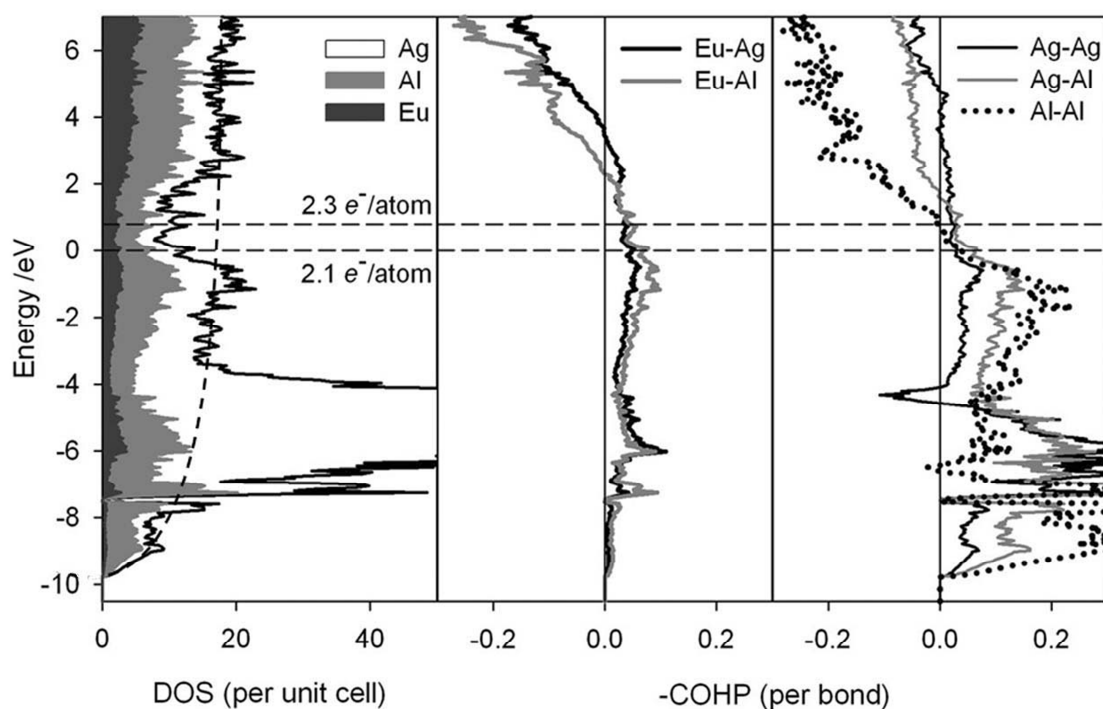


**Figure 5.** The DOS and COHP curves calculated from Model 5. The dashed parabolic line shows the DOS curve of free electrons.

The COHP curves reveal that strong bonding interactions exist between Ag/Al-Ag/Al sites (integrated COHP values at *vec* = 2.1  $e^-$  per atom are: Ag-Ag, 0.83; Ag-Al, 1.27; Al-Al, 1.42), but that the Eu-Ag/Al orbital interactions are weakly bonding (integrated COHP values at *vec* = 2.1  $e^-$  per atom are:

Eu-Ag, 0.30; Eu-Al, 0.38). As shown in the far right of Figure 5, the Fermi levels for the  $vec = 2.1$ - $2.3 e^-$  per atom are located very near the bonding-antibonding crossover for the Al-Al interactions, just below the bonding-antibonding crossover for the Ag-Al interactions and within the nearly nonbonding region for the Ag-Ag COHP curve. Specifically, the upper limit of allowed  $vec$  values, *ca.*  $2.3 e^-$  per atom, is set by the homoatomic Al-Al contacts. So, the orbital interactions within the Ag/Al network are essentially optimized for the BaCd<sub>11</sub>-type phases. Any deviation in  $vec$  will destroy this bonding optimization and, thus, potentially destabilize the structure. This explains why the BaCd<sub>11</sub>-type structure is specifically stabilized in RE-Ag-Al ternaries at the  $vec$  of *ca.*  $2.1$ - $2.3 e^-$  per atom.

## 5.5 Conclusions

EuAg<sub>x</sub>Al<sub>11-x</sub> phases adopting the BaCd<sub>11</sub>-type structure were experimentally and theoretically investigated. Ag and Al atoms share the same sites within the structure, although not entirely in a statistical manner. The *4b* site prefers Ag to Al, which can be rationalized through a Mulliken population analysis with Extended Hückel calculations. First principles calculations with TB-LMTO-ASA approach revealed that Ag and Al tend to be distributed to maximize the number of heteroatomic contacts. A computational model to analyze chemical bonding factors was established accordingly. The computational results successfully explained why this BaCd<sub>11</sub>-type structure EuAg<sub>x</sub>Al<sub>11-x</sub> is stable only at  $vec = 2.1$ - $2.3 e^-$  per atom. Further questions under investigation include the competition between BaCd<sub>11</sub>-type and BaHg<sub>11</sub>-type structures in Eu-Ag-Al ternary system.

## 5.6 Acknowledgements:

This work is supported by NSF DMR 02-441092 and 06-05949. The authors thank Sumohan Misra and Prof. Vitalij K. Pecharsky for magnetization measurements.

**Supporting Information Available:** The powder XRD patterns of EuAg<sub>x</sub>Al<sub>11-x</sub> (when  $x = 3, 4, 7,$  and  $8$ ), the single crystal XRD results of “EuAg<sub>6</sub>Al<sub>5</sub>” samples, and the method of maximizing the number of Ag-Al contacts in EuAg<sub>6</sub>Al<sub>5</sub> (PDF). This information is available free of charge via the Internet at <http://pubs.acs.org>.

## 5.7 References

(1) Schäfer, H. *Annu. Rev. Mater. Sci.* **1985**, *5*, 1.

- (2) Häussermann, U.; Amerioun, S.; Eriksson, L.; Lee, C.-S.; Miller, G. J. *J. Am. Chem. Soc.* **2002**, *124*, 4371.
- (3) You, T.S.; Grin, Y.; Miller, G. J. *Inorg. Chem.* **2007**, *46*, 8801.
- (4) Hume-Rothery, W.; Raynor, G. V. *The Structure of Metals and Alloys*, 1st ed; London: The Inst. of Metals, 1936.
- (5) Schäfer, H.; Eisenmann, B.; Müller, W. *Angew. Chem. Int. Ed.* **1973**, *12* (9), 694.
- (6) Gschneidner Jr, K. A., Pecharsky, V. K., Tsokol, A. O. *Rep. Prog. Phys.* **2005**, *68*, 1479.
- (7) Curro, N. J., Caldwell, T., Bauer, E. D., Morales, L. A., Graf, M. J., Bang, Y., Balatsky, A. V., Thompson, J. D., Sarrao, J. L. *Nature* **2005**, *434*, 622.
- (8) Zürcher, F.; Nesper, R.; Hoffmann, S.; Fässler, T. F. *Z. Anorg. Allg. Chem.* **2001**, *627* (9), 2211.
- (9) Tobash, P. H.; Lins, D.; Bobev, S. *Chem. Mater.* **2005**, *17* (22), 5567.
- (10) (a) Denysyuk, O. V.; Stel'makhovych, B. M.; Kuz'ma, Yu. B. *J. Solid State Chem.* **1994**, *109*, 172. (b) Stel'makhovych, B. M.; Kuz'ma Yu. B. *Dopov. Akad. Nauk Ukr.* **1994**, *3*, 86. (c) Zhak, O. V.; Stel'makhovych, B. M.; Kuz'ma Yu. B. *Russ. Metall.* **1995**, *6*, 158. (d) Kuz'ma Yu. B.; Zhak, O. V.; Shkolyk, S. Yu. *Dopov. Akad. Nauk Ukr.* **1995**, *3*, 101. (e) Zhak, O. V.; Stel'makhovych, B. M.; Kuz'ma Yu. B. *J. Alloys Comp.* **1996**, *237*, 144. (f) Kuz'ma Yu. B.; Zhak, O. V. Sarapina O. S. *Russ. Metall.* **1997**, *2*, 166. (g) Zhak, O. V.; Kuz'ma Yu. B. *J. Alloys Comp.* **1999**, *291*, 175. (h) Stel'makhovych, B. M.; Gumenyuk T. M.; Kuz'ma Yu. B. *J. Alloys Comp.* **2000**, *298*, 164. (i) Gumeniuk, R. V.; Stel'makhovych, B. M.; Kuz'ma Yu. B. *J. Alloys Comp.* **2001**, *321*, 132. (j) Stel'makhovych, B. M.; Zhak, O. V.; Bilas, N. R.; Kuz'ma Yu. B. *J. Alloys Comp.* **2004**, *363*, 243. (k) Cordier, G.; Dörsam, G.; Kniep, R. *J. Magn. Magn. Mater.* **1988**, *76 & 77*, 653.
- (11) Sanderson, M. J., Baneziger, N. C. *Acta Cryst.* **1953**, *6*, 627.
- (12) Kal, S.; Stoyanov, E.; Groy, T. L.; Häussermann U. *Acta Cryst.* **2007**, *C63*, i96.
- (13) Iandelli A.; Palenzona, A. *J. Less-Common Metals* **1967**, *12*, 333.
- (14) Häussermann U.; Svensson C.; Lidin, S. *J. Am. Chem. Soc.* **1998**, *120*, 3867.

- (15) Nordell, K. J. Exploring Aluminum-Rich Intermetallics with Experiment and Theory. Ph.D. Thesis, Iowa State University, Ames, IA, 1997.
- (16) Le Bail, A.; Duroy, H.; Fourquet, J. L. *Mat. Res. Bull.* **1988**, *23*, 447.
- (17) Hunter, B. A.; Howard, C. J. *LHPM-Rietica*, version 1.71: Australian Nuclear Science and Technology Organization, Menai, Australia, 2000.
- (18) *SMART*, version 5.625; Bruker AXS Inc.: Madison, WI, 2001.
- (19) *SAINT+*, version 6.22; Bruker AXS Inc.: Madison, WI, 2001.
- (20) *SADABS*, version 2.03; Bruker AXS Inc.: Madison, WI, 2001.
- (21) *SHELXTL*, version 6.10; Bruker AXS Inc.: Madison, WI, 2000.
- (22) Hoffmann, R. *J. Chem. Phys.* **1963**, *39*(6), 1397.
- (23) Herman, A. *Modelling Simul. Mater. Sci. Eng.* **2004**, *12*, 21.
- (24) Jepsen, O.; Andersen O. K. *TB-LMTO*, version 47; Max-Planck-Institut für Festkörperforschung, Stuttgart, Germany, 2000.
- (25) von Barth, U.; Hedin, L. *J. Phys. C: Solid State Phys.* **1972**, *5*, 1629.
- (26) Lambrecht, W. R. L.; Andersen, O. K. *Phys. Rev. B* **1986**, *34*, 2439.
- (27) Dronskowski, R.; Blöchl, P. *J. Phys. Chem.* **1993**, *97*, 8617.
- (28) (a) Neumann, J. P.; Chang, Y. A. *Trans. Metall. Soc. AIME* **1968**, *242*, 700. (b) Pradhan, S. K.; De, M. *J. Appl. Crystallogr.* **1986**, *19*, 484.
- (29) Pearson W. B. *Z. Kristallogr.* **1980**, *152*, 23.
- (30) Müllmann, R.; Mosel, B. D.; Eckert, H.; Pöttgen, R. *J. Solid State Chem.* **1998**, *137*, 174.
- (31) Hossain, Z.; Nagarajan, R.; Etilé, M.; Godart, C.; Kappler, J. P.; Gupta, L. C.; Vijayaraghavan, R. *J. Magn. Magn. Mater.* **1995**, *150*, 223.
- (32) Gimarc, B. M. *J. Am. Chem. Soc.* **1983**, *105*, 1979.
- (33) Miller, G. J. *Eur. J. Inorg. Chem.* **1998**, 523.



(34) ASM Handbooks Online. <http://products.asminternational.org/hbk/index> (accessed Aug 2008).

## 5.8 Supporting Information

### Powder X-ray Diffraction Patterns of $\text{EuAg}_x\text{Al}_{11-x}$ .

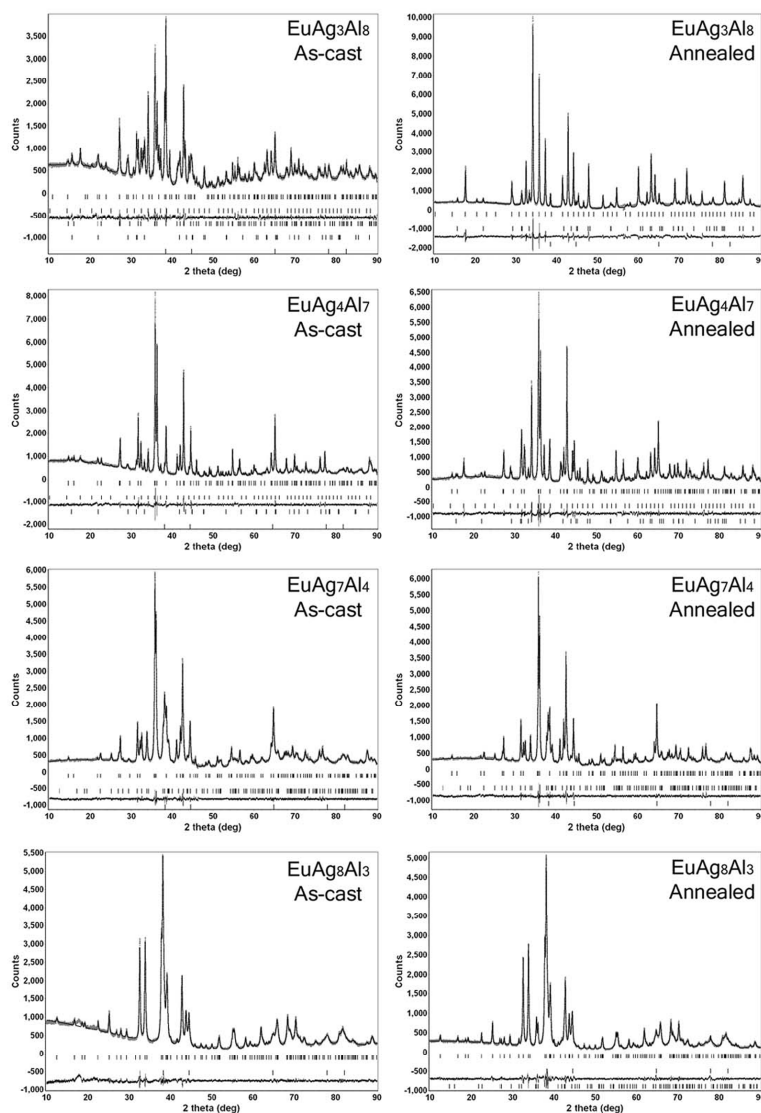


**Figure S1.** The powder XRD patterns of  $\text{EuAg}_x\text{Al}_{11-x}$  samples ( $x = 3, 4, 7, 8$ ).

The X-ray diffraction patterns for the  $\text{EuAg}_x\text{Al}_{11-x}$  series ( $3 \leq x \leq 8$ ) are shown in Figure S1. For  $\text{EuAg}_3\text{Al}_8$ , annealing has a significant effect. The as-cast sample is a mixture of 5 phases:  $\text{BaHg}_{11}$ -type,  $\text{BaCd}_{11}$ -type,  $\text{Th}_2\text{Ni}_{17}$ -type,  $\text{BaAl}_4$ -type, and *fcc* (an Ag-Al binary alloy). After annealing, only



the BaHg<sub>11</sub>-type and BaAl<sub>4</sub>-type phases can be detected by powder XRD and the former became the dominating phase. Further study is focusing on this BaHg<sub>11</sub>-type structure and the results will be included in a subsequent report. The as-cast EuAg<sub>4</sub>Al<sub>7</sub> sample consists of BaHg<sub>11</sub>-type, BaCd<sub>11</sub>-type, BaAl<sub>4</sub>-type, and *fcc* phases. Annealing increased the abundance of the BaHg<sub>11</sub>-type phase. The EuAg<sub>7</sub>Al<sub>4</sub> sample is composed with BaCd<sub>11</sub>-type, Th<sub>2</sub>Zn<sub>17</sub>-type, and *fcc* phases. Annealing did not perceptibly change the phases. The as-cast EuAg<sub>8</sub>Al<sub>3</sub> sample gives an almost pure Th<sub>2</sub>Zn<sub>17</sub>-type phase. The BaCd<sub>11</sub>-type phase shows its diffraction peaks after annealing.

### The Crystallographic Data of EuAg<sub>6</sub>Al<sub>5</sub> samples

**Table S1.** The crystallographic data and selected refinement parameters of the crystals selected from EuAg<sub>6</sub>Al<sub>5</sub> samples (both as-cast and annealed).

	As-cast	Annealed
Empirical formula	EuAg <sub>5.80(7)</sub> Al <sub>5.20(7)</sub>	EuAg <sub>6.02(5)</sub> Al <sub>4.98(5)</sub>
Space group	<i>I4<sub>1</sub>/amd</i> (No. 141)	<i>I4<sub>1</sub>/amd</i> (No. 141)
Lattice parameters	<i>a</i> = 11.0907(11) Å <i>c</i> = 7.1174(10) Å	<i>a</i> = 11.102(3) Å <i>c</i> = 7.125(2) Å
Volume	875.47(17) Å <sup>3</sup>	878.3(4) Å <sup>3</sup>
θ range	3.40°–28.30°	3.40°–28.26°
<i>Z</i>	4	4
Index ranges	–14 ≤ <i>h</i> ≤ 14 –14 ≤ <i>k</i> ≤ 14 –9 ≤ <i>l</i> ≤ 9	–14 ≤ <i>h</i> ≤ 14 –11 ≤ <i>k</i> ≤ 14 –9 ≤ <i>l</i> ≤ 9
Reflections collected	3556	3567
Independent reflections	306 ( <i>R</i> <sub>int</sub> = 0.0469)	306 ( <i>R</i> <sub>int</sub> = 0.0814)
Data/restraints/parameters	306/0/21	306/0/21
Goodness-of-fit on <i>F</i> <sup>2</sup>	1.237	1.058
Final <i>R</i> indices ( <i>I</i> > 2σ( <i>I</i> ))	<i>R</i> 1 = 0.0275; <i>wR</i> 2 = 0.0493	<i>R</i> 1 = 0.0295; <i>wR</i> 2 = 0.0490
<i>R</i> indices (all data)	<i>R</i> 1 = 0.0305; <i>wR</i> 2 = 0.0499	<i>R</i> 1 = 0.0423; <i>wR</i> 2 = 0.0529
Largest diff. peak/hole	1.167/–2.012 e <sup>–</sup> /Å <sup>3</sup>	1.710/–1.186 e <sup>–</sup> /Å <sup>3</sup>

### Maximizing the Number of Ag-Al Contacts in EuAg<sub>6</sub>Al<sub>5</sub>.

The coloring scheme with the maximal number of Ag-Al contacts was found by generating all possible schemes and counting their connections, which was performed by a short program written in the C language. The algorithm is as follows:

Instead of the body-centered complete unit cell (*Z* = 4; 44 Ag/Al atoms), the primitive cell (*Z* = 2; 22 Ag/Al atoms) was used for scheme generating and Ag-Al contacts counting to reduce the computation time. The primitive cell vectors are: (*a*, *b*, and *c* are the basic vectors of the complete unit cell)

$$a' = -0.5a + 0.5b + 0.5c;$$

$$b' = 0.5a - 0.5b + 0.5c;$$

$$c' = 0.5a + 0.5b - 0.5c.$$

The 22 sites for Ag and Al in the primitive cell are listed in Table S2. By reducing the symmetry to triclinic (space group *PI*), the 22 sites are all symmetrically independent.

For the composition of  $\text{EuAg}_6\text{Al}_5$ , 12 out of the 22 sites should be assigned to Ag and the other 10 to Al. The total number of possible coloring schemes is:

$$\frac{22!}{12!10!} = 646,646$$

**Table S2.** The 22 Ag/Al sites in the primitive cell and the 4 equivalent coloring schemes found by maximizing the number of Ag-Al contacts in  $\text{EuAg}_6\text{Al}_5$ .

Wyck. in Complete Cell	Fractional Coordinates in Complete Cell			Model 5	Model 6	Model 7	Model 8
	<i>x</i>	<i>y</i>	<i>z</i>				
<i>4b</i>	1/2	-1/4	-1/8	Ag	Ag	Ag	Ag
	-1/2	1/4	1/8	Ag	Ag	Ag	Ag
<i>8d</i>	0	0	1/2	Al	Al	Ag	Ag
	1/4	1/4	1/4	Ag	Al	Ag	Al
	-1/4	1/4	1/4	Al	Ag	Al	Ag
	1/2	0	0	Ag	Ag	Al	Al
<i>32i</i>	0.1198	0.0442	0.1740	Al	Ag	Al	Ag
	0.1198	-0.0442	-0.1740	Ag	Al	Ag	Al
	-0.1198	0.0442	0.1740	Ag	Al	Ag	Al
	-0.1198	-0.0442	-0.1740	Al	Ag	Al	Ag
	0.2942	0.1302	-0.0760	Al	Al	Ag	Ag
	0.2942	-0.1302	0.0760	Al	Al	Ag	Ag
	-0.2942	0.1302	-0.0760	Al	Al	Ag	Ag
	-0.2942	-0.1302	0.0760	Al	Al	Ag	Ag
	0.2058	0.1302	-0.4240	Ag	Ag	Al	Al
	-0.2058	-0.1302	0.4240	Ag	Ag	Al	Al
	0.3802	-0.0442	-0.3260	Ag	Al	Ag	Al
	-0.3802	0.0442	0.3260	Ag	Al	Ag	Al
	0.2942	-0.3698	0.0760	Ag	Ag	Al	Al
	-0.2942	0.3698	-0.0760	Ag	Ag	Al	Al
	-0.1198	0.5442	-0.1740	Al	Ag	Al	Ag
	0.1198	-0.5442	0.1740	Al	Ag	Al	Ag

All of these coloring schemes were generated and their Ag-Al contacts were counted. To count them, each of the 22 atoms in the primitive cell was tested against all the atoms in the same cell as well as

the 26 neighboring cells (6 face-sharing, 12 edge-sharing, and 8 vertex-sharing). A Ag-Al contact was counted as 1 if it was within the same cell, and as 0.5 if it was between two neighboring cells. Through this the number of Ag-Al connections per primitive cell was obtained.

The maximal number of Ag-Al contacts was found in 4 coloring schemes (Models 5-8, Table S2). They give the same coordination environment of Eu atoms (Figure 4e and 4f) and are thus structurally equivalent. So only one of them (Model 5) was taken for the first principal calculation.

### The C Codes to maximize Ag-Al contacts for the BaCd<sub>11</sub>-type EuAg<sub>6</sub>Al<sub>5</sub>

```
#include <stdio.h>
#include <math.h>
#include <stdlib.h>
/*This file will find the coloring scheme with the maximum Ag-Al contacts for BaCd11-type EuAg6Al5.*/
main()
{ float commfactor1=11.0613; /*lattice parameter a and b in Angstroms*/
  float commfactor2=7.1302; /*lattice parameter c in Angstroms*/
  float AXIS[3][3]={};
  float FRACTCOORD[22][3]={};
  float CARTCOORD[22][3]={};
  float FRACTVECT[27][3]={0,0,0},{1,0,0},{-1,0,0},{0,1,0},{0,-1,0},{0,0,1},{0,0,-1},{1,1,0},{1,-1,0},{-1,1,0},{-1,-1,0},{0,1,1},{0,-1,1},{0,1,-1},{0,-1,-1},{1,0,1},{1,0,-1},{-1,0,1},{-1,0,-1},{1,1,1},{1,1,-1},{1,-1,1},{1,-1,-1},{-1,1,1},{-1,1,-1},{-1,-1,1},{-1,-1,-1}}; /*vectors pointing to the central primitive cell and all 26 neighboring cells: 6 face-sharing, 8 vertex-sharing, and 12 edge sharing*/
  float CARTVECT[27][3]={};
  long m1,m2,m3,m4,p,n;
  int i,j,k,counter;
  int CONFIG[22]={};
  float distance;
  float NEIGHBORS[27][3]={};
  float bondnumber1=0;
  float bondnumber2=0;
  float bondnumber3=0;
  FILE *writeout,*readin;
```

```

float MAX[50][25]={};
double numberdone=0.0;
double completepercentage=0.0;
/*The three basic vectors of a primitive cell in the body-centered tetragonal lattice: (-0.5,0.5,0.5);(0.5,-
0.5,0.5);(0.5,0.5,-0.5). Here they are converted from fractional into cartesian.*/
AXIS[0][0]=-0.5*commfactor1; AXIS[0][1]=0.5*commfactor1; AXIS[0][2]=0.5*commfactor2;
AXIS[1][0]=0.5*commfactor1; AXIS[1][1]=-0.5*commfactor1; AXIS[1][2]=0.5*commfactor2;
AXIS[2][0]=0.5*commfactor1; AXIS[2][1]=0.5*commfactor1; AXIS[2][2]=-0.5*commfactor2;
/*Read the fractional coordinates. The input file "BaCd11_Reduced.txt" contains the fractional coordinates of
all 22 atoms in the primitive cell.*/
readin=fopen("allsites.txt","r");
for (i=0;i<22;i++)
  { for (j=0;j<3;j++)
    { fscanf(readin,"%f\t",&FRACTCOORD[i][j]);}
    fscanf(readin,"\n");
  }
fclose(readin);
/*Converting fractional coordinates into cartesian coordinates.*/
for (i=0;i<22;i++)
  { CARTCOORD[i][0]=FRACTCOORD[i][0]*commfactor1;
    CARTCOORD[i][1]=FRACTCOORD[i][1]*commfactor1;
    CARTCOORD[i][2]=FRACTCOORD[i][2]*commfactor2;
  }
/*Converting the lattice vectors pointing the central and all 26 neighboring cells from fractional into cartesian
vectors.*/
for (i=0;i<27;i++)
  { for (j=0;j<3;j++)
    { CARTVECT[i][j]=FRACTVECT[i][0]*AXIS[0][j]+FRACTVECT[i][1]*AXIS[1][j]+FRACTVECT[i][2]*AXIS[2][j];}
  }
/*Generate coloring schemes and count the number of heteroatomic bonds. The method we adopted here
can be described briefly as following.*/
/*There are 22 atomic positions. We use 1 to represent Ag and 0 to present Al.*/
/*To generate all schemes with 12 1 and 10 0, we just need to scan the binary numbers between
0000000000111111111111 and 1111111111110000000000.*/

```

```

/*All numbers with 12 1 and 10 0 will be selected and counted for their heteroatomic contacts.*/
m1=0; /*m1 is 11111111111111111111 (22 1) in binary.*/
for (i=0;i<22;i++)
{ n=1;
  for (j=1;j<=i;j++)
    { n=n*2;}
  m1=m1+n;
}
m2=0; /*m2 is 00000000001111111111 (12 1) in binary.*/
for (i=0;i<12;i++)
{ n=1;
  for (j=1;j<=i;j++)
    { n=n*2;}
  m2=m2+n;
}
m3=0; /*m3 is 00000000000111111111 (10 1) in binary.*/
for (i=0;i<10;i++)
{ n=1;
  for (j=1;j<=i;j++)
    { n=n*2;}
  m3=m3+n;
}
m4=m1-m3; /*m4 is 11111111111111111111 - 00000000000111111111 = 11111111111000000000
(12 1).*/
for (n=m2;n<=m4;n++)
{ for (i=0;i<22;i++)
  { CONFIG[i]=0;}
  i=0;
  p=n;
  while (p>=1) /*converting digital to binary.*/
  { CONFIG[i]=p%2;
    p=p/2;
    i++;
  }
}

```

```

counter=0;
for (i=0;i<22;i++) /*counting number of 1.*/
    { if (CONFIG[i]==1)
      { counter=counter+1;}
    }
if (counter==12) /*all numbers (schemes) with 12 1 are selected.*/
    { bondnumber1=0;
      bondnumber2=0;
      bondnumber3=0;
      for (i=0;i<22;i++)
          { for (j=0;j<22;j++)
              { if ((CONFIG[i]-CONFIG[j])!=0) /*Heteroatomic contacts are selected - between 1 and 0, not
1 and 1, or 0 and 0.*/
                  { for (k=0;k<27;k++)
                      { NEIGHBORS[k][0]=CARTCOORD[j][0]+CARTVECT[k][0];
                        NEIGHBORS[k][1]=CARTCOORD[j][1]+CARTVECT[k][1];
                        NEIGHBORS[k][2]=CARTCOORD[j][2]+CARTVECT[k][2];
                      }
                      for (k=0;k<27;k++) /*Heteroatomic contacts counting is running through central and all
26 neighboring cells.*/
                          { distance=sqrt((CARTCOORD[i][0]-NEIGHBORS[k][0])*(CARTCOORD[i][0]-
NEIGHBORS[k][0])+(CARTCOORD[i][1]-NEIGHBORS[k][1])*(CARTCOORD[i][1]-
NEIGHBORS[k][1])+(CARTCOORD[i][2]-NEIGHBORS[k][2])*(CARTCOORD[i][2]-NEIGHBORS[k][2]));
                            if ((distance<2.75)&&(distance>0)) /*The numbers of heteroatomic contacts
shorter than 2.75, 2.80, and 3.00 Angstroms are counted separately.*/
                                { bondnumber1=bondnumber1+0.5;
                                  }
                                if ((distance<2.80)&&(distance>0))
                                    { bondnumber2=bondnumber2+0.5;}
                                if ((distance<3.00)&&(distance>0))
                                    { bondnumber3=bondnumber3+0.5;}
                                }
                            }
                        }
                    }
                }
            }
    }

```

```

    }
/*MAX[50][25] contains the top 50 schemes with the highest number of heteroatomic contacts.*/
/*The primary, secondary, and third sorting indices are the numbers of heteroatomic distances shorter than
2.75, 2.80, and 3.00 Angstroms, respectively.*/
/*The three distances can be adjusted to make sure that only one or several symmetrically equivalent
schemes with the maximum heteroatomic contacts are selected.*/
    for (i=0;i<50;i++)
    { if
((bondnumber1>MAX[i][22]) || ((bondnumber1==MAX[i][22])&&(bondnumber2>MAX[i][23])) || ((bondnumber
1==MAX[i][22])&&(bondnumber2==MAX[i][23])&&(bondnumber3>MAX[i][24])))
        { for (j=0;j<22;j++)
            { MAX[i][j]=CONFIG[j];}
          MAX[i][22]=bondnumber1;
          MAX[i][23]=bondnumber2;
          MAX[i][24]=bondnumber3;
        }
        i=49;
    }
    }
    numberdone=numberdone+1;
}
}
writeout=fopen("max.txt","w");
for (i=0;i<50;i++)
{ for (j=0;j<25;j++)
    { fprintf(writeout,"%3.0f ",MAX[i][j]);}
  fprintf(writeout,"\n");
}
fprintf(writeout,"Total: %f\n",numberdone);
fclose(writeout);
}

```

**The input file “allsites.txt”:**

```

0.5000 -0.2500 -0.1250
-0.5000 0.2500 0.1250

```

0.0000 0.0000 0.5000  
0.2500 0.2500 0.2500  
-0.2500 0.2500 0.2500  
0.5000 0.0000 0.0000  
0.1198 0.0442 0.1740  
0.1198 -0.0442 -0.1740  
-0.1198 0.0442 0.1740  
-0.1198 -0.0442 -0.1740  
0.2942 0.1302 -0.0760  
0.2942 -0.1302 0.0760  
-0.2942 0.1302 -0.0760  
-0.2942 -0.1302 0.0760  
0.2058 0.1302 -0.4240  
-0.2058 -0.1302 0.4240  
0.3802 -0.0442 -0.3260  
-0.3802 0.0442 0.3260  
0.2942 -0.3698 0.0760  
-0.2942 0.3698 -0.0760  
-0.1198 0.5442 -0.1740  
0.1198 -0.5442 0.1740



## Chapter 6

### **EuAg<sub>x</sub>Al<sub>11-x</sub> with the BaHg<sub>11</sub>-Type Structure: Composition, Coloring, and Competition with the BaCd<sub>11</sub>-Type Structure**

Modified from a paper published in *Chemistry of Materials*

Fei Wang, Karen Nordell Pearson, Warren E. Straszheim, and Gordon J. Miller

#### **6.1 Abstract**

EuAg<sub>x</sub>Al<sub>11-x</sub> phases adopting the BaHg<sub>11</sub>-type structure (space group  $Pm\bar{3}m$ ,  $Z = 3$ ) were synthesized with high yield by arc melting a mixture loaded as “EuAg<sub>3.5</sub>Al<sub>7.5</sub>” and annealing at 500 °C for 40 days. This phase has a very narrow phase width around EuAg<sub>4.0</sub>Al<sub>7.0</sub>; and it is unstable at 600 °C and 700 °C, at which it transforms into other phases. Magnetometry indicates that Eu is divalent, which gives the valence electron concentration per Ag/Al atom as 2.45 e<sup>-</sup>/atom, higher than in the BaCd<sub>11</sub>-type phases in the Eu-Ag-Al system (2.10–2.30 e<sup>-</sup>/atom). First principles electronic structure calculations, using a computational model structure built by simulating the crystallographic results as well as maximizing the number of heteroatomic (Ag–Al) contacts, can explain why the cubic BaHg<sub>11</sub>-type structure is favored at higher valence electron concentration than the tetragonal BaCd<sub>11</sub>-type structure.

#### **6.2 Introduction**

Polar intermetallics<sup>1-3</sup> represent a significant class of compounds bridging classical, Hume-Rothery electron phases<sup>4</sup> and Zintl phases<sup>5</sup>. Similar to Zintl phases, polar intermetallics also consist of elements with significant differences in electronegativity, but their structures cannot be understood with the octet rule, which applies to Zintl phases; instead, as in Hume-Rothery phases, they are largely determined by valence electron count. However, unlike Hume-Rothery electron phases, polar intermetallics often form abundant complex structures, *e.g.*, NaZn<sub>13</sub>-, ThMn<sub>12</sub>-, BaCd<sub>11</sub>-, and BaHg<sub>11</sub>-types, in which, just as in Zintl phases, the “cations,” *i.e.*, the electropositive metals, have large coordination numbers. Many recent reports also showed that this class of compounds provides a wealth of quasicrystalline phases and their crystalline approximants.<sup>6</sup> Because of such structural abundance and complexity, composition-structure relationships of polar intermetallic compounds are complicated and still remain a challenge to be understood. Further systematic investigations into polar intermetallics are necessary; and these investigations will benefit from a synergism between experiment and theory.

During our investigations into the composition–structure relationship in polar intermetallics, significant effort has been devoted to the RE(rare earth)–Ag–Al systems due to their structural abundance.<sup>7</sup> Researchers have obtained kaleidoscopic complex structures from these systems, including the BaCd<sub>11</sub>-, BaHg<sub>11</sub>-, Th<sub>2</sub>Ni<sub>17</sub>-, Th<sub>2</sub>Zn<sub>17</sub>-, CaCu<sub>5</sub>-, and BaAl<sub>4</sub>-types.<sup>8</sup> The iso-compositional structure types (*i.e.*, the BaCd<sub>11</sub>- vs. BaHg<sub>11</sub>-types, and the Th<sub>2</sub>Ni<sub>17</sub>- vs. Th<sub>2</sub>Zn<sub>17</sub>-types) often compete within a single RE–Ag–Al system as its composition varies. For instance, in Yb–Ag–Al, the BaCd<sub>11</sub>-type structure forms at YbAg<sub>5.3</sub>Al<sub>5.7</sub> and the BaHg<sub>11</sub>-type structure forms at YbAg<sub>4</sub>Al<sub>7</sub>.<sup>81</sup> Similar results have also been obtained in our previous work with the Eu–Ag–Al system.<sup>9</sup> Further investigations into these competing structure types can deepen our understanding of these structures themselves, as well as how they are related to composition.

The BaHg<sub>11</sub>-type structure is one of the most rarely observed among all of the complex structures obtained in RE–Ag–Al ternaries. It has been reported only with RE = Ce,<sup>8k</sup> Yb<sup>81</sup>, and Eu<sup>9</sup> without crystallographic details (only lattice parameters available, without atomic coordinates or thermal parameters). Experimental disagreement also occurs in the Ce–Ag–Al system. Although Cordier obtained BaHg<sub>11</sub>-type CeAg<sub>3.1</sub>Al<sub>7.9</sub> by synthesizing at 1000–1400 °C and annealing at 800 °C,<sup>8k</sup> this phase did not occur in Kuz'ma's phase diagram study at 597 °C,<sup>8c</sup> which was proposed as a temperature effect. The recent reports from Latturmer *et al.* demonstrated more complexity of the BaHg<sub>11</sub>-type structure.<sup>10</sup> Their study of RE–Au–Al and RE–Ag–Al systems showed that, in an Al flux, early transition metals (*e.g.*, Ti and Mo) have a template effect and are essential in the formation of a stuffed BaHg<sub>11</sub>-type structure, which is a quaternary phase, RE<sub>3</sub>(Au/Ag)<sub>6+x</sub>Al<sub>26</sub>T (T is the early transition metal). The authors also analyzed the synthesis method adapted by Cordier<sup>8k,1</sup> and speculated that the possible inclusion of Mo (the crucible material) induced the formation of the BaHg<sub>11</sub>-type structure.

Therefore, although the BaHg<sub>11</sub>-type structure has been long observed in RE–Ag–Al systems, there are still many unsolved “mysteries” about it, *e.g.*, what the phase width is, and how temperature and early transition metals affect its formation. Moreover, site sharing and site preference are commonly observed for Ag and Al atoms in RE–Ag–Al systems. How are Ag and Al distributed in the BaHg<sub>11</sub>-type structure? Lastly, how does this structure type compete with the BaCd<sub>11</sub>-type structure during changes in composition, *viz.*, the molar ratio between Ag and Al, of a RE–Ag–Al system? To answer these questions, we continued our previous work with the EuAg<sub>x</sub>Al<sub>11-x</sub> system<sup>9</sup> and investigated BaHg<sub>11</sub>-type phases using both experiments and quantum mechanical calculations.

### 6.3 Experiments.

**Syntheses.** Pure metals were used for syntheses: Eu (rods, Ames Laboratory, 99.99%), Ag (slugs, Alfa Aesar, 99.99%), and Al (foil, Tenneco). In our previous study of  $\text{EuAg}_x\text{Al}_{11-x}$ , the  $\text{BaHg}_{11}$ -type structure was observed in the systems loaded with “ $\text{EuAg}_4\text{Al}_7$ ” and “ $\text{EuAg}_3\text{Al}_8$ ”.<sup>9</sup> To find out its homogeneity width, we varied the loading composition from “ $\text{EuAg}_4\text{Al}_7$ ” to “ $\text{EuAgAl}_{10}$ ”. For each loading composition, an approximately 0.5 g mixture of pure metals was arc melted under an argon atmosphere into a silvery button, which was turned over and re-melted five times to ensure thorough reaction and homogeneity. There was some ash generated during melting, but the weight loss was always lower than 1 wt%. Every product was stable in air and water but dissolved in 40 wt% nitric acid. The silvery button was then broken into halves. One-half was characterized immediately; and the other half, before characterization, was sealed in a tantalum tube under argon atmosphere, which was then sealed in an evacuated silica jacket and annealed in a tube furnace at 500 °C for 40 days.

**X-Ray Crystallography.** Powder X-ray diffraction (XRD) was carried out on a Huber Imaging Plate Guinier Camera G670 using monochromatized  $\text{Cu K}\alpha_1$  radiation ( $\lambda = 1.54059 \text{ \AA}$ ). This diffractometer has been calibrated with standard silicon powder (NIST,  $a = 5.430940 \pm 0.000035 \text{ \AA}$ ). The exposure time was 1 hour and the step size of  $2\theta$  was  $0.005^\circ$ . The Le Bail technique<sup>11</sup> was used for full pattern decomposition, and the Rietveld method<sup>12</sup> was employed to refine the crystal structure, both of which were accomplished with the software *LHPM-Rietica*.<sup>13</sup>

Small crystals selected from the crushed “ $\text{EuAg}_{3.5}\text{Al}_{7.5}$ ” sample were mounted on the tip of capillary with epoxy for single-crystal XRD experiments, which were carried out at room temperature on a STOE IPDS diffractometer equipped with  $\text{Mo K}\alpha$  radiation ( $\lambda = 0.71073 \text{ \AA}$ ). 80 frames were collected at  $\varphi = 130^\circ$  with  $\omega$  ranging from  $42$  to  $122^\circ$  with the step size of  $1^\circ$ , and the exposure time of 1 min per frame. All data collection, integrations, cell refinements, and absorption corrections were done using *X-Area*.<sup>14</sup> Using *SHELXTL*,<sup>15</sup> the crystal structure was solved with direct methods and refined by full-matrix least-squares on  $F^2$ .

**Magnetometry.** Temperature-dependent magnetic susceptibility was measured with a 6.3 mg sample taken from the annealed product with the loading composition “ $\text{EuAg}_{3.5}\text{Al}_{7.5}$ ”, which is a “pure phase” adopting the  $\text{BaHg}_{11}$ -type structure according to powder XRD. Using a Quantum Design MPMS XL Superconducting Quantum Interference Device (SQUID) magnetometer, at 1 kOe fixed magnetic field, the magnetic susceptibility ( $\chi$ ) was measured as the temperature (T) varied from 5 to 300 K. We

fitted the  $1/\chi$  vs.  $T$  curve with Curie-Weiss law to calculate the effective moment ( $\mu_{\text{eff}}$ ) and the valency of Eu.

**Microscopy.** The annealed sample loaded as “EuAg<sub>3.5</sub>Al<sub>7.5</sub>” was also characterized by scanning electron microscopy (SEM) and energy-dispersive spectroscopy (EDS) to examine its homogeneity and to check the presence of early transition metals, including W (electrode material of the arc melter), Ti (oxygen getter), and Ta (container for annealing). SEM was accomplished using a Hitachi S-2460N variable-pressure scanning electron microscope and EDS was performed with an Oxford Instruments Isis X-ray analyzer. Several grains were taken at random from the broken “EuAg<sub>3.5</sub>Al<sub>7.5</sub>” sample, embedded in epoxy, polished, coated with *ca.* 20 nm of carbon, and examined in high vacuum mode (*ca.*  $5 \times 10^{-6}$  Torr). The accelerating voltage was 20 kV and the beam current was *ca.* 0.5 nA, which produced a count rate of 3000 cps. Multiple points were examined for every sample grain. The standards used for quantitative compositional analysis were elemental Ag and Al, and EuAl<sub>2</sub>. The precision of the compositional analysis under these conditions is within a few tenths of weight percent.

**Electronic Structure Calculations.** To study the electronic structure of the BaHg<sub>11</sub>-type EuAg<sub>x</sub>Al<sub>11-x</sub>, we constructed a few model structures according to the crystallographic results for first principles calculations. Details of these models can be found in the section, Computational Models. Both the Stuttgart *Tight-Binding, Linear-Muffin-Tin Orbital* program with the *Atomic Sphere Approximation* (TB-LMTO-ASA)<sup>16</sup> and the *Vienna ab initio simulation package* (VASP)<sup>17-19</sup> were employed to calculate the total energies and electronic structures of these models.

For TB-LMTO-ASA, we used the von Barth-Hedin local density approximation<sup>20</sup> to treat electron exchange and correlation energy; and we included these atomic orbitals in the basis set: the 6s, 6p (downfolded<sup>21</sup>), and 5d states of Eu; the 5s, 5p, and 4d states of Ag; and the 3s, 3p, and 3d (downfolded) states of Al. Eu 4f states were excluded because magnetometry indicated that Eu is divalent and, thus, its 4f electrons are localized in half-filled 4f orbitals. The Wigner-Seitz radii of the atomic spheres were 2.13 Å for Eu and 1.57 Å for both Ag and Al. This filled the unit cell with a 9.566 % overlap without introducing any empty spheres; an  $8 \times 8 \times 8$   $k$ -points mesh was used in the first Brillouin zone for integration. The density of states (DOS) and crystal orbital Hamiltonian populations (COHP)<sup>22</sup> curves were evaluated and plotted.

VASP calculations were completed to compare the total energies of the model structures. We used the projector augmented-wave (PAW) pseudopotentials<sup>23</sup> and the Perdew-Burke-Ernzerhof generalized

gradient approximation (GGA-PBE).<sup>24</sup> The energy cutoff was 343.6 eV. Reciprocal space integrations were completed over a  $7 \times 7 \times 7$  Monkhorst-Pack  $k$ -points mesh<sup>25</sup> with the linear tetrahedron method<sup>26</sup>. With these settings, the calculated total energy converged to less than 1 meV per atom. The DOS curve calculated by VASP was also plotted and compared with that from TB-LMTO-ASA calculations.

## 6.4 Results and Discussions.

**Synthesis and X-Ray Crystallography.** Our previous work<sup>9</sup> indicated that both loading composition and annealing are pertinent to the formation of the BaHg<sub>11</sub>-type structure in EuAg<sub>x</sub>Al<sub>11-x</sub>. This cubic structure type was not detected by powder XRD when  $x = 5-8$  in the loading composition “EuAg<sub>x</sub>Al<sub>11-x</sub>”; but was obtained when  $x = 3$  and 4. For both of these two systems, annealing at 500 °C increased the abundance of the BaHg<sub>11</sub>-type phase (see its strongest peak at *ca.* 34.3° in Figure 1(a)–(d)), especially for the “EuAg<sub>3</sub>Al<sub>8</sub>” system, in which it is the dominant phase.

To improve the abundance of the BaHg<sub>11</sub>-type phase, we adjusted the loading composition. At first, we tested two loading compositions richer in Al than above, *viz.*, “EuAg<sub>2</sub>Al<sub>9</sub>” and “EuAgAl<sub>10</sub>”. The diffraction patterns of these arc melted and annealed samples are shown in Figure 1(e)–(h). These two loading compositions produce mixed phases, among which the BaHg<sub>11</sub>-type structure occurs, and annealing at 500 °C also slightly increased its abundance. However, its abundances in these two samples are both lower than in the “EuAg<sub>3</sub>Al<sub>8</sub>” sample (Figure 1(d), (f), (g)). Therefore, higher Al content does not facilitate the formation of the BaHg<sub>11</sub>-type phase.

We then made the Al content lower than in “EuAg<sub>3</sub>Al<sub>8</sub>” and loaded “EuAg<sub>3.5</sub>Al<sub>7.5</sub>”. The powder XRD patterns for arc melted and subsequent annealed samples are in Figure 2. The pattern of the arc melted sample (Figure 2(a)) is close to the arc melted “EuAg<sub>3</sub>Al<sub>8</sub>” system (Figure 1(c)). After annealing at 500 °C, all peaks in the powder pattern can be indexed with a single BaHg<sub>11</sub>-type phase (Figure 2(b)). Rietveld refinement was then applied to the powder pattern and the results are listed in Tables 1 and 2. Although powder XRD characterizes this sample as a “pure phase”, it was very difficult to find a good quality single crystal from this annealed “EuAg<sub>3.5</sub>Al<sub>7.5</sub>” sample. We extracted only one single crystal which was qualified and carried out single crystal XRD and refinement upon it. The results are also listed in Tables 1 and 2.

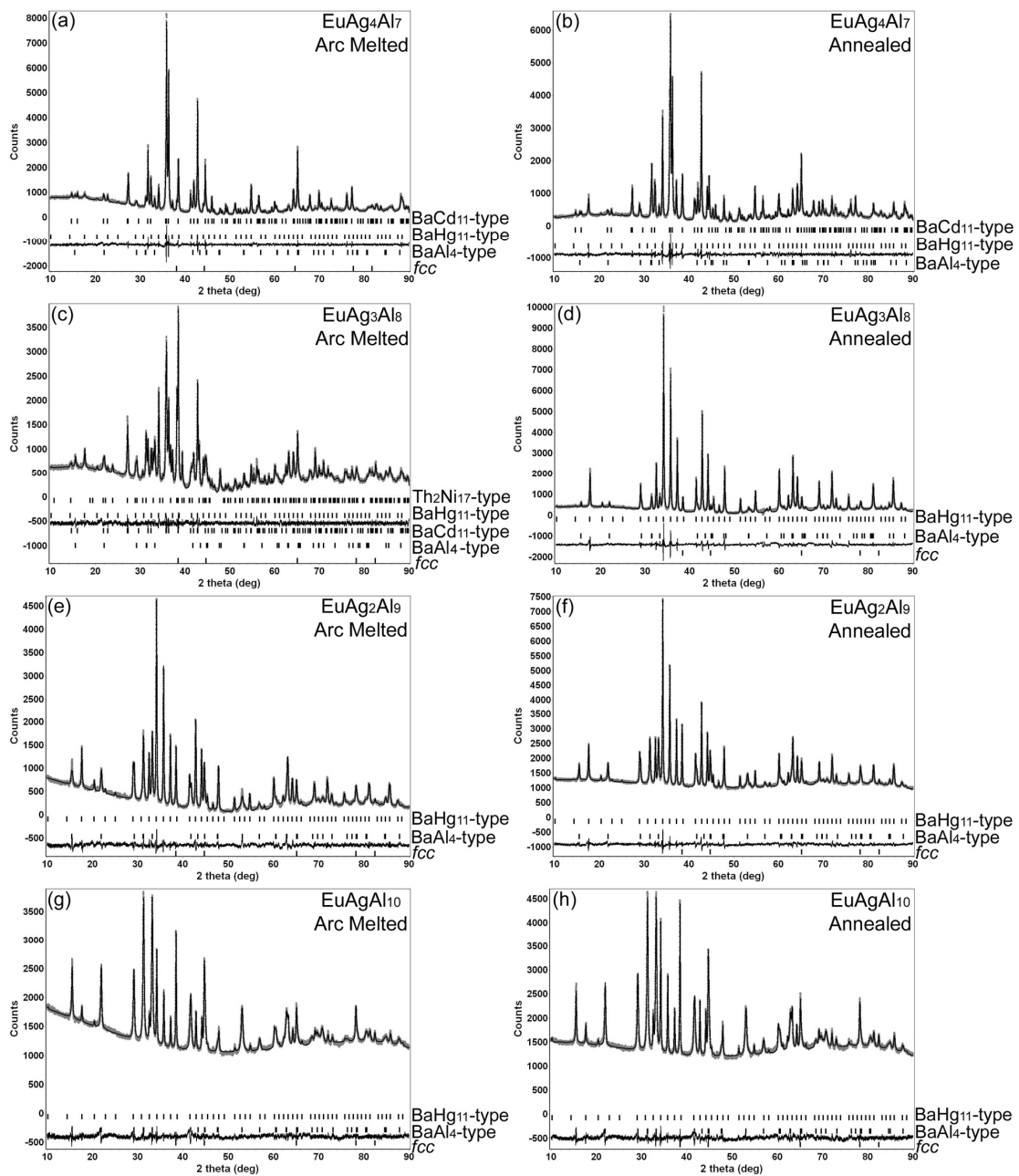


**Figure 1.** The powder XRD patterns of arc melted and annealed samples with various loading compositions. Le Bail refinement was applied to every pattern.

Comparison shows that the Rietveld and the single crystal refinements agree well with one another in lattice parameter (with 0.2% difference) and atomic positions. The refined compositions differ slightly from one another: the single crystal technique gives  $\text{EuAg}_{3.5(2)}\text{Al}_{7.5(2)}$ , which is very close to the loading composition; but Rietveld refinement gave higher Ag content,  $\text{EuAg}_{3.67(3)}\text{Al}_{7.33(3)}$ .

Moreover, the isotropic displacement parameters ( $U_{iso}$ ) refined by the Rietveld technique are much larger. This could arise because the Rietveld powder refinement averages over an inhomogeneous bulk material (the inhomogeneity was shown later by EDS) and the inhomogeneity (*e.g.*, in atomic positions) is absorbed by parameters such as site occupancy factors (SOF) and  $U_{iso}$ .

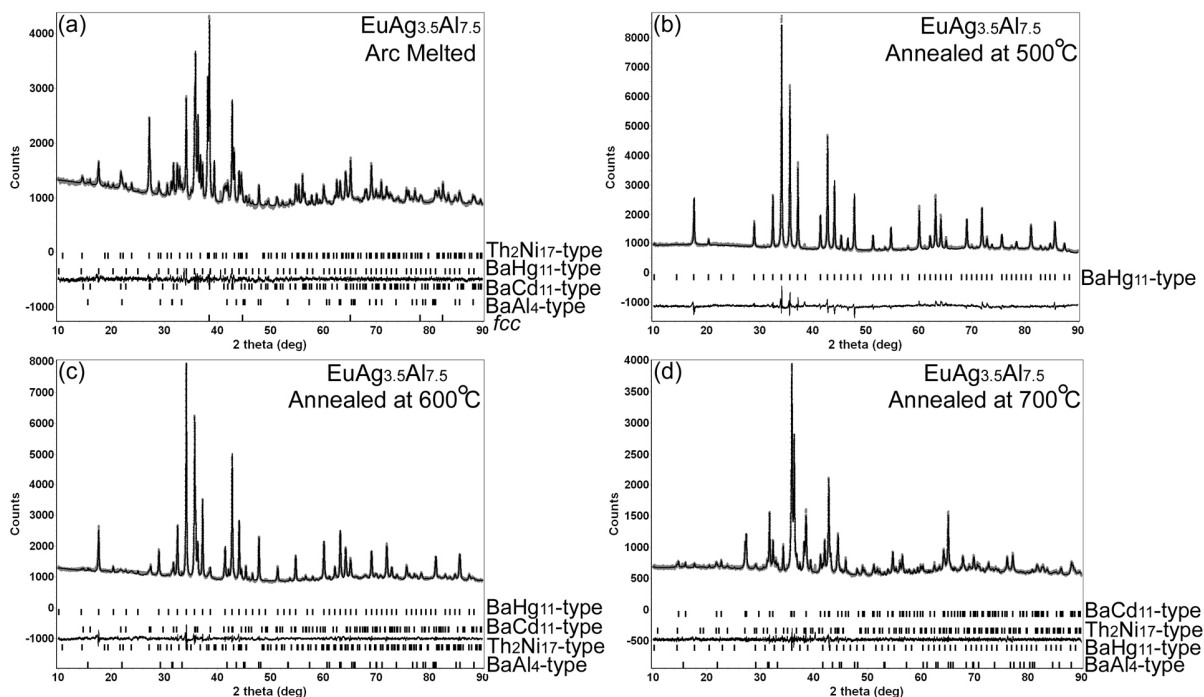


**Figure 2.** The powder XRD patterns of arc melted and annealed “ $\text{EuAg}_{3.5}\text{Al}_{7.5}$ ” samples. Le Bail refinement was applied to (a), (c), and (d); and Rietveld refinement was applied to (b).

Just like many other RE-Ag-Al phases, Ag and Al share the same sites ( $8g$ ,  $12i$ ,  $12j$ ) in the asymmetric unit, but these sites are not shared equally. Compared with the average Ag/Al ratio ( $3.5/7.5 = 0.32/0.68$ ), the  $8g$  site prefers Ag and the  $12i$  site favors Al. An even higher preference occurs on the  $1b$  site, which is exclusively occupied by Ag. We attempted refinement with this site being shared by Ag and Al: it gave the occupancy Ag/Al = 0.94/0.06(7); and the corresponding R values are  $R1 = 0.0599$  and  $wR2 = 0.0961$ , which is not a statistically significant improvement over the other refinement, according to a Hamilton test.<sup>27</sup> Therefore, we assigned solely Ag to the  $1b$  site. This result agrees with Cordier’s study<sup>28</sup> of  $\text{BaHg}_{11}$ -type  $\text{CaAg}_4\text{Al}_7$ , in which this site was also filled with only Ag.



**Table 1.** Summary of crystal structure refinement parameters of the annealed “EuAg<sub>3.5</sub>Al<sub>7.5</sub>” sample.

Space group	$Pm\bar{3}m$ (No. 221)	
Z	3	
Refinement Methods	Rietveld	Single Crystal
Lattice parameters	$a = 8.70063(6)$ Å	$a = 8.7208(10)$ Å
Empirical formula	EuAg <sub>3.67(3)</sub> Al <sub>7.33(3)</sub>	EuAg <sub>3.5(2)</sub> Al <sub>7.5(2)</sub>
Volume	658.645(9) Å <sup>3</sup>	663.24(13) Å <sup>3</sup>
2θ range	10.00°-90.00°	4.68°-53.26°
Goodness-of-fit	1.354	1.178
R indices	R <sub>p</sub> = 0.0285	R1 = 0.0599 ( $I > 2\sigma(I)$ )
	R <sub>wp</sub> = 0.0374	wR2 = 0.0963 ( $I > 2\sigma(I)$ )
	R <sub>exp</sub> = 0.0322	R1 = 0.0937 (all data)
	R <sub>B</sub> = 0.024	wR2 = 0.1039 (all data)
Reflections collected	2207	
Independent reflections	181 (R <sub>int</sub> = 0.2145)	
Index ranges	-9 ≤ $h$ ≤ 11; -11 ≤ $k$ ≤ 8; -9 ≤ $l$ ≤ 11	
Largest diff. peak/hole	1.809/-1.777 e <sup>-</sup> /Å <sup>3</sup>	

**Table 2.** The atomic coordinates and isotropic displacement parameters from crystal structure refinement of the annealed “EuAg<sub>3.5</sub>Al<sub>7.5</sub>” sample.

Atom	Wyck.	x	y	z	Rietveld Refinement			Single Crystal Refinement		
					Coordinates	SOF	$U_{iso}/\text{Å}^2$	Coordinates	SOF	$U_{iso}/\text{Å}^2$
Eu1	3d	1/2	0	0		1	0.0051(3)		1	0.014(1)
Ag1	1b	1/2	1/2	1/2		1	0.0065(6)		1	0.030(2)
Ag/Al2	8g	x	x	x	x = 0.1640(1)	0.416/0.584(4)	0.0146(5)	x = 0.1658(4)	0.41/0.59(2)	0.035(2)
Ag/Al3	12i	0	y	y	y = 0.3453(2)	0.204/0.796(3)	0.0114(5)	y = 0.3444(5)	0.23/0.77(2)	0.023(2)
Ag/Al4	12j	1/2	y	y	y = 0.2661(1)	0.353/0.647(2)	0.0060(4)	y = 0.2667(3)	0.30/0.70(1)	0.015(2)

The BaHg<sub>11</sub>-type structure has been described in some earlier reports<sup>28-30</sup>. It can be understood by a structure scheme based on a “tetrahedron star”, which is a tetrahedron with every face capped by an atom. In a unit cell of BaHg<sub>11</sub>-type EuAg<sub>3.5</sub>Al<sub>7.5</sub> (Figure 3(a)), there are eight tetrahedra formed by Ag/Al2(8g) and Ag/Al4(12j) sites. The Ag1(1b) site caps one face of each tetrahedron, which makes Ag1(1b) sit in a cuboctahedron formed by Ag/Al4(12j) (Figure 3(b)). The Ag/Al3(12i) sites cap all of the other faces of the eight tetrahedra. The Eu atom sits in the center of a polyhedron shown in Figure



3(c). The Ag/Al atoms surrounding Eu form five squares. Eu atom centers a square formed by Ag/Al4(12*j*) atoms, which is “sandwiched” by two larger squares formed by Ag/Al3(12*i*) atoms and two smaller squares formed by Ag/Al2(8*g*) atoms. Selected interatomic distances are listed in Table 3. These distances are calculated from lattice parameters from powder data and atomic positions from single crystal data. It shows that the Ag/Al–Ag/Al distances are not uniform in this structure: those involving Ag/Al3(12*i*) (*ca.* 2.63–2.77 Å) are shorter than the others (> 2.87 Å). These distances in the BaHg<sub>11</sub>-type phase are comparable to those observed in BaCd<sub>11</sub>-type EuAg<sub>*x*</sub>Al<sub>11-*x*</sub>.<sup>9</sup>

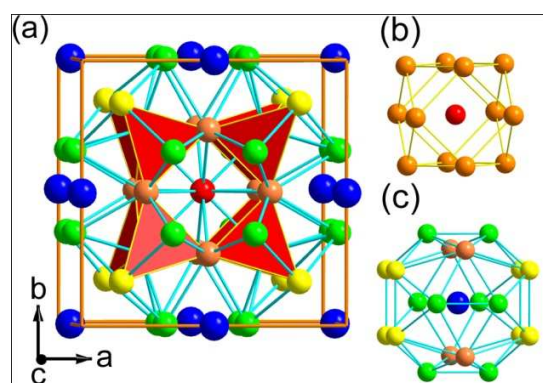


**Figure 3.** The crystal structures of BaHg<sub>11</sub>-type EuAg<sub>*x*</sub>Al<sub>11-*x*</sub>: (a) unit cell; (b) the coordination environment of Ag1(1*b*); and (c) the coordination environment of Eu1(3*d*). Blue: Eu1(3*d*); red: Ag1(1*b*); yellow: Ag/Al2(8*g*); green: Ag/Al3(12*i*); orange: Ag/Al4(12*j*).

Several variants of the BaHg<sub>11</sub>-type structure have been reported for ternary aluminides and indides.<sup>10,31,32</sup> The variances occur in two aspects: the 1*a* (0, 0, 0) site being stuffed with transition metals (*e.g.*, Ag, Au, or Pd); and of splitting the 12*i* site. We also introduced these two variances to our refinement of the BaHg<sub>11</sub>-type structure to see whether we could obtain any improvements. Stuffing the 1*a* with Ag gave a negative occupancy on this site. Allowing 12*i* site splitting lowered the R values (R1 = 0.0578, wR2 = 0.0889), but, according to a Hamilton test,<sup>27</sup> this change is not a statistically significant improvement. Moreover, the split 12*i* sites are problematic: they have much higher uncertainties in atomic coordinates (see Supporting Information, Tables S1 and S2). Therefore, our BaHg<sub>11</sub>-type phase does not have these reported structural variances.

**EDS and Homogeneity Range.** Although powder XRD can detect only the BaHg<sub>11</sub>-type structure in the annealed “EuAg<sub>3.5</sub>Al<sub>7.5</sub>” sample, its SEM image (Figure 4) reveals that it is not a completely homogeneous phase, which explains why it was difficult to extract good-quality single crystals for XRD. Figure 4 shows a light-gray background (*e.g.*, spots 3, 4, 5, and 6, the major phase) including

some patches (the minor phases) in different colors: darker gray (*e.g.*, spots 1 and 2), white (*e.g.*, spot 7), gray with white outline (*e.g.*, spot 8), and black (*e.g.*, spots 9). The compositions on spots 1–9 were analyzed by EDS and are listed in Table 4. The light-gray background is the dominant phase, which is the BaHg<sub>11</sub>-type phase according to powder XRD. The sampling spots (3–6) on the gray background give compositions with small variations but also all are very close to EuAg<sub>4.0</sub>Al<sub>7.0</sub>, which indicates greater Ag contents than obtained from XRD refinements. This deviation could, again, be attributed to the heterogeneity of the product, which affects the SOF and thus the composition in refinement.

**Table 3.** Selected interatomic distances of the BaHg<sub>11</sub>-type EuAg<sub>x</sub>Al<sub>11-x</sub>.

Atom Pair		Distances /Å
Eu1—	Ag/Al2	3.5521(4)
	Ag/Al3	3.288(2)
	Ag/Al4	3.281(4)
Ag1—	Ag/Al4	2.870(4)
Ag/Al2—	Ag/Al2	2.885(8)
	Ag/Al3	2.629(5)
Ag/Al3—	Ag/Al3	2.708(8)
	Ag/Al4	2.771(2)
Ag/Al4—	Ag/Al4	2.870(4)

The minor phases do not manifest themselves in powder XRD, but their structures can be deduced by examining their compositions. The composition at spot 7 (the white patch) is Eu<sub>1.02(2)</sub>Ag<sub>5.31(4)</sub>Al<sub>5.67(6)</sub>, which falls in the homogeneity range (EuAg<sub>5</sub>Al<sub>6</sub>–EuAg<sub>6</sub>Al<sub>5</sub>) of the BaCd<sub>11</sub>-type phase.<sup>9</sup> The gray patches with white outline (spot 8) have the compositions close to Eu(Ag,Al)<sub>4</sub>. This is probably a BaAl<sub>4</sub>-type phase, which occurs frequently in Eu-Ag-Al ternary systems. The black patches (spot 9) are almost pure Al. The identity of the darker gray patches (spots 1 and 2) cannot be determined at this stage. They are probably closely related to the BaHg<sub>11</sub>-type phase because they also have EuAg<sub>x</sub>Al<sub>11-x</sub> compositions but they are slightly richer in Al (*ca.* EuAg<sub>3.7</sub>Al<sub>7.3</sub>) than the dominant BaHg<sub>11</sub>-type phase. Further investigations are necessary.

The annealed “EuAg<sub>3</sub>Al<sub>8</sub>” and “EuAg<sub>4</sub>Al<sub>7</sub>” samples were also analyzed with SEM and EDS (Supporting Information). The BaHg<sub>11</sub>-type phases in these two samples also give compositions very close to EuAg<sub>4.0</sub>Al<sub>7.0</sub>, indicating that the BaHg<sub>11</sub>-type EuAg<sub>x</sub>Al<sub>11-x</sub> at 500 °C has a very narrow homogeneous range around EuAg<sub>4.0</sub>Al<sub>7.0</sub>. Moreover, in the “EuAg<sub>4</sub>Al<sub>7</sub>” sample, the BaCd<sub>11</sub>-type and

BaHg<sub>11</sub>-type phases are both abundant. They are clearly different in composition: the former is EuAg<sub>5</sub>Al<sub>6</sub>–EuAg<sub>6</sub>Al<sub>5</sub> and the latter is EuAg<sub>4.0</sub>Al<sub>7.0</sub>; *i.e.*, they strictly abide to their homogeneity ranges.

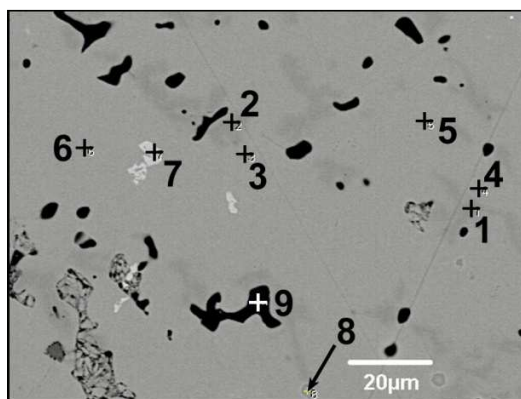


**Figure 4.** The SEM image of the “EuAg<sub>3.5</sub>Al<sub>7.5</sub>” sample annealed at 500 °C for 40 days. Elemental analysis with EDS was performed on the nine spots marked as 1–9.

As mentioned above, early transition metals facilitate the formation of BaHg<sub>11</sub>-type structure in RE–Au–Al and RE–Ag–Al systems.<sup>10</sup> Our syntheses involved W (the arc welder electrode), Ti (the oxygen getter for arc melting), and Ta (the container for annealing). However, EDS detected none of these transition metals in the “EuAg<sub>3</sub>Al<sub>8</sub>”, “EuAg<sub>3.5</sub>Al<sub>7.5</sub>”, and “EuAg<sub>4</sub>Al<sub>7</sub>” samples. So, under the synthetic conditions we adopted, the formation of BaHg<sub>11</sub>-type EuAg<sub>x</sub>Al<sub>11-x</sub> was not templated by early transition metals.

**Thermal Stability.** The “EuAg<sub>3.5</sub>Al<sub>7.5</sub>” sample was subsequently annealed at 600 and 700 °C, each for 10 days, in an attempt to improve its crystallinity and homogeneity. However, the subsequent powder patterns revealed that, at these temperatures, the BaHg<sub>11</sub>-type EuAg<sub>x</sub>Al<sub>11-x</sub> transforms into other phases. After annealing at 600 °C (Figure 2(c)), the BaHg<sub>11</sub>-type phase remained dominant; however, the sample was no longer “pure” because the BaCd<sub>11</sub>-type and Th<sub>2</sub>Ni<sub>17</sub>-type phases emerged. At 700 °C (Figure 2(d)), the BaHg<sub>11</sub>-type phase almost disappeared; and the BaCd<sub>11</sub>-type and Th<sub>2</sub>Ni<sub>17</sub>-type phases became major phases. Therefore, besides composition, the stability of BaHg<sub>11</sub>-type EuAg<sub>x</sub>Al<sub>11-x</sub> is also largely dictated by temperature: at 700 °C, it is no longer thermodynamically stable. This is one of the reasons why BaHg<sub>11</sub>-type RE–Ag–Al phases are less commonly observed than the other phases.

**Magnetometry and the Valence Electron Concentration of BaHg<sub>11</sub>-type EuAg<sub>x</sub>Al<sub>11-x</sub>.** The temperature dependent magnetic susceptibility ( $\chi$ ) and reciprocal susceptibility ( $1/\chi$ ) of BaHg<sub>11</sub>-type

$\text{EuAg}_x\text{Al}_{1-x}$  is shown in Figure 5. Above 20 K, this phase is paramagnetic and follows the Curie-Weiss law. At *ca.* 17 K, there is a transition from paramagnetism to ferromagnetism. In the  $1/\chi$  vs. T curve, the data between 20 K and 300 K were fitted with the Curie-Weiss law, from which the effective moment was calculated (to be  $7.95 \mu_B$ ). This value is very close to the  $\mu_{\text{eff}}$  of free  $\text{Eu}^{2+}$  ( $7.94 \mu_B$ ), indicating the divalency of Eu in this ternary phase.

**Table 4.** EDS composition analysis results of “ $\text{EuAg}_{3.5}\text{Al}_{7.5}$ ” annealed at 500 °C for 40 days (spots 1–9 are marked in Figure 4).

Spot	Atomic Fraction			Composition	Structure
	Eu	Ag	Al		
1	0.089(1)	0.303(2)	0.608(5)	$\text{Eu}_{1.07(2)}\text{Ag}_{3.63(3)}\text{Al}_{7.30(6)}$	Unknown
2	0.087(1)	0.308(2)	0.605(5)	$\text{Eu}_{1.05(2)}\text{Ag}_{3.69(3)}\text{Al}_{7.26(6)}$	
3	0.088(1)	0.329(3)	0.583(5)	$\text{Eu}_{1.05(2)}\text{Ag}_{3.95(3)}\text{Al}_{7.00(6)}$	BaHg <sub>11</sub> -type
4	0.090(1)	0.322(3)	0.588(5)	$\text{Eu}_{1.08(2)}\text{Ag}_{3.87(3)}\text{Al}_{7.05(6)}$	
5	0.086(1)	0.333(3)	0.581(5)	$\text{Eu}_{1.03(2)}\text{Ag}_{4.00(3)}\text{Al}_{6.97(6)}$	
6	0.086(1)	0.328(3)	0.586(5)	$\text{Eu}_{1.03(2)}\text{Ag}_{3.93(3)}\text{Al}_{7.04(6)}$	BaCd <sub>11</sub> -type
7	0.085(2)	0.443(3)	0.472(5)	$\text{Eu}_{1.02(2)}\text{Ag}_{5.31(4)}\text{Al}_{5.67(6)}$	
8	0.205(1)	0.132(2)	0.663(6)	$\text{Eu}_{1.02(1)}\text{Ag}_{0.66(1)}\text{Al}_{3.32(3)}$	BaAl <sub>4</sub> -type*
9	0.001(1)	0.014(1)	0.984(4)	$\text{Ag}_{0.014(1)}\text{Al}_{0.984(4)}$	<i>fcc</i>

\* EDS shows that there is also some Si (atomic fraction < 0.06) present in and only in the BaAl<sub>4</sub>-type phase. (That Si appears to be an alloying element in the Al foil.)

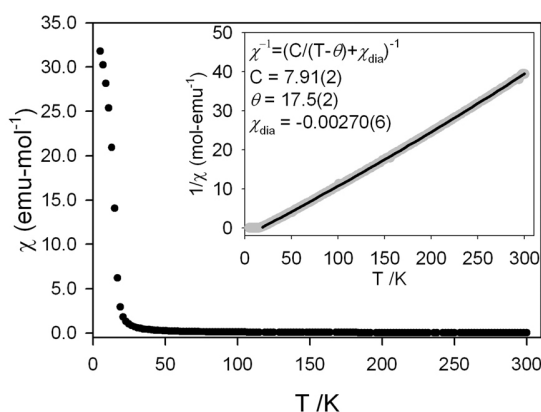


**Figure 5.** The temperature dependency of magnetic susceptibility and reciprocal susceptibility of the annealed “ $\text{EuAg}_{3.5}\text{Al}_{7.5}$ ” sample. The effective moment  $\mu_{\text{eff}} = 2.82795 \times (7.91)^{1/2} = 7.95 \mu_B$ , which is close to the  $\mu_{\text{eff}}$  of free  $\text{Eu}^{2+}$  ( $7.94 \mu_B$ ).

**Table 5.** The valence electron concentration (*vec*) of several BaHg<sub>11</sub>-type ternary compounds. The number of valence electrons of Ce, Yb, and Pd are counted as 3, 2, and 0.

Compositions	vec	Ref.
EuAg <sub>4.0</sub> Al <sub>7.0</sub>	2.45	
CaAg <sub>4</sub> Al <sub>7</sub>	2.45	28
YbAg <sub>4</sub> Al <sub>7</sub>	2.45	8l
CeAg <sub>3.1</sub> Al <sub>7.9</sub>	2.71	8k
YbPd <sub>2.1-3.4</sub> Ga <sub>8.9-7.6</sub>	2.25-2.61	33

The valence electron concentration (*vec*) of EuAg<sub>x</sub>Al<sub>11-x</sub>, with respect to the content of electronegative metals Ag and Al, can then be calculated as:

$$vec = \frac{2 + 1 \times x + 3 \times (11 - x)}{11} = \frac{35 - 2x}{11} = 3.18 - 0.18x$$

. From this equation, the BaHg<sub>11</sub>-type phases, EuAg<sub>4.0</sub>Al<sub>7.0</sub>, have a *vec* at 2.45 e<sup>-</sup>/atom. The *vec* values of some other BaHg<sub>11</sub>-type ternaries are listed in Table 5. All of them are higher than the *vec* of BaCd<sub>11</sub>-type REAg<sub>x</sub>Al<sub>11-x</sub> (*ca.* 2.10–2.30 e<sup>-</sup>/atom)<sup>9</sup>. Therefore, the “rule of thumb” governing the competition between these two 1:11 phases is that the BaHg<sub>11</sub>-type structure is stabilized at higher *vec* than the BaCd<sub>11</sub>-type structure. The same conclusion was reached by Häussermann<sup>29</sup> in his study of the binary compounds BaCd<sub>11</sub> and BaHg<sub>11</sub> with Extended Hückel calculations using second moment scaling. These calculations showed that, although they are isoelectronic (both have *vec* = 2.18 e<sup>-</sup>/atom), the maximum stability of BaCd<sub>11</sub> occurs at *vec* = *ca.* 2.10 e<sup>-</sup>/atom while BaHg<sub>11</sub> is at *vec* = *ca.* 2.55 e<sup>-</sup>/atom, confirming that *vec* determines the relative stabilities of these two 1:11 phases. However, this also raises the question for the two binary compounds, BaCd<sub>11</sub> and BaHg<sub>11</sub>, themselves, namely, why BaHg<sub>11</sub> does not form the expected BaCd<sub>11</sub>-type structure? Our preliminary study shows that a reason is related to the relativistic effect of the Hg atom, results of which will be discussed in a separate report.

**Computational Models.** To study how *vec* affects the stability of the BaHg<sub>11</sub>-type EuAg<sub>x</sub>Al<sub>11-x</sub>, it is necessary to analyze its electronic structure through quantum mechanical calculations, for which reasonable model structures need to be built. We constructed the model structures in the following way. The lattice parameters and atomic positions of each model structure were taken from crystallographic data (Table 1 and 2). The 3*d* and 1*b* positions can be unambiguously filled with Eu and Ag. The site sharing between Ag and Al on 8*g*, 12*i*, and 12*j* sites was treated by lowering the symmetry from cubic to triclinic (space group *P1*). The original 8*g* positions were then broken into

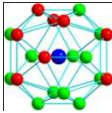
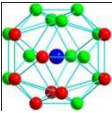
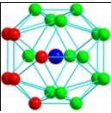
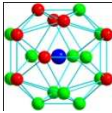
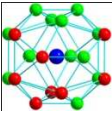
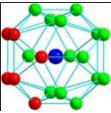
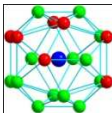
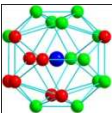
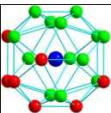
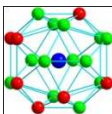
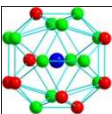
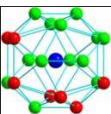
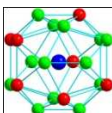
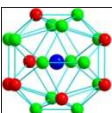
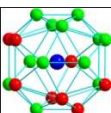
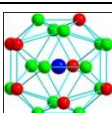
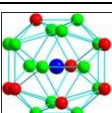
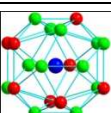
eight  $1a$  positions, which were assigned with 4 Ag and 4 Al atoms (Ag/Al = 0.5/0.5). Likewise, the  $12i$  positions were assigned with 3 Ag and 9 Al atoms (Ag/Al = 0.25/0.75) and the  $12j$  positions with 4 Ag and 8 Al atoms (Ag/Al = 0.33/0.67). These Ag/Al ratios are very close to those listed in Table 2 and the resulting composition is  $\text{EuAg}_4\text{Al}_7$ , which is also close to the experimental value. Then, the “coloring problem”<sup>34</sup> needs to be addressed: fixing the Ag/Al ratios as listed above, there are multiple ( $C_8^4 \times C_{12}^3 \times C_{12}^4 = 7,623,000$  where  $C_n^m = n!/[m! \times (n-m)!]$ ) possible assignments (or “coloring schemes”) of Ag and Al; and we should select the one which gives the lowest total energy. We calculated the total energies with both LMTO and VASP upon several random coloring schemes (Model 1–4 in Table 6). Although LMTO gives larger energy differences between coloring schemes than VASP, they show the same trend: the more heteroatomic (Ag–Al) contacts a coloring scheme has, the lower its total energy is. The same trend was also discovered in the  $\text{BaCd}_{11}$ -type  $\text{EuAg}_x\text{Al}_{11-x}$  in our previous study.<sup>9</sup> According to this trend, we constructed Model 5 by maximizing Ag–Al contacts (the method of maximizing Ag–Al contacts was described in Ref. 9). Calculation shows that its total energy is indeed lower than the four random models as expected. Therefore, Model 5 is an appropriate model structure for  $\text{BaHg}_{11}$ -type  $\text{EuAg}_x\text{Al}_{11-x}$ . The details of Models 1–5 are included in Supporting Information.

**DOS and COHP.** The DOS and COHP curves of Model 5 calculated with TB-LMTO-ASA are shown in Figure 6. The VASP calculation also gives a DOS curve (Supporting Information), which is very close to the one shown in Figure 6. In the DOS curve, the  $4d$  bands of Ag manifest as a large peak spanning from *ca.*  $-7.5$  to *ca.*  $-4.5$  eV. Leaving this  $4d$  peak out, the overall shape of the DOS curve resembles a parabola (the feature of a non-interacting electron gas) with a state-deficient region (pseudogap) at *ca.*  $-0.5$  to  $0.5$  eV, corresponding to  $vec = 2.32$ – $2.58$   $e^-/\text{atom}$  according to a rigid band approximation. So, when  $vec = 2.45$   $e^-/\text{atom}$  ( $\text{EuAg}_{4.0}\text{Al}_{7.0}$ ), the Fermi level is located in the pseudogap; and the Fermi level falls outside the pseudogap when  $vec = 2.10$ – $2.30$   $e^-/\text{atom}$  ( $\text{EuAg}_5\text{Al}_6$ – $\text{EuAg}_6\text{Al}_5$ ).

The COHP curves for Eu–Ag/Al, Ag–Ag, and Ag–Al contacts have relatively gradual bonding-antibonding crossovers. At  $vec = 2.45$   $e^-/\text{atom}$ , the Fermi level is located in their weakly bonding regions. The Al–Al COHP curve, however, has a very steep bonding-antibonding crossover (*i.e.*, Al–Al interactions switch from strongly bonding abruptly to strongly antibonding) and  $vec = 2.45$   $e^-/\text{atom}$  locates the Fermi level very close to the crossover (at *ca.*  $2.55$   $e^-/\text{atom}$ ). A  $vec$  value much higher than  $2.45$   $e^-/\text{atom}$  will, thus, occupy states that are strongly Al – Al antibonding and destabilize the structure. On the other hand, if the  $vec$  is much lower than  $2.45$   $e^-/\text{atom}$ , *e.g.*, at  $2.10$ – $2.30$   $e^-/\text{atom}$ ,

the structure will also be destabilized because those states that are strongly Ag–Ag, Ag–Al, and Al–Al bonding will be largely depleted. Therefore, the *vec* of 2.45 e<sup>-</sup>/atom is very close to the optimum value for the orbital interactions within the Ag/Al framework of the BaHg<sub>11</sub>-type EuAg<sub>x</sub>Al<sub>11-x</sub>. By comparison, the *vec* value that optimizes Ag/Al–Ag/Al interactions in BaCd<sub>11</sub>-type EuAg<sub>x</sub>Al<sub>11-x</sub> is 2.30 e<sup>-</sup>/atom.<sup>9</sup> This explains the rule governing the competition between the BaHg<sub>11</sub>- and BaCd<sub>11</sub>-type structures in EuAg<sub>x</sub>Al<sub>11-x</sub> ternary systems: the BaHg<sub>11</sub>-type structure is favored at higher *vec* (*ca.* 2.45 e<sup>-</sup>/atom) than the BaCd<sub>11</sub>-type structure (*ca.* 2.30 e<sup>-</sup>/atom).

**Table 6.** The total energies of the model structures.\*

Model	Coordination Environment of the 3 Eu Atoms (red: Ag; green: Al)			E <sub>total</sub> per f.u. (eV)		Number of Ag–Al Contacts per Unit Cell	
				LMTO	VASP	< 2.80 Å	< 2.90 Å
1				1.38	0.89	30	54
2				1.00	0.66	36	62
3				0.58	0.37	40	66
4				0.33	0.21	44	70
5				0.00	0.00	50	76

\*These models all have the same composition (EuAg<sub>4</sub>Al<sub>7</sub>) and same Ag/Al ratio on the original 8g (0.5/0.5), 12i (0.25/0.75), and 12j (0.33/0.67) positions. Model 1–4 are random coloring schemes. Model 5 is obtained by maximizing Ag–Al contacts. The total energy of Model 5 is taken as reference (0.00 eV). Details of these five models are included in the Supporting Information.



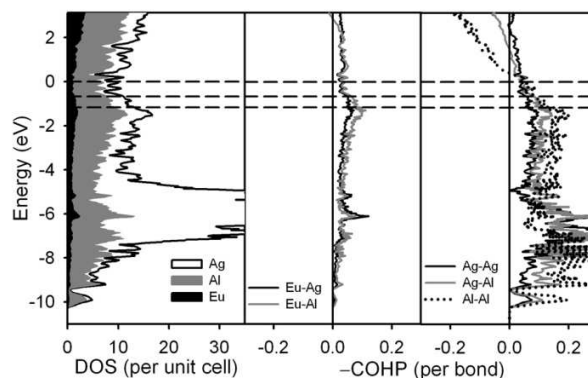


**Figure 6.** The DOS and COHP curves calculated with Model 5 using TB-LMTO-ASA. The four dashed straight line are the locations of the Fermi levels when  $vec =$  (from top) 2.45, 2.30, and 2.10  $e^-/\text{atom}$ . The parabolic dashed line shows the DOS of the non-interacting electron gas.

## 6.5 Conclusions.

The BaHg<sub>11</sub>-type EuAg<sub>x</sub>Al<sub>11-x</sub> phases were synthesized and characterized. Temperature has important effects on this phase: annealing at 500 °C gives a “pure phase”, while it transforms into BaCd<sub>11</sub>- and Th<sub>2</sub>Ni<sub>17</sub>-type phases at 600 °C and 700 °C. Composition is also pertinent: the cubic BaHg<sub>11</sub>-type structure can only be obtained within a narrow phase around EuAg<sub>4.0</sub>Al<sub>7.0</sub>, which gives a  $vec$  of 2.45  $e^-/\text{atom}$ . This value is higher than the  $vec$  of the BaCd<sub>11</sub>-type EuAg<sub>x</sub>Al<sub>11-x</sub> phases (2.10–2.30  $e^-/\text{atom}$ ). First principles electronic structure calculations were performed with a model structure built by simulating crystallographic results and maximizing Ag–Al contacts. The calculation results explained why the BaHg<sub>11</sub>-type structure forms at higher  $vec$  value than the BaCd<sub>11</sub>-type structure in the EuAg<sub>x</sub>Al<sub>11-x</sub> system.

## 6.6 Acknowledgment.

This work is supported by NSF DMR 02-441092 and 06-05949. We thank Dr. Sumohan Misra and Prof. Vitalij K. Pecharsky for magnetization measurements. We also thank Prof. Susan E. Lattner for her valuable discussions and suggestions.

**Supporting Information Available:** The results of single crystal refinement with 12i site splitting, the SEM and EDS results of the annealed “EuAg<sub>3</sub>Al<sub>8</sub>” and “EuAg<sub>4</sub>Al<sub>7</sub>” samples, the details of Models 1–5, and the DOS curve of Model 5 from VASP calculation (PDF). This material is available free of charge via the Internet at <http://pubs.acs.org>.



## 6.7 References

- (1) (a) Belin, C.; Tillard-Charbonnel, M. *Prog. Solid State Chem.* **1993**, *22*, 59. (b) Belin, C.; Tillard-Charbonnel, M. *Coord. Chem. Rev.* **1998**, *180*, 529.
- (2) Corbett, J. D. *Angew. Chem., Int. Ed.* **2000**, *39*, 670.
- (3) Häussermann, U.; Amerioun, S.; Eriksson, L.; Lee, C.-S.; Miller, G. J. *J. Am. Chem. Soc.* **2002**, *124*, 4371.
- (4) Hume-Rothery, W.; Raynor, G. V. *The Structure of Metals and Alloys*, 1st ed; London: The Inst. of Metals, 1936.
- (5) Schäfer, H.; Eisenmann, B.; Müller, W. *Angew. Chem. Int. Ed.* **1973**, *12* (9), 694.
- (6) (a) Lin, Q.; Corbett, J. D. *J. Am. Chem. Soc.* **2005**, *127*, 12786. (b) Lin, Q.; Corbett, J. D. *J. Am. Chem. Soc.* **2007**, *129*, 6789.
- (7) Nordell, K. J. Exploring Aluminum-Rich Intermetallics with Experiment and Theory. Ph.D. Thesis, Iowa State University, Ames, IA, 1997.
- (8) (a) Denysyuk, O. V.; Stel'makhovych, B. M.; Kuz'ma, Yu. B. *J. Solid State Chem.* **1994**, *109*, 172. (b) Stel'makhovych, B. M.; Kuz'ma Yu. B. *Dopov. Akad. Nauk Ukr.* **1994**, *3*, 86. (c) Zhak, O. V.; Stel'makhovych, B. M.; Kuz'ma Yu. B. *Russ. Metall.* **1995**, *6*, 158. (d) Kuz'ma Yu. B.; Zhak, O. V.; Shkolyk, S. Yu. *Dopov. Akad. Nauk Ukr.* **1995**, *3*, 101. (e) Zhak, O. V.; Stel'makhovych, B. M.; Kuz'ma Yu. B. *J. Alloys Comp.* **1996**, *237*, 144. (f) Kuz'ma Yu. B.; Zhak, O. V. Sarapina O. S. *Russ. Metall.* **1997**, *2*, 166. (g) Zhak, O. V.; Kuz'ma Yu. B. *J. Alloys Comp.* **1999**, *291*, 175. (h) Stel'makhovych, B. M.; Gumenyuk T. M.; Kuz'ma Yu. B. *J. Alloys Comp.* **2000**, *298*, 164. (i) Gumeniuk, R. V.; Stel'makhovych, B. M.; Kuz'ma Yu. B. *J. Alloys Comp.* **2001**, *321*, 132. (j) Stel'makhovych, B. M.; Zhak, O. V.; Bilas, N. R.; Kuz'ma Yu. B. *J. Alloys Comp.* **2004**, *363*, 243. (k) Cordier, G.; Dörsam, G.; Kniep, R. *J. Magn. Magn. Mater.* **1988**, *76 & 77*, 653. (l) Schank, C.; Tegel, U.; Henseleit, R.; Grauel, A.; Olesch, G.; Geibel, C.; Cordier, G.; Kniep, R.; Steglich, F. *J. Alloys Comp.* **1994**, *207/208*, 333.
- (9) Wang, F.; Pearson, K. N.; Miller, G. J. *Chem. Mater.*, **2009**, *21*, 230.
- (10) (a) Lattner, S. E.; Kanatzidis, M. G. *Inorg. Chem.* **2004**, *43*, 2. (b) Lattner, S. E.; Bilec, D.; Mahanti, S. D.; Kanatzidis, M. G. *Inorg. Chem.* **2009**, *48*, 1346.

- (11) Le Bail, A.; Duroy, H.; Fourquet, J. L. *Mat. Res. Bull.* **1988**, *23*, 447.
- (12) Rietveld, H. M. *J. Appl. Cryst.* **1969**, *2*, 65.
- (13) Hunter, B. A.; Howard, C. J. *LHPM-Rietica*, version 1.71: Australian Nuclear Science and Technology Organization, Menai, Australia, 2000.
- (14) *X-Area*, Stoe & Cie. GmbH, Hilpertstraße 10, D64295 Darmstadt, Germany.
- (15) *SHELXTL*, version 6.10; Bruker AXS Inc.: Madison, WI, 2000.
- (16) Jepsen, O.; Andersen O. K. *TB-LMTO*, version 47; Max-Planck-Institut für Festkörperforschung, Stuttgart, Germany, 2000.
- (17) (a) Kresse, G.; Hafner, J. *Phys. Rev. B* **1993**, *47*, 558. (b) Kresse, G.; Hafner, J. *Phys. Rev. B* **1994**, *49*, 14251.
- (18) Kresse, G.; Furthmüller, J. *Comput. Mat. Sci.* **1996**, *6*, 15.
- (19) Kresse, G.; Furthmüller, J. *Phys. Rev. B* **1996**, *54*, 11169.
- (20) von Barth, U.; Hedin, L. *J. Phys. C: Solid State Phys.* **1972**, *5*, 1629.
- (21) Lambrecht, W. R. L.; Andersen, O. K. *Phys. Rev. B* **1986**, *34*, 2439.
- (22) Dronskowski, R.; Blöchl, P. *J. Phys. Chem.* **1993**, *97*, 8617.
- (23) Dresse, G.; Joubert, D. *Phys. Rev.* **1999**, *59*, 1758.
- (24) Perdew, J. P.; Burke, K.; Ernzerhof, M. *Phys. Rev. Lett.* **1996**, *77*, 3865.
- (25) Monkhorst, H. J.; Pack, J. D. *Phys. Rev. B* **1976**, *13*, 5188.
- (26) Blöchl, P. E.; Jepsen, O.; Andersen, O. K. *Phys. Rev. B* **1994**, *49*, 16223.
- (27) Hamilton, W. C. *Acta Cryst.* **1965**, *18*, 502.
- (28) Cordier, G.; Czech E.; Schäfer, H. *J. Less-Common Met.* **1985**, *108*, 225.
- (29) Häussermann U.; Svensson C.; Lidin, S. *J. Am. Chem. Soc.* **1998**, *120*, 3867.
- (30) Pearson W. B. *Z. Kristallogr.* **1980**, *152*, 23.

- (31) Gladyshevskii, R. E.; Cenxual, K. *J. Alloys Comp.* **1996**, 266-271, 266.
- (32) Li, B.; Corbett, J. D. *Inorg. Chem.* **2006**, 45, 3861.
- (33) Grin, Yu. N.; Hiebl, K.; Rogl, P.; Godart, C.; Alleno, E. *J. Alloys Comp.* **1997**, 252, 88.
- (34) Miller, G. J. *Eur. J. Inorg. Chem.* **1998**, 523.

## 6.8 Supporting Information

### Single Crystal Refinement with 12i Site Splitting.

**Table S1.** The refinement parameters of the single crystal selected from annealed “EuAg<sub>3.5</sub>Al<sub>7.5</sub>” sample with 12i site splitting.

Empirical formula	EuAg <sub>3.5(2)</sub> Al <sub>7.5(2)</sub>
Space group	<i>Pm-3m</i> (No. 221)
Lattice parameters	<i>a</i> = 8.7208(10) Å
Volume	663.24(13) Å <sup>3</sup>
<i>Z</i>	3
$\theta$ range	2.34°-26.63°
Index ranges	$-9 \leq h \leq 11$ ; $-11 \leq k \leq 8$ ; $-9 \leq l \leq 11$
Reflections collected	2207
Independent reflections	181 ( $R_{\text{int}} = 0.2145$ )
Goodness-of-fit on $F^2$	1.201
Final <i>R</i> indices ( $I > 2\sigma(I)$ )	$R1 = 0.0578$ ; $wR2 = 0.0889$
<i>R</i> indices (all data)	$R1 = 0.0933$ ; $wR2 = 0.0966$
Largest diff. peak/hole	1.966/-1.926 e <sup>-</sup> /Å <sup>3</sup>

**Table S2.** The atomic coordinates and isotropic displacement parameters from single crystal refinement of the “EuAg<sub>3.5</sub>Al<sub>7.5</sub>” sample with 12i site splitting.

Atom	Wyck.	x	y	z	SOF	$U_{\text{iso}}/\text{Å}^2$
Eu1	3 <i>d</i>	1/2	0	0	1	0.014(1)
Ag1	1 <i>b</i>	1/2	1/2	1/2	1	0.030(2)
Ag/Al2	8 <i>g</i>	0.1657(4)	0.1657	0.1657	0.42/0.58(2)	0.027(4)
Ag3	12 <i>i</i>	0	0.356(4)	0.356	0.23 (2)	0.019(9)
Al3	12 <i>i</i>	0	0.330(4)	0.330	0.77(2)	0.009(7)
Ag/Al4	12 <i>j</i>	1/2	0.2667(3)	0.2667	0.30/0.70(1)	0.015(2)

### SEM and EDS Results of The Annealed “EuAg<sub>3</sub>Al<sub>8</sub>” and “EuAg<sub>4</sub>Al<sub>7</sub>” Samples.

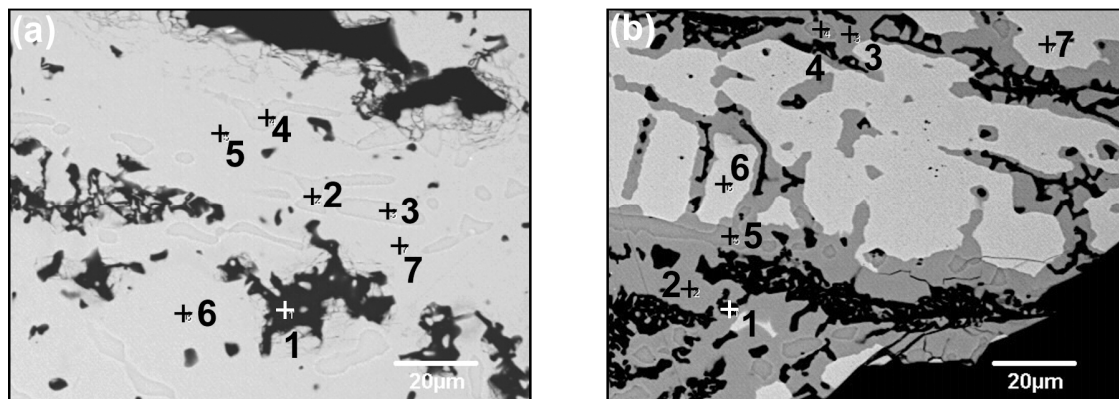


**Figure S1.** The SEM image of the “EuAg<sub>3</sub>Al<sub>8</sub>” and “EuAg<sub>4</sub>Al<sub>7</sub>” samples annealed at 500 °C for 40 days. Elementary analysis with EDS was performed and the results are listed in Table S3.

**Table S3.** The EDS composition analysis results of “EuAg<sub>3.5</sub>Al<sub>7.5</sub>” annealed at 700 °C for 10 days (spots are marked as in Figure S1).

Spot	Atomic Fraction			Composition	Structure*
	Eu	Ag	Al		
a1	0	0.011(1)	0.989(3)	Ag <sub>0.011(1)</sub> Al <sub>0.989(3)</sub>	<i>fcc</i>
b1	0.008(1)	0.036(1)	0.956(5)	Ag <sub>0.036(1)</sub> Al <sub>0.956(5)</sub>	
a2	0.199(1)	0.124(2)	0.677(6)	Eu <sub>1.00(1)</sub> Ag <sub>0.62(1)</sub> Al <sub>3.38(3)</sub>	BaAl <sub>4</sub> -type
a3	0.212(1)	0.100(2)	0.688(6)	Eu <sub>1.06(1)</sub> Ag <sub>0.50(1)</sub> Al <sub>3.44(3)</sub>	
a4	0.210(1)	0.102(1)	0.688(6)	Eu <sub>1.05(1)</sub> Ag <sub>0.51(1)</sub> Al <sub>3.44(3)</sub>	
b4	0.217(1)	0.114(2)	0.669(6)	Eu <sub>1.08(1)</sub> Ag <sub>0.57(1)</sub> Al <sub>3.34(3)</sub>	
b5	0.214(1)	0.122(2)	0.664(6)	Eu <sub>1.07(1)</sub> Ag <sub>0.61(1)</sub> Al <sub>3.32(3)</sub>	
a5	0.086(1)	0.329(2)	0.584(5)	Eu <sub>1.03(2)</sub> Ag <sub>3.95(3)</sub> Al <sub>7.01(6)</sub>	BaHg <sub>11</sub> -type
a6	0.083(1)	0.329(3)	0.588(5)	Eu <sub>1.00(2)</sub> Ag <sub>3.95(3)</sub> Al <sub>7.06(6)</sub>	
a7	0.087(1)	0.330(3)	0.583(5)	Eu <sub>1.04(2)</sub> Ag <sub>3.96(3)</sub> Al <sub>7.00(6)</sub>	
b2	0.088(1)	0.329(3)	0.584(5)	Eu <sub>1.05(2)</sub> Ag <sub>3.94(3)</sub> Al <sub>7.00(6)</sub>	BaCd <sub>11</sub> -type
b3	0.088(1)	0.328(3)	0.584(5)	Eu <sub>1.05(2)</sub> Ag <sub>3.94(3)</sub> Al <sub>7.01(6)</sub>	
b6	0.088(2)	0.440(3)	0.472(5)	Eu <sub>1.05(2)</sub> Ag <sub>5.28(4)</sub> Al <sub>5.67(6)</sub>	BaCd <sub>11</sub> -type
b7	0.085(2)	0.437(3)	0.478(5)	Eu <sub>1.02(2)</sub> Ag <sub>5.24(4)</sub> Al <sub>5.73(6)</sub>	

\* The structures are assigned by comparing the compositions and the phases identified from powder XRD patterns.

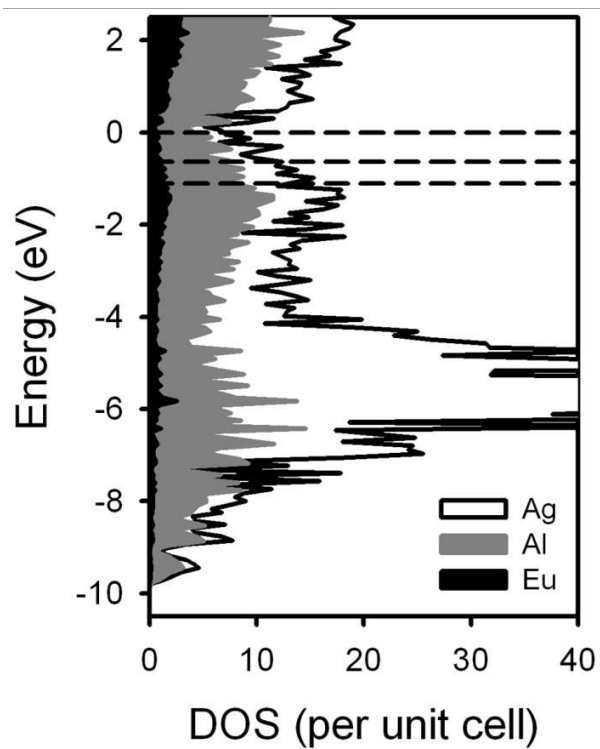
## The Details of Computational Models.

**Table S4.** The model structures for computation.\*

Wyck	Fractional Coordinates			Model 1	Model 2	Model 3	Model 4	Model 5	Wyck	Fractional Coordinates			Model 1	Model 2	Model 3	Model 4	Model 5
	x	y	z							x	y	z					
3d	1/2	0	0						12i	0.3453	0	0.6547	Al	Al	Al	Al	Al
	0	1/2	0			Eu				0.6547	0.3453	0	Al	Al	Ag	Ag	Ag
	0	0	1/2							0.6547	0	0.3453	Al	Al	Al	Al	Al
1b	1/2	1/2	1/2			Ag			12j	0.3453	0.6547	0	Al	Al	Ag	Al	Al
8g	0.164	0.164	0.164	Ag	Ag	Ag	Ag	Ag		0.6547	0	0.6547	Al	Al	Al	Ag	Ag
	0.836	0.836	0.164	Ag	Ag	Ag	Ag	Ag		0.6547	0.6547	0	Al	Al	Al	Al	Al
	0.836	0.164	0.836	Al	Al	Al	Al	Al		0.5	0.2661	0.2661	Ag	Ag	Al	Al	Al
	0.164	0.836	0.836	Al	Al	Al	Al	Al		0.5	0.7339	0.2661	Al	Al	Ag	Ag	Ag
	0.164	0.164	0.836	Al	Ag	Ag	Ag	Ag		0.5	0.2661	0.7339	Ag	Ag	Al	Al	Al
	0.836	0.836	0.836	Al	Al	Al	Al	Al		0.5	0.7339	0.7339	Al	Al	Al	Al	Al
	0.164	0.836	0.164	Ag	Al	Ag	Ag	Ag		0.2661	0.5	0.2661	Ag	Ag	Ag	Ag	Ag
0.836	0.164	0.164	Ag	Ag	Al	Al	Al	0.2661	0.2661	0.5	Al	Al	Ag	Ag	Ag		
12i	0	0.3453	0.3453	Ag	Ag	Al	Al	Al	0.2661	0.5	0.7339	Ag	Ag	Al	Al	Al	
	0	0.6547	0.3453	Al	Al	Al	Al	Al	0.7339	0.2661	0.5	Al	Al	Ag	Ag	Ag	
	0	0.3453	0.6547	Al	Ag	Ag	Ag	Al	0.7339	0.5	0.2661	Al	Al	Al	Al	Al	
	0	0.6547	0.6547	Al	Al	Al	Al	Ag	0.2661	0.7339	0.5	Al	Al	Al	Al	Al	
	0.3453	0	0.3453	Ag	Ag	Al	Al	Al	0.7339	0.5	0.7339	Al	Al	Al	Al	Al	
0.3453	0.3453	0	Ag	Al	Al	Al	Al	0.7339	0.7339	0.5	Al	Al	Al	Al	Al		

\* The five models have the same composition,  $\text{EuAg}_4\text{Al}_7$ ; and they also have the same Ag/Al ratio on each Wyckoff site. Model 1~4 are random models;

Model 5 is obtained through maximizing Ag–Al contacts.

**The DOS Curve of Model 5 from VASP Calculation.**

**Figure S2.** The DOS curve of Model 5 calculated using VASP. It is very close to those calculated with TB-LMTO-ASA. The three dashed straight lines are the locations of the Fermi levels when  $vec =$  (from top) 2.45, 2.30, and 2.10 per atom.

### The C Codes to maximize Ag-Al contacts for the BaHg<sub>11</sub>-type EuAg<sub>4</sub>Al<sub>7</sub>

```

#include <stdio.h>
#include <math.h>
#include <stdlib.h>
main()
{ float commfactor1=8.70063; /*lattice parameter a in Angstrom*/
  float AXIS[3][3]={1,0,0},{0,1,0},{0,0,1};
  float FRACTCOORD[33][3]={};
  float CARTCOORD[33][3]={};
  float FRACTVECT[27][3]={0,0,0},{1,0,0},{-1,0,0},{0,1,0},{0,-1,0},{0,0,1},{0,0,-1},{1,1,0},{1,-1,0},{-1,1,0},{-1,-1,0},{0,1,1},{0,-1,1},{0,1,-1},{0,-1,-1},{1,0,1},{1,0,-1},{-1,0,1},{-1,0,-1},{1,1,1},{1,1,-1},{1,-1,1},{1,-1,-1},{-1,1,1},{-1,1,-1},{-1,-1,1},{-1,-1,-1}}; /*vectors pointing to the central primitive cell and all 26 neighboring cells: 6 face-sharing, 8 vertex-sharing, and 12 edge sharing*/
  float CARTVECT[27][3]={};
  long m1,m2,m3,m4,p,n;
  int i,j,k;
  int counter1, counter2, counter3;
  float CONFIG[33]={};
  float distance;
  float NEIGHBORS[27][3]={};
  float bondnumber1=0;
  float bondnumber2=0;
  float bondnumber3=0;
  FILE *writeout,*readin;
  float MAX[50][36]={};
  double numberdone=0.0;
  /*Read the fractional coordinates.*/
  readin=fopen("allsites.txt","r");
  for (i=0;i<33;i++)
    { for (j=0;j<3;j++)
      { fscanf(readin,"%f\t",&FRACTCOORD[i][j]);
        fscanf(readin,"\n");
      }
    }
  fclose(readin);

```



```

/*Converting fractional coordinates into cartesian coordinates.*/
for (i=0;i<33;i++)
  { for (j=0;j<3;j++)
      { CARTCOORD[i][j]=(FRACTCOORD[i][0]*AXIS[0][j]+FRACTCOORD[i][1]*AXIS[1][j]+FRACTCOORD[i][2]*
AXIS[2][j])*commfactor1;}
  }
/*Converting lattice vectors into cartesian vectors.*/
for (i=0;i<27;i++)
  { for (j=0;j<3;j++)
      { CARTVECT[i][j]=(FRACTVECT[i][0]*AXIS[0][j]+FRACTVECT[i][1]*AXIS[1][j]+FRACTVECT[i][2]*AXIS[2][j])
*commfactor1;}
  }
/*Generate coloring schemes and count the number of heteroatomic bonds.*/
/*The method is the same with that employed in the BaCd11-type structure except that there are now
restrictions to each site.*/
/*There are totally 33 positions. The first one (1b) is assigned to Ag (1).*/
/*Positions 2 to 9 (8g) have to have 4 Ag (1) and 4 Al (0).*/
/*Positions 10 to 21 (12i) have to have 3 Ag (1) and 9 Al (0).*/
/*Positions 22 to 33 (12j) have to have 4 Ag (1) and 8 Al (0).*/
m1=0;
for (i=0;i<32;i++)
  { n=1;
    for (j=1;j<=i;j++)
      { n=n*2;}
    m1=m1+n;
  }
m2=0;
for (i=0;i<11;i++)
  { n=1;
    for (j=1;j<=i;j++)
      { n=n*2;}
    m2=m2+n;
  }
m3=0;

```

```

for (i=0;i<21;i++)
{
n=1;
for (j=1;j<=i;j++)
{
n=n*2;}
m3=m3+n;
}
m4=m1-m3;
CONFIG[0]=1; /*The 1b site is assigned to Ag (1).*/
for (n=m2;n<=m4;n++)
{
for (i=1;i<33;i++)
{
CONFIG[i]=0;}
i=1;
p=n;
while (p>=1)
{
CONFIG[i]=p%2;
p=p/2;
i++;
}
counter1=0;
counter2=0;
counter3=0;
for (i=1;i<9;i++)
{
if (CONFIG[i]==1)
{
counter1=counter1+1;}
}
for (i=9;i<21;i++)
{
if (CONFIG[i]==1)
{
counter2=counter2+1;}
}
for (i=21;i<33;i++)
{
if (CONFIG[i]==1)
{
counter3=counter3+1;}
}
if ((counter1==4)&&(counter2==3)&&(counter3==4))

```

```

{ bondnumber1=0;
bondnumber2=0;
bondnumber3=0;
for (i=0;i<33;i++)
{ for (j=i;j<33;j++)
    { if (abs(CONFIG[i]-CONFIG[j])==1)
        { for (k=0;k<27;k++)
            { NEIGHBORS[k][0]=CARTCOORD[j][0]+CARTVECT[k][0];
              NEIGHBORS[k][1]=CARTCOORD[j][1]+CARTVECT[k][1];
              NEIGHBORS[k][2]=CARTCOORD[j][2]+CARTVECT[k][2];
            }
          for (k=0;k<27;k++)
            { distance=sqrt((CARTCOORD[i][0]-NEIGHBORS[k][0])*(CARTCOORD[i][0]-
NEIGHBORS[k][0])+(CARTCOORD[i][1]-NEIGHBORS[k][1])*(CARTCOORD[i][1]-
NEIGHBORS[k][1])+(CARTCOORD[i][2]-NEIGHBORS[k][2])*(CARTCOORD[i][2]-NEIGHBORS[k][2]));
              if (distance<2.75)
                { bondnumber1=bondnumber1+1;}
              if (distance<2.80)
                { bondnumber2=bondnumber2+1;}
              if (distance<2.90)
                { bondnumber3=bondnumber3+1;}
            }
          }
        }
    }
  }
for (i=0;i<50;i++)
{ if
((bondnumber1>MAX[i][33]) || ((bondnumber1==MAX[i][33])&&(bondnumber2>MAX[i][34])) || ((bondnumber
1==MAX[i][33])&&(bondnumber2==MAX[i][34])&&(bondnumber3>MAX[i][35])))
    { for (j=0;j<33;j++)
        { MAX[i][j]=CONFIG[j];}
      MAX[i][33]=bondnumber1;
      MAX[i][34]=bondnumber2;
      MAX[i][35]=bondnumber3;
    }
  }
}

```

```

        i=49;
        }
    }
    numberdone=numberdone+1;
}
}
writeout=fopen("max.txt","w");
for (i=0;i<50;i++)
{ for (j=0;j<36;j++)
    { fprintf(writeout,"%3.0f ",MAX[i][j]);
      fprintf(writeout,"\n");
    }
  fprintf(writeout,"Total: %f\n",numberdone);
  fclose(writeout);
}

```

**The input file "allsites.txt":**

```

0.5    0.5    0.5
0.164  0.164  0.164
0.836  0.836  0.164
0.836  0.164  0.836
0.164  0.836  0.836
0.164  0.164  0.836
0.836  0.836  0.836
0.164  0.836  0.164
0.836  0.164  0.164
0      0.3453  0.3453
0      0.6547  0.3453
0      0.3453  0.6547
0      0.6547  0.6547
0.3453 0      0.3453
0.3453 0.3453 0
0.3453 0      0.6547
0.6547 0.3453 0
0.6547 0      0.3453

```

0.3453 0.6547 0  
0.6547 0 0.6547  
0.6547 0.6547 0  
0.5 0.2661 0.2661  
0.5 0.7339 0.2661  
0.5 0.2661 0.7339  
0.5 0.7339 0.7339  
0.2661 0.5 0.2661  
0.2661 0.2661 0.5  
0.2661 0.5 0.7339  
0.7339 0.2661 0.5  
0.7339 0.5 0.2661  
0.2661 0.7339 0.5  
0.7339 0.5 0.7339  
0.7339 0.7339 0.5

## Chapter 7

### Stacking Polymorphs in $Gd_5Si_4$ , $Gd_5Ge_4$ , and $Gd_5Si_2Bi_2$ :

#### A Computational Investigation

##### 7.1 Introduction

$RE_5T_4$  (RE = rare earth metals; T = triel, tetrel, pnictogen, or their combinations) are a class of materials showing exceptional magnetocaloric effects (MCEs)<sup>1-4</sup> and have been intensively studied.<sup>5-7</sup> Their crystal structures feature the same motif – isocompositional  $RE_5T_4$  “slabs”. Depending on composition, the stacking sequence of these “slabs” varies considerably.

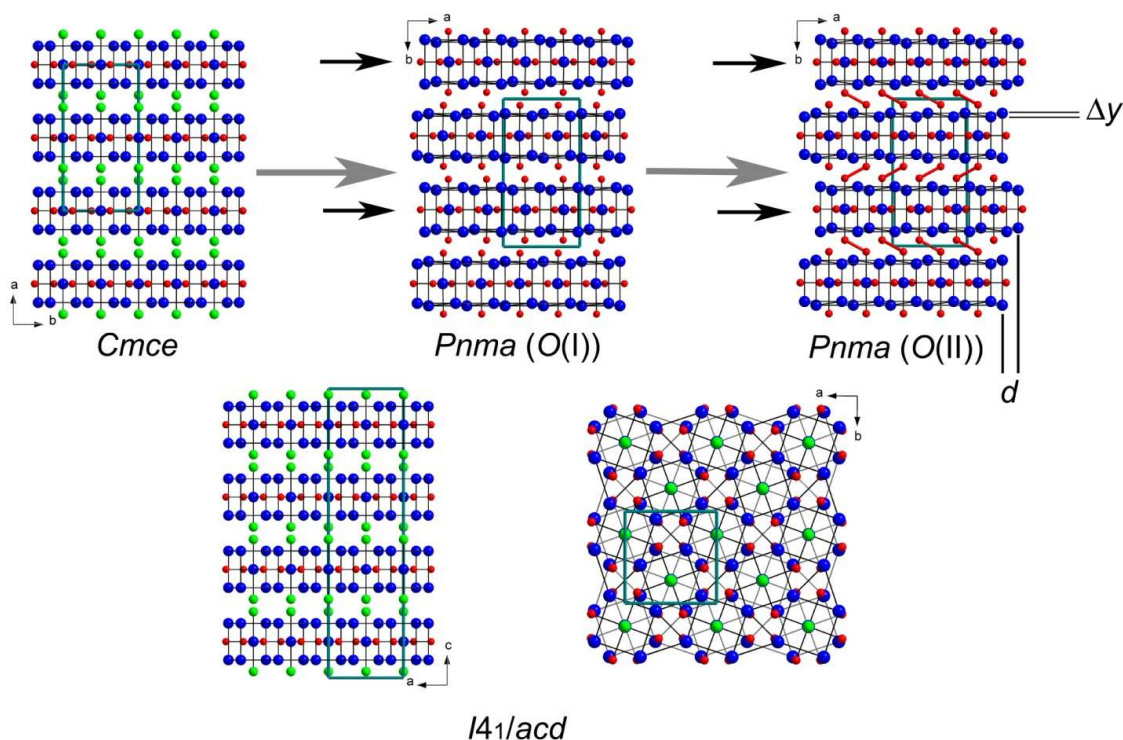


**Figure 1.** The structures of  $Gd_5T_4$  in  $Cmce$ ,  $Pnma (O(I))$ ,  $Pnma (O(II))$ , and  $I4_1/acd$ . Blue: Gd; green: Bi; red: Si/Ge.

In this report, we are studying three examples,  $Gd_5Si_4$ ,  $Gd_5Ge_4$ , and  $Gd_5Si_2Bi_2$ , in four structure types,  $Pnma-O(I)$  (adopted by  $Gd_5Si_4$ <sup>8</sup>),  $Pnma-O(II)$  (adopted by  $Gd_5Ge_4$ <sup>7</sup>),  $I4_1/acd$  (adopted by  $Gd_5Si_2Bi_2$ <sup>9</sup>), and  $Cmce$  (adopted by  $Gd_5Si_{2.5}Bi_{1.5}$ <sup>9</sup>). These structures are shown in Figure 1.  $Pnma$  is a subgroup of  $Cmce$  and the  $Pnma$  structures,  $O(I)$  and  $O(II)$ , are distortions from the  $Cmce$  structure by sliding every second slab along the  $a$  direction in the  $Pnma$  setting, quantized with  $d$  as shown in Figure 1.

Also, the slabs in the *Cmce* structure are flat but “buckled” in the *Pnma* structures, an effect which is shown as  $\Delta y$  in Figure 1. The differences between *O(I)* and *O(II)* are the magnitudes of  $d$  and  $\Delta y$ . On the other hand, the *Cmce* structure differs from the *I4<sub>1</sub>/acd* structure in the periodicity of the stacking sequence: in *Cmce*, every slab repeats every second slab but in *I4<sub>1</sub>/acd*, every slab repeats every fourth slab. If viewed along the stacking direction (the lower right picture in Figure 1), two adjacent slabs in the *Cmce* and *I4<sub>1</sub>/acd* structures have nearly identical displacements. In *Cmce*, displacement of the third slab reverses the first shift, whereas in *I4<sub>1</sub>/acd* displacement of the third slab is orthogonal to the first shift. As a result, the *Cmce* structure has an “...ABABABAB...” stacking sequence and the *I4<sub>1</sub>/acd* structure has an “...ABCDABCD...” stacking sequence. Moreover, the *Pnma* structures also show a stacking sequence “...ABABABAB...”.

The differences in stacking sequence between these structures are intriguing. In this report, by studying them with quantum mechanical calculations, we are attempting to rationalize the causes of these differences. Firstly, we tried to elucidate the reason of the distortion from *Cmce* to *Pnma*. Special attention was paid to the T-T interactions between slabs, which get stronger as  $d$  increases. We then compared *Cmce* and *I4<sub>1</sub>/acd* to investigate the differences between them.

## 7.2 Computational Details

### 7.2.1 Computational Model Structures

Besides the stacking sequence, these structures are also different within a single slab. For instance, the *Cmce* and *I4<sub>1</sub>/acd* structures have flat slabs ( $\Delta y = 0$ ) while the *Pnma* structures have buckled slabs ( $\Delta y \neq 0$ ). To eliminate the differences of a single slab and to focus on only the effects of the stacking sequence, we developed model structures with “regular slabs”, which are constructed according to the experimental slabs but are more symmetrical. For demonstration, we compare the experimental and the “regular slab” models of  $\text{Gd}_5\text{Si}_4$  in Table 1 and Figure 2. The “regular slab” models have the same unit cell volume and  $b$  lattice parameter with the experimental structure. The  $a$  and  $c$  parameters in the model structures are set equal to the geometric averages of the experimental  $a$  and  $c$  values. The “regular slabs” are flat, meaning that the  $y$  coordinates of the Gd1 and Gd2 sites are equal and are obtained by averaging the experimental  $y$  coordinates of Gd1 and Gd2 (see Table 1; e.g.,  $0.1098 = (0.09726 + 0.12232)/2$ ). The  $x$  and  $z$  coordinates are arranged so that viewed from the direction perpendicular to the “regular slab”, Gd atoms form two parallel  $3^2434$  nets of precise squares and equilateral triangles, while the Si atoms are located above/below the centers of each triangle and additional Gd atoms (Gd3) are above/below the center of each square (Figure 2). This slab satisfies

the symmetry requirements of all three space groups, and thus, can be stacked into all three structure types.

### 7.2.2 VASP Calculations

We used the *Vienna ab initio simulation package* (VASP)<sup>10-12</sup> to calculate the energy terms of the “regular slab” models. The projector augmented-wave (PAW)<sup>13</sup> pseudopotentials were adopted with the Perdew-Burke-Ernzerhof generalized gradient approximation (PBE-GGA).<sup>14</sup> The energy cutoffs are 245.3 eV for Gd<sub>5</sub>Si<sub>4</sub> and Gd<sub>5</sub>Si<sub>2</sub>Bi<sub>2</sub> and 173.8 eV for Gd<sub>2</sub>Ge<sub>4</sub>. The first Brillouin zone was sampled with a  $7 \times 7 \times 7$  Monkhorst-Pack mesh.<sup>15</sup> The “regular slab” model structures were also optimized using the conjugate gradient algorithm.<sup>16</sup> Here, a  $5 \times 5 \times 5$  Monkhorst-Pack mesh was used. The total energy,  $E_{\text{TOT}}$ , is partitioned into an electrostatic term,  $E_{\text{ES}}$ , and an electronic term,  $E_{\text{electronic}}$ , to apply the analysis demonstrated in Chapter 3 and 4.

**Table 1.** The comparison of lattice parameters and atomic positions between the experimental structure and the “regular slab” model of Gd<sub>5</sub>Si<sub>4</sub>.

		Experimental Structure ( <i>Pnma</i> ) <sup>8</sup>			“Regular Slab” <i>Pnma</i> Models		
		$a = 7.4836(6) \text{ \AA}, b = 14.745(12) \text{ \AA},$			$a = c = 7.6152 \text{ \AA}, b = 14.745 \text{ \AA}.$		
		$c = 7.7491(6) \text{ \AA}, V = 213.77 \text{ \AA}^3/\text{f.u.}, d/a = 0.21$			$V = 213.77 \text{ \AA}^3/\text{f.u.}, d/a \text{ tunable}.$		
Atom	Wyck.	$x$	$y$	$z$	$x$	$y$	$z$
Gd1	$8d$	0.47087(4)	0.09726(2)	0.68267(4)	$0.5670 - d/2a$	0.1098	0.6830
Gd2	$8d$	0.31616(4)	0.12232(2)	0.17963(4)	$0.4330 - d/2a$	0.1098	0.1830
Gd3	$4c$	0.14402(5)	1/4	0.51095(6)	$0.25 - d/2a$	1/4	0.5000
Si1	$8d$	0.1437(2)	0.0399(1)	0.4728(2)	$0.25 - d/2a$	0.0399	0.5000
Si2	$4c$	0.0211(3)	1/4	0.0993(3)	$0.6443 - d/2a$	1/4	0.1057
Si3	$4c$	0.2588(3)	1/4	0.8758(3)	$0.3557 - d/2a$	1/4	0.8943

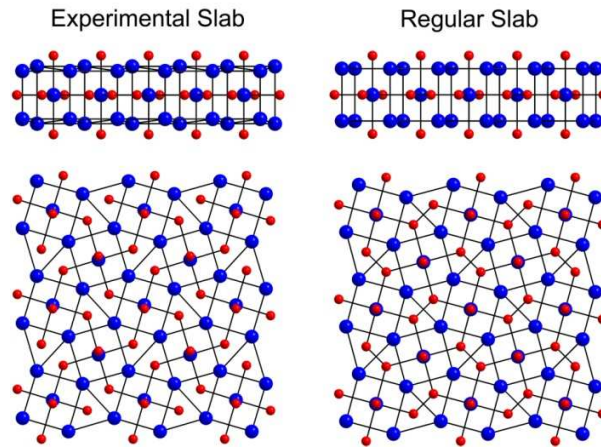


**Figure 2.** The comparison between an experimental Gd<sub>5</sub>Si<sub>4</sub> slab and a regular Gd<sub>5</sub>Si<sub>4</sub> slab.



### 7.2.3 LMTO Calculations

The Stuttgart *Tight-Binding, Linear-Muffin-Tin Orbital* program with *Atomic Sphere Approximation* (TB-LMTO-ASA)<sup>17</sup> was employed to calculate the crystal orbital Hamiltonian population (COHP)<sup>18</sup> of the T-T interactions between two neighboring slabs. The exchange and correlation energy was treated with the von Barth-Hedin local density approximation.<sup>19</sup> The basis sets include  $6s$ ,  $6p$  (down-folded),<sup>20</sup> and  $5d$  for Gd,  $3s$  and  $3p$  for Si,  $4s$  and  $4p$  for Ge, and  $5s$  and  $5p$  for Bi. Reciprocal space integrations were performed with an  $8 \times 4 \times 8$   $k$ -points mesh.

## 7.3 Results and Discussions

### 7.3.1 *Cmce* vs *Pnma*

As mentioned above, the difference between the *Cmce* and *Pnma* stacking sequences can be quantified with  $d$  as shown in Figure 1. In *Cmce* stacking, as in  $\text{Gd}_5\text{Si}_{2.5}\text{Bi}_{1.5}$ ,<sup>9</sup>  $d = 0$ . The crystallographic data of  $\text{Gd}_5\text{Si}_4$  (*Pnma*,  $O(\text{I})$ )<sup>8</sup> and  $\text{Gd}_5\text{Ge}_4$  (*Pnma*,  $O(\text{II})$ )<sup>7</sup> generate, respectively,  $d/a = 0.212$  and  $0.081$ . So,  $O(\text{I})$  has larger  $d$  than  $O(\text{II})$ , an effect which leads to shorter T-T distances between two neighboring slabs – the shortest inter-slab Ge-Ge distance in  $\text{Gd}_5\text{Ge}_4$  is  $3.635 \text{ \AA}$ <sup>7</sup> whereas its counterpart Si-Si in  $\text{Gd}_5\text{Si}_4$  is  $2.488 \text{ \AA}$ .<sup>8</sup> So, Si-Si bonding seems to be one of the driving forces for the *Cmce* to *Pnma* distortion; the validity of this assumption needs to be tested.

To study the effects of  $d$ , we constructed *Pnma* “regular slab” model structures with tunable  $d/a$  values, as shown in Table 1. The *Cmce* stacking was treated as *Pnma* with  $d/a = 0$ . Also, we examined three compositions:  $\text{Gd}_5\text{Si}_4$ ,  $\text{Gd}_5\text{Ge}_4$ , and  $\text{Gd}_5\text{Si}_2\text{Bi}_2$ . For  $\text{Gd}_5\text{Si}_2\text{Bi}_2$ , Bi was assigned to the T sites between slabs and Si to the T sites within slabs, just as crystallography reveals.<sup>9</sup> To eliminate any volume effects, each composition was built into “regular slab” model structures at three volumes:  $213.77$ ,  $221.70$  and  $244.73 \text{ \AA}^3/\text{f.u.}$ , which are the experimental volumes, respectively, of  $\text{Gd}_5\text{Si}_4$ ,  $\text{Gd}_5\text{Ge}_4$ , and  $\text{Gd}_5\text{Si}_2\text{Bi}_2$ . Different compositions were then compared at the same volumes.

The energy terms calculated using VASP are plotted in Figure 3 as a function of  $d/a$ . Given the same “regular slabs”, regardless of composition and volume, the distortion from *Cmce* to *Pnma*, i.e., increasing  $d/a$ , invariably causes increasing  $E_{\text{ES}}$  rising and decreasing  $E_{\text{electronic}}$ . For  $E_{\text{TOT}}(d/a)$ , composition does differ –  $\text{Gd}_5\text{Si}_4$  reveals a clear minimum around  $d/a = 0.25$ ,  $\text{Gd}_5\text{Ge}_4$  also has a minimum around  $d/a = 0.21$ , but it is less perceivable than in  $\text{Gd}_5\text{Si}_4$ , and  $\text{Gd}_5\text{Si}_2\text{Bi}_2$  has  $E_{\text{TOT}}$  monotonously increasing without any perceptible minimum.

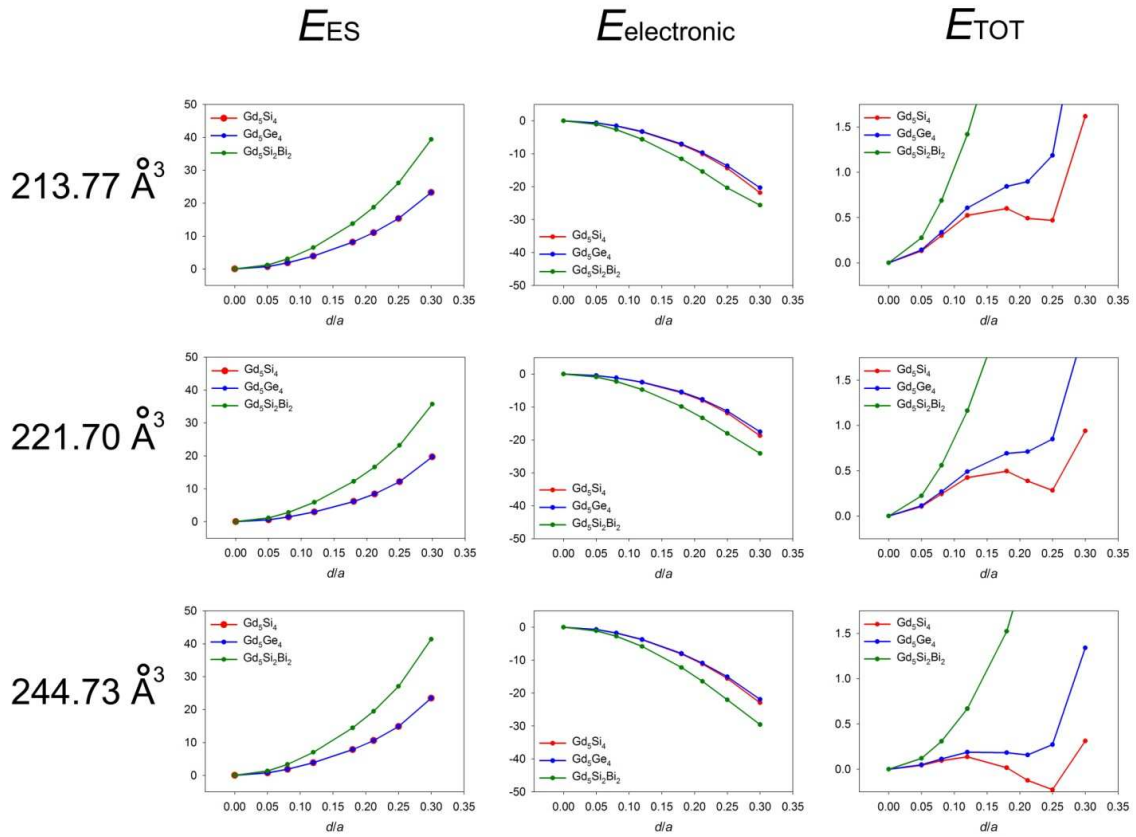


**Figure 3.** The effects of  $d/a$  on energy terms of the “regular slab” models.

It is very probable that the minimum in  $E_{TOT}$  is caused by the inter-slab T-T interactions as assumed above. This can be seen by correlating the  $Gd_5Si_4$   $E_{TOT}$  curves with the Si-Si COHP curves (Figure 4). For hypothetical  $Cmce$  and  $O(II)$  structures, the Si-Si interactions are weak. When  $d/a$  increases to 0.12 and 0.18, where the  $Gd_5Si_4$   $E_{TOT}$  curves crest, the interactions are significant and there is a sharp antibonding peak right below the Fermi level. As  $E_{TOT}$  approaches its minimum, i.e., at  $d/a = 0.21$  and 0.25, the sharp antibonding peak diminishes. The inter-slab Ge-Ge and Bi-Bi COHP curves reveal the same pattern. This indicates that at  $d/a = 0.12$  and 0.18, T-T antibonding states are still largely populated. Further increasing  $d/a$  will shorten the inter-slab T-T distances and the energies of antibonding states will rise, shift above the Fermi level, and be depleted. This diminishing of the sharp antibonding peak will contribute to a drop in electronic energy and cause the minima in  $E_{TOT}$ .

The lack of a minimum in the  $E_{TOT}$  curve of  $Gd_5Si_2Bi_2$  can be attributed to its rapidly rising  $E_{ES}$  when  $d/a$  increases (Figure 3). The reason for such rapid increase in  $E_{ES}$  is that the core (nucleus plus core electrons) of Bi has +5 charge (could Bi be treated as a core with +3 charge and 2 inert pair

electrons?), one more than the +4 values of Si and Ge cores. So, when Bi atoms get closer, they bear more repulsion between the cores than Si and Ge. Indeed,  $E_{\text{electronic}}$  also drops more rapidly in  $\text{Gd}_5\text{Si}_2\text{Bi}_2$  than the other two compositions, but it does not compensate for the increase in  $E_{\text{ES}}$ . For instance, at  $d/a = 0.30$ ,  $E_{\text{ES}}$  of  $\text{Gd}_5\text{Si}_2\text{Bi}_2$  is about 40 eV higher than those of  $\text{Gd}_5\text{Si}_4$  and  $\text{Gd}_5\text{Ge}_4$ , but  $E_{\text{electronic}}$  is only less than 10 eV lower. Thus, the rapidly rising  $E_{\text{ES}}$  will overwhelm any electronic effects, including Bi-Bi bonding, causing  $E_{\text{TOT}}$  to rise monotonously.

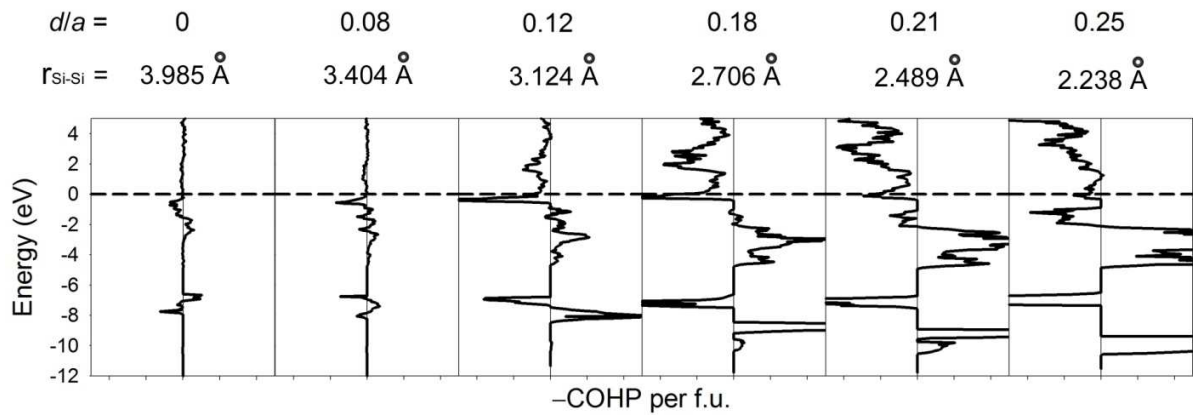


**Figure 4.** The effects of  $d/a$  on the inter-slab Si-Si COHP in  $\text{Gd}_5\text{Si}_4$  (calculated at  $213.77 \text{ \AA}^3/\text{f.u.}$ ).

**Table 2.** The structures obtained through the optimization of the “regular slab” model structures.

		$\text{Gd}_5\text{Si}_4$ opt. $O(I)$			$\text{Gd}_5\text{Si}_4$ opt. $O(II)$			$\text{Gd}_5\text{Si}_4$ opt. $Cmce$		
		$a = 7.5145 \text{ \AA}, b = 14.6993 \text{ \AA}, c = 7.7413 \text{ \AA}, d/a = 0.21$			$a = 7.5759 \text{ \AA}, b = 14.6689 \text{ \AA}, c = 7.7413 \text{ \AA}, d/a = 0.09$			$a = 7.6259 \text{ \AA}, b = 14.6820 \text{ \AA}, c = 7.6371 \text{ \AA}, d/a = 0$		
Atom	Wyck.	$x$	$y$	$z$	$x$	$y$	$z$	$x$	$y$	$z$
Gd1	$8d$	0.4656	0.0996	0.6848	0.4870	0.0993	0.3189	0.4277	0.1102	0.3271
Gd2	$8d$	0.3141	0.1223	0.1800	0.1296	0.1181	0.6656	0.0723	0.1102	0.6729
Gd3	$4c$	0.1437	1/4	0.5118	0.2968	1/4	0.0006	1/4	1/4	0
Si1	$8d$	0.1414	0.0408	0.4727	0.2907	0.0426	0.9653	1/4	0.0451	0
Si2	$4c$	0.0180	1/4	0.1028	0.4214	1/4	0.6043	0.3645	1/4	0.6158
Si3	$4c$	0.2588	1/4	0.8749	0.1908	1/4	0.3724	0.1355	1/4	0.3842
		$\text{Gd}_5\text{Ge}_4$ opt. $O(II)$			$\text{Gd}_5\text{Ge}_4$ opt. $Cmce$			$\text{Gd}_5\text{Si}_2\text{Bi}_2$ opt. $Cmce$		
		$a = 7.6989 \text{ \AA}, b = 14.7893 \text{ \AA}, c = 7.7882 \text{ \AA}, d/a = 0.08$			$a = 7.7319 \text{ \AA}, b = 14.8095 \text{ \AA}, c = 7.7444 \text{ \AA}, d/a = 0$			$a = 7.9527 \text{ \AA}, b = 15.4502 \text{ \AA}, c = 7.9671 \text{ \AA}, d/a = 0$		
Atom	Wyck.	$x$	$y$	$z$	$x$	$y$	$z$	$x$	$y$	$z$
Gd1	$8d$	0.4760	0.1010	0.3218	0.4249	0.1105	0.3302	0.4225	0.1258	0.3312
Gd2	$8d$	0.1229	0.1168	0.6610	0.0751	0.1105	0.6698	0.0863	0.1274	0.6674
Gd3	$4c$	0.2882	1/4	0.9983	1/4	1/4	0	0.2542	1/4	0.0006
Si1	$8d$	0.2815	0.0437	0.9664	1/4	0.0453	0	0.2531	0.0417	0.9967
Si2	$4c$	0.4183	1/4	0.6151	0.3734	1/4	0.6251	0.3838	1/4	0.6276
Si3	$4c$	0.1717	1/4	0.3636	0.1265	1/4	0.3749	0.1249	1/4	0.37

We executed structural optimization at fixed volumes for all “regular slab” models using VASP. The optimized structures and their energy terms are listed, respectively, in Tables 2 and 3. For  $\text{Gd}_5\text{Si}_4$ , the

model structures with  $d/a > 0.18$  were optimized into a same  $O(I)$  structure; the models with  $d/a$  between 0.05 and 0.12 were optimized into a same  $O(II)$  structure; and the model structure with  $d/a = 0$  stayed as  $Cmce$  during optimization. For all of these three optimized structures, the  $O(I)$  structure gives the lowest  $E_{TOT}$  and it is very close to the experimental structure shown in Table 1. Comparing its energy terms to those of the optimized  $Cmce$  structure, it has higher  $E_{ES}$  and lower  $E_{electronic}$ , indicating that the  $O(I)$  structure is stabilized by electronic effects. The optimized  $O(II)$  structure is also lower in  $E_{TOT}$  than the  $Cmce$  structure. However, opposite to  $O(I)$ , it is caused by a lower  $E_{ES}$ , not  $E_{electronic}$ .

**Table 3.** The energy terms of the optimized structures.

	Gd <sub>5</sub> Si <sub>4</sub> opt. $O(I)$	Gd <sub>5</sub> Si <sub>4</sub> opt. $O(II)$	Gd <sub>5</sub> Si <sub>4</sub> opt. $Cmce$	Gd <sub>5</sub> Ge <sub>4</sub> opt. $O(II)$	Gd <sub>5</sub> Ge <sub>4</sub> opt. $Cmce$
$E_{ES}$ (eV/f.u.)	3.0170	-5.9170	0	-5.3908	0
$E_{electronic}$ (eV/f.u.)	-3.1999	5.8687	0	5.3640	0
$E_{TOT}$ (eV/f.u.)	-0.1828	-0.0483	0	-0.0268	0

Optimization only located two structures in Gd<sub>5</sub>Ge<sub>4</sub>. The “regular slab”  $Cmce$  model stayed as  $Cmce$ . All the others were optimized into an  $O(II)$  structure, which is close to the experimental structure of Gd<sub>5</sub>Ge<sub>4</sub>.<sup>7</sup> It offers lower  $E_{TOT}$  than the optimized  $Cmce$  structure and, just as in Gd<sub>5</sub>Si<sub>4</sub>, is because of its lower  $E_{ES}$ , not  $E_{electronic}$ . All Gd<sub>5</sub>Si<sub>2</sub>Bi<sub>2</sub> “regular slab” models were optimized into an  $Cmce$  structure, indicating that there are no stable or metastable  $Pnma$  structures.

In conclusion, the distortion from  $Cmce$  to  $Pnma$  in Gd<sub>5</sub>Si<sub>4</sub> and Gd<sub>5</sub>Ge<sub>4</sub> are caused by different reasons. For Gd<sub>5</sub>Si<sub>4</sub>, it is caused by electronic reasons, among which is the inter-slab Si-Si bonding. For Gd<sub>5</sub>Ge<sub>4</sub>, it is caused by nuclei or cores – the atomic arrangement in the  $O(II)$  structure affords lower electrostatic energy. The calculation results on Gd<sub>5</sub>Si<sub>2</sub>Bi<sub>2</sub> can explain why Gd<sub>5</sub>Si<sub>2.5</sub>Bi<sub>1.5</sub> prefers the  $Cmce$  to the  $Pnma$  structure – the Bi core has larger charge (+5) than Si/Ge (+4) so replacing Si/Ge with Bi between slabs will lead to stronger repulsion and thus larger  $E_{ES}$ , preventing the distortion.

### 7.3.2 $Cmce$ vs $I4_1/acd$ in Gd<sub>5</sub>Si<sub>2</sub>Bi<sub>2</sub>

While the distortion from  $Cmce$  to  $Pnma$  can be described with two neighboring slabs, we have to consider at least three slabs to see the difference between  $Cmce$  and  $I4_1/acd$ . If we only consider two neighboring slabs in “regular slab” model structures,  $Cmce$  and  $I4_1/acd$  stackings are the same, meaning that there is no short range geometrical difference between these two stacking sequences.

The difference occurs when we consider the second nearest slab, which is one slab ( $30.700/4 = 7.675$  Å) away. Such a long range structural difference is not expected to generate any significant differences. This is confirmed by comparing the energy terms of “regular slab” *Cmce* and  $I4_1/acd$  structures at the same volume ( $244.73 \text{ \AA}^3/\text{f.u.}$ ). Table 5 shows that  $E_{\text{ES}}$  is almost equal in these two structure types while  $E_{\text{electronic}}$  and  $E_{\text{TOT}}$  are both 2 meV/f.u. lower in the  $I4_1/acd$  stacking, which is not sufficient to explain the structural preference. Moreover, we isotropically varied the volumes of these two model structures and plotted the  $E(V)$  curves (Figure 5) of them and they are right on top of each other. Therefore, if we stack the same slabs in the *Cmce* and  $I4_1/acd$  sequences, they will give the same energy and even the same compressibility. Stacking itself does not make the difference between them. Their difference must stem from the geometric differences with a single slab.

**Table 4.** The comparison between the experimental structure, the “regular slab”  $I4_1/acd$  model structure, and the structure obtained from structural optimization of the “regular slab”  $I4_1/acd$  model.

	Experimental			“Regular Slab”			Optimized		
$a$ (Å)	7.9858(9)			7.9858			7.9613		
$c$ (Å)	30.700(6)			30.700			30.8893		
Gd1	0.3322	0.9168	0.06152	0.3170	0.9330	0.0615	0.3321	0.9183	0.0633
Gd2	0	1/4	3/8	0	1/4	3/8	0	1/4	3/8
Bi1	0	1/4	0.97841	0	1/4	0.9784	0	1/4	0.9791
Si2	0.3658	0.6158	1/8	0.3493	0.5993	1/8	0.3711	0.6211	1/8

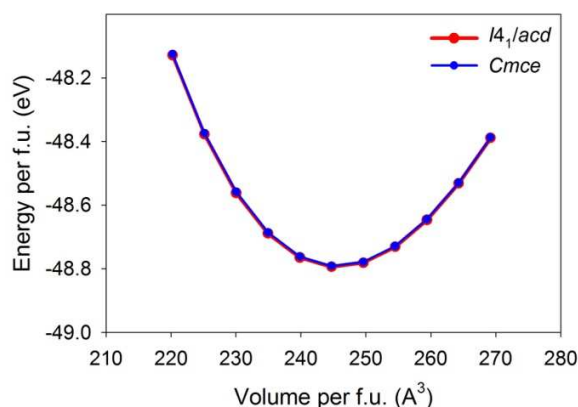
We then optimized the “regular slab” model structures. The optimized *Cmce* structure is in Table 2 and the optimized  $I4_1/acd$  structure is in Table 4, with the latter close to the experimental structure of  $\text{Gd}_5\text{Si}_2\text{Bi}_2$ . Comparison of the energy terms between these two optimized structures (Table 5) shows that, although the differences in  $E_{\text{ES}}$  and  $E_{\text{electronic}}$  are significant, with  $E_{\text{ES}}$  favoring  $I4_1/acd$  and  $E_{\text{electronic}}$  favoring *Cmce*, their  $E_{\text{TOT}}$  values are still fairly close, only 4 meV/f.u. lower in  $I4_1/acd$ . There is still no clue about the cause of the structural difference. More investigations are required.

## 7.4 Conclusions

By constructing the “regular slab” models, comparing their energy terms, and optimizing them, we identified the causes of *Cmce* to *Pnma* distortion. The *O*(I) structure is stabilized by electronic reasons, among which is the inter-slab T-T covalent interactions. The *O*(II) structure is stabilized by affording lower electrostatic energy. The same method, however, failed to rationalize the difference between *Cmce* and  $I4_1/acd$  structures. Further investigations are required.

**Table 5.** The energy terms of  $Gd_5Si_2Bi_2$  in the “regular slab” and the optimized  $Cmce$  and  $I4_1/acd$  structures.

	“Regular Slab” $Cmce$	“Regular Slab” $I4_1/acd$	Optimized $Cmce$	Optimized $I4_1/acd$
$E_{ES}$ (eV/f.u.)	0	-0.00005	0	-0.15063
$E_{electronic}$ (eV/f.u.)	0	-0.00205	0	0.14647
$E_{TOT}$ (eV/f.u.)	0	-0.00210	0	-0.00416

**Figure 5.** The  $E(V)$  curves of  $Gd_5Si_2Bi_2$  in “regular slab”  $I4_1/acd$  and  $Cmce$  structures.

## 7.5 References:

- (1) Pecharsky, V. K.; Gschneidner, K. A. Jr. *Encyclopedia of Condensed Matter Physics*; Elsevier: Amsterdam, 2005, pp 236.
- (2) Warburg, E. *Ann. Phys.* **1881**, 13, 141.
- (3) Debye, P. *Ann. Phys.* **1926**, 81, 1154.
- (4) Giaque, W. F. *J. Am. Chem. Soc.* **1927**, 49, 1864.
- (5) Holtzberg, F.; Gambino, R. J.; McGuire, T. R. *J. Phys. Chem. Solids* **1967**, 28, 2283.
- (6) Pecharsky, V. K.; Gschneidner, K. A. Jr. *Phys. Rev. Lett.* **1997**, 78, 4494.
- (7) Misra, S.; Miller, G. J. *J. Am. Chem. Soc.* **2008**, 130, 13900.
- (8) Mozharivsky, Yu.; Tsokol, A. O.; Miller, G. J. *Z. Kristallogr.* **2006**, 221, 493.
- (9) Svitlyk, V.; Campbell, B. J.; Mozharivskyj, Yu. *Inorg. Chem.* **2009**, 48, 10364.

- (10) (a) Kresse, G.; Hafner, J. *Phys. Rev. B* **1993**, *47*, 558. (b) Kresse, G.; Hafner, J. *Phys. Rev. B* **1994**, *49*, 14251.
- (11) Kresse, G.; Furthmüller, J. *Comput. Mat. Sci.* **1996**, *6*, 15.
- (12) Kresse, G.; Furthmüller, J. *Phys. Rev. B* **1996**, *54*, 11169.
- (13) Kresse, G.; Joubert, D. *Phys. Rev.* **1999**, *59*, 1758.
- (14) Perdew, J. P.; Burke, K.; Ernzerhof, M. *Phys. Rev. Lett.* **1996**, *77*, 3865.
- (15) Monkhorst, H. J.; Pack, J. D. *Phys. Rev. B* **1976**, *13*, 5188.
- (16) Press, W. H.; Flannery, B. P.; Teukolsky, S. A.; Vetterling, W. T. *Numerical Recipes*; Cambridge University Press: New York, 1986.
- (17) Jepsen, O.; Andersen O. K. *TB-LMTO*, version 47; Max-Planck-Institut für Festkörperforschung, Stuttgart, Germany, 2000.
- (18) Dronskowski, R.; Blöchl, P. *J. Phys. Chem.* **1993**, *97*, 8617.
- (19) von Barth, U.; Hedin, L. *J. Phys. C: Solid State Phys.* **1972**, *5*, 1629.
- (20) Lambrecht, W. R. L.; Andersen, O. K. *Phys. Rev. B* **1986**, *34*, 2439.

## Chapter 8

### Conclusions and Future Work

The work in this dissertation rationalized the crystal structures of four classes of compounds and addressed the problems that are not covered by the Zintl-Klemm concept. The conclusions deepen our understanding of the composition-structure relationships of Zintl and polar intermetallic phases and also point to more questions that require further investigations.

(1) By studying the well-known Zintl phases, alkali metal trielides, we found out that it is not sufficient to consider only valence electron transfer and covalency. To rationalize the structures of Zintl phases, we need to consider the effects of metallicity, ionicity, and covalency comprehensively. They compete with one another and favor different structures. Several affecting factors were identified, including relativistic effects, electronegativity differences, and atomic size ratios, and they can affect metallicity, ionicity, covalency and their competition, causing structural variations. The energy partition scheme developed in this part can be applied to any other crystalline phases. It segregates the effect of core positions ( $E_{ES}$ , a function of only core positions, without any relations with where electrons are) from the effect of valence electron localization ( $E_{\text{electronic}}$ ). One of the limitations of this scheme is that the effects of volume upon  $E_{ES}$  and  $E_{\text{electronic}}$  have not yet been quantitatively evaluated, so we can only make qualitative comparison between two structures if they are at different volumes. Finding a way to quantitatively evaluate the volume effects will make our energy partition scheme more powerful.

(2) The comparison between the 1-D zigzag ribbon and the 3-D diamond network in  $A_2AuBi$  ( $A =$  alkali metal) reminds us that besides  $s$  and  $p$  states,  $d$  states can also be actively involved in the covalent interactions between the electronegative elements in Zintl phases, so we should not equalize the Zintl-Klemm formalism with simple electron counting rules such as octet rules, which only applies to  $s-p$  systems. Also, a 3-D electronegative network cannot provide efficient covalent stabilization when the electropositive atoms are large. It will break down into structure motifs with lower dimension, which offers efficient covalent interactions. This part also predicts that  $Na_2AuBi$  will transform from the 1-D zigzag ribbon into the cubic double diamond structure under a pressure higher than 3.29 GPa. It is worthwhile to test this theoretical prediction with high pressure synthesis and X-ray crystallography.



(3) The competition between the  $BaCd_{11}$ - and  $BaHg_{11}$ -type structures in the  $EuAg_xAl_{11-x}$  systems was rationalized with valence electron counting – the  $BaHg_{11}$ -type structure requires more valence electrons to optimize the interactions between Ag/Al atoms. The challenge was the “coloring problem”. Our method, which firstly calculates random coloring schemes to determine whether heteroatomic/homoatomic contacts are energetically favored and then maximizing the number of heteroatomic/homoatomic contacts, can be generally applied to other systems where the coloring problem needs to be handled. For future work, it will be valuable to study  $BaCd_{11}$  and  $BaHg_{11}$  themselves. Why do they adopt different structures while they are isoelectronic? What other factors beside valence electron count can lead to this structural difference?

(4) The preliminary study upon  $Gd_5T_4$  reveals that the distortions from the  $Cmce$  to the  $O(I)$  and  $O(II)$  structures, although the latter two have the same space group,  $Pnma$ , is caused by different reasons.  $O(I)$  is stabilized by electronic energy term, one reason of which is the effect of inter-slab T-T interactions.  $O(II)$  is stabilized not by electrons but by cores – it offers lower electrostatic energy term. The comparison between  $Cmce$  and  $I4_1/acd$  was not successful and requires further study. Moreover, there are more stacking sequences than the three discussed in this work. A complete study needs to be carried out over all of them. Also, as materials with promising magnetocaloric effect, we should also consider the magnetism in these phases.